Electron paramagnetic resonance of some 3d ions in magnesium oxide

Skinner, A.R

Electron Paramagnetic Resonance of some 3d ions in Magnesium Oxide.

by

A.R. Skinner, B.Sc. (Dunelm)

University College

A Thesis submitted to the University of Durham in candidature for the degree of Doctor of Philosophy.

June, 1986.

CONTENTS

ABSTRACT

Electron paramagnetic resonance (E.P.R.) and reflection high energy electron diffraction (RHEED) techniques have been used to study the distribution of iron, chromium and manganese in lightly doped magnesium oxide (MgO) single crystals and powders.

E.P.R. single crystal spectra were recorded at room temperature for all three systems (with the dopants at various concentrations). From these spectra, which agreed with previously published data, the valency states (i.e. Fe^{3+}, Cr^{3+} and Mn^{2+}) of the isolated ions and the symmetry of the sites they occupy were identified. The single crystal Spin-Hamiltonian parameters were used in computer simulations developed to predict the powder spectra and a comparison with the corresponding experimentally observed powder spectra allowed the features due to Fe^{3+}, Cr^{3+} or Mn^{2+} in powdered MgO to be identified.

The distribution of the dopant ions within the MgO lattice has been investigated in some detail. The magnitudes of the isolated ion spectral linewidths and their dependence upon dopant concentration were compared with the predictions of dipolar broadening theory and this showed that the manganese dopant is homogeneously distributed in MgO, (the range of the exchange interaction for Mn^{2+} being at the most 3.65Å) whereas iron and chromium are not.

In Cr/MgO, at the higher dopant concentrations (9,500 p.p.m. and 15,100 p.p.m.), the diffraction patterns obtained from RHEED showed the presence of a separate phase which was identified as the spinel magnesiochromite, $MgCr_2O_4$.

In the same samples there was some evidence in the E.P.R spectra of the presence of a line formerly attributed in the literature to precipitates of $MgCr_2O_4$ in MgO. The discrepancy between the observed cubic Cr^{3+} isolated ion central transition linewidths and those measured by de Biasi and Fernandes (which were consistent with the predictions of their dipolar broadening theory for n = 5 i.e. the range of the exchange interaction for Cr^{3+} ions in MgO was found by de Biasi and Fernandes to be 5.95Å) allowed the spinel and isolated ion concentrations in each of the chromium doped samples to be calculated.

In Fe/MgO the cubic Fe^{3+} central transition linewidth remained approximately constant over the whole range of dopant concentrations examined indicating a constant isolated Fe^{3+} ion concentration which must therefore, at least in the more heavily doped samples, be lower than the total nominal iron concentration. The remaining iron is assumed to exist in clusters and an intense broad line, seen in all the spectra, is attributed to this clustered material. The clusters must be relatively disordered because RHEED showed no evidence of a separate phase with a regular crystal structure.

The E.P.R. line broadening of the fine structure transitions in the cubic Fe^{3+} and Mn^{2+} spectra and the variation of the peak height of the central transition in the cubic Cr^{3+} spectrum implied that strain is present in the regions of the MgO lattice surrounding all three dopants when they exist as isolated ions.

Annealing heat treatments were performed for the iron and chromium doped samples and further linewidth analysis (after heat treatment) supported the above interpretation.

ACKNOWLEDGEMENTS

Firstly, I would like to thank my supervisor, Dr. J.S. Thorp, both for his help and interest in my research throughout the three years I spent in Durham as a postgraduate student and also for his continued enthusiasm regarding this work since then.

My gratitude also extends to:

Professor G.G. Roberts for the use of the departments' facilities;

The technical staff, headed by Mr. F. Spence;

Mr. A. Gracie for typing this thesis;

The S.E.R.C. for the award of a postgraduate studentship;

All my friends at the Universities of Durham and York who have contributed greatly towards making my time in academic research so enjoyable.

Finally, I would especially like to thank my mother and sister; but for their unflagging support and encouragement this thesis might not have been completed.

CHAPTER ONE

1.1 INTRODUCTION

The major industrial use of magnesium oxide is as an electrically insulating refractory oxide which will maintain its insulating properties over a range of temperatures. Applications include being used as the insulator between filament and casing in electrical heating elements and as the insulator surrounding instrumentation cables in nuclear reactor cores. Although generally reliable, sudden electrical breakdown of the insulating MgO may occur, particularly if it is subject to high temperatures. Neither the nature of the electrical conduction mechanism nor the mechanism of dielectric breakdown in magnesium oxide has been unambiguously settled, despite extensive studies of these phenomena carried out over the last twenty or thirty years. In this area, impurities (which are present in the purest commercially available samples and which may also diffuse in at high temperatures from the surrounding filament or heater element) are thought to be important.

Many of the impurities likely to diffuse into MgO are transition metal ions of the iron group and thus an extensive investigation of transition metal doped MgO has been carried out in this department in order to try and determine what influence these impurities have on the insulating properties of magnesia. Several dopant species have been investigated at various dopant concentrations using in the main two analytical techniques. Firstly, Electron Paramagnetic Resonance (E.P.R.) has been used to

determine the dopant valence states and the symmetry of the sites occupied by the dopant ions; secondly, dielectric measurements, across several decades of frequency, have been undertaken.

Studies of bought in doped single crystals, mainly in the as received state, constitute the major proportion of this work. More recently, formation of the spinel $MgFe_2O_4$ in iron-doped magnesium oxide subjected to a variety of heat treatments has been investigated with a view to correlating spinel cluster formation with changes in the dielectric properties of the doped magnesia. The heat treatments mocked the operating conditions of MgO when used as an insulator in electrical heating elements and it was hoped that a study of the spinel precipitates might point to the reasons why dielectric breakdown at elevated temperatures occurs in this material.

In this work bought in single crystals and powders of MgO doped with chromium, iron and manganese at various concentrations have been studied at room temperature using E.P.R. and RHEED. Characterization of the E.P.R. powder spectra of these transition metals in MgO was deemed to be important since in industry this material is usually used in powder form. In addition, the E.P.R. and RHEED investigations of the doped single crystals and powders have revealed that even in the as received samples clustering of iron and chromium dopant ions takes place whereas, in contrast, manganese dopant ions are homogenously dispersed throughout the host lattice. The clustering/ non-clustering tendancies of these transition metals have not been considered in previous investigations of similar

bought in samples carried out in this department.

The isolated transition metal ions were detected and characterized in both the single crystals and powders using E.P.R. Computer simulations using single crystal data were compared with the experimental powder spectra in order to identify the features in these spectra attributable to particular impurity species. In the particular case of the iron doped MgO samples, an E.P.R. spectrum attributed to a phase consisting of "clustered" Fe^{3+} ions, O^{2-} ions, Mg^{2+} ions and vacancies was also detected.

The isolated ion spectral linewidths were analysed in terms of dipolar broadening theory. This analysis allowed the concentrations of isolated Cr^{3+} ions and "clustered" Cr^{3+} ions to be calculated for all the chromium doped samples. Using RHEED the "clustered" Cr^{3+} phase was identified as the spinel magnesiochromite ($MgCr_2O_4$).

The dipolar linewidths of the spectra recorded from the manganese doped samples clearly demonstrated that the Mn^{2+} ions are randomly distributed throughout the MgO lattice and that the range of the exchange interaction for Mn^{2+} in MgO is at the most 3.65Å.

Finally, evidence is presented which demonstrates that strain exists in the regions of the lattice occupied by isolated transition metal ions for all the dopants examined. Certain samples were subjected to heat treatment which was found to have an "annealing" effect, reducing the lattice distortion around the dopant ions.

Some general information concerning defects and impurities in magnesium oxide is presented in Chapter Two. The experimental techniques employed in E.P.R. are described

in Chapter Three. The theoretical aspects of E.P.R. relevant to this work are discussed in Chapters Four to Six. Finally, the experimental results are presented and discussed: for Cr/MgO in Chapter Seven; for Mn/MgO in Chapter Eight and for Fe/MgO in Chapter Nine.

1.2 PREVIOUS WORK

1.2.1 CHROMIUM DOPED MAGNESIUM OXIDE

Chromium was first detected in MgO using the E.P.R. technique as isolated Cr^{3+} ions in sites of octahedral symmetry.[1.1] Since then, the spectrum reported by Low[1.1] has been observed by several other groups of workers.[1.2-1.5] Cr^{3+} has also been found in sites whose symmetry is lower than cubic, namely tetragonal [1.2,1.5, 1.6-1.9] and orthorhombic.[1.2,1.5,1.10-1.12] Cr^{2+} is not detectable using normal E.P.R. methods but has been observed using the technique known as Acoustic Paramagnetic Resonance (A.P.R.)[1.13-1.16] The spectrum of Cr^{+} in MgO has also been reported, but this species is only present in samples which have been subjected to ionizing radiations.[1.17] Finally, an E.P.R. spectrum due to Cr^{3+} pairs in a straight line configuration (i.e. Cr^{3+} - O - Cr^{3+}) has been reported.[1.18]

Chromium tends to adopt the (+3) oxidation state, even in the MgO lattice where it substitutes for a (+2) ion. In fact, Cr^{2+} is only found in appreciable quantities in MgO/Cr samples which have been prepared in a reducing atmosphere.[1.19-1.21] The Cr^{3+} ions which enter the MgO lattice show a strong preference for octahedral

co-ordination.[1.22-1.24] This tendency is confirmed by E.P.R. : in MgO/Cr the cubic Cr^{3+} spectrum is always much more intense than that of any other Cr^{3+} species.

However, it is difficult for Cr^{3+} ions to compensate for their single excess positive charge with respect to the Mg^{2+} ions of the host lattice either by valency variation (see above discussion) or by the inclusion of cationic vacancies. This leads to a lack of solubility of Cr^{3+} ions in MgO : there seems to be a very low (approximately one atomic percent) "saturation" concentration of isolated ions which the MgO lattice can support. Any remaining Cr^{3+} ions tend to cluster and form (with Mg^{2+} ions, O^{2-} ions and vacancies) precipitates of the spinel $MgCr_2O_4$ which is electrically neutral and therefore provides its own internal charge compensation.

The lack of solubility of Cr^{3+} in MgO and the consequent formation of magnesiochromite has been studied by several groups of workers[1.19-1.21,1.25,1.26] using a variety of analytical techniques including E.P.R., x-ray diffraction, diffuse reflectance spectroscopy and magnetic susceptibility measurements. It has been established that incorporation of equal quantities of Cr^{3+} and Li^{+} ions leads to dispersion of the chromium ions.[1.25,1.26] This is because no charge compensation is required for Cr^{3+} - Li^{+} pairs.

From the above discussion, the following conclusions may be drawn concerning the expected behaviour of small quantities of chromium in the magnesium oxide lattice:

(i) The chromium exists mainly as Cr^{3+} ions.

(ii) Up to a certain doping level most of the Cr^{3+} ions are isolated and substitute for Mg^{2+} ions.

(iii) In these circumstances, the Cr^{3+} excess charge will be compensated by Mg^{2+} vacancies (one vacancy for every two Cr^{3+} ions).

(iv) The compensation may be local (such ions have E.P.R. spectra which show that the symmetry of the sites they occupy is non-cubic) or, more likely, non-local, (such ions give rise to the cubic Cr^{3+} E.P.R. spectrum). It is interesting to note that, even if the charge compensation is non-local, lattice strain (presumably caused by the size mismatch between the substitutional Cr^{3+} ions and the Mg^{2+} cations of the host lattice) may be present in the regions of the crystal surrounding dopant ions and, if so, this leads to broadening of the lines in the cubic Cr^{3+} spectrum.[1.4]

(v) At higher doping levels (greater than one atomic percent) the Cr^{3+} ions cluster and combine with Mg^{2+} ions, O^{2-} ions and vacancies to form precipitates of the spinel phase, $MgCr_2O_4$.

1.2.2 MANGANESE DOPED MAGNESIUM OXIDE

E.P.R. studies of manganese doped magnesium oxide single crystals and powders have been extensive. The first spectrum observed, that of isolated Mn^{2+} ions in cubic sites in single crystal MgO, was reported by Low in

1957.[1.27] Since then, this spectrum has been the subject of further investigations. Drumheller and Rubins[1.28] observed "forbidden" hyperfine transitions of the type $\Delta M = \pm 1$, $\Delta m = \pm 1$ in the cubic Mn^{2+} spectrum of single crystal MgO:Mn. Experimentally, the intensity of these transitions varied as $(\sin 4\theta)^2$. With the Mn^{2+} ions in a purely cubic field, this type of intensity variation of the forbidden hyperfine lines is expected because of the admixture of the cubic zero-field splitting parameter, a, with the off-diagonal terms in the spin Hamiltonian. In addition, many quantum transitions of Mn^{2+} in cubic sites in MgO have been observed.[1.29]

The spectral linewidths of Mn^{2+} in octahedral sites in single crystal MgO have also been investigated. It has been reported that the peak-to-peak linewidths are concentration dependent (closely following a $(\text{concentration})^{\frac{1}{2}}$ law) and that the lineshape is Lorentzian.[1.30] Application of uniaxial stress to MgO:Mn single crystals shifts the magnetic field positions of the fine structure transitions in each hyperfine pentad.[1.31] In the presence of random internal crystal strains the same transitions are broadened by an amount proportional to $(2M - 1)^2$ where M is the electronic quantum label of the transition.[1.31]

The E.P.R. spectrum of Mn^{2+} ions in cubic symmetry in powdered MgO has been reported.[1.32-1.34] Only the six $M = +\frac{1}{2} \longleftrightarrow -\frac{1}{2}, m$ and the "forbidden" $M = +\frac{1}{2} \longleftrightarrow -\frac{1}{2}$, $\Delta m = \pm 1$ transitions observed in the single crystal spectrum survive in the powder spectrum. In some cases, small shoulders and divergences associated with the fine structure transitions have been detected.[1.33,1.34]

Other similar spectra have been attributed to Mn^{2+} ions in sites of <100> axial symmetry either on the basis that the intensity ratio of the forbidden lines to the allowed lines is too high for the crystal field surrounding the Mn^{2+} ions to be purely cubic,[1.35] or on the basis that the peak height of the $M = +\frac{1}{2} \longleftrightarrow -\frac{1}{2}$, m lines decreases and their width increases as m increases (in a purely cubic field all six $M = +\frac{1}{2} \longleftrightarrow -\frac{1}{2}$, m lines have the same heights and widths).[1.32,1.36] Methods due to Allen[1.37] and Bleaney and Rubins[1.38] have been used to calculate the value of the fine structure constant, D, which determines the magnitude of the axial distortion of the cubic crystal field.

Computer simulations of the powder spectrum of Mn^{2+} ions in both cubic and axial fields in MgO have been compared with experimental spectra and it was found that, in high surface area powders, the crystal field surrounding the Mn^{2+} ions has both axial and cubic components.[1.39] In low surface area powders the Mn^{2+} ions occupy sites of purely cubic symmetry.[1.32,1.40]

An E.P.R. spectrum attributed to Mn^{2+} pairs in MgO has been reported in samples with a relatively high manganese content (approximately one atomic percent)[1.41], but when the manganese concentration is lower than this, the body of evidence suggests that in both single crystal and low surface area powder materials the dopant exists as isolated Mn^{2+} ions in sites of octahedral symmetry. In high surface area powders the site symmetry changes to <100> axial because a large proportion of the dopant ions are located near to the sample surface where the lattice is

severely distorted.

When the concentration of manganese is very high (approximately five atomic percent or greater) a very intense broad Lorentzian line which completely swamps the six $M = +\frac{1}{2} \longleftrightarrow -\frac{1}{2}, m$ lines of the powder spectrum due to isolated Mn^{2+} ions in cubic sites is observed.[1.42,1.43] This line has been attributed to clusters of manganese ions coupled by exchange.[1.43] Other reports have identified a broad line observed in the powder spectra of manganese doped magnesia samples heat treated in air when the manganese concentration is greater than two atomic percent with the phase Mg_6MnO_8 (in this phase the Mn^{4+} ions are coupled by exchange).[1.20,1.44] Addition of lithium enables manganese ions to enter into solid solution as Mn^{3+} and/or Mn^{4+} depending on the lithium/manganese ratio.[1.44,1.45] For samples heat treated in hydrogen the dopant is almost all present as Mn^{2+} (with a small fraction existing as Mn^{4+} in the Mg_6MnO_8 phase). Also, for powder samples initially prepared under reducing conditions and then heat treated in air, if the Mn^{2+} ions are originally isolated and in purely cubic sites (i.e. those incorporated in the bulk of the sample) then they are not oxidized to Mn^{4+} (which consequently forms the Mg_6MnO_8 phase) even at temperatures as high as $1000^{o}C$.

From the above discussion we may conclude that:

(i) If the manganese concentration is low, the dopant exists as isolated Mn^{2+} ions in sites of cubic symmetry in both single crystal and low surface area powdered MgO.

(ii) In high surface area MgO:Mn powders the site symmetry changes from cubic to <100> axial.

(iii) At intermediate dopant concentrations (greater than 0.5 but less than 2.0 atomic percent) Mn^{2+} pairs are formed.

(iv) At high manganese concentrations (greater than 2.0 atomic percent) large scale clustering of the dopant occurs so that very few isolated Mn^{2+} ions remain.

(v) The valency adopted by the majority of the manganese ions varies in heavily doped samples depending upon the heat treatment history of those samples:

if prepared in air, the manganese exists mainly as Mn^{4+} and ordering of clusters of ions may occur to form the phase Mg_6MnO_8.

if prepared in a reducing (usually hydrogen) atmosphere the manganese is present as Mn^{2+}.

(vi) Clustering of manganese ions in heavily doped samples, whether prepared in an oxidizing or a reducing atmosphere, may be avoided by the addition of lithium.

1.2.3 IRON DOPED MAGNESIUM OXIDE

E.P.R. spectra due to both Fe^{3+} and Fe^{2+} isolated ions in sites of octahedral symmetry have been reported following investigations of single crystal MgO lightly doped with iron.[1.5,1.46-1.51]

In the case of the cubic Fe^{3+} spectrum, transitions for which $\Delta M = 2,3,4\&5$ as well as the allowed $\Delta M = \pm 1$ transitions have been observed.[1.52,1.53] The effect of uniaxial stress on the cubic Fe^{3+} spectrum is similar to its effect on the cubic Mn^{2+} spectrum: application of pressure to a MgO:Fe single crystal shifts the magnetic field positions of the fine structure lines in this spectrum.[1.31] Also, as in the case of the cubic Mn^{2+} spectrum, in the presence of random internal crystal strains the lines in the cubic Fe^{3+} spectrum are broadened by an amount proportional to $(2M - 1)^2$. The cubic Fe^{2+} spectrum is only detectable at low temperatures (less than 77K) because of the short relaxation time of this ion. E.P.R. spectra due to Fe^{3+} ions in sites of non-cubic symmetry have also been reported.[1.54,1.55] Fe^{+} is not normally present in iron doped MgO, but this species has been produced in samples subjected to ionizing radiations and its E.P.R. spectrum was subsequently recorded.[1.48,1.56]

Thus, the E.P.R. evidence suggests that small quantities of iron may exist either as Fe^{2+} or as Fe^{3+} in MgO. Brynestad and Flood[1.57] showed that heat treatment of a sample, the ambient atmosphere and pressure during the heat treatment and the total iron concentration are the important factors in determining which of these valency states is adopted by the majority of the iron dopant.

The effect of heat treatment upon the valence state of the dopant in MgO:Fe has been determined by following the variation of the intensities of the cubic Fe^{2+} and Fe^{3+} spectral lines with heat treatment[1.58] and the conclusions drawn from this investigation broadly agree with those of

Brynestad and Flood.[1.57] However, accurate determination of concentration from E.P.R. spectral line intensities is difficult for two main reasons. Firstly, there are inaccuracies inherent in the method; secondly, and perhaps more importantly, change of ionic valency state may not be the only effect of heat treatment. Clustering of impurities and vacancies may also occur and unless both processes can be accurately monitored at the same time, it is impossible to tell the extent to which each contributes to changes in spectra which take place as a result of heat treatment.

The clustering phenomenon in MgO:Fe was first studied in detail by Fine and various co-workers[1.59-1.63] using electron microscopy and magnetometry. It was found that, for samples containing between about one and five atomic percent of iron, heat treatment in the region of 700^{o}C produced precipitates of non-stoichiometric magnesioferrite which were coherent with the host lattice. The composition of the precipitates (in terms of the exact cation content and distribution) was found to depend upon aging temperature,[1.60] whilst their final size depended upon the total iron concentration in the MgO crystal.[1.63]

Further investigations using x-ray diffraction, E.P.R., magnetometry and electron microscopy techniques[1.50,1.51, 1.64-1.68] have shown that in lightly doped MgO:Fe samples prepared in air, a small fraction of the dopant exists as isolated Fe^{3+} ions in cubic sites whilst the remaining dopant ions cluster to form precipitates of magnesioferrite. The clusters can be dissolved by addition of lithium, the degree of dissolution depending on the Li^{+}/Fe^{3+} ratio. If the ratio of Li^{+} to Fe^{3+} ions is equal to or exceeds one,

then total dissolution of the clusters takes place and the Fe^{3+} ions are homogenously dispersed throughout the host lattice.[1.66,1.68] If the MgO:Fe samples are prepared in a reducing atmosphere, then the dopant exists as isolated Fe^{2+} ions in cubic sites.[1.20,1.66,1.68]

Spectra recorded from MgO:Fe powders have also been reported in the literature.[1.39,1.69] The features observed have in all cases been found to be attributable to isolated Fe^{3+} ions in cubic sites. Assignment of these features has been based on the agreement between their observed and theoretically predicted field positions. The theoretical predictions of Beltran-Lopez and Castro-Tello[1.39] were incorporated into a computer simulation of the powder absorption curve of the $M = +\frac{1}{2} \longleftrightarrow -\frac{1}{2}$ transition for isolated Fe^{3+} ions in cubic sites in MgO.

In conclusion, for MgO:Fe samples doped with up to approximately one atomic percent of iron, it is reasonable to assume that:

(i) The iron may be in the (+2) or (+3) valency state.

(ii) Heat treatment may alter the spectral state of the iron.

(iii) In either valency state, the isolated iron ions are expected to substitute for Mg^{2+}.

(iv) When the iron is present as Fe^{3+}, the excess charge of this ion will be compensated by Mg^{2+} vacancies (considerations of electrical neutrality dictate

that there will be one vacancy for every two Fe^{3+} ions).

(v) Compensation of the Fe^{3+} excess charge may be local or non-local: the two situations are distinguishable by E.P.R. (if the compensation is non-local we observe the cubic Fe^{3+} spectrum whereas if the compensation is local we observe a spectrum attributable to Fe^{3+} ions in non-cubic sites).

(vi) Appropriate heat treatment or preparation conditions will cause precipitation of clusters of magnesioferrite, the stoichiometry of which can vary.

REFERENCES

1.1 W. Low Phys. Rev. 105, 801 (1957)

1.2 J.E. Wertz and P. Auzins Phys. Rev. 106, 484 (1957)

1.3 J.S. Thorp, M.D. Hossain and L.J.C. Bluck J. Mat. Sci. 14, 2853 (1979)

1.4 J.S. van Wieringen and J.G. Rensen, Paramagnetic Resonance, Proc. 1st Internat. Conf., Jerusalem, Vol I, Ed. W. Low, Academic Press, (1963) p.105.

1.5 J.E. Wertz, J.W. Orton and P. Auzins J. Appl. Phys. Supplement 33, 322 (1962).

1.6 J.E. Wertz and P. Auzins J. Phys. Chem. Solids 28, 1557 (1967).

1.7 S.A. Marshall, J.A. Hodges and R.A. Serway Phys. Rev. 136A, 1024 (1964)

1.8 B. Henderson and T.P.P. Hall Proc. Phys. Soc. 90, 511 (1967).

1.9 R.A. Serway, S.A. Marshall and R.B. Robinson Phys. Stat. Sol. (B) 56, 319 (1973).

1.10 J.H.E. Griffiths and J.W. Orton Proc. Phys. Soc. 73, 948 (1959)

1.11 A.J.B. Codling and B. Henderson J. Phys. C:Solid State Phys. 4, 1242 (1971)

1.12 J.J. Davies and J.E. Wertz J. Phys. C: Solid State Phys. 8, 1235 (1975).

1.13 F.G. Marshall and V.W. Rampton J. Phys. C: Solid State Phys. 1, 594 (1968).

1.14 J.R. Fletcher, F.G. Marshall, V.W. Rampton, P.M. Rowell and K.W.H. Stevens Proc. Phys. Soc. 88, 127 (1968).

1.15 F.S. Ham Phys. Rev. B 4, 3854 (1971).

1.16 J.R. Fletcher and K.W.H. Stevens J. Phys. C: Solid State Phys. 2, 444 (1969).

1.17 G. Rius and A. Herve Solid State Comm. 11, 795 (1972).

1.18 J. Marguglio and Y.M. Kim J. Chem. Phys. 62, 1497 (1975)

1.19 M. Valigi Z. Phys. Chem(Frankfurt), N.F. 97, 241 (1975)

1.20 D. Cordischi, D. Gazzoli and M. Valigi J. Solid State Chem. 24, 371 (1978)

1.21 M. Valigi and A. Cimino Z. Phys Chem(Frankfurt), N.F. 99, 131 (1976).

1.22 D.S. McClure J. Phys. Chem. Solids 3, 311 (1957).

1.23 J.D. Dunitz and L.E. Orgel J. Phys. Chem. Solids 3, 318 (1957).

1.24 G. Blasse, Philips Res. Repts. Supplement N 3 (1964).

1.25 A. Cimino, M. Lo Jacono, P. Porta and M. Valigi Z Phys. Chem(Frankfurt), N.F. 51, 301 (1966).

1.26 D. Cordischi, J.C. Vickerman and A. Cimino Trans Faraday Soc. 66, 1312 (1970).

1.27 W. Low Phys. Rev. 105, 793 (1957).

1.28 J.E. Drumheller and R.S. Rubins Phys. Rev. 133, A1099 (1964).

1.29 F. Chiarini, M. Martinelli and G. Ranieri J. Mag. Res. 14, 60 (1974).

1.30 M.D. Hossain, J.S. Thorp and A.D. Inglis "E.S.R. Linewidths in Mn^{2+}/MgO" (Unpublished).

1.31 E.R. Feher Phys. Rev. 136, A145 (1964).

1.32 D. Cordischi, R.L. Nelson and A.J. Tench Trans. Faraday Soc. 65, 2740 (1969).

1.33 N.G. Kakazei and M.V. Vlasova, J. Appl. Spectroc. (U.S.A.), Translated From Zhurnal Prikladnoi Spektroskopii 24, 150 (1976).

1.34 J. Rubio O., E. Munoz P., J. Boldu O., Y. Chen and M.M. Abraham J. Chem. Phys. 70, 633 (1979).

1.35 G.J. Wolga and R. Tseng Phys. Rev. 133, A1563 (1964)

1.36 T. Yamamura, A. Hasegawa, Y. Yamada and M. Miura Bull. Chem. Soc. Japan 43, 3377 (1970).

1.37 B.T. Allen J. Phys. Chem. 43, 3820 (1965).

1.38 B. Bleaney and R.S. Rubins Proc. Phys. Soc. 77, 103 (1961)

1.39 V. Beltran-Lopez and J. Castro-Tello J. Mag. Res. 39, 437 (1980).

1.40 S. Eidels-Dubovoi and V. Beltran-Lopez J. Mag. Res. 32, 441 (1978).

1.41 E.A. Harris J. Phys. C: Solid State Phys. 5, 338 (1972).

1.42 R.A. Weeks and A. Chatelain J. Am. Cer. Soc. 61, 297 (1978).

1.43 F. Gesmundo and P.F. Rossi J. Solid State Chem. 8, 297 (1973).

1.44 D. Cordischi and M. Lo Jacono Z. Phys. Chem. (Frankfurt), N.F. 74, 93 (1971)

1.45 A. Cimino, M. Lo Jacono, P. Porta and M. Valigi Z. Phys. Chem.(Frankfurt), N.F. 59, 134 (1968)

1.46 W. Low Proc. Phys. Soc.(London) B69, 1169 (1956).

1.47 W. Low and M. Weger Phys. Rev. 118, 1130 (1960).

1.48 A.M. Stoneham, K.A. Müller and W. Berlinger Solid State Comm. 10, 1005 (1972).

1.49 F.A. Modine, E. Sonder and R.A. Weeks J. Appl. Phys. 48, 3514 (1977).

1.50 J.S. Thorp, R.A. Vasquez, C. Adcock and W. Hutton J. Mat. Sci. 11, 89 (1976).

1.51 A.D. Inglis and J.S. Thorp J. Mat. Sci. 16, 1887 (1981)

1.52 J.L. Kolopus and L.V. Holroyd Phys. Stat. Sol. 8, 711 (1965).

1.53 R.S. de Biasi Phys. Stat. Sol. B 87, K29 (1978).

1.54 B. Henderson, J.E. Wertz, T.P.P. Hall and R.D. Dowsing J. Phys. C: Solid State Phys. 4, 107 (1971).

1.55 R.A. Weeks, J. Gastineau and E. Sonder Phys. Stat. Sol. A 61, 265 (1980)

1.56 J.W. Orton, P. Auzins, J.H.E. Griffiths and J.E. Wertz Proc. Phys. Soc. 78, 554 (1961).

1.57 J. Brynestad and H. Flood Z. Fur Elektrochem. 62, 953 (1958).

1.58 E. Sonder, T.G. Stratton and R.A. Weeks J. Chem. Phys. 70, 4603 (1979)

1.59 G.W. Groves and M.E. Fine J. Appl. Phys. 35, 3587 (1964).

1.60 G.P. Wirtz and M.E. Fine J. Appl. Phys. 38, 3729 (1967)

1.61 G.P. Wirtz and M.E. Fine J. Am. Cer. Soc. 51, 402 (1968)

1.62 K.M. Woods and M.E. Fine J. Am. Cer. Soc. 52, 186 (1969).

1.63 K.M. Woods and M.E. Fine J. Appl. Phys. 40, 3425 (1969)

1.64 J.S. Thorp, A.P. Johnson and C. Savage J. Mat. Sci. Lett. 4, 221 (1985).

1.65 R.S. de Biasi Magn. Lett. 1, 103 (1978).

1.66 D. Cordischi, F. Pepe, M. Schiavello and M. Valigi J. Chem. Soc., Faraday I 73, 62 (1977).

1.67 A.D. Inglis, G.J. Russell and J.S. Thorp J. Mat. Sci. 17, 2939 (1982).

1.68 M. Valigi, F. Pepe and M. Schiavello J. Chem. Soc., Faraday I 71, 1631 (1975).

1.69 J.L. Boldu, E. Munoz P., Y. Chen and M.M. Abraham J. Chem. Phys. 80, 574 (1984).

CHAPTER TWO

CRYSTALLOGRAPHY AND HEAT TREATMENT OF THE DOPED MAGNESIUM OXIDE SAMPLES

2.1 THE CRYSTAL STRUCTURE OF MAGNESIUM OXIDE

Magnesium oxide is an ionic solid which crystallizes with the "sodium chloride" or "rocksalt" structure.[2.1] This structure may be described as a cubic close packed array of oxygen ions with magnesium ions occupying all the octahedral interstices. The Mg^{2+} ions are arranged in a face-centred cubic (F.C.C.) pattern as are the O^{2-} ions; the two interpenetrating F.C.C. sublattices are aligned but one is displaced from the other along a reference <100> axis of the cubic unit cell by a distance equal to half the lattice parameter, a. Thus each Mg^{2+} ion is octahedrally surrounded by six O^{2-} ions and similarly each O^{2-} ion is octahedrally surrounded by six Mg^{2+} ions to form a regular three-dimensional array (the co-ordination number for both ions is therefore six). In terms of atomic co-ordinates the MgO structure has ions at the following locations:

Mg^{2+} at $\frac{1}{2},0,0$; $0,\frac{1}{2},0$; $0,0,\frac{1}{2}$; $\frac{1}{2},\frac{1}{2},\frac{1}{2}$

O^{2-} at $0,0,0$; $0,\frac{1}{2},\frac{1}{2}$; $\frac{1}{2},0,\frac{1}{2}$; $\frac{1}{2},\frac{1}{2},0$

where the atomic co-ordinates are expressed as fractions of the unit cell length (lattice parameter) along three mutually perpendicular <100> type directions. A pictorial representation of the MgO unit cell is shown in Figure 2.1.

The ratio of the radius of the cation to that of the anion is often the most important factor in determining

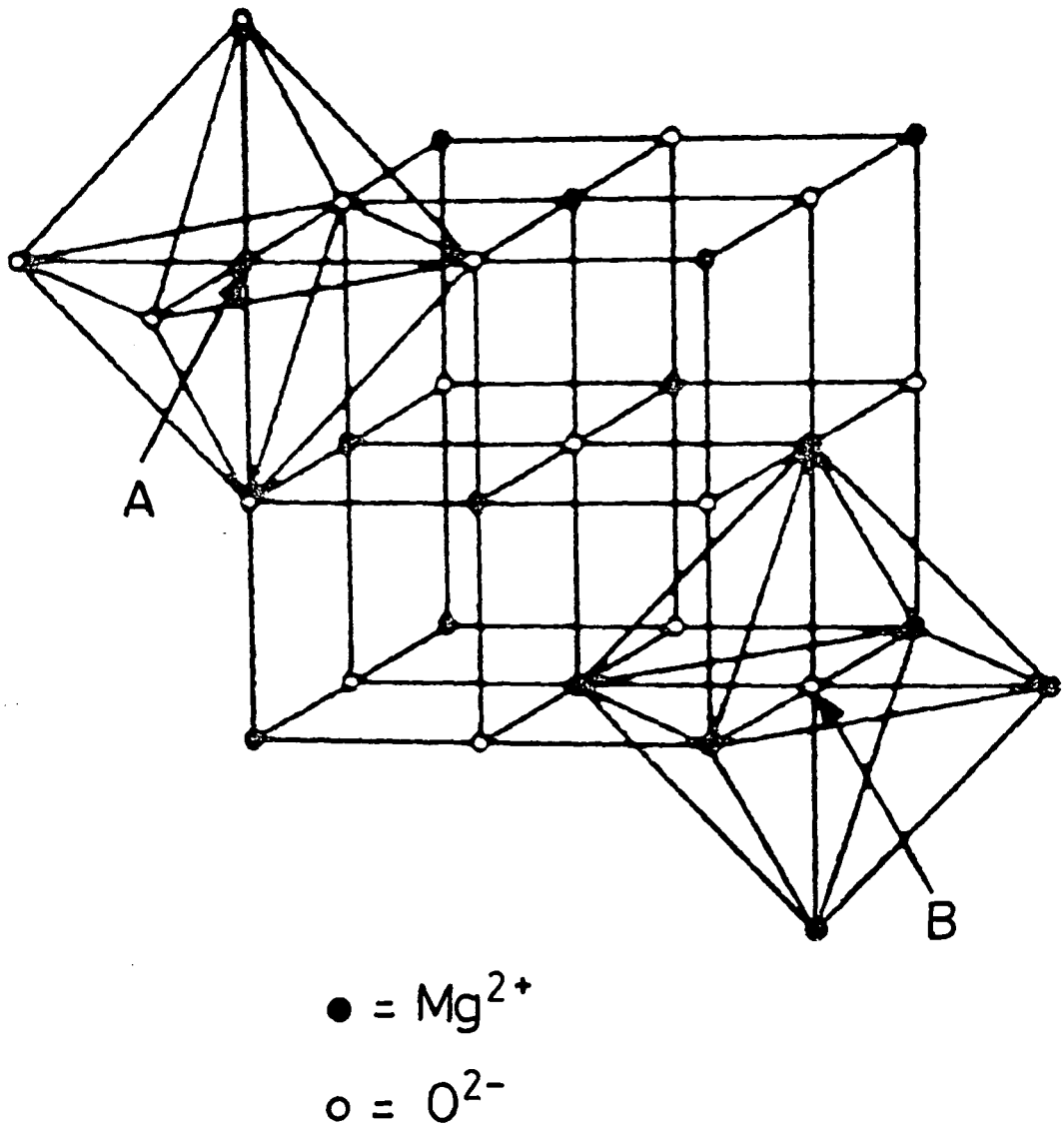

FIGURE 2.1 THE CRYSTAL STRUCTURE OF MgO SHOWING THE OCTAHEDRAL CO-ORDINATION OF THE Mg^{2+} (A) and O^{2-} (B) IONS.

the structure of an ionic compound. If we assume that the anions and cations are hard spheres of fixed radii and that the coordination number will be as high as possible, then we can predict the crystal structure from the value of this ratio.[2.2]

An ionic solid will have an "idealized" rocksalt structure if the anions are in mutual contact as well as in contact with the cations. For such a compound, as Figure 2.2(a) shows, $r_+/r_- = (\sqrt{2} - 1)$ where r_+ & r_- are, respectively, the cationic and anionic radii.

If the ratio r_+/r_- is less than 0.414 $(= \sqrt{2} - 1)$ then the anions will be in contact with each other but not with the cations. Thus compounds for which $r_+/r_- < 0.414$ will not adopt the sodium chloride structure because this would result in there being large electrostatic forces of repulsion between the anions. Such materials tend to adopt the zinc blende (cubic ZnS) structure, even though the coordination number of the cations is reduced to four by doing so (the cations are tetrahedrally surrounded by anions), because this structure allows the anions to be in mutual contact as well as in contact with the cations when the radius ratio, r_+/r_-, is much less than 0.414.[2.2]

If the radius ratio exceeds 0.414 then the rocksalt structure is still favoured but the anions now become separated from each other although they remain in contact with the cations. However, when r_+/r_- reaches a value of 0.732 the cesium chloride structure becomes favourable because at this high value of the radius ratio adoption of the CsCl structure increases the cation coordination number to eight whilst at the same time allowing the

anions to remain in mutual contact as well as in contact with the cations.[2.2]

Thus compounds of the type MX (where M is a cation and X is an anion) will tend to adopt the sodium chloride structure if the ratio r_+/r_- lies between 0.414 and 0.732. If $r_+/r_- = 0.414$ then the compound has the "idealized" rocksalt structure (Figure 2.2(a)); if $0.732 > r_+/r_- > 0.414$ then the compound still has the sodium chloride structure but the anions, although in contact with the cations, are separated from each other (see Figure 2.2(b)).

Reference to Figures 2.2(a) and (b) shows that if a compound crystallizes with the rocksalt structure, whether idealized or not, then, in terms of the ionic radii, the lattice parameter, a, is given by:

$$a = 2(r_+ + r_-) \qquad (2.1)$$

If our assumption that the ions are hard, incompressible spheres with fixed radii is valid then, by substituting appropriate values of r_+ (= $r(Mg^{2+})$) and r_-(= $r(O^{2-})$) into equation 2.1, we should obtain a value for the lattice parameter of magnesium oxide which corresponds to that measured experimentally using X-ray diffraction methods (a_{exp} = 4.2112Å at 21°C [2.1]).

The ions would behave like hard spheres and their radii would not vary from compound to compound if the bonding between them were purely ionic in character. This is because if the bonding were totally ionic, complete electron transfer from cation to anion would take place

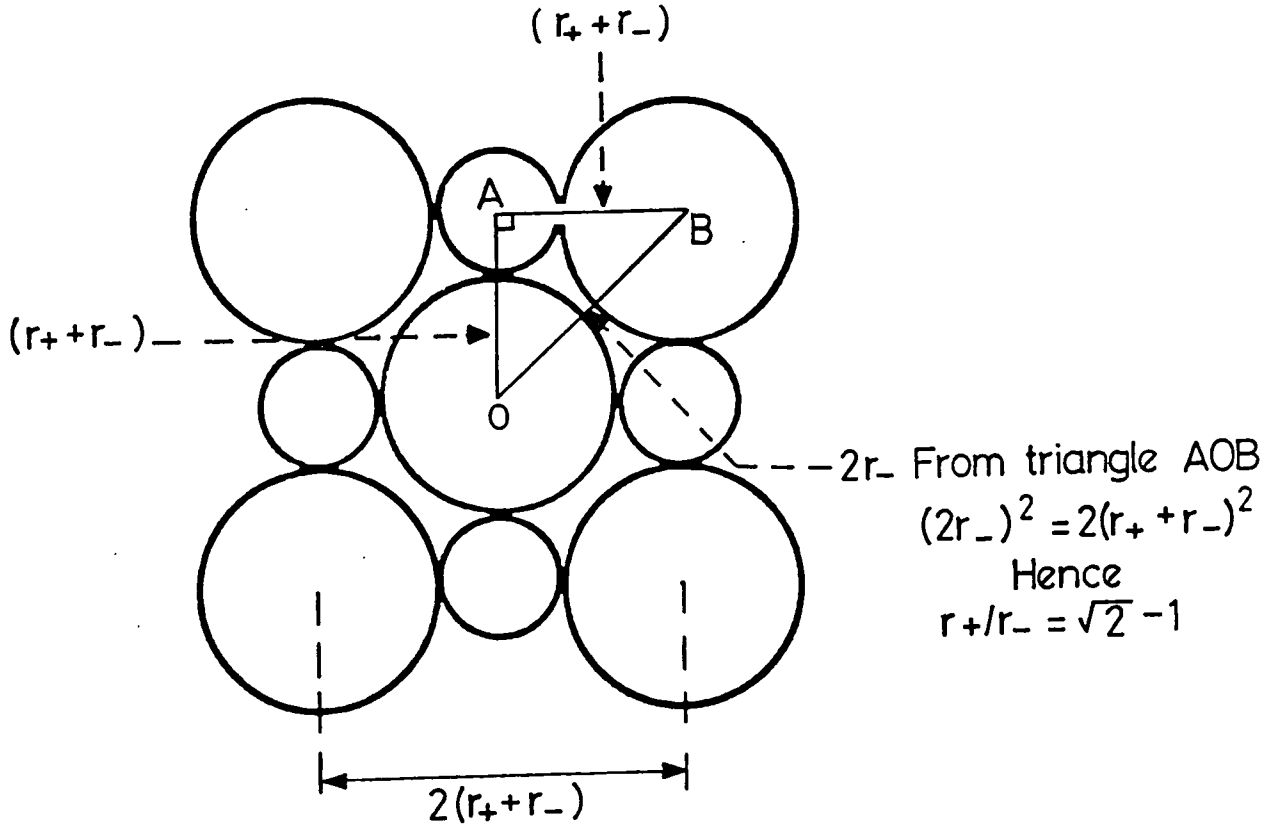

FIGURE 2.2(a) A CROSS SECTION OF THE UNIT CELL OF A COMPOUND WITH THE "IDEALIZED" ROCKSALT STRUCTURE.

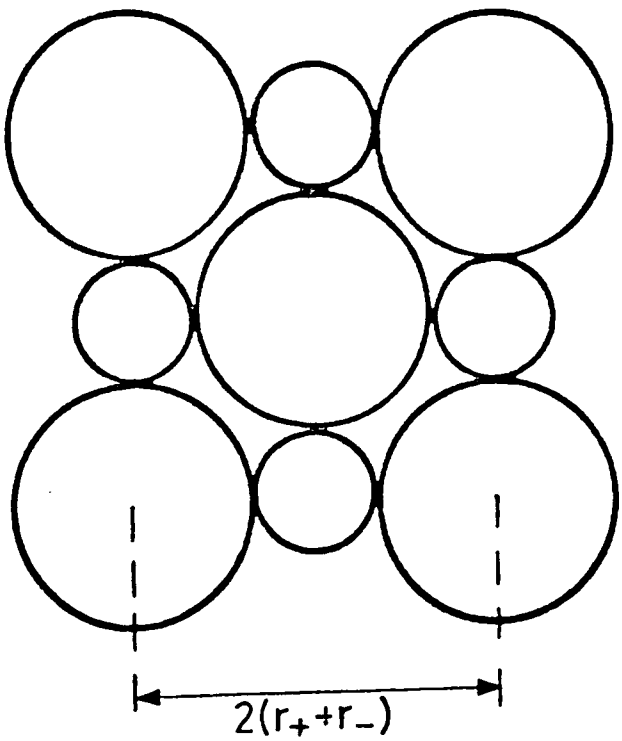

FIGURE 2.2(b) A CROSS SECTION OF THE UNIT CELL OF MgO SHOWING THE SEPARATION OF THE ANIONS.

thereby preventing any overlap of the cationic and anionic wave functions.

However, the bonding in any real ionic crystal is always partially covalent in nature (Bluck,[2.3] using an approach due to Pauling[2.4], showed that the percentage ionic character in the MgO bond is only 68%). The covalent aspect to the bonding causes the anionic and cationic electron clouds to overlap in the region of the bond so that the separation of the cation and anion is determined rather by the strength of the bond than by their respective ionic radii. Hence, in the presence of covalent bonding the ions are much more tightly packed than they would be if they were purely ionically bonded incompressible spheres with fixed radii.

Therefore, precise determination of individual ionic radii is very difficult because the spherical symmetry of the outer electronic shells is distorted as a result of covalent bonding. This distortion in turn causes the radius of an ion in a compound to be heavily dependent upon its electronic spin state and also upon its coordination number in that compound. Slight variations in the radius of an ion may also be found among compounds in which that ion has the same coordination number and electronic spin state.

Nevertheless, ionic radii have been estimated using several methods of approach and much of the work in this area has been reviewed by Shannon and Prewitt[2.5] They considered a large number of reported experimental observations of interatomic distances and assumed a linear

relationship between ionic volume and unit cell volume for a series of isotypic oxides and fluorides. Shannon and Prewitt deduced that the ionic radii of Mg^{2+} and O^{2-} in six-fold coordination are:

$$r(Mg^{2+}) = 0.72\text{Å}; \qquad r(O^{2-}) = 1.40\text{Å}$$

Substitution of these values into equation 2.1 yields a value for the lattice parameter, a, of 4.24Å. Bearing in mind the empirical nature of the methods used to determine ionic radii, this value is in remarkably good agreement with that found experimentally (4.2112Å). It is likely that the measured value of a is slightly smaller than that suggested by equation 2.1 because of the effects of covalent bonding, which as explained above, will cause the actual inter-ionic distances to be less than those calculated assuming that the ions are hard spheres.

Using Shannon and Prewitt's values of $r(Mg^{2+})$ and $r(O^{2-})$ the radius ratio, r_+/r_- for MgO is 0.514. We may conclude from this that MgO does not have the "idealized" rocksalt structure (Figure 2.2(a)); instead it adopts the structure shown in Figure 2.2(b) which has the anions in contact with the cations but separated from each other.

2.2 DEFECTS AND IMPURITIES IN THE MAGNESIUM OXIDE SAMPLES

The arc-fusion method was used to grow the doped magnesium oxide samples examined in this work which were obtained from W. & C. Spicer Ltd. of Cheltenham. The nominal concentrations, in parts per million (p.p.m.) by

weight, of the dopant species in the crystals studied were as follows:

MgO:Cr	MgO:Fe	MgO:Mn
800	310	840
3,600	2,300	1,400
7,400	4,300	2,900
9,500	8,500	
15,100	11,900	
	12,900	

The nominal dopant concentrations listed above were determined (using X-ray fluorescence techniques) by Johnson, Matthey & Co. and were claimed by the manufacturers to be accurate to within 2%.

The chromium doped crystals were all green in colour, the shade of green becoming progressively darker as the dopant concentration increased. The samples containing iron ranged in colour from cloudy white through progressively darker shades of green to olive green as the iron concentration increased. The three MgO:Mn samples were pink, the deepness of the pink colour increasing with the manganese concentration.

The doped single crystals purchased from Spicer were approximately 0.1 cm thick and 1cm x 1cm in area; they had been cleaved so that the edges of the crystal slices laid along three mutually perpendicular <100> directions. Further cleaving along the <100> directions produced samples approximately 0.1 cm thick and 0.3cm x 0.8cm in area. x-ray back reflection photographs confirmed the

orientation of these smaller cleaved slices, from which the single crystal E.P.R. spectra were recorded.

Powder samples were prepared by crushing Spicer single crystal chippings with a mortar and pestle. The powders were sieved through a 185μm mesh in order to control the upper limit of the particle size and thereby ensure that a large number of crystallites (at least 20,000) were undergoing resonance when the powder spectra were recorded.

The E.P.R. spectra reported in Chapters 7 to 9 show that the chromium dopant exists as Cr^{3+} ions in MgO, the iron dopant as Fe^{3+} ions and the manganese dopant as Mn^{2+} ions. It is generally accepted that the dopant ions substitute for Mg^{2+} in the host lattice[2.6-2.8] and the recorded E.P.R. spectra support this suggestion, since they show that the dopant ions occupy sites of octahedral symmetry.

Isolated impurity ions will distort the MgO host lattice in the region of the sites they occupy because of the size mismatch between them and the Mg^{2+} ions which usually occupy these sites. Shannon and Prewitt[2.5] give the ionic radii of Mn^{2+}, Fe^{3+} and Cr^{3+} in high spin states in octahedral symmetry as:

$$r(Mn^{2+}) = 0.82\text{Å}; \quad r(Fe^{3+}) = 0.65\text{Å}; \quad r(Cr^{3+}) = 0.62\text{Å}$$

Mn^{2+}, being larger than Mg^{2+}, will tend to set up a compressional strain in the region of the lattice where it is located. Fe^{3+} and Cr^{3+} are both smaller than Mg^{2+} and hence the lattice will tend to 'collapse in' on these ions thereby setting up a local ~~extensional~~ tensile strain. Both

types of lattice distortion i.e. whether the MgO bonds are stretched or compressed, may result in so called 'strain broadening' of the E.P.R. lines in the isolated ion spectrum (see section 6.3). Evidence that the E.P.R. lines of isolated Mn^{2+}, Cr^{3+} and Fe^{3+} ions in MgO are strain broadened is presented in Chapters 7 to 9.

Whilst Mn^{2+} and Mg^{2+} have the same valency, Fe^{3+} and Cr^{3+} have excess positive charge with respect to the Mg^{2+} ion of the host lattice and therefore substitution of these ions for Mg^{2+} will require some form of charge compensation. Three possibilities have been suggested for the mechanism by which this occurs.

Firstly, Li^{+} ions may be incorporated into the host lattice in equal quantities with the trivalent ion to provide the necessary charge compensation.[2.9,2.10] Although MgO will readily accept lithium into its lattice as a dopant analysis shows that it is not present in significant amounts unless deliberately introduced. As the MgO crystals examined were not deliberately doped with lithium this method of charge compensation is considered unlikely.

Secondly, compensation for the excess charge of trivalent ions may be provided by interstitial O^{2-} ions. This is also considered unlikely because such interstitials have a high energy of formation ($\sim$ 12eV) and, in addition, because of their large size, O^{2-} ions in interstitial sites would seriously distort the lattice.

Finally, it is probable that charge compensation is provided by cation vacancies. Since, for full charge compensation, one vacancy is required for every two

trivalent impurity ions it is perhaps surprising that the E.P.R. spectra of isolated Fe^{3+} and Cr^{3+} ions in octahedral symmetry are so readily detected.[2.11,2.12] From the cubic symmetry displayed by the E.P.R. spectra of Fe^{3+} and Cr^{3+}, we may conclude that the compensating vacancies are at a distance of at least two lattice parameters from the sites occupied by the trivalent impurity ions.

The large number of cationic vacancies required to compensate for the excess charge of trivalent impurity ions probably accounts for the low solubility of Fe^{3+} and Cr^{3+} in MgO.[2.9,2.10] Evidence discussed in Chapters 7 and 9 shows that, even at low impurity concentrations, only a fraction of the Fe^{3+} or Cr^{3+} dopant ions enter into solid solution in the MgO samples examined. The dissolved Fe^{3+} and Cr^{3+} ions give rise, respectively, to the E.P.R. spectra of isolated Fe^{3+} and Cr^{3+} ions in cubic symmetry sites mentioned earlier. The remainder of the trivalent impurity ions are shown in Chapters 7 and 9 to associate together, in the case of Cr^{3+} to form the spinel $MgCr_2O_4$ and in the case of Fe^{3+} to form a clustered iron phase which may be the spinel $MgFe_2O_4$. When manganese is the impurity species no such problems of charge compensation arise, and, as shown in Chapter 8, even in the MgO crystal containing the greatest amount of manganese (2,900 p.p.m.) all the dopant enters into solid solution and exists as isolated Mn^{2+} ions.

The causes of association between trivalent impurity ions in MgO were considered by Gourdin, Kingery and Driear.[2.13,2.14] As mentioned earlier, interstitials of

magnesium, oxygen or the dopant species are not expected to exist in isolation because of their high energy of formation (the E.P.R. spectra of Fe^{3+}, Cr^{3+} and Mn^{2+} in MgO prove that, when isolated, these ions do not occupy interstitial sites, rather they occupy sites of octahedral symmetry and probably substitute for Mg^{2+} ions). However, it can be shown that, if combined in appropriate configurations with cation vacancies such interstitials will be very stable.[2.13] Gourdin and Kingery[2.13] considered the formation of complex clusters, of the type which would be required to bring about a localized change in the structure from rocksalt to spinel. They showed that combinations of several of these complex defects (the aggregate so formed modelling a substantial portion of the spinel unit cell) were energetically the most stable.

It seems, therefore, that trivalent impurity ions cluster together in MgO in order to reduce the energy of the system. It is energetically unfavourable for the trivalent impurity ions and the vacancies required to compensate their excess charge to exist in isolation and only a small fraction do so. Large clusters of impurity ions and vacancies are more stable than small ones and so substantial aggregates tend to form (the mobility of the trivalent ion in the MgO lattice is important in determining the size of such aggregates). Again, to lower the energy of the system, a structural rearrangement may take place within the aggregates; in many cases this leads to the aggregates adopting the spinel structure and precipitating out from the MgO host.

It is impossible to prepare magnesium oxide without inadvertently including a large variety of impurity species in the crystals. Single crystal magnesium oxide grown by Spicer typically contains the impurities shown in Table 2.1 at the concentrations indicated. Of course, samples deliberately doped with iron, chromium or manganese will contain much more of the dopant species than of any other impurity. Nevertheless, in the doped samples examined by E.P.R., lines due to impurities other than the dopant species were observed. These lines were much weaker than those belonging to the E.P.R. spectra of the deliberately introduced dopants and no attempt was made to identify them with any particular impurity.

Although grown in dislocations and low angle grain boundaries are plentiful in MgO,[2.15] the x-ray back reflection photographs obtained from the doped samples did not show any evidence of their presence. The diffraction spots were sharp and well defined in all cases indicating good single crystal quality; the RHEED diffraction patterns obtained from the chromium doped crystals were also typical of single crystal material. From the x-ray and RHEED data we may conclude that in the samples examined here misorientation between grains cannot be more than a few minutes of arc.

Point defects (anion and cation vacancies) also occur in substantial numbers in MgO and may be readily detected using E.P.R. (after suitable treatment of the MgO samples which induces the vacancies to trap holes or electrons[2.16]). The point defects referred to here occur in undoped MgO and do not include the cation vacancies required for charge

Impurity	ppm.wt. present
Aluminium	35
Calcium	20
Silicon	15
Iron	3
Nickel	2
Manganese	0.1
Phosphorus	2
Lead	< 1
Sulphur	5
Copper	< 1
Zinc	5
Vanadium	< 2
Chromium	< 1
Arsenic,Potassium	< 5
Titanium	<20
Barium	<0.5
Sodium	1
Zirconium	3

TABLE 2.1 Typical impurities and their concentrations in Spicer single crystal MgO.

compensation purposes if the MgO is doped with a trivalent impurity ion.

2.3 THE SPINEL CRYSTAL STRUCTURE

As mentioned in the previous section, the results discussed in Chapters 7 and 9 show that formation of the spinel magnesiochromite ($MgCr_2O_4$) takes place in the MgO:Cr samples and that a clustered iron phase, which may be the spinel magnesioferrite ($MgFe_2O_4$), exists in the iron doped magnesium oxide samples. It therefore seems appropriate to describe the crystal structure adopted by spinels at this point.

The general formula of spinel-like compounds is XY_2O_4, where X is usually a divalent cation and Y a trivalent cation. The crystal structure is cubic and, like the magnesium oxide structure described in section 2.1, is based upon a close-packed face-centred cubic arrangement of the oxygen anions. However, the spinel unit cell is much larger than that of MgO and contains a total of 32 anions and 24 cations.

The 24 cations fill the interstitial sites in the cubic close packed array of O^{2-} ions; there are a total of 96 such sites in each unit cell. 64 of the interstitial sites are each tetrahedrally surrounded by four O^{2-} anions and the remaining 32 are each octahedrally surrounded by six O^{2-} anions. Only one eighth of the tetrahedral or type 'A' sites and one half of the octahedral or type 'B' sites are actually occupied by cations. The unit cell of the spinel structure is illustrated in Figure 2.3.

In the case of "normal" spinels the divalent cations

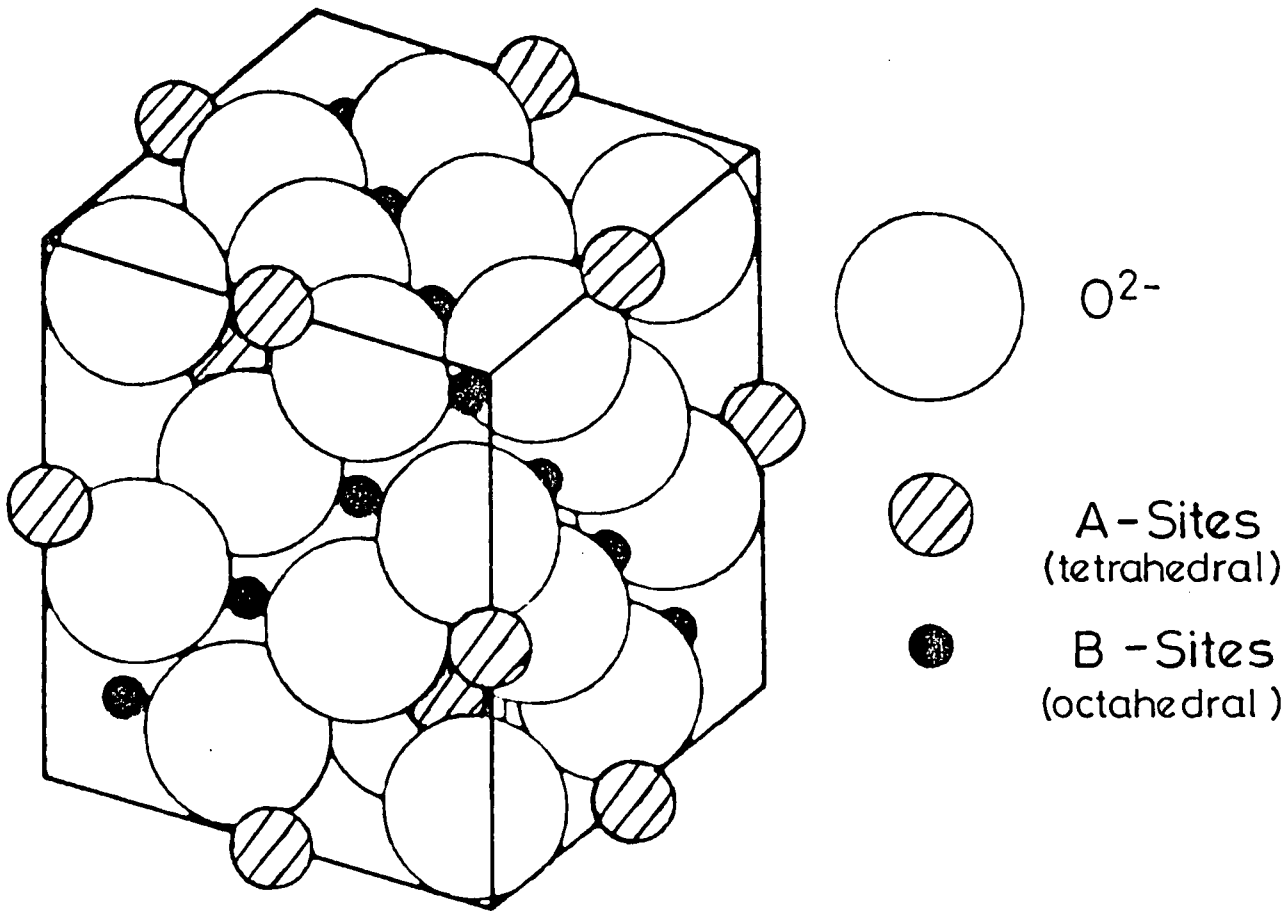

FIGURE 2.3 THE UNIT CELL OF A NORMAL SPINEL.

occupy the tetrahedral A sites and the trivalent cations occupy the octahedral B sites. A spinel is referred to as being "inverse" if half the trivalent cations occupy A sites (the remaining trivalent and divalent cations are randomly distributed among the octahedral B sites). Disordered spinels have the divalent and trivalent cations randomly distributed over all the A and B sites.

Magnesiochromite is a normal spinel (the 8 Mg^{2+} ions occupy tetrahedral sites and the 16 Cr^{3+} ions occupy octahedral sites in the unit cell). This is because the crystal field stabilization energy of Cr^{3+} ions is much greater in octahedral than in tetrahedral sites and therefore they will preferentially occupy the octahedral interstices.[2.17]

No such gain in crystal field stabilization energy would be achieved if the Fe^{3+} ions in magnesioferrite occupied all the octahedral sites. In fact, $MgFe_2O_4$ may be described as an inverse spinel, although the inversion is not complete (about 90% of the Mg^{2+} ions occupy octahedral sites, the remaining 10% occupy tetrahedral sites).[2.17-2.20] The Mg^{2+} and Fe^{3+} ions in magnesioferrite are simply distributed among the tetrahedral and octahedral interstices in such a way so as to minimise the electrostatic lattice energy of the crystal.

Since the spinel and magnesium oxide crystal structures are both based on the same cubic close packed array of O^{2-} anions, precipitates of compounds with the spinel structure tend to form in MgO with their crystallographic axes aligned with those of the host lattice i.e. the lattice of the spinel precipitate is in

register with that of the host MgO crystal. That precipitates of $MgCr_2O_4$ and $MgFe_2O_4$ can form in MgO without distorting the arrangement of the anions in the surrounding host lattice is also suggested by the fact that the lattice parameters of these compounds are almost exactly twice that of MgO ($a_{MgO} = 4.2112\text{Å}$ [2.1]; $a_{MgCr_2O_4} = 8.32\text{Å}$ [2.21]; $a_{MgFe_2O_4} = 8.37\text{Å}$ [2.21]).

Another interesting feature of spinels is that the ratio of divalent to trivalent cations can vary over quite a wide range; evidence presented in the literature suggests that precipitates of magnesioferrite in iron doped MgO are rich in magnesium.[2.18,2.22,2.23]

2.4 HEAT TREATMENT OF THE DOPED MAGNESIUM OXIDE SAMPLES

An attempt was made to anneal both single crystal and powder samples of magnesium oxide doped with iron and chromium by means of heat treatment. It was hoped that heat treatment of these samples would remove strain from the regions of the host lattice surrounding isolated Fe^{3+} and Cr^{3+} ions, which was known to be present because the lines in the E.P.R. spectra of isolated Fe^{3+} and Cr^{3+} ions were "strain broadened" (see Chapters 7 and 9).

The heat treatments were carried out in a furnace wound with Kanthal A which had a silica glass liner. The samples were loaded in a silica boat and placed in the centre of the furnace where the temperature profile was almost flat. A thermocouple, placed as close to the sample boat as possible, was connected to a temperature controller and this arrangement enabled the required temperature to

be set and maintained. A steady flow of oxygen gas through the furnace ensured that the annealing was carried out in an oxydizing atmosphere.

An annealing temperature of 500^{o}C was chosen. The phase diagrams of the MgO-Fe_2O_3 and MgO-$MgCr_2O_4$ systems, illustrated in Figures 2.4 and 2.5 respectively, indicate that, at this temperature and for dopant concentrations of the order of 1%, two phases will exist in each system. In the case of chromium doped MgO these phases are a solid solution of Cr^{3+} ions in MgO and the spinel $MgCr_2O_4$. In the case of iron doped MgO the two phases are magnesio-wustite (a solid solution of iron oxide in magnesium oxide) and magnesioferrite ($MgFe_2O_4$).

It was assumed that when the doped samples were grown, they were allowed to cool down slowly from the growth temperature to room temperature. To model the initial preparation conditions, our samples were gradually cooled down from the annealing temperature of 500^{o}C (at which, in most cases, they were held for 24 hours) to room temperature over a period of 10 hours. In this way it was hoped that the aim of the heat treatment, which was to remove the strain from the doped samples but, at the same time, to maintain the room temperature distribution of the dopant between the isolated ion and clustered (spinel) phases (whose presence in the as received samples was, as indicated above, deduced from the phase diagrams of the MgO-Fe_2O_3 and MgO-$MgCr_2O_4$ systems) would be achieved. In any case, it was felt that the annealing procedure would be more effective if the samples were cooled to room temperature over a period of time.

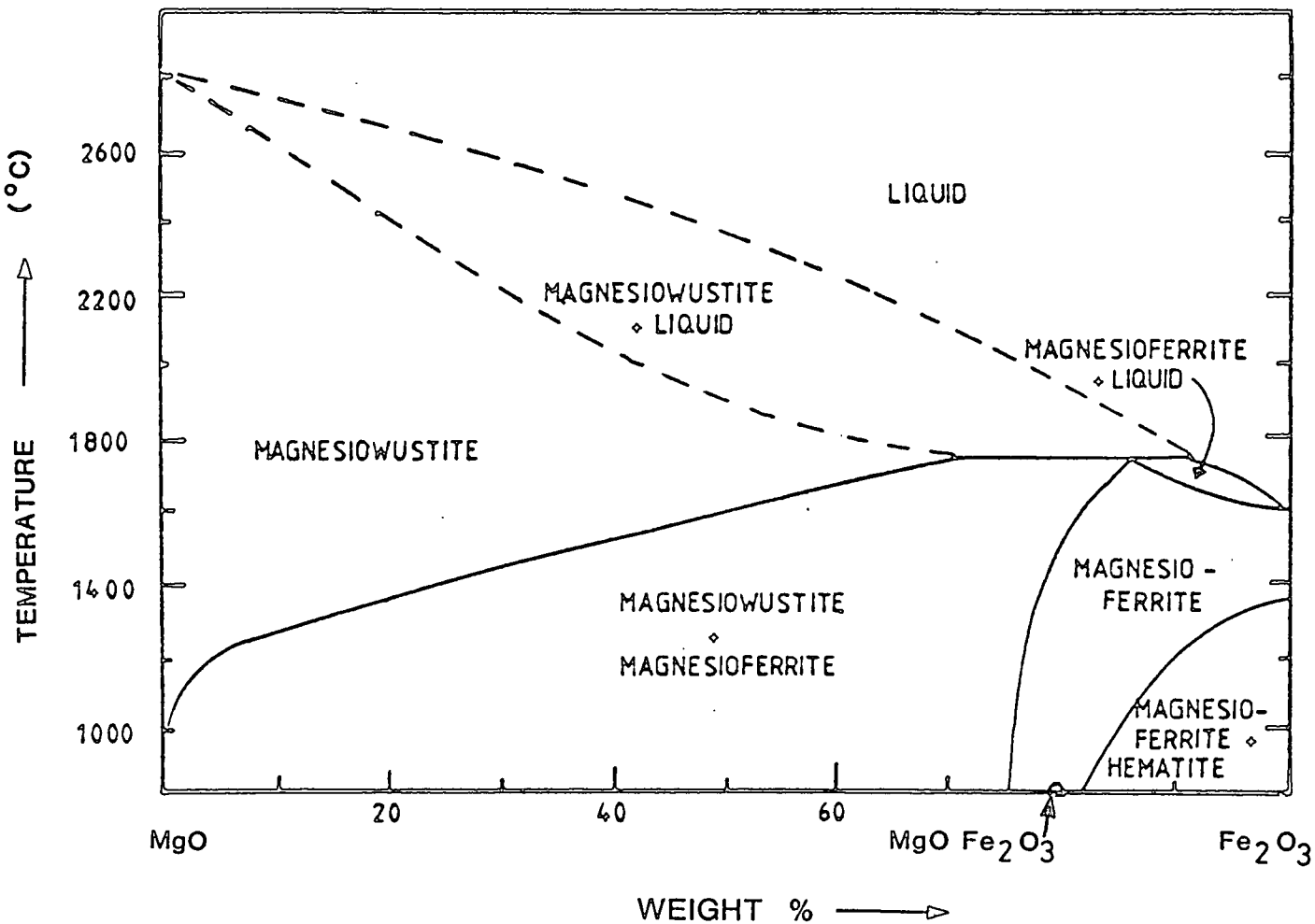

FIGURE 2.4 PHASE EQUILIBRIUM DIAGRAM FOR THE SYSTEM MgO - Fe_2O_3 (AFTER PHILLIPS et al.[2.24]).

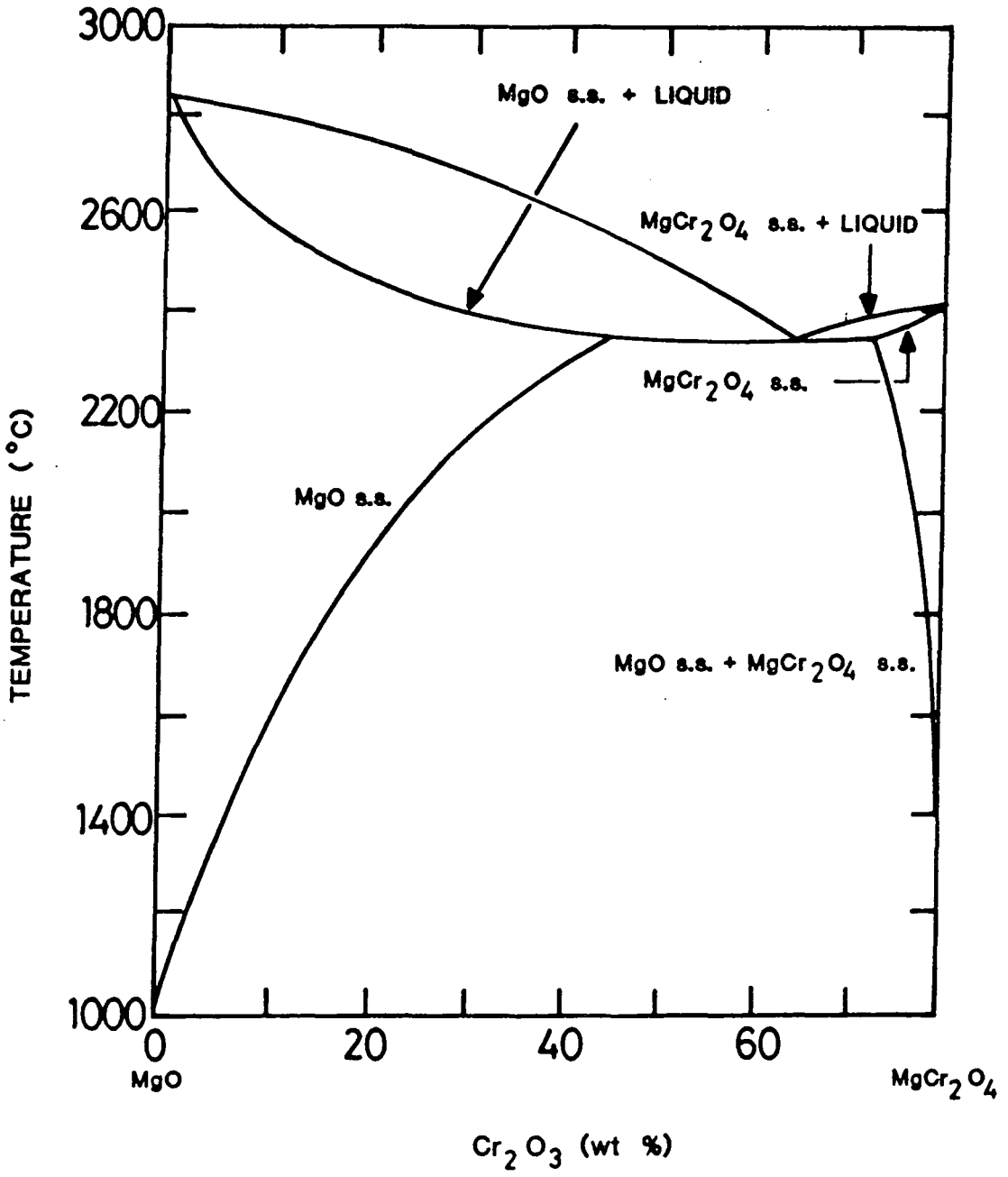

FIGURE 2.5 PHASE EQUILIBRIUM DIAGRAM FOR THE SYSTEM $MgO - MgCr_2O_4$ (AFTER ALPER et al.[2.25]).

Brynestad and Flood[2.26] investigated the effect of various heat treatments upon the valency of iron in iron doped MgO. Their results are summarized by the graphs illustrated in Figures 2.6(a) and (b). Figure 2.6(a) shows that, in air, up to temperatures of approximately 700^{o}C most of the iron exists in the Fe^{3+} state, but that above 700^{o}C the fractional concentration of Fe^{3+} gradually reduces with increasing temperature, the reduction (from Fe^{3+} to Fe^{2+}) being greatest for the material in which the total iron concentration is highest. However, if the heat treatment is carried out in oxygen, the reduction of the fraction of iron in the Fe^{3+} state is minimized (see Figure 2.6(b)). Although the iron and chromium doped samples were annealed at 500^{o}C, at which temperature the dopant should exist almost entirely in the trivalent state, it was felt that maintenance of an oxygen atmosphere would guarantee that reduction of trivalent ions to the divalent state did not take place.

In the as received state, the more lightly doped MgO:Cr single crystals (those containing 800 p.p.m., 3,600p.p.m. and 7,400 p.p.m. of chromium) did not display diffraction spots due to the spinel $MgCr_2O_4$ in their RHEED diffraction patterns. Consequently, these crystals were heat treated at 800^{o}C in an oxygen atmosphere for 10 hours and then quenched to room temperature. It was hoped that the higher temperature would promote growth of the spinel phase and that quenching would preserve the high temperature distribution of the Cr^{3+} ions between the solid solution and clustered phases thereby enabling the spinel spots to be observed on re-examination of these samples by RHEED.

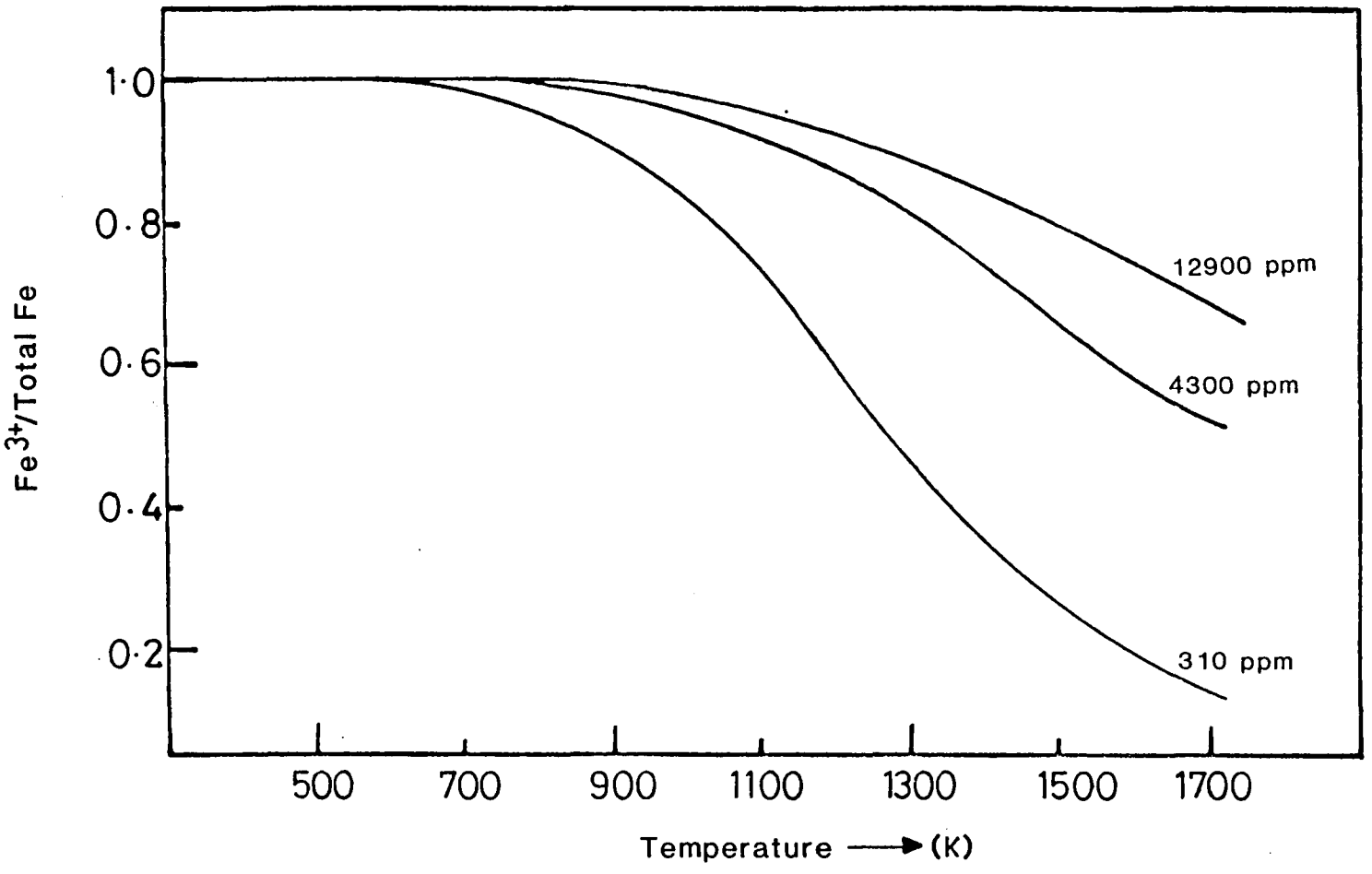

FIGURE 2.6(a) THE VARIATION, IN AIR, OF THE FRACTIONAL CONCENTRATION OF Fe^{3+} WITH TOTAL IRON CONTENT AND TEMPERATURE.

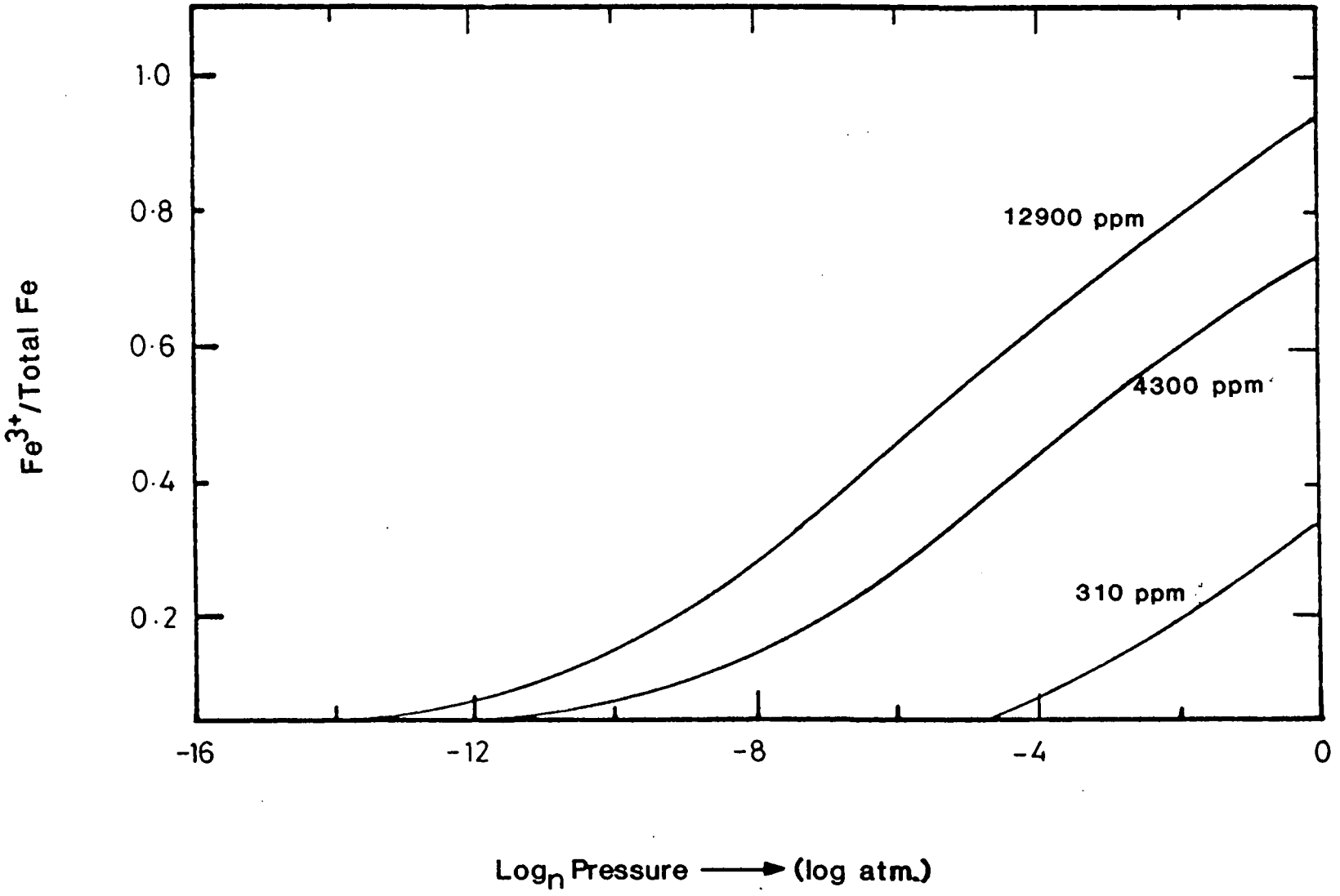

FIGURE 2.6(b) THE VARIATION OF THE FRACTIONAL CONCENTRATION OF Fe^{3+} WITH TOTAL IRON CONTENT AND OXYGEN PRESSURE AT 1573K.

REFERENCES

2.1 R.W.G. Wyckoff "Crystal Structures", Vol. I. Wiley Interscience, N.Y. (1965).

2.2 F.A. Cotton and G. Wilkinson "Advanced Inorganic Chemistry", 3rd Ed., Wiley-Interscience, N.Y. (1972).

2.3 L.J.C. Bluck "Optical and magnetic resonance studies of doped magnesium oxide", M.Sc. thesis, Durham University, (1979), ~~unpublished~~.

2.4 L. Pauling, "The nature of the chemical bond", Cornel University Press, (1960).

2.5 R.D. Shannon and C.T. Prewitt Acta. Cryst. B25, 925 (1969)

2.6 J.S. Thorp, R.A. Vasquez, C. Adcock and W. Hutton J. Mat. Sci. 11, 89 (1976)

2.7 J.S. Thorp, M.D. Hossain and L.J.C. Bluck J Mat. Sci. 14, 2853 (1979)

2.8 M.D. Hossain, J.S. Thorp and A.D. Inglis "E.S.R. Linewidths in Mn^{2+}/MgO" (private communication. ~~unpublished~~).

2.9 A. Cimino, M.Lo. Jacono, P. Porta and M. Valigi Z. Phys. Chem. (Frankfurt), N.F. 51, 301 (1966).

2.10 M.Valigi, F. Pepe and M. Schiavello J. Chem. Soc. Faraday I 71, 1631 (1975)

2.11 W. Low Proc. Phys. Soc. (London) B69, 1169 (1956).

2.12 W. Low Phys. Rev. 105, 801 (1957)

2.13 W.H. Gourdin and W.D. Kingery J. Mat. Sci. 14, 2053 (1979)

2.14 W.H. Gourdin, W.D. Kingery and J. Driear J. Mat. Sci. 14, 2074 (1979).

2.15 B. Henderson Phil. Mag. 9, 153 (1964).

2.16 A. Henderson and J.E. Wertz "Defects in the alkaline earth oxides", Taylor and Francis Ltd., London (1977).

2.17 J.D. Dunitz and L.E. Orgel J. Phys. Chem. Solids 3, 318 (1957)

2.18 P. Reijnen Philips Res. Reports 23, 151 (1968).

2.19 G.W. Groves and M.E. Fine J. Appl. Phys. 35, 3587 (1964).

2.20 A.D. Inglis "Clustering in iron-doped magnesium oxide", Ph.D. Thesis, Durham University, (1981), ~~unpublished~~.

2.21 L. Bragg and G.F. Claringbull "The crystalline state - Vol. IV - Crystal Structures of Minerals", G. Bell and Sons Ltd., London (1965).

2.22 L.C.F. Blackman Trans. Faraday Soc. 55, 391 (1959).

2.23 G.P. Wirtz and M.E. Fine J. Appl. Phys. 38, 3729 (1967).

2.24 B. Phillips, S. Somiya and A. Muan J. Am. Ceram. Soc. 44, 169 (1961).

2.25 A.M. Alper,R.N.McNally, R.C. Doman and F.G. Keihn J. Am. Ceram. Soc. 47, 30 (1964).

2.26 J. Brynestad and H. Flood Z. Fur Elektrochem. 62, 953 (1958).

CHAPTER THREE

E.P.R. EXPERIMENTAL TECHNIQUES

A Varian V4502-15 E.P.R. spectrometer, operating in the x-band ($\sim$ 9.5GHz) region of the microwave spectrum, was used to record the E.P.R. spectra reported in Chapters Seven to Nine. The block diagram of Figure 3.1 identifies the various components of the spectrometer and also shows the relationships between them. The physical and engineering principles pertinent to the design of such an instrument and the various experimental techniques available to the E.P.R. spectroscopist have been extensively covered by Poole.[3.1] It is considered sufficient here to explain the functions of the component parts of the spectrometer system and also how an operator would use the instrument illustrated in Figure 3.1 to record an E.P.R. spectrum.

Microwave power is supplied by a V-153-C klystron. The microwaves pass through an isolator and a variable attenuator to a hybrid-tee (microwave bridge) which divides the power equally between two arms, one arm (arm 2) terminating in an absorbing load and the other arm (arm 3) leading to the resonant cavity. The E.P.R. spectra reported in this work were recorded with the sample placed in a rectangular V4531 multi-purpose cavity operating in the TE_{102} mode. In this particular mode of operation, the field patterns produced by standing electromagnetic waves in the cavity are such that in order to achieve the optimum conditions for detecting magnetic resonance (i.e. that the sample should be in a region of maximum magnetic field and

A.F. = AUDIO FREQUENCY; P.S.D. = PHASE SENSITIVE DETECTOR

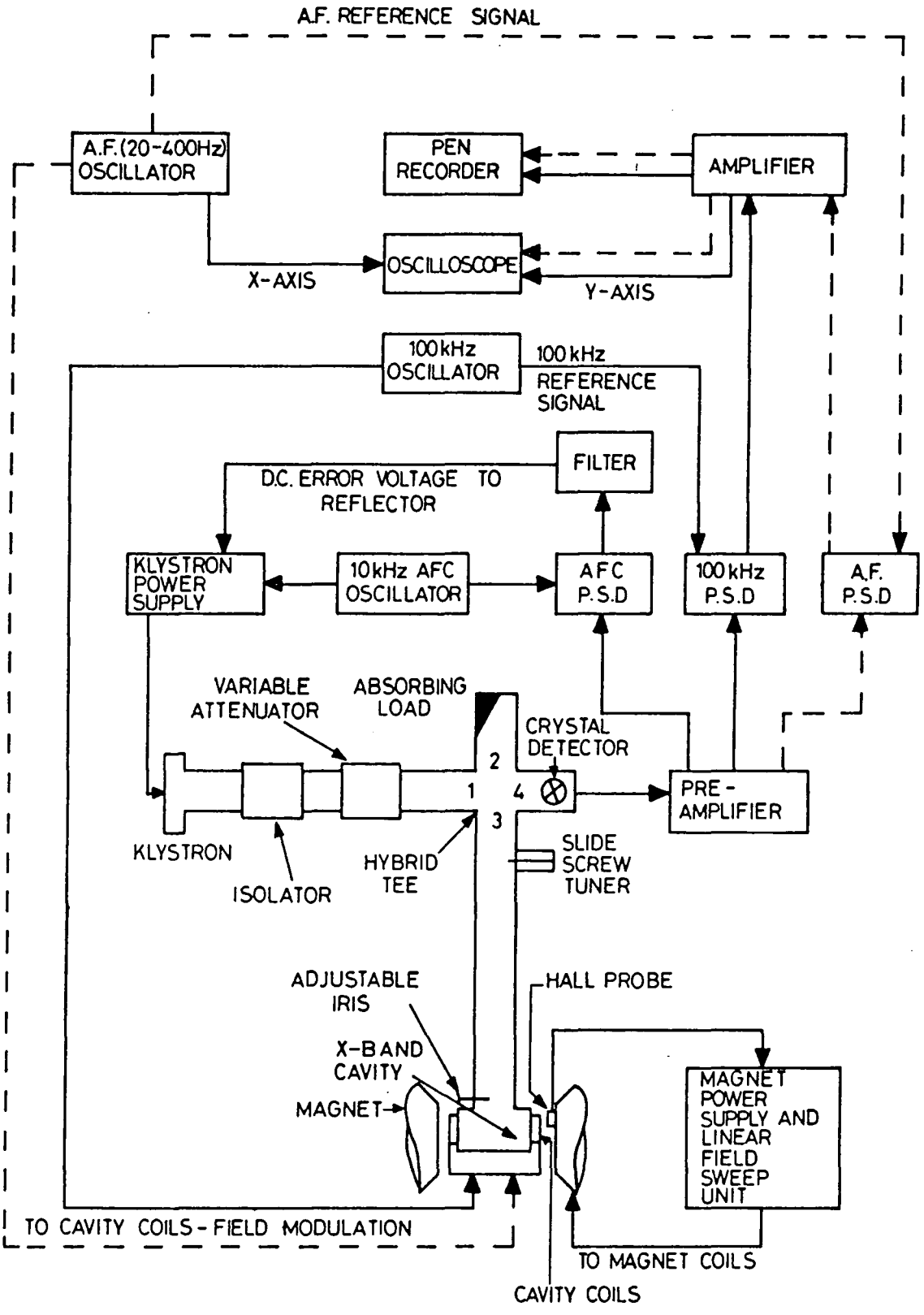

FIGURE 3.1 BLOCK DIAGRAM OF VARIAN V4502 - 15 E.P.R. SPECTROMETER.

minimum electric field) the sample was positioned in the centre of the cavity.

Both the resonant frequency and the impedance of the cavity change with its loading and therefore the microwave circuit must be retuned each time that a new sample is inserted into the cavity. For the purpose of tuning the power mode of the klystron is displayed on the oscilloscope. The power mode display is obtained by using the audio frequency sweep unit to modulate the klystron reflector voltage and also to drive the x-axis of the oscilloscope. The power output of the klystron varies with the reflector voltage and produces a signal in the crystal detector situated in arm 4 of the microwave bridge; this signal is displayed on the y-axis of the oscilloscope.

The klystron, whose frequency was adjustable both mechanically and electronically, was tuned to the cavity resonant frequency by positioning the cavity absorption dip in the centre of the klystron power mode. The cavity resonant frequency was measured with a Hewlett-Packard X532B frequency meter.

A variable iris allows the cavity impedance to be matched to that of the waveguide leading to it so that no power is reflected from arm 3. A proper impedance match is achieved when the absorption dip in the klystron power mode extends to the base-line of the oscilloscope display (indicating that all the power supplied to arm 3 by the klystron at the cavity resonant frequency is being absorbed by the cavity and the waveguide of arm 3).

When the cavity is properly matched, no power reaches

the detector crystal in arm 4. However, the crystal requires a bias current to be passing through it if it is to be at all sensitive to the signals which it is expected to detect. To provide a bias current, a small metal probe (called a slide screw tuner) is positioned in arm 2 to reflect a small amount of microwave power to the detector which causes a current to flow in it. The amount of power reflected is controlled by the distance that the probe is inserted into the waveguide and the phase of the reflected voltage is controlled by shifting the position of the probe along the waveguide.

Once the klystron frequency is set to the cavity frequency it is held at that frequency by the automatic frequency control (AFC) system. An oscillator modulates the klystron reflector voltage (and hence the klystron frequency) at 10 kHz and also provides a reference signal to the AFC phase sensitive detector. When the klystron centre frequency (f_o) corresponds to the resonant frequency of the sample cavity (f_r) a 20kHz signal is detected at the crystal diode (see Figure 3.2(a)). If the centre frequency of the klystron drifts from that of the resonant cavity a 10kHz voltage is detected by the crystal diode, the phase of which depends on whether the klystron centre frequency is higher or lower than the resonant cavity frequency and the amplitude of which depends on the relative difference between f_o and f_r (see Figures 3.2(b) and (c)). This 10kHz error voltage (it may be regarded as an error voltage since its phase and amplitude are dependent on the relationship between f_o and f_r) is phase detected and

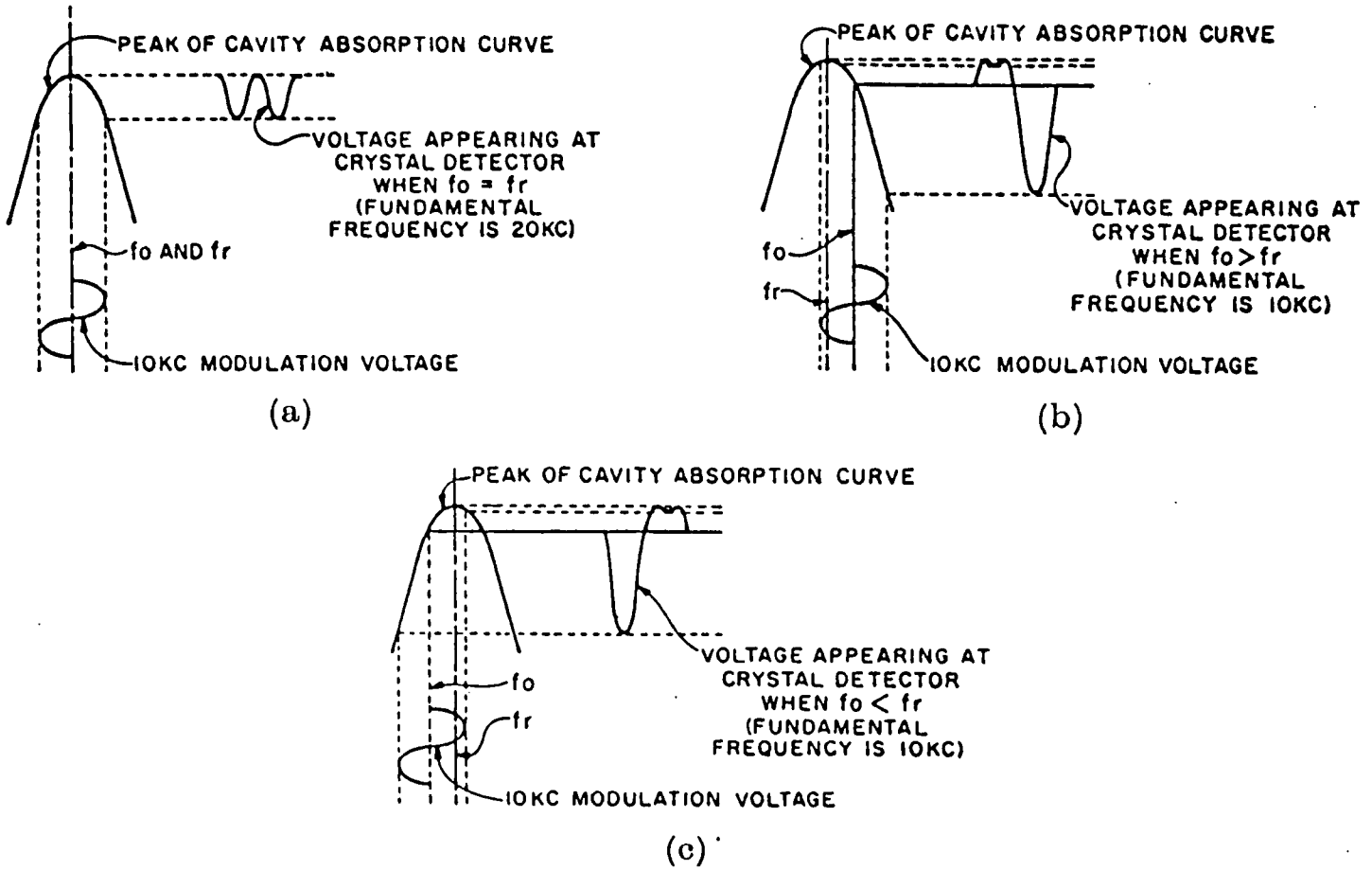

FIGURE 3.2 OUTPUT VOLTAGES FROM RESONANT CAVITY AS A RESULT OF AFC MODULATION; (a) WHEN $f_o = f_r$, (b) WHEN $f_o > f_r$, (c) WHEN $f_o < f_r$.

filtered to produce a d.c. output voltage which is used to control the klystron reflector voltage. This ensures that, whilst the AFC system is in operation, the centre frequency of the klystron always corresponds to that of the sample cavity.

The d.c. magnetic field was provided by a V-3603 12" electromagnet. The field in the magnet gap was monitored by a Hall probe which supplies a control voltage to the magnet power supply. This enables the operator to set the desired magnetic field sweep range and time automatically with a V-FR2503 Fieldal unit. The magnetic field sweep was calibrated with a Newport Instruments P2 proton magnetometer.

When paramagnetic resonance takes place, the quality factor (Q) of the sample cavity changes and some power is reflected from arm 3 which reaches the crystal detector in arm 4. To enhance the signal to noise ratio the d.c. magnetic field was modulated at 100kHz by means of coils embedded in the cavity walls. Although modulation at audio frequencies (20 - 400Hz) was also available, the spectra were recorded using 100kHz modulation because the signal to noise ratio increases with the modulation frequency (the noise is mainly generated in the crystal detector; its level after the signal has been passed through the phase sensitive detector is proportional to 1/f where f is the modulation frequency).

As a result of the 100kHz sine wave modulation of the static magnetic field the microwave energy reflected from the cavity during paramagnetic resonance is also

modulated at the same frequency. The phase and amplitude of the modulated microwave energy both depend upon the characteristics of the E.P.R. absorption line and the value of the static magnetic field (with superimposed modulation) relative to the resonance line (see Figure 3.3(a)). A faithful representation of the E.P.R. absorption lineshape (which is absolutely vital if linewidth measurements are to be taken from the recorded spectra) will only be obtained if the modulation field amplitude is much less than the signal linewidth. Otherwise, the signal voltage reaching the detector crystal is distorted (see Figures 3.3(b) & (c)) and in extreme cases the recorded line will be reduced in amplitude and artificially broadened (see Figure 6.2(b)).

During paramagnetic resonance the modulated microwave energy strikes the crystal detector and induces a 100kHz signal in it. This signal provides the input to a 100kHz phase sensitive detector which also receives a reference voltage from the 100kHz oscillator. The relative phases of the signal and reference voltages are adjusted so that a first harmonic presentation of the original E.P.R. absorption line is obtained from the output of the phase sensitive detector. The first derivative E.P.R. signal is integrated over a long period of time in comparison with the time periods of the random (noise) input signals to the phase sensitive detector. This procedure averages out almost all of the noise signals and thus we only record the E.P.R. signal information. The integrated signal is traced out on a chart recorder, the trace being a first harmonic representation of the original E.P.R. absorption line.

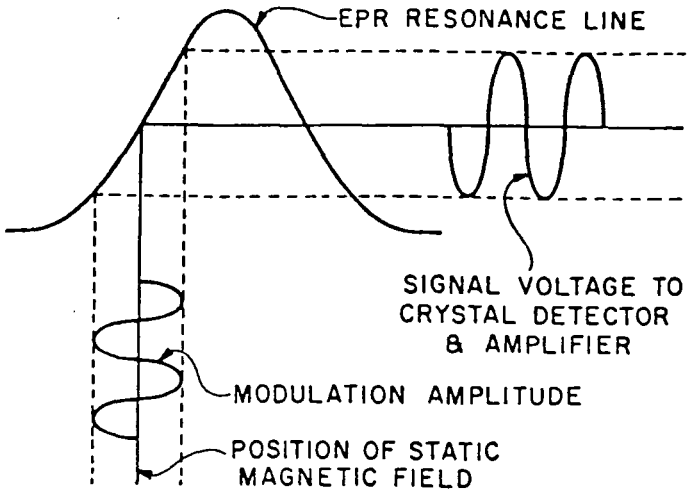

(a)

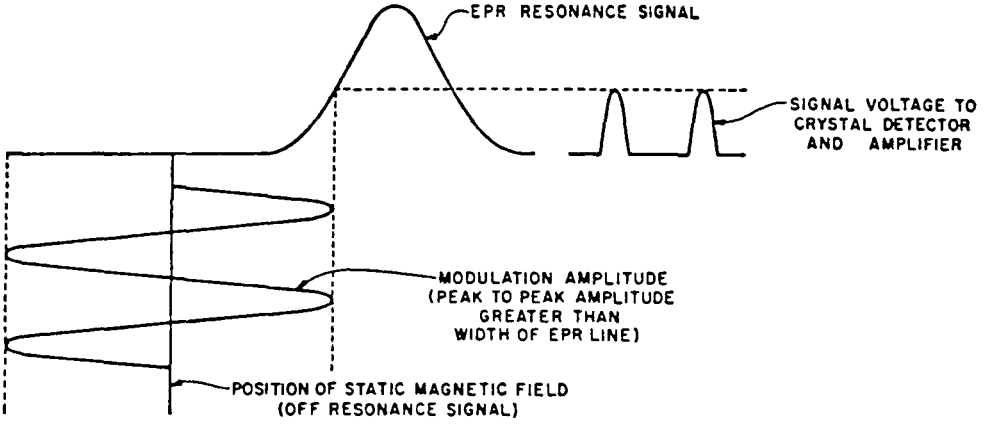

(b)

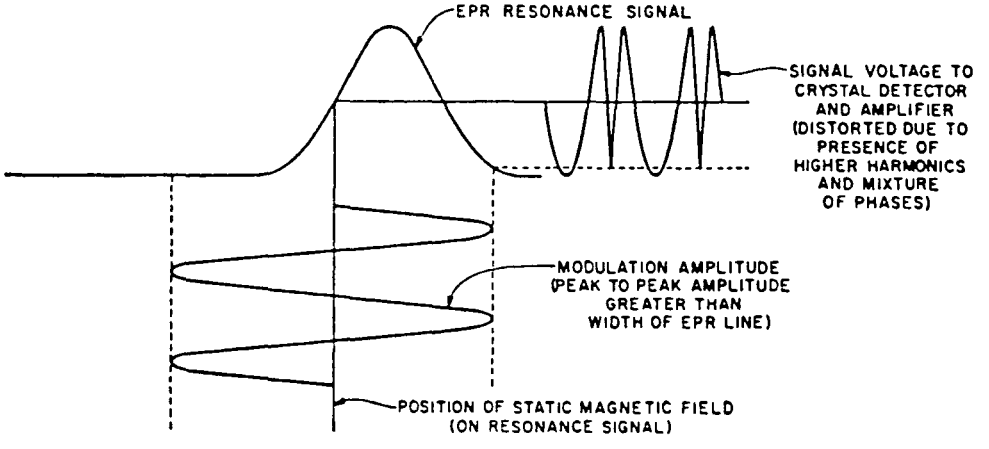

(c)

FIGURE 3.3 MAGNETIC FIELD MODULATION OF AN E.P.R. RESONANCE LINE; (a) UNDISTORTED SIGNAL VOLTAGE APPEARS AT THE CRYSTAL DETECTOR WHEN MODULATION AMPLITUDE $\ll$ E.P.R. LINEWIDTH, (b) and (c) SIGNAL VOLTAGE DISTORTION AT CRYSTAL DETECTOR WHEN MODULATION AMPLITUDE > E.P.R. LINEWIDTH.

The E.P.R. signal, in its first derivative form, may also be displayed on the oscilloscope by directing the output voltage of the 100kHz phase sensitive detector to the y-axis of the oscilloscope. The x-axis of the oscilloscope is driven by the audio frequency sweep unit which also modulates the static magnetic field. The amplitude of the audio frequency sweep is much greater than that of the 100kHz modulation field. In effect, the magnetic field is swept completely through the E.P.R. signal, modulated at 100kHz, several times a second by the audio frequency sweep unit.

Single crystal samples were mounted on a spectroscopically pure 4 mm diameter quartz rod which was held in place by a goniometer attached to the top of the cavity. The samples were cleaved along <100> directions and precisely positioned on a flat machined facet at the bottom of the rod which was located in the centre of the cavity. At the top of the rod a second facet was machined with its flat face set at an angle of 90^{o} to that of the first facet. This allowed the sample to be aligned with respect to the magnetic field. The sample could then be rotated by means of the geared drive on the goniometer, and positioned to within one half of a degree of any required angle, relative to its initial orientation.

Powder samples were contained in spectroscopically pure quartz tubes, sealed at one end, with external diameters of 4mm and internal diameters of 2 mm. Since the crystallites in the powder are randomly oriented, alignment of the sample with respect to the magnetic field

is not necessary. The volume of powder responsible for the E.P.R. absorption was contained in a 1 cm length of the quartz tube. Since the powder samples were sieved through a 185 μm mesh, a simple calculation shows that the number of crystallites undergoing resonance is at least 20,000.

REFERENCES

3.1 C.P. Poole "Electron Spin Resonance", Wiley-Interscience, N.Y. (1967).

CHAPTER FOUR

THE INTERPRETATION OF E.P.R. SPECTRA I: SINGLE CRYSTAL LINE POSITIONS AND INTENSITIES

Electron Paramagnetic Resonance (E.P.R.) is probably the most powerful technique available for investigating the microscopic physical characteristics of paramagnetic impurity centres and defects distributed in a host lattice of diamagnetic ions (such as that formed by Magnesium Oxide).

The experimentally observed spectra arise from induced transitions between the lowest energy levels of paramagnetic ions. In this Chapter we will not be concerned with dynamic effects other than the E.P.R. transition itself. The experimental data under consideration thus consists of a series of transition energies or line positions and the corresponding relative intensities (linewidths give information about dynamic effects and will be considered separately in Chapter Six).

It is convenient and customary to analyse such data in terms of a "Spin Hamiltonian". It must be clearly stated at this point that the Spin Hamiltonian is simply a model which allows much of the experimental data to be summarised in terms of a small number of parameters. In addition to these parameters a complete Spin Hamiltonian includes operators for the effective electronic spin, the external magnetic field and any nuclear spins. The eigenfunctions of the Spin Hamiltonian determine the allowed energy levels of the system, or at least those of interest to an E.P.R. experimentalist.

The Spin Hamiltonian parameters describe the behaviour

of the experimentally observed energy levels in considerable detail and their evaluation can provide important information about the type of impurity present, its charge state and local environment. However, a complete understanding of the experimental results rests upon equating the Spin Hamiltonian parameters with energy levels calculated from a more fundamental consideration of the interactions to which a paramagnetic ion is subjected in a crystalline environment and under the influence of an external magnetic field.

The main concern of this chapter will be the evaluation of appropriate Spin Hamiltonians for Cr^{3+}, Mn^{2+} and Fe^{3+} in MgO although some aspects of the more fundamental description of the energy levels of these ions will, of necessity, make their way into the text.

4.1 THE FREE ION AND THE GENERAL SPIN HAMILTONIAN

In a free atom or ion of the first transition series, Russell-Sanders (L-S) and spin-orbit coupling combine to form spectroscopic states characterized by their spin, orbital and total angular momenta (S, L & J respectively). The (2J + 1) degeneracy of each state is lifted by an external magnetic field, H, and a small oscillating magnetic field perpendicular to H can induce transitions between adjacent levels within the (2J + 1) manifold when the resonance condition

$$h\nu = g_J \beta H \qquad (4.1)$$

(β = the Bohr magneton, ν = frequency of oscillating magnetic field)

is satisfied. The Landé splitting factor, g_J, is defined for a term with given L, S and J values by the equation:[4.1]

$$g_J = \frac{J(J+1)(g_L+g_S) + [L(L+1) - S(S+1)](g_L-g_S)}{2J(J+1)} \qquad (4.2a)$$

which reduces to the usual Landé formula

$$g_J = 1 + \frac{J(J+1) + S(S+1) - L(L+1)}{2J(J+1)} \qquad (4.2b)$$

if we set g_L(the orbital g-value) = 1 and g_S(the spin g-value) = 2 exactly. Within a given term the (2J+1) levels are equally spaced and resonance occurs at a single field, whatever may be its orientation.

A paramagnetic impurity centre in a diamagnetic host lattice has a more complicated energy level system than the free ion because its outer electrons (the 3d electrons for first transition series ions) are fully exposed to the electrostatic field (called the crystal field) arising from the charges on the surrounding diamagnetic ions. Although there is no interaction between the crystal field and the spin moment, which is therefore free to orientate in an

external magnetic field, the orbital motion of the electrons is seriously restricted with the result that the orbitals are "locked" into the field. The crystal field therefore partially or wholly removes the orbital degeneracy of the ground state, compared to which each of the resulting crystal field levels has a reduced orbital moment. In this way the spin and orbital angular momenta are largely decoupled and the reduction of the orbital moment by the action of the crystal field is referred to as "quenching". Obviously, in the solid, the simple spin-orbit coupling scheme which is used in the free ion case to determine the ground state (characterized by its L, S and J values) cannot be used.

The complete Hamiltonian for an isolated paramagnetic ion in a crystal lattice (with the orders of magnitude of the energy terms appropriate for first transition series ions) takes the form:[4.2]

$$\mathcal{H} = \mathcal{H}_{ee}(\text{Coulombic term} \sim 10^5 cm^{-1}) + \mathcal{H}_{CF}(\text{crystal field term} \sim 10^4 cm^{-1}) + \mathcal{H}_{LS}(\text{spin-orbit coupling term} \sim 10^2 cm^{-1} \text{ in the free ion}) + \mathcal{H}_{SS}(\text{spin-spin coupling term} \sim 1\ cm^{-1}) + \mathcal{H}_{Ze}(\text{Zeeman term} \sim 1 cm^{-1}) + \mathcal{H}_{HF}(\text{hyperfine interaction term} \sim 10^{-3} cm^{-1}) + \text{smaller terms} \quad (4.3)$$

For a particular system, some of the terms in the very general Hamiltonian of equation 4.3 may be insignificant or equal to zero and can be omitted. The remaining terms are considered individually, in order of decreasing magnitude,

that is to say each successive term is regarded as a peturbation of the previously established energy level system. The effect of applying peturbation theory each time that a new term is added to the total Hamiltonian is to shift and split the existing energy levels.

As in the free ion, the dominant Coulombic term ($\mathcal{H}_{el}$) determines the electronic configuration and spectroscopic term of the ground state (for example, the electronic configuration of Cr^{3+} is $3d^3$ and it will be shown in section 4.2 that the spectroscopic ground state of this ion is ^4F).

For first transition series ions the second largest term in equation 4.3 is the crystal field term, $\mathcal{H}_{CF}$, which, as already described, splits the spectroscopic ground state into several crystal field levels with reduced orbital moments. The ground crystal field levels of the $(3d)^n$ ions in octahedral symmetry (which is the symmetry of the site occupied by a substitutional ion in MgO) are either orbital singlets, doublets or triplets. The real orbital moments of these levels can be equated with "effective" orbital angular momenta (L') values of 0, $\frac{1}{2}$ and 1 respectively. Since the spin moment does not interact with the crystal field the "effective" total angular momentum, J', is compounded of S and L'; i.e. $J' = L' + S$. Using the effective angular momentum values, L' and J', together with the real spin momentum, S, the spin-orbit levels (described by the spin-orbit coupling term, $\mathcal{H}_{LS}$, in equation 4.3) for a particular crystal field level may be derived using the spin-orbit coupling technique in much the same way as the same technique is

used in the free ion case to determine the spin-orbit levels of a particular spectroscopic state (a more detailed description of this procedure is given in section 4.3).

E.P.R. spectral lines arise from transitions between the lowest lying energy levels of a paramagnetic species and the transition energies are at most a few cm^{-1}. The spectroscopic states of the 3d group are separated by $10^5 cm^{-1}$, the crystal field levels by $\sim 10^4 cm^{-1}$ and the spin-orbit levels (characterized by their L', S and J' values) by $\sim 10^2 cm^{-1}$. Therefore the E.P.R. spectrum of a 3d ion arises from transitions between the $(2J'+1)$ levels of the lowest spin-orbit state, which may be regarded as the ground state and treated as if it were isolated from the higher lying levels even though these levels may influence the ground state considerably. The relative energies of the $(2J'+1)$ levels are dictated by the remaining terms in the full Hamiltonian of equation 4.3 ($\mathcal{H}_{SS}$, $\mathcal{H}_{Ze}$, $\mathcal{H}_{HF}$ and smaller terms) which are small and therefore the $(2J'+1)$ levels usually remain close enough together for transitions between them to be observed even after these terms have been taken into account. A Hamiltonian containing only these smaller terms will give the energies of the $(2J'+1)$ levels relative to the energy of the spin-orbit ground state; this is sufficient for our needs since we only need the difference in energy between the levels to fully describe the E.P.R. spectrum. Therefore the Hamiltonian used to describe an E.P.R. spectrum is a truncated form of the full Hamiltonian containing only those terms which express the divergence of the $(2J'+1)$ levels of the ground state in an external magnetic field H; this truncated expression is known as the "Spin Hamiltonian"

The general Spin Hamiltonian derived by Abragam and Pryce[4.3] is essentially a polynomial in J' which also contains terms describing hyperfine interactions involving a nucleus of spin I and may be expressed as follows:

$$\mathcal{H}_S = H\cdot g\cdot S + S\cdot A\cdot I + S\cdot D\cdot S \quad (+ \text{ smaller terms}) \qquad (4.4)$$

In the above expression S has been used to represent the effective total angular momentum, J' in order to correspond with the usual notation. g, A and D are tensor quantities which may be satisfactorily defined in terms of their values along three principal axes (x, y and z), the z axis being taken by convention to be the principal axis of symmetry of the crystal field.

Abragam and Pryce[4.3] arrived at equation 4.4 after carrying out a peturbation calculation (to second order) which involved all the terms in the Hamiltonian of equation 4.3 except the two largest ($\mathcal{H}_{el}$ and $\mathcal{H}_{CF}$). To facilitate their calculation they first transformed the various terms in the Hamiltonian into the appropriate angular momentum operators. The terms arising from the peturbation calculation were then grouped together in order to define new variables which could be identified with experimentally measurable parameters i.e. the tensors g, A and D. Hence each of these tensors represents the sum of several contributions each of which arises from a particular interaction taking place within the paramagnetic species; sometimes the individual contributions can be independently evaluated to provide very important

information about the detailed electronic structure (for further details of the peturbation calculation see Low[4.4] p39-52). The Spin Hamiltonian of equation 4.4 is very general; for a particular case the form taken by the Spin Hamiltonian must conform to the total symmetry about the ion in the crystal.

The interpretation of the individual terms in equation 4.4 is as follows: the first term is due to the Zeeman interaction i.e. the direct interaction of the unpaired electrons with an external magnetic field, H. If H has direction cosines ℓ, m and n with respect to a set of axes x, y and z the value of the g tensor is given by the relation:

$$g^2 = \ell^2 g_x^{\,2} + m^2 g_y^{\,2} + n^2 g_z^{\,2} \qquad (4.5)$$

The Zeeman term in equation 4.4 then becomes:

$$\mathcal{H}_S(\text{Zeeman}) = g\beta H \cdot S \qquad (4.6)$$

If the crystal field has cubic symmetry g is simply equivalent to a numerical constant. If the crystalline field is anisotropic, the contribution of the orbital magnetic moment to the moment of the ground state varies with the direction of the crystal field with respect to the applied external field. For each given direction

there is an appropriate g factor, defined by equation 4.5.

The g-factor of equations 4.5 and 4.6 measures the splitting between the $(2J'+1)$ levels of the ground state in an external field, H, and is obviously numerically different to the Landé g-factor of the free ion. Therefore, to minimise confusion, this g-factor is known as the spectroscopic splitting factor. Its numerical value, to first order, for a ground state of given L', S and J' values, may be calculated using an equation analagous to equation 4.2a, which gives the Landé g-factor of the free ion (details of the calculation of spectroscopic splitting factors are given in section 4.3). A small second order contribution to the g-factor arises from the admixture of higher lying crystal field levels into the ground state.

The second term in equation 4.4 expresses the magnetic hyperfine structure. The contributions to the hyperfine structure constant, A, originate from unpaired s electrons, from an orbital contribution and a small spin-orbit contribution. In an anisotropic crystal field the A tensor assumes a form similar to that assumed by the g-tensor under the same conditions i.e.

$$g^2A^2 = \ell^2 g_x^2 A_x^2 + m^2 g_y^2 A_y^2 + n^2 g_z^2 A_z^2 \qquad (4.7)$$

The hyperfine term in the Spin Hamiltonian then becomes:

$$\mathcal{H}_S \text{ (hyperfine)} = AI\cdot S \qquad (4.8)$$

Again, like the g tensor, the A tensor reduces to a numerical constant in a cubic crystal field.

The spin-spin term in equation 4.4 contains the D tensor which is a measure of the splitting of the ground state in a non cubic field. This splitting, which occurs even in zero magnetic field, is caused in part by the spin-orbit coupling and also by the spin-spin contribution in an unsymmetrical crystal field. The initial splitting gives rise to what is called the "fine structure" of the spectrum i.e. the $2J'$ individual transitions between the $(2J'+1)$ levels of the ground state are found to occur at different magnetic field values.

4.2 THE ELECTRONIC GROUND STATE AND CRYSTAL FIELD LEVELS

The Hamiltonian operator, $\mathcal{H}_{el}$, predicts several allowed electronic states, each of which is characterized by unique values for the total orbital and spin angular momenta. A qualitative method exists for determining the number and type of such states for an atom.[4.5] This method is sufficient for our needs since it allows us to predict and characterize in terms of the quantum numbers L and S the ground electronic state in which we are interested (the energy of an EPR transition is of the order of $1cm^{-1}$ whereas the electronic states are separated by many thousands of cm^{-1})

The procedure involves the use of the Russell-Saunders or LS coupling scheme which, fortunately, is valid for the elements of the first transition series. The LS coupling scheme allows the following definitions to be made:

$$M_L = m_\ell^{(1)} + m_\ell^{(2)} + m_\ell^{(3)} \ldots\ldots + m_\ell^{(n)}$$

$$M_S = m_s^{(1)} + m_s^{(2)} + m_s^{(3)} \ldots\ldots + m_s^{(n)} \qquad (4.9)$$

where M_L = the component of L in a reference direction

M_S = " " " S " " " "

$m_\ell^{(i)}$ = the m_ℓ value of the ith electron

$m_s^{(i)}$ = " m_s " " " " "

n = the total number of electrons in the atom.

Only partly filled shells need be considered as M_L and M_S will obviously both be equal to zero for a filled shell. For a partly filled shell there is always more than one way of assigning m_ℓ and m_s values to the various electrons. For convenience, + and - superscripts will be used to represent $m_s = +\frac{1}{2}$ and $m_s = -\frac{1}{2}$ respectively. Thus if the first electron has $m_\ell = 1$, $m_s = +\frac{1}{2}$, the second electron has $m_\ell = 2$, $m_s = -\frac{1}{2}$, the third electron has $m_\ell = 0$, $m_s = +\frac{1}{2}$ etc., this will be written as $(1^+, 2^-, 0^+..)$ Such a specification for all electrons will be called a microstate.

The technique will now be demonstrated by applying it to the Cr^{3+} ion, which has a $3d^3$ electronic configuration. All possible ways of assigning m_ℓ and m_s values to the three 3d electrons must be considered except those that are either prohibited by the exclusion principle or are

physically redundant. Thus microstates such as $(1^+, 1^+)$ and $(0^-, 0^-)$ are prohibited because of the exclusion principle and two microstates such as $(1^+, 0^-)$ and $(0^-, 1^+)$ are identical (and therefore treated as a single microstate) since there is no physical distinction between the "first electron" and the "second electron".

Table 4.1 shows a tabulation of the microstates for the $3d^3$ electronic configuration, in which they are arranged according to their M_L and M_S values. The maximum and minimum values of M_L are 5 and -5 respectively, each of which is associated with M_S values of $+\frac{1}{2}$ and $-\frac{1}{2}$. These must be the two extreme M_L values derived from a state with $L = 5$ and $S = \frac{1}{2}$, namely a ^2H state. Also belonging to this ^2H state must be microstates with $M_S = +\frac{1}{2}, -\frac{1}{2}$ and $M_L = 4,3,2,1,0,-1,-2,-3,-4$. If a set of 22 microstates appropriate to the ^2H state is now deleted, the remaining maximum and minimum values of M_L are 4 and -4, each of which is again associated with M_S values of $+\frac{1}{2}$ and $-\frac{1}{2}$. These must be the two extreme M_L values from a state with $L = 4$ and $S = \frac{1}{2}$ i.e. a ^2G state. When the set of microstates representing the ^2G state is removed the procedure used to determine the prescence of the ^2H and ^2G states can be repeated and it is found that the permitted states of the $3d^3$ configuration are:

$$^2H,\ ^2G,\ ^4F,\ ^2F,\ \text{two}\ ^2D,\ ^4P\ \text{and}\ ^2P.$$

Hund's rules state that:

i) In the ground state spin momenta combine to give the maximum value consistent with the Pauli exclusion principle.

M_L	M_S			
	$3/2$	$1/2$	$-1/2$	$-3/2$
5		$(2^+ 2^- 1^+)$	$(2^+ 2^- 1^-)$	
4		$(2^+ 2^- 0^+)$ $(2^+ 1^+ 1^-)$	$(2^+ 2^- 0^-)$ $(2^- 1^+ 1^-)$	
3	$(2^+ 1^+ 0^+)$	$(2^+ 1^- 0^+)$ $(2^- 1^+ 0^+)$ $(2^+ 1^+ 0^-)$ $(2^+ 2^- -1^+)$	$(2^+ 1^- 0^-)$ $(2^- 1^- 0^-)$ $(2^- 1^+ 0^+)$ $(2^+ 2^- -1^-)$	$(2^- 1^- 0^-)$
2	$(2^+ 1^+ -1^+)$	$(2^+ 1^- -1^+)$ $(2^- 1^+ -1^+)$ $(2^+ 1^+ -1^-)$ $(2^+ 0^+ 0^-)$ $(1^+ 1^- 0^+)$ $(2^+ 2^- -2^+)$	$(2^- 1^+ -1^-)$ $(2^- 1^- -1^+)$ $(2^+ 1^- -1^-)$ $(2^- 0^+ 0^-)$ $(1^- 1^- 0^-)$ $(2^+ 2^- -2^-)$	$(2^- 1^- -1^-)$
1	$(2^+ -2^+ 1^+)$ $(2^+ 0^+ -1^+)$	$(2^+ -2^- 1^+)$ $(2^- -2^+ 1^+)$ $(2^+ -2^+ 1^-)$ $(2^+ 0^+ -1^-)$ $(2^+ 0^- -1^+)$ $(2^- 0^+ -1^+)$ $(1^+ 0^+ 0^-)$ $(1^+ 1^- -1^+)$	$(2^+ -2^- 1^-)$ $(2^- -2^+ 1^-)$ $(2^- -2^- 1^+)$ $(2^+ 0^- -1^-)$ $(2^- 0^+ -1^-)$ $(2^- 0^- -1^+)$ $(1^- 0^+ 0^-)$ $(1^+ 1^- -1^-)$	$(2^- -2^- 1^-)$ $(2^- 0^- -1^-)$
0	$(2^+ -2^+ 0^+)$ $(1^+ -1^+ 0^+)$	$(2^+ -2^+ 0^-)$ $(2^+ -2^- 0^+)$ $(2^- -2^+ 0^+)$ $(1^+ -1^+ 0^-)$ $(1^+ -1^- 0^+)$ $(1^- -1^+ 0^+)$ $(2^+ -1^- -1^+)$ $(-2^+ 1^- 1^+)$	$(2^+ -2^- 0^-)$ $(2^- -2^+ 0^-)$ $(2^- -2^- 0^+)$ $(1^+ -1^- 0^-)$ $(1^- -1^+ 0^-)$ $(1^- -1^- 0^+)$ $(2^- -1^+ -1^-)$ $(-2^- 1^+ 1^-)$	$(2^- -2^- 0^-)$ $(1^- -1^- 0^-)$
-1	$(2^+ -2^+ -1^+)$ $(-2^+ 0^+ 1^+)$	$(2^+ -2^- -1^+)$ $(2^- -2^+ -1^+)$ $(2^+ -2^+ -1^-)$ $(-2^+ 0^+ 1^-)$ $(-2^+ 0^- 1^+)$ $(-2^- 0^+ 1^+)$ $(0^+ 0^- -1^+)$ $(1^+ 1^- -1^+)$	$(2^+ -2^- -1^-)$ $(2^- -2^+ -1^-)$ $(2^- -2^- -1^+)$ $(-2^+ 0^- 1^-)$ $(-2^- 0^+ 1^-)$ $(-2^- 0^- 1^+)$ $(0^+ 0^- -1^-)$ $(1^+ 1^- -1^-)$	$(2^- -2^- -1^-)$ $(-2^- 0^- 1^-)$
-2	$(-2^+ 1^+ -1^+)$	$(-2^+ 1^- -1^+)$ $(-2^+ 1^+ -1^-)$ $(-2^- 1^+ -1^+)$ $(-2^+ 0^+ 0^-)$ $(-1^+ -1^- 0^-)$ $(2^+ -2^+ -2^-)$	$(-2^+ 1^- -1^-)$ $(-2^- 1^+ -1^-)$ $(-2^- 1^- -1^+)$ $(-2^- 0^+ 0^-)$ $(-1^+ -1^- 0^-)$ $(2^- -2^+ -2^-)$	$(-2^- 1^- -1^-)$
-3	$(-2^+ -1^+ 0^+)$	$(-2^+ -1^+ 0^-)$ $(-2^+ -1^- 0^+)$ $(-2^- -1^+ 0^+)$ $(-2^+ -2^- 1^+)$	$(-2^+ -1^- 0^-)$ $(-2^- -1^+ 0^-)$ $(-2^- -1^- 0^+)$ $(-2^+ -2^- 1^-)$	$(-2^- -1^- 0^-)$
-4		$(-2^+ -2^- 0^+)$ $(-2^+ 1^+ -1^-)$	$(-2^+ -2^- 0^-)$ $(-2^- 1^+ -1^-)$	
-5		$(-2^+ -2^- 1^+)$	$(-2^+ -2^- 1^-)$	

TABLE 4.1 The microstates of the $3d^3$ (Cr^{3+}) electronic configuration.

ii) When the maximum value of S has been thus determined, the orbital momenta combine in a similar manner to give the maximum value of L.

Application of Hund's rules to the allowed states of the $3d^3$ configuration shows that the ground state of the Cr^{3+} ion is the ^4F state.

Both the Fe^{3+} and Mn^{2+} ions have a $3d^5$ electronic configuration. A similar treatment to that described above for the Cr^{3+} ion shows that the allowed states for the Mn^{2+} and Fe^{3+} ions are ^6S, ^4G, ^4P, ^4D, ^2I, ^4F, ^2D, two ^2F, ^2H, ^2G and ^2S. Using Hund's rules the ground state is found to be the ^6S state.

As described in section 4.1, in doped MgO the isolated paramagnetic ions are subjected to strong internal electric fields created by the charges on the surrounding diamagnetic ions. To understand the effect that these internal fields have upon the electronic states described above, the problem must first be simplified by assuming that the surrounding diamagnetic ions can be regarded as point charges placed at approximate lattice points.[4.6-4.9] The effect of the ligands is to set up a static electric field which acts on the paramagnetic ion. The problem then resolves itself into finding the energy levels in a Stark field of certain strength and symmetry determined by the static charges. To calculate the effect of this electrostatic or crystal field potential, $\mathcal{H}_{CF}$, upon the electronic energy levels peturbation theory is often used. Therefore, it is necessary to know the order of magnitude of the potentials. Experimental data (obtained from optical spectra) shows that in the 3d or iron group

the crystal field is of moderate strength, being larger than the spin-orbit coupling but smaller than the Coulombic interaction. Therefore in this case peturbation theory is applied before calculating $\mathcal{H}_{LS}$.

It has already been explained that the crystal field only exerts an influence upon the orbital motion of the electrons. Therefore only electronic states with orbital degeneracy will be split into several component parts by a crystal field. Hence S and P states (L=0 and L=1 respectively) are not split by any crystal field whereas in an octahedral crystal field a D state (L=2) is split into an orbital triplet (T_2) and an orbital doublet (E) and an F state (L=3) is split into two orbital triplets (T_1 and T_2) and an orbital singlet (A_2). The splittings of the various electronic states of the $3d^3$ and $3d^5$ configurations in an octahedral field are shown in Figures 4.1 and 4.2 respectively. It will be noticed that the ground state of the Fe^{3+} and Mn^{2+} ions (^6S) is unaffected by the octahedral field whereas the ground state of the Cr^{3+} ion (^4F) is split into an orbital singlet (which is lowest in energy) and two orbital triplets.

4.3 SPIN-ORBIT COUPLING IN THE SOLID STATE

It has already been shown how the L-S coupling scheme may be used to determine the various allowed electronic states of the first transition series atoms and ions. The degeneracy of the electronic states may be partially removed by the crystal field; further splitting of the levels may be caused by the spin-orbit interaction, $\mathcal{H}_{LS}$.

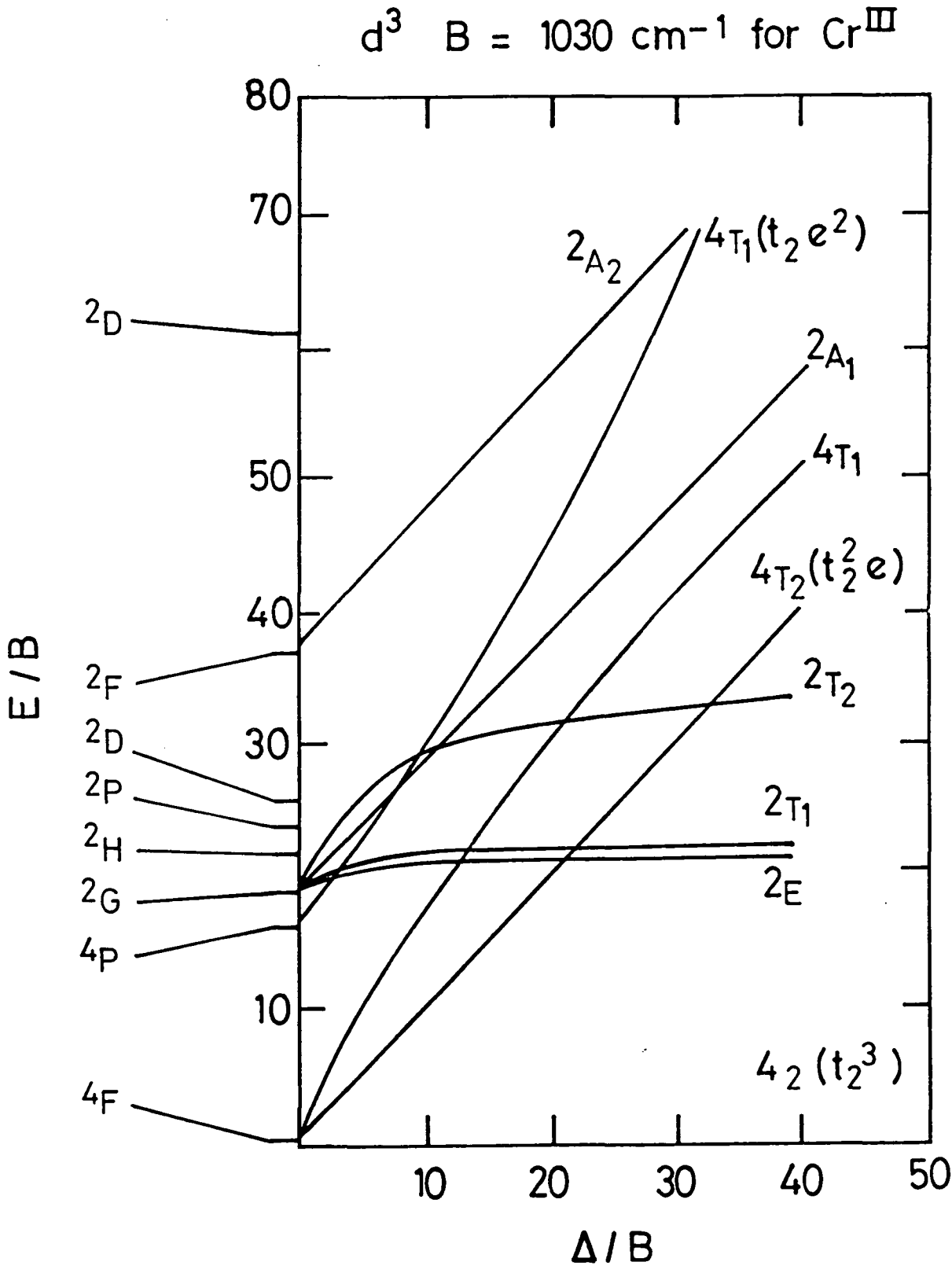

FIGURE 4.1 SPLITTING OF STATES OF THE d^3 CONFIGURATION BY AN OCTAHEDRAL FIELD (AFTER TANABE AND SUGANO [4.10]).

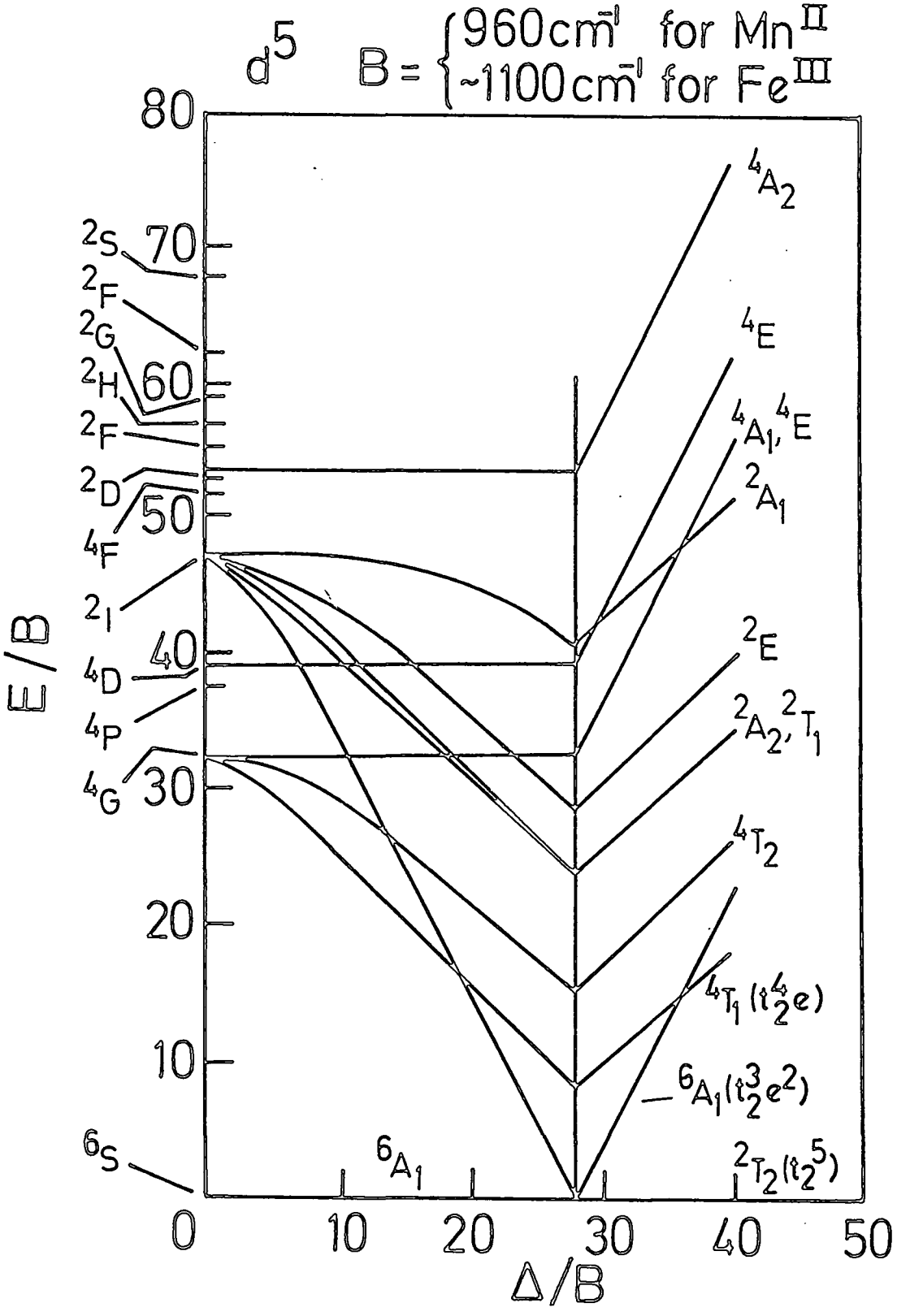

FIGURE 4.2 SPLITTING OF STATES OF THE d^5 CONFIGURATION BY AN OCTAHEDRAL FIELD (AFTER TANABE AND SUGANO [4.10]).

The electronic states are often referred to as multiplets because of the fact that they consist of several components which, in general, differ in energy by much less than one such state differs from another. In the free ion, these components of the multiplet have different values of total angular momentum, J, which is a result of the combination of the orbital and spin angular momenta, L & S. The L-S coupling scheme provides a set of rules which enable the allowed values of J and the differences in energy between the levels with different values of J to be determined.

Abragam and Pryce[4.3] have demonstrated how the use of the L-S coupling scheme may be extended to cover the case of isolated transition metal ions in crystals, where the electronic energy levels are seriously disrupted by the crystal field. As we are particularly interested in the case of Cr^{3+} in an octahedral crystal field, this will be used as an example to illustrate Abragam and Pryce's method.

Figure 4.1 shows that in an octahedral field the electronic ground state of Cr^{3+} (^4F) splits into an orbital singlet, which is lowest in energy, and two higher lying triplets. The orbital singlet can be regarded as having an effective orbital angular momentum, L', equal to zero. The problem is now similar to that of a free ion with $L'=0$ and $S=3/2$, and since $L'=0$ the spin-orbit interaction does not split the orbital singlet. The fourfold spin degeneracy of this level is removed by an external magnetic field and the spin energy levels diverge linearly with the field.

Using suitable representations each of the higher

lying triplets may be compared with a perturbed p electron. It then becomes possible to assign each triplet an effective L' of unity. Any operator within one of the triplets can be expressed as an equivalent operator within $L' = 1$. In EPR the operator L_z is of particular importance and this transforms to the equivalent operator $\alpha L_z'$ within $L' = 1$, where α is a numerical constant equal to $^1/_2$ for the T_2 triplet and $-^3/_2$ for the T_1 triplet. The energy levels of each triplet may now be evaluated using an analagous method to that used for the free-ion case.

Each triplet has $L' = 1$ and $S = ^3/_2$ giving rise to spin-orbit levels for $J' = ^5/_2$, $^3/_2$ and $^1/_2$. The energy of the spin-orbit levels is given by the expression[4.11]

$$E_J = {}^1/_2 \lambda \alpha \; [J'(J'+1) - L'(L'+1) - S(S+1)] \qquad (4.10)$$

Substitution of the appropriate values of L', S, J' & shows that the T_2 triplet has energy levels at $^3\lambda/_4(J' = ^5/_2)$, $-\lambda/_2(J' = ^3/_2)$ and $-^5\lambda/_4(J' = ^1/_2)$ and that the T_1 triplet has energy levels at $-^9\lambda/_4(J' = ^5/_2)$, $^3\lambda/_2(J' = ^3/_2)$ and $^{15}\lambda/_4(J' = ^1/_2)$.

The Zeeman term, which describes the effect of an external magnetic field upon the spin-orbit levels, may be written as [4.11]

$$\mathcal{H}_{Ze} = \beta \vec{H} \cdot (g_{L'} \vec{L'} + g_s \vec{S}) = g \beta \vec{H} \cdot \vec{J'} \qquad (4.11)$$

where $g_s = 2.0023$ (the free electron value) and $g_{L'}$ is the product αg_L (g_L, the orbital g-value, although nominally equal to one is often less than unity because of covalency effects). Then within $J' = L' + S$ the g-value is

$$g = {}^1/_2(g_{L'} + g_s) + {}^1/_2(g_{L'} - g_s)\,\frac{L'(L'+1) - S(S+1)}{J'(J'+1)} \qquad (4.12)$$

For each triplet $L' = 1$ in equation 4.12 and for the orbital singlet ($^4A_2$) $L' = 0$. The energy level diagram of Figure 4.3 shows the g values obtained for each spin-orbit level using equation 4.12. The g-value defined here is the spectroscopic splitting factor of equation 4.5. EPR transitions within a particular J'manifold will obey equation 4.1 although the g value in equation 4.1 now becomes the spectroscopic splitting factor defined by equation 4.12.

4.4 HYPERFINE STRUCTURE[4.12]

In the solid state, the magnetic hyperfine structure term takes the simple form of equation 4.8 i.e.

$$\mathcal{H}\ (\text{hyperfine}) = AI \cdot S$$

provided that equation 4.7 is used to determine the hyperfine structure constant, A. If A is isotropic (as it will be for paramagnetic ions in MgO because of the cubic crystal field), in zero magnetic field the effective spin S (equivalent to J') and the nuclear spin I couple together to form a set of levels with quantum numbers $F = (S+I)$, $(S+I-1)$, ... $|S-I|$. The energy of a level with quantum

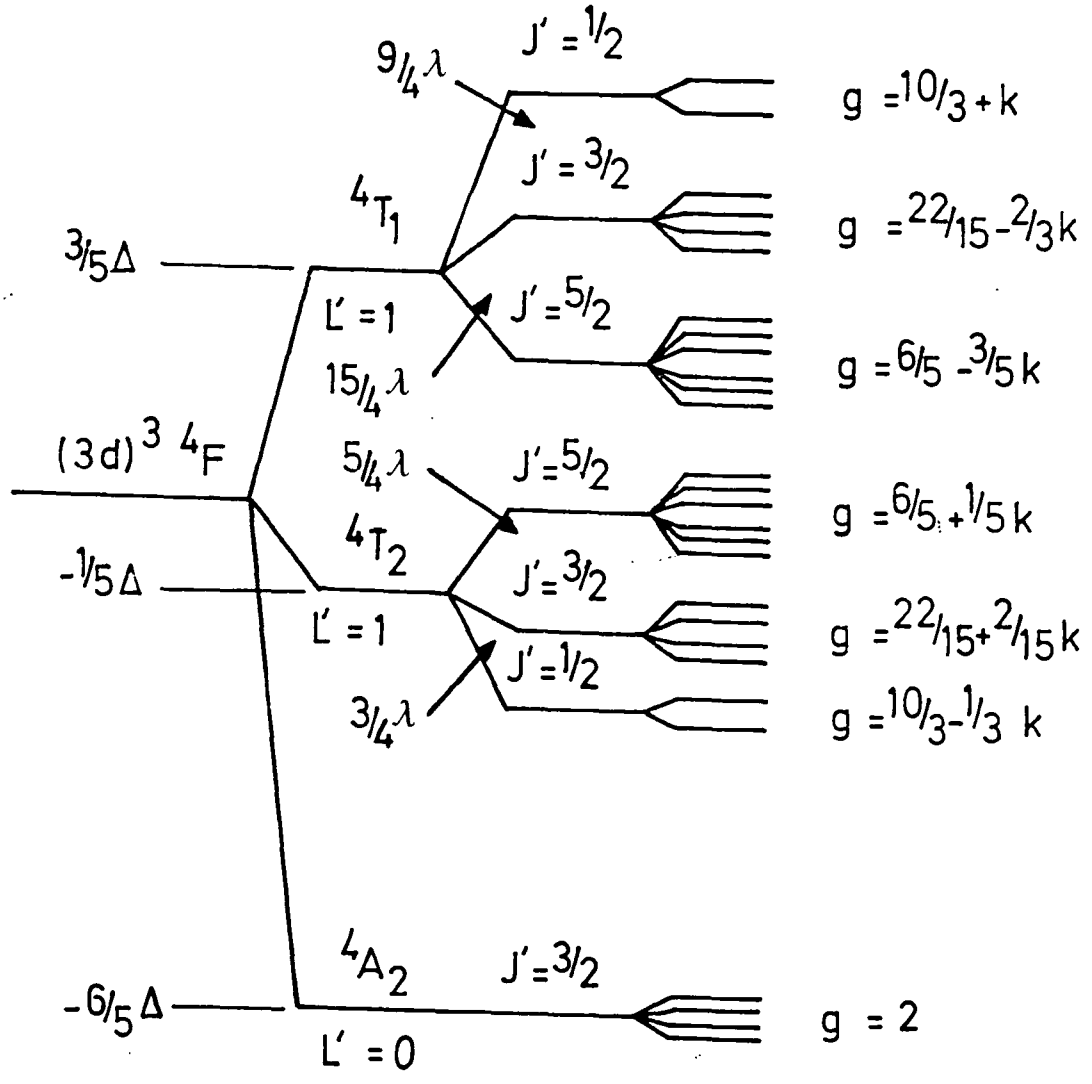

FIGURE 4.3 ENERGY LEVEL DIAGRAM AND g-VALUES FOR THE Cr^{3+} ($3d^3$) ION IN AN OCTAHEDRAL FIELD. THE g-VALUES INVOLVE THE FACTOR $k(= g_L)$ TO ALLOW FOR POSSIBLE COVALENT BONDING, WHICH MAKES $k < 1$. Δ IS KNOWN AS THE CUBIC CRYSTAL FIELD SPLITTING CONSTANT (AFTER STEVENS AND BATES[4.11]).

number F is

$$W_F = {}^1/_2 A[F(F+1) - S(S+1) - I(I+1)] \qquad (4.13)$$

so that the separation between successive levels is

$$W_F - W_{F-1} = AF \qquad (4.14)$$

The splitting of the hyperfine multiplet in zero magnetic field given by equation 4.14 is shown in Figure 4.4a for the system $S = {}^3/_2$, $I = {}^3/_2$.

At the magnetic field values typically used in an EPR experiment ($\sim$ 1 Tesla) the magnetic hyperfine energy is generally smaller than the Zeeman energy. Under these conditions we can use the "strong field" approximation ($A \ll g \beta H$). Using this approximation it can be shown that the levels diverge linearly and, to first order, are given by

$$W = g \beta HM + AMm - g_I \beta Hm \qquad (4.15)$$

where M is the electronic magnetic quantum number, m is the nuclear magnetic quantum number and g_I is the nuclear spectroscopic splitting factor ($\sim 10^{-3}$g). Equation 4.15 includes the electronic Zeeman energy and gives the total energy of the levels of the spin-orbit ground state of an

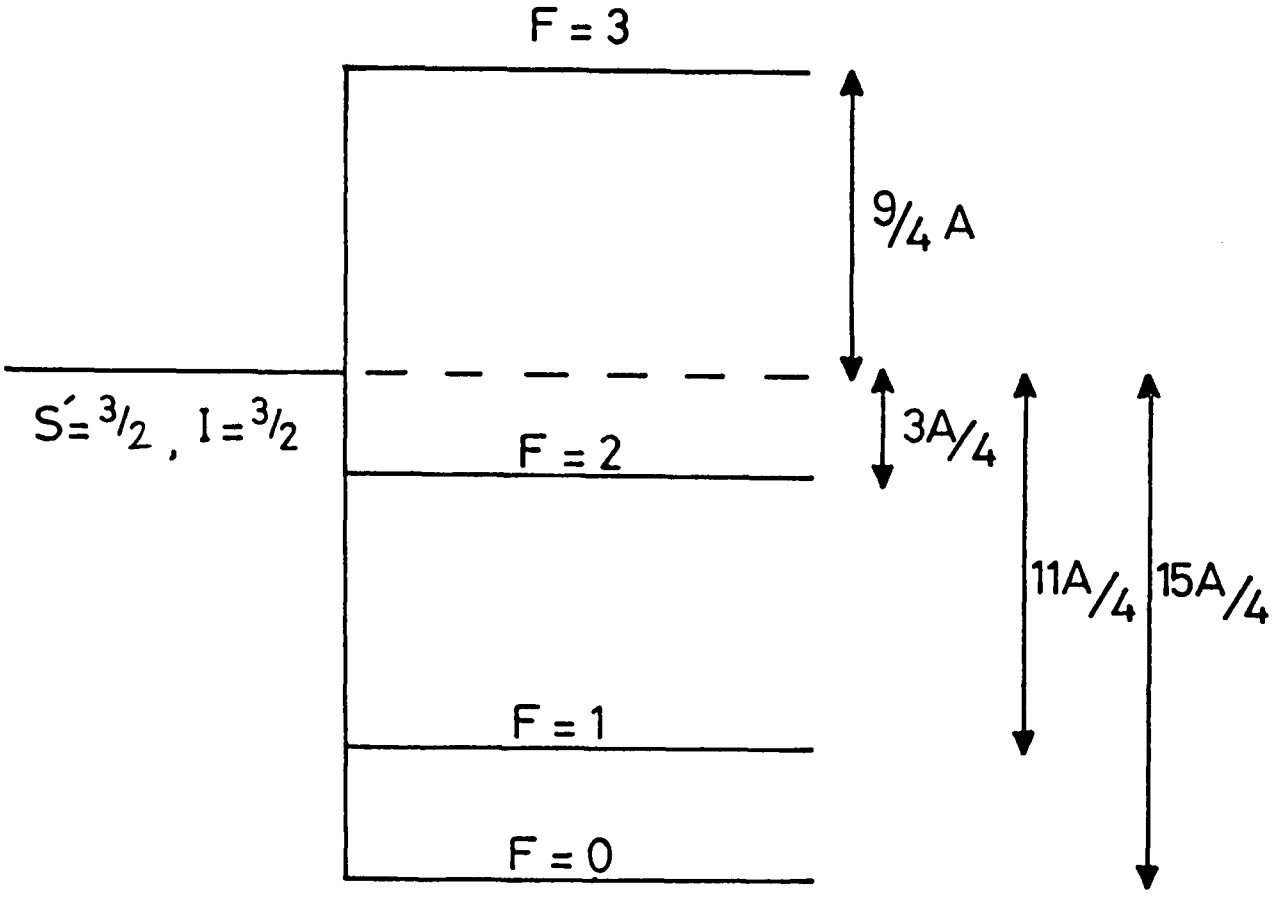

FIGURE 4.4(a) MAGNETIC HYPERFINE MULTIPLET IN ZERO MAGNETIC FIELD FOR THE SYSTEM $S' = 3/2$, $I = 3/2$.

ion with effective spin S and nuclear spin I i.e. equation 4.15 is a solution (under strong field conditions) of the Spin Hamiltonian

$$\mathcal{H} = g\,\beta\, H\cdot S + AS\cdot I - g_I\,\beta\,(H\cdot I)$$

The last term in the above Hamiltonian represents the nuclear Zeeman interaction.

The effect of the hyperfine term, AMm, in equation 4.15 is to split each electronic level into (2I+1) equally spaced levels (the displacements of the levels caused by the nuclear Zeeman term, $-g_I\,\beta Hm$, are small and can usually be ignored). The physical reasoning behind this effect is that the nucleus may assume (2I+1) orientations in the magnetic field produced by a combination of the external field, H, and the surrounding electrons. Each orientation of the nucleus has associated with it a nuclear magnetic field, H_n, which therefore also has (2I+1) equally spaced values and the electronic moment thus precesses about a combined field $(H+H_n)$. Because there are (2I+1) values of $H_n$the precessional frequency of the electronic moment can take on (2I+1) values which will cause each electronic level to split into (2I+1) new levels. This hyperfine splitting in the strong field limit is illustrated in Figure 4.4b for the system $S = {}^3/_2$, $I = {}^3/_2$.

The selection rules $\Delta M = \pm 1$, $\Delta m = 0$ determine the allowed hyperfine transitions. Application of these rules to equation 4.15 shows that the allowed transitions are

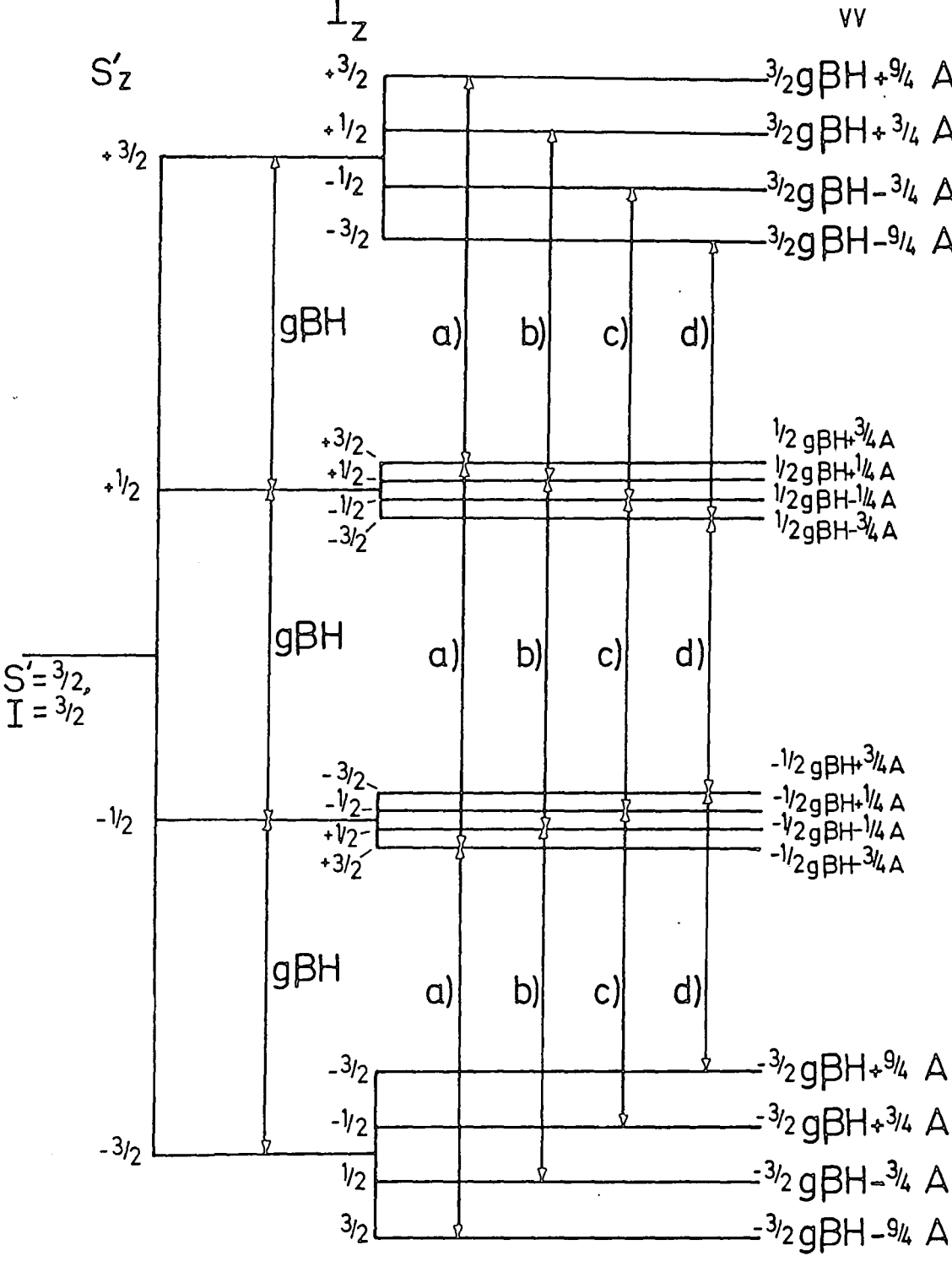

THE INDICATED TRANSITIONS HAVE ENERGIES

a) $m = +3/2$: $h\nu = g\beta H + 3/2\,A$

b) $m = +1/2$: $h\nu = g\beta H + 1/2\,A$

c) $m = -1/2$: $h\nu = g\beta H - 1/2\,A$

d) $m = -3/2$: $h\nu = g\beta H - 3/2\,A$

FIGURE 4.4(b) HYPERFINE ENERGY LEVELS IN A STRONG EXTERNAL MAGNETIC FIELD H ALONG THE z AXIS, FOR A SYSTEM WITH $S' = 3/2$, $I = 3/2$. THE DIAGRAM CORRESPONDS TO THE STRONG FIELD LIMIT, EQUATION 4.15, EXCEPT THAT DISPLACEMENTS DUE TO THE NUCLEAR ZEEMAN TERM $-g_I \beta H m$ ARE OMITTED. NOTE THAT THE ORDER OF THE NUCLEAR LEVELS DUE TO THE MAGNETIC HYPERFINE INTERACTION REVERSES WITH THE SIGN OF S'_z. THE TRANSITIONS ALLOWED BY THE SELECTION RULES $\Delta M = \pm 1$, $\Delta m = 0$ ARE INDICATED ALONG WITH THE TRANSITION ENERGIES.

equally spaced at

$$h\nu = g\beta H + Am \qquad (4.16)$$

In terms of the argument used to explain the origin of the hyperfine structure, equation 4.16 is equivalent to the electronic magnetic resonance taking place in a field $(H+H_n)$, where $H_n = (Am/g\beta)$ is the steady component of the nuclear field in the direction of H.

In strong magnetic fields, when anisotropy is present (including anisotropy in the g factor) equation 4.15 is still valid to a first approximation, with g given by equation 4.5 and A by equation 4.7. In this approximation, the energy levels diverge linearly with H but with separations that depend upon the orientation of the magnetic field.

Since the separations of the (2I+1) hyperfine levels are small, the population of all the levels is approximately equal at normal temperatures and therefore the (2I+1) lines are equally intense as well as equidistant. This makes it easy to discriminate the hyperfine structure from the fine structure.

If second order effects are taken into account an energy

$$W = \frac{A^2}{2h\nu}\left\{ M[I(I+1) - m^2] - m[S(S+1) - M^2]\right\} \qquad (4.17)$$

is added to equation 4.15.

The fairly simple expressions which we have used to define the positions of the hyperfine energy levels in zero and strong magnetic fields do not apply in weak and intermediate magnetic fields. In fact, the expressions for the energy level positions in these field regions are quite complex [4.13] but it is not proposed to describe them in detail here since all the experimental measurements undertaken for this work were in the strong field region.

4.5 THE SPIN HAMILTONIAN OF Cr^{3+} IN MgO

Paramagnetic resonance is concerned with the investigation of the lowest energy levels of paramagnetic ions. Therefore for Cr^{3+} in the octahedral crystal field of MgO it is the $^4A_2$ orbital singlet which is responsible for the paramagnetic resonance absorption and for the purposes of EPR spectroscopy this level may be regarded in isolation, as the next highest triplet (T_2) is separated by about 10^4 cm^{-1}.

The $^4A_2$ state acts like a ^4S state and it might be expected that the Spin Hamiltonian is simply

$$\mathcal{H}_s = g \beta H \cdot S \qquad (4.18)$$

In the cubic field the three predicted electronic transitions should coincide to give one line with a g-factor corresponding to an orbital singlet i.e. $g \sim 2$.

However, the chromium spectrum is complicated by the

fact that there is a stable isotope (Cr^{53}) of about 9.55% abundance with a nuclear spin of $^3/_2$ [4.14,4.15]. This results in a small but detectable hyperfine structure and the complete Spin Hamiltonian becomes [4.16]

$$\mathcal{H}_s = g\beta H \cdot S + AI \cdot S \qquad (4.19)$$

Including second order effects, the transitions occur at

$$H = H_o - Am - {}^{A^2}/_{2H_o}\,[I(I+1) - m^2 + m(2M-1)] \qquad (4.20)$$

where $H_o = {}^{h\nu}/_{g\beta}$ (ν is the applied field frequency).

At high magnetic fields the selection rules $\Delta M = \pm 1$, $\Delta m = 0$ apply and the allowed transitions fall into four groups

a) $m = +^3/_2$

$$M = {}^3/_2 : \quad H = H_o - {}^3/_2 A - {}^{9A^2}/_{4H_o}$$

$$M = {}^1/_2 : \quad H = H_o - {}^3/_2 A - {}^{3A^2}/_{4H_o} \qquad (4.21)$$

$$M = -{}^1/_2 : \quad H = H_o - {}^3/_2 A + {}^{3A^2}/_{4H_o}$$

b) $m = +^1/_2$

$$M = {}^3/_2 \;:\; H = H_o - {}^1/_2A - {}^{9A^2}/_{4H_o}$$

$$M = {}^1/_2 \;:\; H = H_o - {}^1/_2A - {}^{7A^2}/_{4H_o}$$

$$M = -{}^1/_2 \;:\; H = H_o - {}^1/_2A - {}^{5A^2}/_{4H_o}$$

c) $m = -^1/_2$

$$M = {}^3/_2 \;:\; H = H_o + {}^1/_2A - {}^{5A^2}/_{4H_o}$$

$$M = {}^1/_2 \;:\; H = H_o + {}^1/_2A - {}^{7A^2}/_{4H_o} \qquad (4.21)$$

$$M = -{}^1/_2 \;:\; H = H_o + {}^1/_2A - {}^{9A^2}/_{4H_o}$$

d) $m = -^3/_2$

$$M = {}^3/_2 \;:\; H = H_o + {}^3/_2A + {}^{3A^2}/_{4H_o}$$

$$M = {}^1/_2 \;:\; H = H_o + {}^3/_2A - {}^{3A^2}/4H_o$$

$$M = -{}^1/_2 \;:\; H = H_o + {}^3/_2A - {}^{9A^2}/_{4H_o}$$

All the transitions of equation 4.21 are indicated in Figure 4.5 which shows the energy levels of the ground state ($^4A_2$). Experimentally, the terms in A^2/H_o are found to be very small ($A \sim 1.8$mT, $H_o \sim 340$mT at X-band[4.17]) and

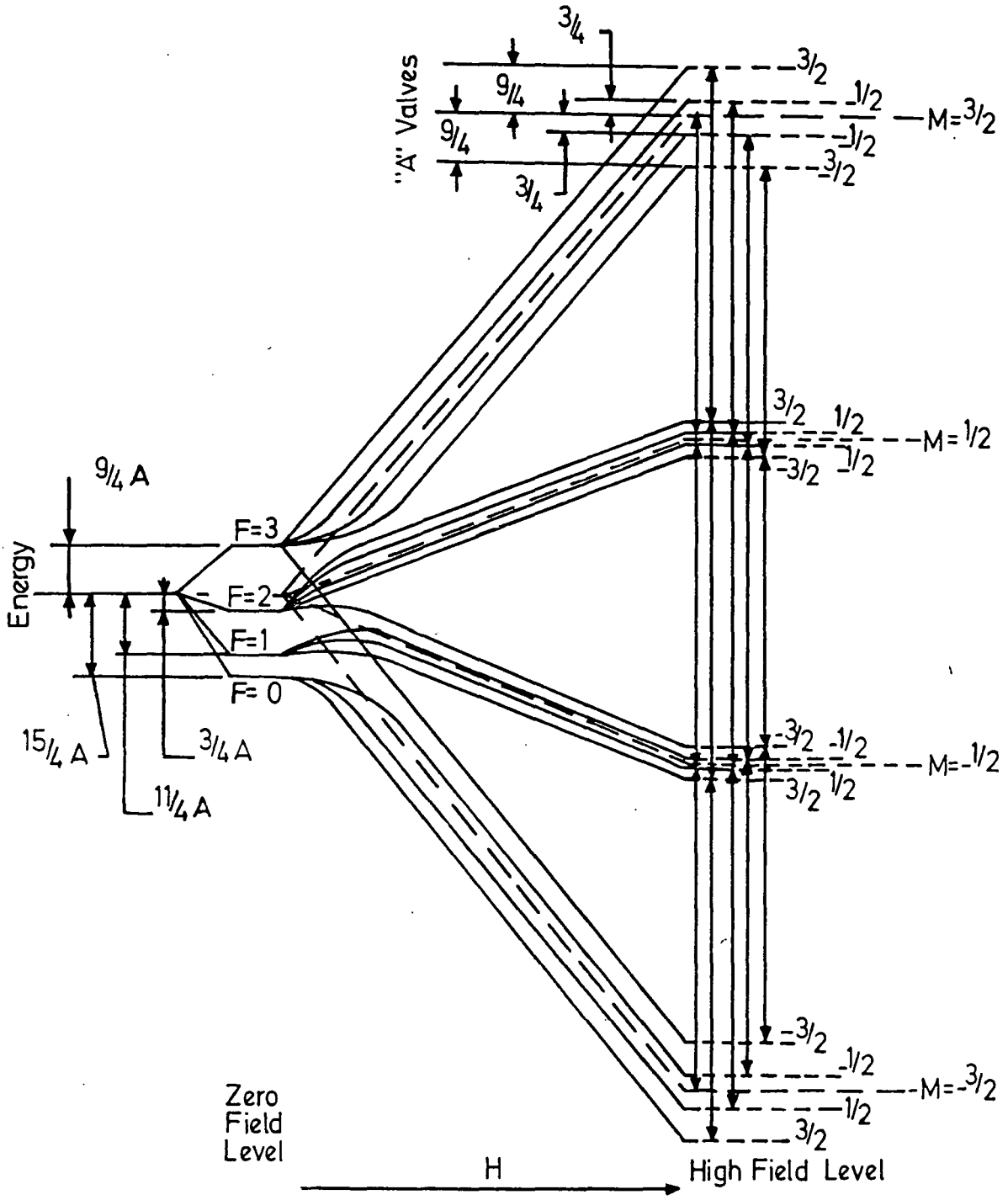

FIGURE 4.5 A SCHEMATIC ENERGY LEVEL DIAGRAM OF THE ELECTRONIC ENERGY LEVELS OF Cr^{3+} IN MgO IN ZERO AND STRONG MAGNETIC FIELDS, TOGETHER WITH THE SPLITTING CAUSED BY THE NUCLEAR SPIN. THE DASHED LINE -- INDICATES THE ENERGY LEVELS OF THE EVEN ISOTOPES OF CHROMIUM, THE SOLID LINE — THOSE OF THE ODD ISOTOPES OF Cr^{53}. THE OBSERVED TRANSITIONS ARE INDICATED BY ARROWS.

the three transitions for each value of m are unresolved to give four hyperfine lines at magnetic field values of:

a) $m = +^{3}/_{2}$

$$H = H_o - {}^{3}/_{2}A$$

b) $m = +^{1}/_{2}$

$$H = H_o - {}^{1}/_{2}A \qquad (4.22)$$

c) $m = -^{1}/_{2}$

$$H = H_o + {}^{1}/_{2}A$$

d) $m = -^{3}/_{2}$

$$H = H_o + {}^{3}/_{2}A$$

The EPR spectrum of the isotopes of chromium without a nuclear spin can be described by the Hamiltonian of equation 4.18 and the spectrum consists of a single line with a g-value of 1.9800[4.16]. The deviation of the g-value from the "spin only" value of 2.0023 is caused by a contribution from the triplet T_2 to the orbital moment of the ground state. From crystal field theory it can be shown that[4.18]

$$g - g_e = {}^{-8\lambda}/_{\Delta} \qquad (4.23)$$

where g_e is the spin only g-value. Putting g = 1.9800 and $\Delta = 22.700cm^{-1}$ [4.15] in equation 4.23 yields $\lambda = 63cm^{-1}$ and the ratio of $\lambda / \lambda_o = 0.69$ where λ_o is the spin-orbit coupling constant of the ^4F state of the free ion ($\lambda_o = 91cm^{-1}$ [4.11]).

Since the Cr^{53} isotope is only 9.55% abundant each hyperfine structure line has an intensity of approximately $^1/_{42}$ [4.15] of that of the main line at g = 1.9800. All five lines of the spectrum are isotropic.

4.6 THE SPIN HAMILTONIAN OF Fe^{3+} IN MgO

In the cubic crystal field of MgO the Fe^{3+} ion has a $^6S_{5/2}$ electronic ground state which is an orbital singlet. The only isotope of iron with a nuclear spin, Fe^{57}, has a natural abundance of only 2.4% which is too low to expect any hyperfine structure which is present to be detectable. Therefore the observed spectrum arises from the isotopes of iron with no nuclear spin. It might be expected that the six spin levels of the ground state of these isotopes diverge linearly in an applied magnetic field and that the five resulting EPR transitions coincide to yield a single isotropic line with a g-value of approximately 2. The Spin Hamiltonian used to describe such a spectrum would only contain the Zeeman term (equation 4.18).

However, group theoretical considerations [4.19] indicate that even a cubic field splits the six fold degenerate ground state into twofold and fourfold degenerate levels. Although, to a first approximation, neither a cubic crystal field nor the spin-orbit interaction can split the $^6S_{5/2}$ state, Van Vleck and Penney[4.20] have shown that the crystalline cubic field can influence the electron spins through higher order interactions involving spin-orbit coupling with excited states. To account for this splitting of the ground state in the octahedral crystal field of MgO an additional term has to be added to the Hamiltonian of

equation 4.18 so that the effective Spin Hamiltonian becomes:[4.21,4.22]

$$\mathcal{H}_S = g\,\beta\,H\cdot S + \frac{1}{6}a\left\{S_x^4+S_y^4+S_z^4-\frac{1}{5}[S(S+1)(3S^2+3S-1)]\right\} \quad (4.24)$$

where S is the effective spin ($=^5/_2$); S_x is the projection of S on the x axis etc; and 3a is the separation of the twofold and fourfold degenerate levels in zero magnetic field.

Both g and a are determined experimentally and it is found that the g-factor is slightly greater than the free electron value ($g = 2.0037$[4.21]) due to the admixture of higher energy terms into the ground state term as a result of covalent bonding.[4.23] The small departure of the g-factor from the spin only value shows that the ground state is relatively "pure" and that the admixture of higher lying electronic states is slight.

The eigenvalues of equation 4.24 have been evaluated by Debye[4.24] and by Kronig and Bouwcamp,[4.25] and, to a good approximation, in a strong external magnetic field the energy levels are given by the expressions listed in Table 4.2. These eigenvalues may be used in conjunction with the experimentally determined values of g and a to plot the variation of the energy of the levels with applied magnetic field for any direction of applied field. Figure 4.6 shows this variation when the field is applied along a <100> direction. Also shown in Figure 4.6, at magnetic field positions appropriate for an applied microwave frequency of 9.1GHz, are the five main $\Delta m_s = 1$ electronic transitions

LEVEL	ENERGY
$\pm 5/2$	$\pm 5/2\ g\beta H + 1/2\ pa \pm (212 - 24p - 113p^2)(a^2/240 g\beta H)$
$\pm 3/2$	$\pm 3/2\ g\beta H - 3/2\ pa \pm (12 + 8p - 15p^2)(a^2/16 g\beta H)$
$\pm 1/2$	$\pm 1/2\ g\beta H + pa \pm (-2 - 3p + 5p^2)(a^2/3 g\beta H)$

The parameter $p = 1 - 5\psi$ and $\psi = \ell^2m^2 + m^2n^2 + \ell^2n^2$ where ℓ, m and n are the direction cosines of the applied magnetic field referred to the cubic axes of the crystal i.e.

$$\ell = \sin\theta \sin\phi \qquad m = \sin\theta \cos\phi \qquad n = \cos\theta$$

TABLE 4.2 The energy levels of a $^6S_{5/2}$ state ion in an octahedral site and strong magnetic field (after Debye[4.24] and Kronig & Bouwkamp[4.25]).

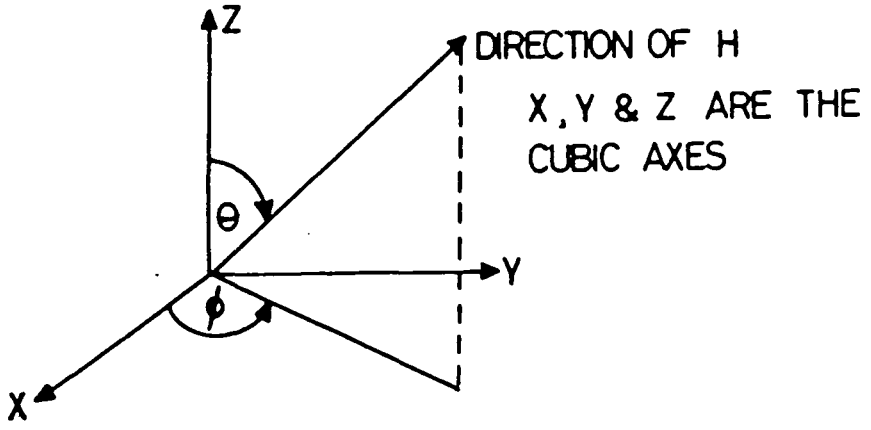

The angles θ and ϕ are defined as shown in the diagram above.

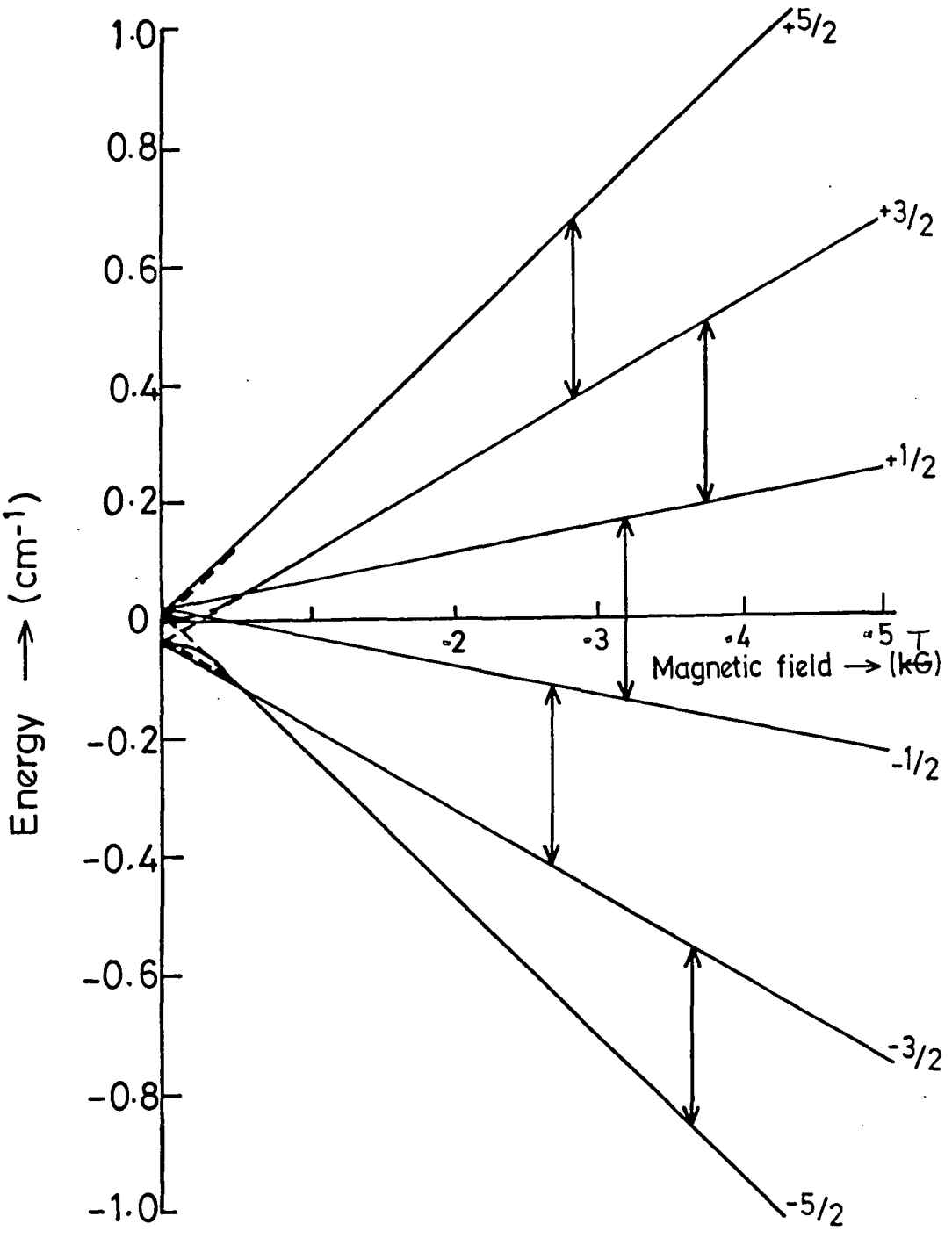

FIGURE 4.6 ZEEMAN LEVELS FOR A $^6S_{5/2}$ STATE; H// <100> (AFTER DEBYE[4.24]).

THE $\Delta m_S = 1$ TRANSITIONS FOR Fe^{3+} IN CUBIC SITES IN MgO AT 9.1 GHz ARE SHOWN.

which are responsible for the EPR spectrum of Fe^{3+} in MgO. The transition energies for the $\Delta m_s = 1$ transitions may be deduced from the eigenvalues of Table 4.2 and are listed separately in Table 4.3. Although $\Delta m_s = 2$[4.26] and even $\Delta m_s = 3,4\&5$[4.27] transitions have been reported, magnetic fields of 200mT and greater are sufficient at x-band to exclude all but the $\Delta m_s = 1$ transitions.

To first order, the $\Delta m_s=1$ lines form a symmetric pattern, the $\pm\,{}^3/_2 \longleftrightarrow \pm\,{}^1/_2$ transitions being located at $(\pm\,{}^5/_2 pa)$ and the $\pm{}^5/_2 \longleftrightarrow \pm{}^3/_2$ transitions at $(\mp 2pa)$ from the central $+\frac{1}{2} \longleftrightarrow -\frac{1}{2}$ transition. All five lines are allowed whatever the orientation and therefore the spectrum has the same form for all directions of applied field. However, the outer pairs of lines are highly anisotropic, their positions depending upon the quantity p. Since p can be written in the form [4.28]

$$2p/5 = \ell^4 + m^4 + n^4 - {}^3/_5 \qquad (4.25)$$

and the cubic potential of the fourth degree that is responsible for the splitting of the ground state is given by

$$V_{cub} = x^4 + y^4 + z^4 - {}^3/_5 r^4 \qquad (4.26)$$

the displacements of the outer lines vary with angle in a

TRANSITION	TRANSITION ENERGY	RELATIVE INTENSITY
$5/2 \leftrightarrow 3/2$	$h\nu = g\beta H + 2pa + (2 - 9p - 7p^2)(a^2/15g\beta H)$	5
$3/2 \leftrightarrow 1/2$	$h\nu = g\beta H - 5/2pa + (68 + 72p - 125p^2)(a^2/48g\beta H)$	8
$1/2 \leftrightarrow 1/2$	$h\nu = g\beta H + (-2 - 3p + 5p^2)(2a^2/3g\beta H)$	9
$-1/2 \leftrightarrow -3/2$	$h\nu = g\beta H + 5/2pa + (68 + 72p - 125p^2)(a^2/48g\beta H)$	8
$-3/2 \leftrightarrow -5/2$	$h\nu = g\beta H - 2pa + (2 - 9p - 7p^2)(a^2/15g\beta H)$	5

Table 4.3 The transition energies and relative intensities for the $\Delta m_s = 1$ transitions of a $^6S_{5/2}$ ion in an octahedral site.

way which reflects the symmetry of the crystal field (the form of the Spin Hamiltonian is also dictated by the crystal field symmetry, as the second term in equation 4.24 is simply the operator equivalent of equation 4.26). The isofrequency plot illustrated in Figure 4.7 shows the anisotropic nature of the outer pairs of lines and the contrasting, almost isotropic behaviour of the central $+\frac{1}{2} \longleftrightarrow -\frac{1}{2}$ transition.

The relative intensity of an absorption line resulting from a transition between the states labelled by m_s & $m_s - 1$ is given by the square of the matrix element of $S_+(=S_x+iS_y)$ between the two states, which is[4.29]

$$\text{Relative Intensity} = S(S+1) - m_s(m_s - 1) \qquad (4.27)$$

The relative intensities of the $\Delta m_s=1$ transitions have been given along with the transition energies in Table 4.3.

Equation 4.27 is only valid if the spin system is at thermal equilibrium i.e. if the energy difference between adjacent spin levels is much less than kT so that all the levels are almost equally populated. At low temperatures (in the liquid helium range) and high magnetic fields the lower lying levels (the $m_s=-^5/_2$ and $m_s=-^3/_2$ levels in this case) are more heavily populated. Absorption lines originating from these levels become relatively more intense compared to those originating from the higher lying levels ($m_s=+^3/_2$ & $m_s=+^5/_2$). Thus, if we observe the spectrum at

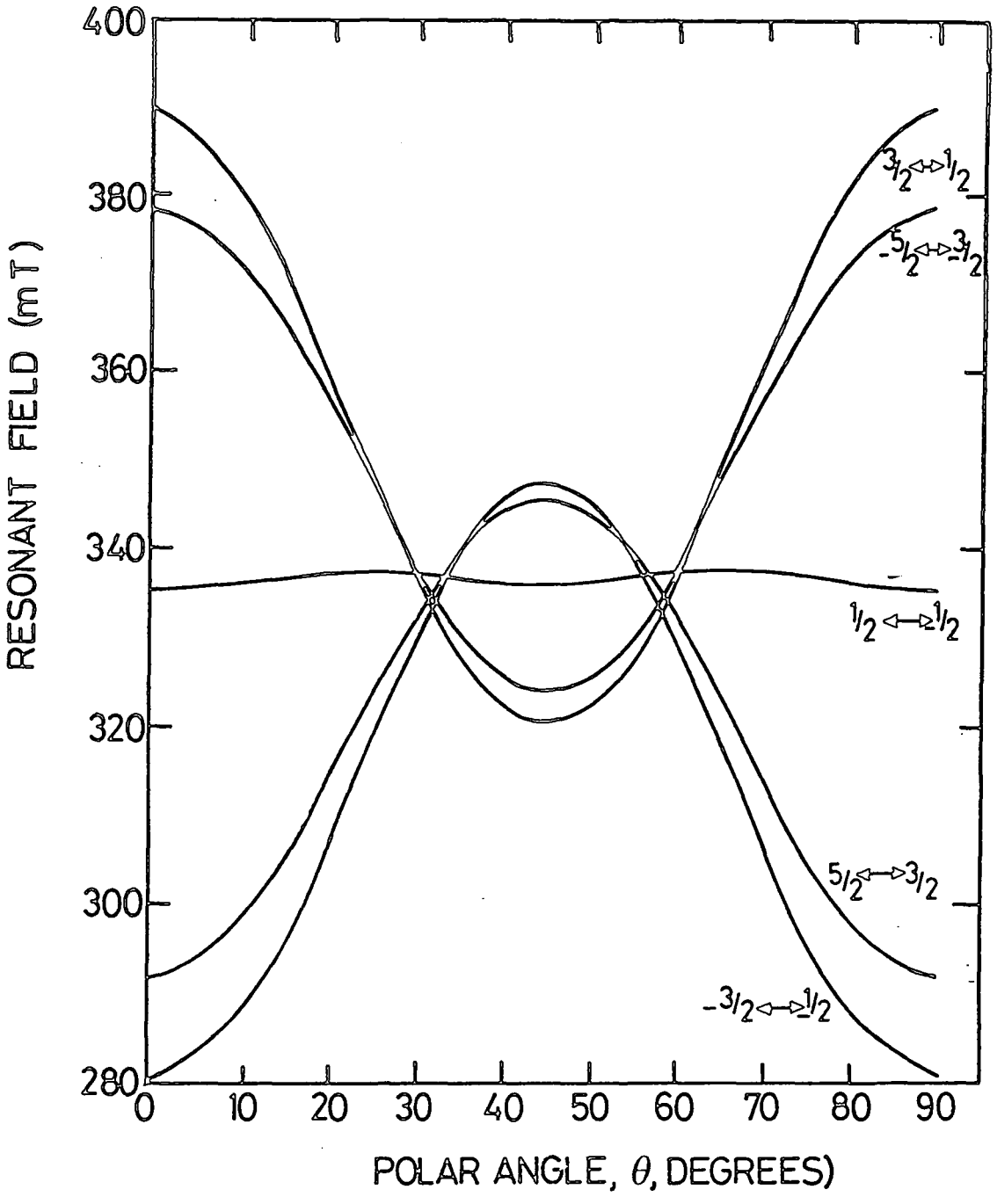

FIGURE 4.7 THE CALCULATED VARIATION OF THE RESONANT FIELD WITH POLAR ANGLE IN THE {100} PLANE AT 9.4 GHz FOR THE $\Delta m_s = 1$ TRANSITIONS OF Fe^{3+} IN MgO USING THE EXPERIMENTALLY DETERMINED VALUES OF g(2.0037) AND a(21.6mT).

low temperature, one of the pair of lines at $\pm 2pa$ from the central transition will increase in intensity relative to the other and this may be labelled the $-{}^{5}/_{2} \longleftrightarrow -{}^{3}/_{2}$ transition and similarly one of the pair of lines displaced by $\pm {}^{5}/_{2}pa$ from the $+\frac{1}{2} \longleftrightarrow -\frac{1}{2}$ transition will increase in intensity relative to the other and may be labelled the $-{}^{3}/_{2} \longleftrightarrow -{}^{1}/_{2}$ transition. If, in addition, the external magnetic field is directed along a <100> direction so that p is positive, inspection of Table 4.3 shows that the $-{}^{5}/_{2} \longleftrightarrow -{}^{3}/_{2}$ transition falls at a higher field and the $-{}^{3}/_{2} \longleftrightarrow -{}^{1}/_{2}$ transition at a lower field than the central $+\frac{1}{2} \longleftrightarrow -\frac{1}{2}$ transition if a is positive and conversely if a is negative. This low temperature experiment enables us to determine the sign of a and for Fe^{3+} in MgO it is found that a is positive[4.30].

4.7 THE SPIN HAMILTONIAN OF Mn^{2+} IN MgO

In the cubic crystal field of MgO Mn^{2+}, like Fe^{3+}, has a ${}^{6}S_{5/2}$ electronic ground state. However, the spectrum of Mn^{2+} is more complex than that of Fe^{3+} because the only naturally occuring isotope of manganese, Mn^{55}, has a nuclear spin of ${}^{5}/_{2}$which gives rise to a large hyperfine structure. This is somewhat surprising since, according to theory, no hyperfine structure would normally be expected for an S state ion. To explain this anomaly it has been suggested that configurational interaction may result in admixture of states of the type $3s3d^{5}4s$ to the $3d^{5}$ ground state [4.31].

Unpaired s electrons are very potent in giving a large contribution to the hyperfine structure splitting because of

the Fermi term[4.32] $2\gamma\beta\beta_n[{}^1/_3(8\pi)\psi^2(0)]S\cdot I$ and only a small admixture of such states could account for the hyperfine structure. However, the calculated admixture, while of the right sign, was about ten times smaller than the experimental value [4.33] so that a detailed explanation of the s-electron effect in the paramagnetic resonance spectrum of Mn^{2+} is still lacking.

The Spin Hamiltonian of Mn^{2+} is the same as that of Fe^{3+} except that the term AI.S is added to represent the hyperfine structure interaction and therefore the total Hamiltonian is given by:[4.34]

$$\mathcal{H}_s = g\beta H\cdot S + \tfrac{1}{6}a[S_x^4+S_y^4+S_z^4-\tfrac{1}{5}S(S+1)(3S^2+3S-1)] + AI\cdot S \quad (4.28)$$

In the cubic crystal field A is isotropic and, in strong magnetic fields, the hyperfine contribution to the energy levels is simply a combination of equations 4.15 and 4.17 i.e.

$$W_{HF} = AMm + \frac{A^2}{2h\nu}\left\{M[I(I+1)-m^2] - m[S(S+1)-M^2]\right\} \quad (4.29)$$

The total energy of the levels is obtained by adding equation 4.29 to the eigenvalues of Table 4.2. The selection rules $\Delta m=0$, $\Delta M=\pm 1$ apply so that one has to add

$$Am + [I(I+1) - m^2 + m(2M-1)] \frac{A^2}{2h\nu} \qquad (4.30)$$

to the formulae for the various electronic transitions (Table 4.3) to obtain the total transition energies.

A more convenient expression for the line positions was derived by Matarrese and Kikuchi[4.35] who showed that the resonant magnetic field, $H(M,m)$ for the transition $(M,m) \longleftrightarrow (M-1,m)$ is given by:

$$H(M,m) = H_o - Am - \frac{A^2}{2H_o}[\frac{35}{4} - m^2 + m(2M-1)] - \ldots$$

$$\ldots \quad -(\frac{a}{384})(35\cos^4\theta - 30\cos^2\theta + 3 + 5\sin^4\theta\cos 4\phi)x \ldots \qquad (4.31)$$

$$\ldots \quad x(56M^3 - 84M^2 - 134M + 81)$$

where $H_o = \frac{h\nu}{g\beta}$ and θ and ϕ are the spherical angular coordinates of the magnetic field relative to the <100> axis (as defined in the diagram below Table 4.2). Although equation 4.31 ignores terms in $(a^2/g\beta H)$ it predicts the line positions accurately enough in this particular case.

The numerical values of A and H_o are obtained by noting that

$$H(\tfrac{1}{2},m) - H(\tfrac{1}{2},-m) = -2mA \qquad (4.32a)$$

and

$$H(\tfrac{1}{2},m) + H(\tfrac{1}{2},-m) = 2H_o - \frac{A^2}{H_o}[(\frac{35}{4}-m^2)] \qquad (4.32b)$$

The g-factor is isotropic in the cubic field and therefore we may use the relationship

$$h\nu = g\beta H_o$$

to calculate its value. The S ground state is relatively free of admixtures from higher lying levels so the g-value is close to the free electron value ($g = 2.0014$[4.34]).

It is found experimentally that the spectrum consists of six groups of five lines;[4.34] this pattern arises because the five fine structure transitions are each divided into six components by the hyperfine interaction with the nuclear magnetic moment of Mn^{2+}. The form of the spectrum leads us to the conclusion that the hyperfine structure constant, A, is larger than the fine structure constant, a ($A = -8.67mT$, $a = +1.996mT$[4.34]). To first order, the fine structure lines of each hyperfine group

behave exactly like the complete Fe^{3+} spectrum, having the same separations, relative intensities, quantum labels and angular dependence. This is because, in this approximation, the separation of similar fine structure lines in adjacent hyperfine groups is simply the numerical value of A.

However, since A is large, second order hyperfine effects cannot be ignored and the terms in $(\frac{A^2}{H_o})$ in equation 4.31 have a marked effect on the line positions. For any particular hyperfine group (i.e. for a given value of m), if the applied field is directed along the <100> direction so that $\theta = 0°$ and $\phi = 0°$, the separations of the fine structure lines are given by the expressions of Figure 4.8(a) which are derived from equation 4.31. Since A may be determined in the manner described above, for each hyperfine group two values of a may be calculated using the expressions of Figure 4.8(a). The magnitude of a is determined by averaging the values obtained from all six hyperfine groups.

Inspection of equation 4.31 shows that if A is negative transitions with m positive fall at higher magnetic fields than with m negative and conversely if A is positive. Bearing this in mind, the equations of Figure 4.8(a) show that, if M is parallel to the <100> direction, the separation between the $M = {}^3/_2 \longleftrightarrow {}^1/_2$ and $M = -{}^3/_2 \longleftrightarrow -{}^1/_2$ transitions is larger at low fields than the same separation at high fields by $(\frac{A^2}{H_o})(4m)$ if A and a have opposite sign. If A and a have the same sign, then this separation is smaller at low fields. The opposite holds true for the $M = +{}^5/_2 \longleftrightarrow +{}^3/_2$ to $M = -{}^5/_2 \longleftrightarrow -{}^3/_2$ separation. The various possibilities are shown in Figure 4.8(b) for the

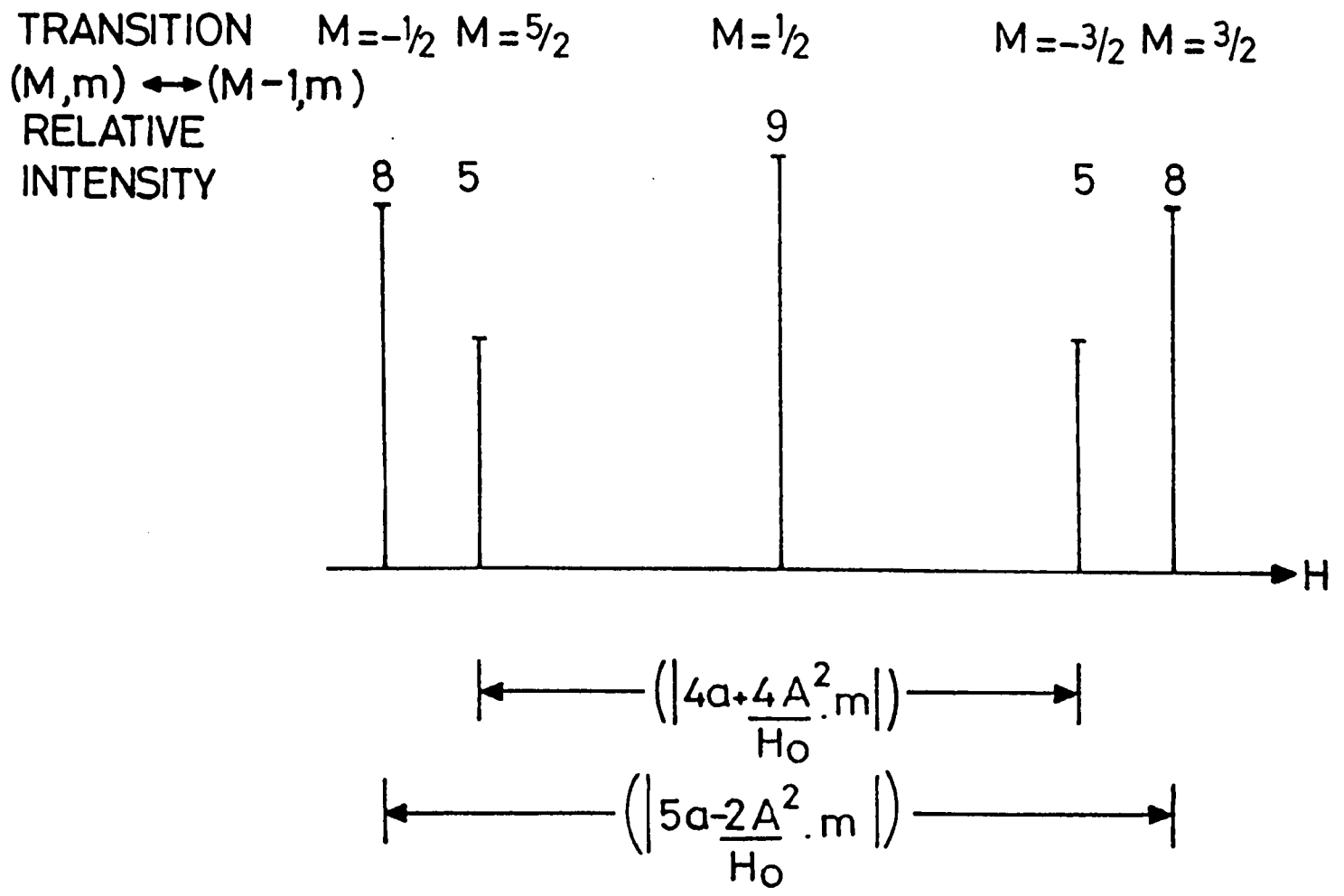

FIGURE 4.8(a) A SCHEMATIC REPRESENTATION OF THE FINE STRUCTURE PATTERN OF THE Mn^{2+} SPECTRUM IN MgO FOR AN UNSPECIFIED VALUE OF m. THE EQUATIONS SHOWN REPRESENT THE LINE SEPARATIONS WHEN H IS PARALLEL TO THE <100> DIRECTION. THE TRANSITIONS HAVE BEEN LABELLED FOR THE CASE WHEN a IS POSITIVE.

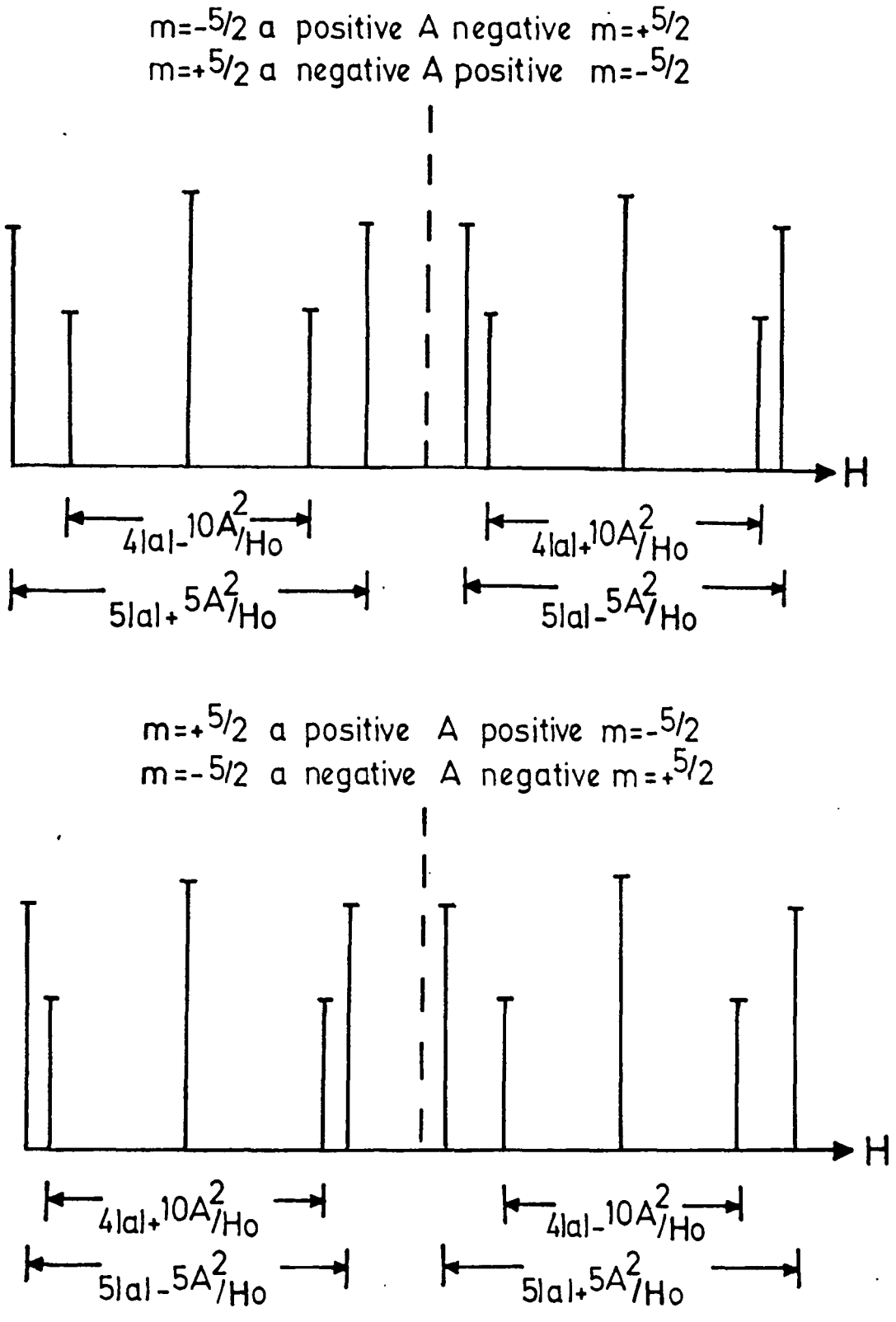

FIGURE 4.8(b) SCHEMATIC SPECTRUM OF THE FINE STRUCTURE FOR $m = +5/2$ AND $m = -5/2$. THE UPPER DIAGRAM SHOWS THE SPECTRUM WHEN A AND a HAVE OPPOSITE SIGNS. THE DOTTED LINE INDICATES THE OMISSION FROM THE DIAGRAM OF THE PENTADS $m = \pm 3/2$ AND $m = \pm 1/2$. THE LOWER DIAGRAM SHOWS THE SPECTRUM WHEN A AND a HAVE THE SAME SIGN. NOTE THAT THE $M = \pm 3/2 \leftrightarrow \pm 1/2$ AND $M = \pm 5/2 \leftrightarrow \pm 3/2$ TRANSITIONS FALL NEARLY TOGETHER AT HIGH FIELDS WHEN $^{a}/A$ IS NEGATIVE AND AT LOW FIELDS WHEN $^{a}/A$ IS POSITIVE. THE FIRST CASE IS THE ONE WHICH IS FOUND EXPERIMENTALLY (AFTER LOW(4.34)).

$m = \pm {}^{5}/_{2}$ hyperfine groups, which are found at the extreme ends of the spectrum. The situation found experimentally is illustrated schematically in Figure 4.8(c) which shows that the $M = \pm {}^{5}/_{2} \longleftrightarrow \pm {}^{3}/_{2}$ and $M = \pm {}^{3}/_{2} \longleftrightarrow \pm {}^{1}/_{2}$ transitions within individual hyperfine groups gradually converge as the magnetic field increases. Therefore we may conclude that A and a have opposite signs. If the low temperature experiment described for the Fe^{3+} ion is carried out under exactly the same conditions for Mn^{2+} we find that a is positive and therefore A must be negative[4.34]. The quantum labels assigned to the transitions in Figure 4.8(c) were allocated in accord with the deduced signs of A and a. Figure 4.8(c) also shows that although the fine structure lines within a particular hyperfine group vary in intensity in the predicted manner, the relative intensities of comparable transitions within different hyperfine groups are the same. Finally, since the hyperfine terms are isotropic the lines in each fine structure group will vary with angle in the same way as the complete Fe^{3+} spectrum, although the prescence of the $(\frac{A^2}{H_o})$ terms in the expressions for the transition energies will alter the relative separations by a constant amount.

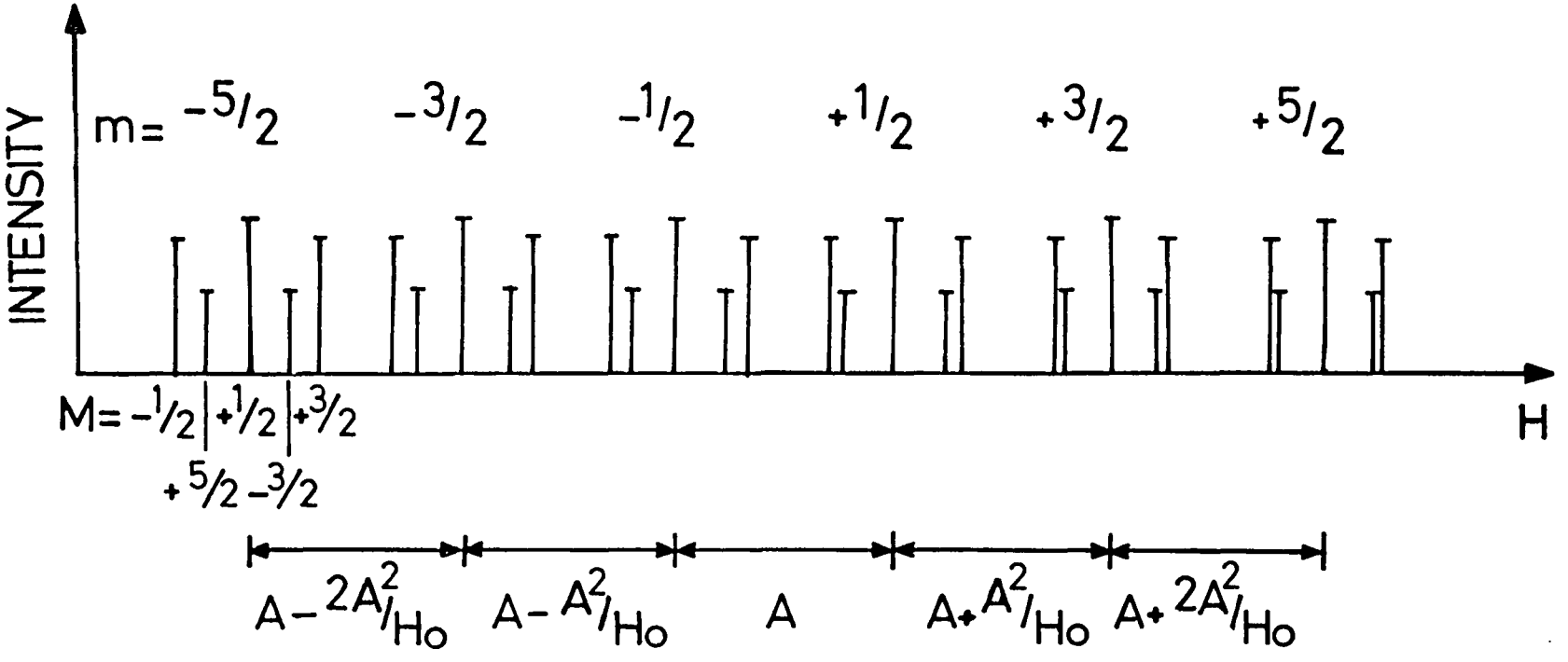

FIGURE 4.8(c) A SCHEMATIC REPRESENTATION OF THE ENTIRE SPECTRUM OF Mn^{2+} IN MgO FOR H PARALLEL TO <100>, SHOWING THE SEPARATION OF THE HYPERFINE GROUPS. THE ORDER OF THE QUANTUM NUMBERS M IS THE SAME FOR EACH VALUE OF m.

REFERENCES

4.1 A. Abragam and B. Bleaney "Electron paramagnetic resonance of transition ions". Clarendon Press, Oxford (1970) p3-4

4.2 C.P. Poole and H.A. Farach "The theory of magnetic resonance" Wiley-Interscience, N.Y. (1972), p.2.

4.3 A. Abragam and M.H.L. Pryce Proc. Roy. Soc. A205, 135 (1951)

4.4 W. Low "Paramagnetic resonance in solids", Solid State Physics Supplement 2, Academic Press, N.Y. (1960)

4.5 F.A. Cotton and G. Wilkinson "Advanced Inorganic Chemistry", 3rd Ed., Wiley Interscience, N.Y. (1972)

4.6 H.B. Kramers Proc. Amsterdam Acad. Sci. 32, 1176 (1929)

4.7 W.G. Penney and R. Schlapp Phys Rev 41, 194 (1932)

4.8 J.H. Van Vleck Phys Rev 41, 208 (1932)

4.9 R. Schlapp and W.G. Penney Phys Rev 42, 666 (1932)

4.10 Y. Tanabe and S. Sugano J. Phys. Soc. Japan 9, 753 (1954)

4.11 K.W.H. Stevens and C.A. Bates "Crystal Field Theory in magnetic oxides" Part I (Ed. D.J. Craik), Wiley-Interscience, N.Y., (1975)

4.12 Reference 4.1 p.5-8 and p.25-30.

4.13 G. Breit and I.I. Rabi Phys. Rev. 38, 2082 (1931)

4.14 B. Bleaney and K.D. Bowers Proc. Phys. Soc. (London) A64, 1135 (1951)

4.15 K.D. Bowers Proc Phys. Soc. (London) A65, 860 (1952)

4.16 W. Low Phys. Rev. 105, 801 (1957)

4.17 This work, Chapter 7.

4.18 J. Weber, H. Ennen, U Kaufmann and J. Schneider Phys. Rev. B21, 2394 (1980)

4.19 H. Bethe Ann. Physik 3, 133 (1929)

4.20 J.H. Van Vleck and W.G. Penney Phil. Mag. 17, 961 (1934)

4.21 W. Low Proc. Phys. Soc. (London) B69, 1169 (1956)

4.22 J.H.E. Griffiths and J.W. Orton Proc. Phys. Soc. (London) 73, 948 (1959)

4.23 Reference 4.1, p.441.

4.24 P. Debye Ann. Physik. 32, 85 (1938)

4.25 R. de L. Kronig and C.J. Bouwcamp Physica 6,290 (1939)

4.26 R.S. de Biasi Phys. Stat. Sol. (b) 87, K29 (1978)

4.27 J.L. Kolopus and L.V. Holroyd Phys. Stat. Sol. 8, 711 (1965)

4.28 Reference 4.1 p.142-147.

4.29 G.W. Ludwig and H.H. Woodbury "Electron Spin Resonance in Semiconductors" in Solid State Physics, Vol. 13, Academic Press, N.Y.,(1962) p.235.

4.30 W. Low Phys. Rev. 105, 792 (1957)

4.31 A. Abragam Phys. Rev. 79, 534 (1950)

4.32 E. Fermi, Z. Physik 60, 320 (1930)

4.33 A. Abragam, J. Horowitz and M.H.L. Pryce Proc. Roy. Soc. (London) A230, 169 (1955)

4.34 W. Low Phys. Rev. 105, 793 (1957)

4.35 L.M. Matarrese and C. Kikuchi J. Phys. Chem. Solids 1, 117 (1956)

CHAPTER FIVE

THE INTERPRETATION OF EPR SPECTRA II: THE ANALYSIS OF POWDER SPECTRA

5.1 THE RELATIVE MERITS OF SOME MAJOR TECHNIQUES EMPLOYED IN POWDER SPECTRA ANALYSIS

Most methods used to predict the spectra of powdered or polycrystalline materials have a common starting point. This is the assumption that such a material may be regarded as an ensemble of sites randomly oriented with respect to the applied magnetic field. Thus the resulting E.P.R. spectrum is the sum over the resonance conditions satisfied by all of these randomly oriented sites (such a sum is termed a powder pattern). The resonance condition for any particular site may be found by inserting the relevant angular information into the single crystal Spin Hamiltonian since this Hamiltonian describes the angular variation of the spectrum. It naturally follows that the powder pattern may be regarded as the sum of the single crystal resonance conditions over all angles.

Expressed mathematically, the powder pattern is given by the solution of the equation:[5.1 - 5.3]

$$S(H)dH = {}^{1}/_{4\pi} \sum_{m} \int_{H}^{H+dH} \ell_{m}(\Omega) d\Omega(H_{m}) \qquad (5.1)$$

The above equation assumes that each individual site or "crystallite" has an equal probability of being oriented in any element of solid angle, $d\Omega$, with respect to the direction of the applied field, H. The quantity S(H) is known as the shape function and represents the normalised amplitude of the resonance absorption signal at the field H. The integration in equation 5.1 is over those (probably disconnected) elements of solid angle $d\Omega\ (H_m)$ such that $H<H_m<H+dH$ where H_m is the resonance field derived from an appropriate resonance condition. The quantity $\ell_m(\Omega)$ is the transition probability for the m^{th} component of the spectrum and, except for strong anisotropy in g, this is independent of the angle which the oscillating field inducing transitions makes with the principal axes of the system and may be taken outside the integral.

The various methods employed in powder spectrum analysis only differ in their approach to solving equation 5.1. In this Chapter several different ways of arriving at a solution of equation 5.1 will be described, all of which have their own particular advantages and disadvantages.

The first method, described in detail in section 5.2, does not in fact attempt to solve equation 5.1 (which frequently involves computing techniques since the integration is often carried out numerically). Instead, we attempt to calculate the magnetic fields at which powder absorption peaks occur. These fields are associated with points where the integrand of equation 5.1 reaches a singularity i.e. points such that [5.4]

$$\left(\partial H/\partial\theta\right)_{\phi} = \left(\partial H/\partial\phi\right)_{\theta} = 0 \qquad (5.2)$$

The major advantage of this technique lies in its straightforwardness: simple differentiation of the resonance conditions which apply to the single crystal spectrum and application of the boundary conditions of equation 5.2 will yield the field positions of the powder absorption peaks. Such a process can obviously be carried out by hand and no elaborate integration techniques involving computers are required. In addition, the resonant field values which satisfy equation 5.2 are often those which are found for a single crystal sample when the external magnetic field is directed along certain high symmetry axes of the crystal for example, the <100>, <110> and <111> directions. Therefore, the measured positions of peaks in the single crystal spectrum when the magnetic field is directed along particular high symmetry axes often correspond to the positions of peaks in the powder spectrum.

Although the procedure described above predicts the positions of features in the powder spectrum, its major disadvantage lies in the fact that it gives little or no information concerning lineshapes and linewidths. Such information is obviously important since it reveals much about the interactions taking place, firstly between the paramagnetic ions and, secondly, between an individual paramagnetic ion and the surrounding diamagnetic lattice. In particular, powder linewidths may be greater than those of the single crystal due to strain introduced during the powdering process. Moreover, information about lineshapes and linewidths is difficult to obtain directly from the powder spectrum since the absorption lines of powders (which are recorded experimentally, like those of the single

crystal, as first derivitives) are not usually simple in shape (for example, Lorentzian or Gaussian) even if those of the corresponding single crystals are.

Another disadvantage is encountered when dealing with highly anisotropic lines, since for such lines the number of crystallites correctly oriented to contribute towards the absorption peaks of the powder will be small which will make the absorption peaks difficult to detect. If a spectrum contains many such anisotropic lines the powder absorption peaks due to these lines may be undetectable and the amount of useful information obtainable using the differentiation method is small.

In sections 5.3 and 5.4 two different approaches which utilize computing techniques to produce simulations of the powder spectrum will be described. For all the methods described in sections 5.3 and 5.4, as the generation of the simulation proceeds, steps are involved which allow the computed powder spectrum to be convoluted with a particular lineshape function (usually Lorentzian or Gaussian) of a given width. If several trial simulations are undertaken, the lineshape and linewidth that give the best fit to the experimental powder spectrum can be determined either by the least squares method or by eye (which is usually accurate enough). Having determined the lineshape function and linewidth it is often possible to deduce from these the type and magnitude of the mechanism or mechanisms responsible for the line broadening in the powder. Obviously, because of this, the computer simulation techniques hold a major advantage over the differentiation method described earlier.

The simulation procedures described in section 5.3 numerically integrate equation 5.1 using Monte Carlo or Monte Carlo type techniques which have been developed in the Department.[5.5 - 5.7] The resonant fields of all transitions are calculated for many small elements of solid angle, $d\Omega$, each of which is characterized by its angular co-ordinates θ and ϕ. The number of times that this procedure generates a particular resonant field is then plotted against magnetic field and the resulting histogram represents the simulated powder pattern which at this point may be convoluted with a lineshape function to attempt to reproduce the line broadening found in the real powder. The three numerical methods described in section 5.3 have the basic features outlined above in common and only differ in that each technique employs a different procedure to select a set of values for the angular co-ordinates θ and ϕ of the small elements of solid angle $d\Omega$.

Besides yielding lineshape and linewidth data the numerical integration procedures are also advantageous because of their great adaptability. Any powder pattern may be simulated simply by inserting the appropriate resonance conditions (with the angular variation of the resonance fields expressed in terms of θ and ϕ) and relative intensities. The rest of the simulation procedure remains the same for all cases (of course, the lineshape functions and linewidths involved in the convolution process will, in general, need to be altered for different cases but the construction of the computer programmes used to generate simulations for the various numerical methods allows such alterations to be carried out quite easily).

Monte Carlo methods also lend themselves particularly well to situations where the crystal field parameters are distributed around a mean value (usually due to strain in the material). This is because the resonant field for each element of solid angle may be calculated using a crystal field parameter drawn at random from a given continuous distribution.

However, identification of a powder spectrum using any one of the numerical techniques relies upon a general agreement being found between the simulated and experimental traces. The major drawback, therefore, is that the numerical methods do not predict the positions of any of the features in the powder spectrum in terms of the crystal field parameters.

In section 5.4, a method of powder spectrum simulation developed by Beltran-Lopez and Castro-Tello[5.8] is described which applies specifically to $^6S_{5/2}$ ions (such as Mn^{2+} and Fe^{3+}) in a cubic crystal field. Two expressions for the quantity $d\Omega/dS$ (Ω here represents the quantity $\Omega(H_m)$ found in equation 5.1) are obtained each of which is valid for a particular range of the parameter $S = \frac{1}{4}(\sin^2 2\theta + \sin^4\theta \sin^2 2\phi)$. Since the two expressions obtained are complex, for convenience a computer is used to plot $d\Omega/dS$ against S which effectively represents the powder pattern. Evaluation of the two analytical solutions of equation 5.1 using a computer has the added advantage that the powder pattern obtained may be convoluted with an appropriate lineshape function and linewidth.

Clearly, in terms of its range of application, this method compares unfavourably with the numerical integration

techniques described earlier. A relatively long and complicated mathematical derivation is required, the end product of which is a simulation procedure applicable to a specific type of ion in a certain crystal field symmetry which may not be adapted to apply to other ions or other crystal field symmetries.

However, the usefulness of Beltran-Lopez and Castro-Tello's technique lies in the fact that it predicts the positions of the powder absorption peaks in terms of the crystal field parameter, a. This obviously allows a to be measured directly for the powder and compared with the value obtained from single crystal samples.

Finally, in section 5.5 the equivalence of the various powder spectrum simulation techniques described in sections 5.3 and 5.4 is demonstrated. From this it was assumed that each simulation method provides an accurate representation of the powder spectrum expected from a collection of randomly oriented single crystallites.

From the above discussion it will be clear that each of the methods of powder spectrum analysis described provide unique information and it is often necessary to use them in conjunction in order to extract the maximum possible information from an experimental powder spectrum.

The procedures adopted to predict E.P.R. powder spectra described here regard the problem as being one primarily of geometry i.e. the powder spectrum is regarded as the sum over the resonance conditions satisfied by small single crystallites oriented at random. Implicit in this point of view is the assumption that the local environment of a paramagnetic ion in a powder sample is the same as it is in

the corresponding single crystal. This assumption is not always valid, and since E.P.R. spectroscopy is particularly sensitive to any changes in the environment of a paramagnetic species, serious discrepancies will arise between the theoretical and experimental powder spectrum if any such changes are not properly taken into account.

The possibility of introducing strain into a powder during the powdering process has already been discussed. In certain cases (particularly for high surface area powders which have a high ratio of near-to-surface to bulk paramagnetic ions) distortions may be so great that the symmetry of the site occupied by the paramagnetic ions is changed, for example, from cubic to axial.[5.9,5.10] In addition, chemical processes, such as the chemisorption of gases [5.9,5.10] may occur, either inadvertently or by deliberate design. Processes such as these will obviously lead to changes in the local environment of a paramagnetic ion located at the surface (for example, the local site symmetry may be altered if the chemical species involved are the same as the ligands surrounding the paramagnetic ion in the bulk material; if they are different even the type of ligands surrounding the paramagnetic ion may be altered). Again, such effects are more noticeable for high surface area powders with their large proportion of paramagnetic ions concentrated at the surface.

The type of surface effects described show that a real powder and a collection of randomly oriented crystals are not necessarily equivalent. However, a knowledge of the expected powder spectrum from randomly oriented single crystals enables surface effects, which are of great interest

in the areas of surface physics, catalysis and other related fields, to be discerned since surface effects only show up as distortions on the otherwise reliably known spectrum of the randomly oriented bulk crystals.

The powders studied in this work were prepared by grinding up single crystals and sieving the resulting chippings through a fairly coarse mesh (185μm). The large grain size of each individual crystallite should minimize surface effects since the majority of the paramagnetic ions will be located in the bulk, far from the surface. Therefore, it was hoped that the experimental powder spectra could be described simply in terms of the model used as a basis for the simulation procedures described in this Chapter i.e. that the powder could be regarded as a random collection of small single crystals.

5.2 THE USE OF DIFFERENTIATED SINGLE CRYSTAL RESONANCE CONDITIONS TO PREDICT THE POSITIONS OF POWDER ABSORPTION PEAKS

The principles behind the use of differentiated single crystal resonance conditions to predict the positions of powder absorption peaks have already been outlined in section 5.1. Stationary points in $H(\theta,\phi)$, that is, points which satisfy equation 5.2, represent an infinity in the shape function, S(H) of equation 5.1. Since S(H) represents the normalised amplitude of the resonance absorption signal at the field H, such points obviously give rise to peaks in the absorption.

In this section it will be demonstrated how the technique may be applied specifically to the Mn^{2+} and Fe^{3+} ions in MgO. Although in this work we are also interested

in the powder spectrum of the Cr^{3+} ion in MgO, inspection of equations 4.20 to 4.22 shows that the spectrum of this ion in MgO is isotropic. From this it may be deduced that equation 5.2 is satisfied for all values of H which is equivalent to saying that the single crystal and powder spectra of Cr^{3+} in MgO are expected to be identical.

Let us turn now to the Mn^{2+} ion in MgO. The resonant magnetic fields, H(M,m), for the $(M,m) \leftrightarrow (M-1,m)$ transitions, to first order in a and second order in A, are given by equation 4.31:

$$H(M,m) = H_o - Am - A^2/2H_o[35/4 - m^2 + m(2M-1)] -$$

$$-a/384(35\cos^4\theta - 30\cos^2\theta + 3 + 5\sin^4\theta\cos 4\phi) \times \quad (4.31)$$

$$\times(56M^3 - 84M^2 - 134M + 81)$$

The only angular dependent term in the above expression is the term in a. Therefore, differentiating equation 4.31 with respect to θ and ϕ we obtain

$$\left(\frac{\partial H}{\partial \theta}\right)_\phi = C[60\sin\theta\cos\theta - 140\sin\theta\cos^3\theta + 20\sin^3\theta\cos\theta\cos 4\phi] \quad (5.3a)$$

$$\left(\frac{\partial H}{\partial \phi}\right)_\theta = -20C[\sin^4\theta\sin 4\phi] \quad (5.3b)$$

where $C = {}^{a}/384(56M^3 - 84M^2 - 134M + 81)$

For the $(M = \frac{1}{2} \longleftrightarrow -\frac{1}{2}, m)$ transitions the bracket $(56M^3 - 84M^2 - 134M + 81)$ is equal to zero. Hence equations 5.3a and 5.3b are equal to zero for all values of H and these transitions are, to first order in a, isotropic. The field positions are therefore the same as those of the single crystal i.e.

$$H(\tfrac{1}{2},m) = H_o - Am - {}^{A^2}/2H_o[{}^{35}/4 - m^2] \qquad (5.4)$$

For the other fine structure lines, the values of θ and ϕ which, when substituted into equations 5.3a and 5.3b satisfy equation 5.2 are: $(\theta = 0^\circ)$, $(\theta = 54.74^\circ, \phi = \pi/4)$, $(\theta = \pi/2, \phi = \pi/4)$, $(\theta = \pi/4, \phi = \pi/2)$ and $(\theta = \pi/4, \phi = 0^\circ)$. These are the stationary values of $H(\theta,\phi)$, the first of which represents the z axis or equivalent <100> directions. The second represents <111> directions and the last three represent equivalent <110> directions. The <100> and <111> axes represent shoulders on the powder absorption curve while the <110> axes represent divergences. The characteristics of these powder absorption curve peaks are summarised in Table 5.1. Figure 5.1 shows a schematic E.P.R. powder absorption spectrum for the $M \longleftrightarrow M\text{-}1 (M \neq \frac{1}{2})$ transition. The derivitive presentation will have a single peak (either positive or negative) at a shoulder and a double peak crossing zero (both positive and negative) at a divergence.

Several groups of workers[5.11 - 5.13] have identified

CRITICAL POINT	DESCRIPTION	AXIS	FIELD POSITION
$\theta = 0^{\circ}$	SHOULDER	<001>	$H_o' - C$
$\theta = 54.74^{\circ}$ $\phi = \pi/4$	SHOULDER	<111>	$H_o' + 2C/3$
$\theta = \pi/2$ $\phi = \pi/4$	DIVERGENCE	[110]	$H_o' + C/4$
$\theta = \pi/4$ $\phi = \pi/2$	DIVERGENCE	[011]	$H_o' + C/4$
$\theta = \pi/4$ $\phi = 0^{\circ}$	DIVERGENCE	[101]	$H_o' + C/4$

$$H_o' = H_o - Am - A^2/2H_o[35/4 - m^2 + m(2M-1)]$$

$$C = a/48(56M^3 - 84M^2 - 134M + 81)$$

Table 5.1 Predicted powder absorption peaks for the $M \leftrightarrow M-1$ ($M \neq \frac{1}{2}$) transitions of Mn^{2+} in MgO: the same absorption peaks are predicted for Fe^{3+} in MgO except that $H_o' = H_o$ (after Rubio et al[5.10]).

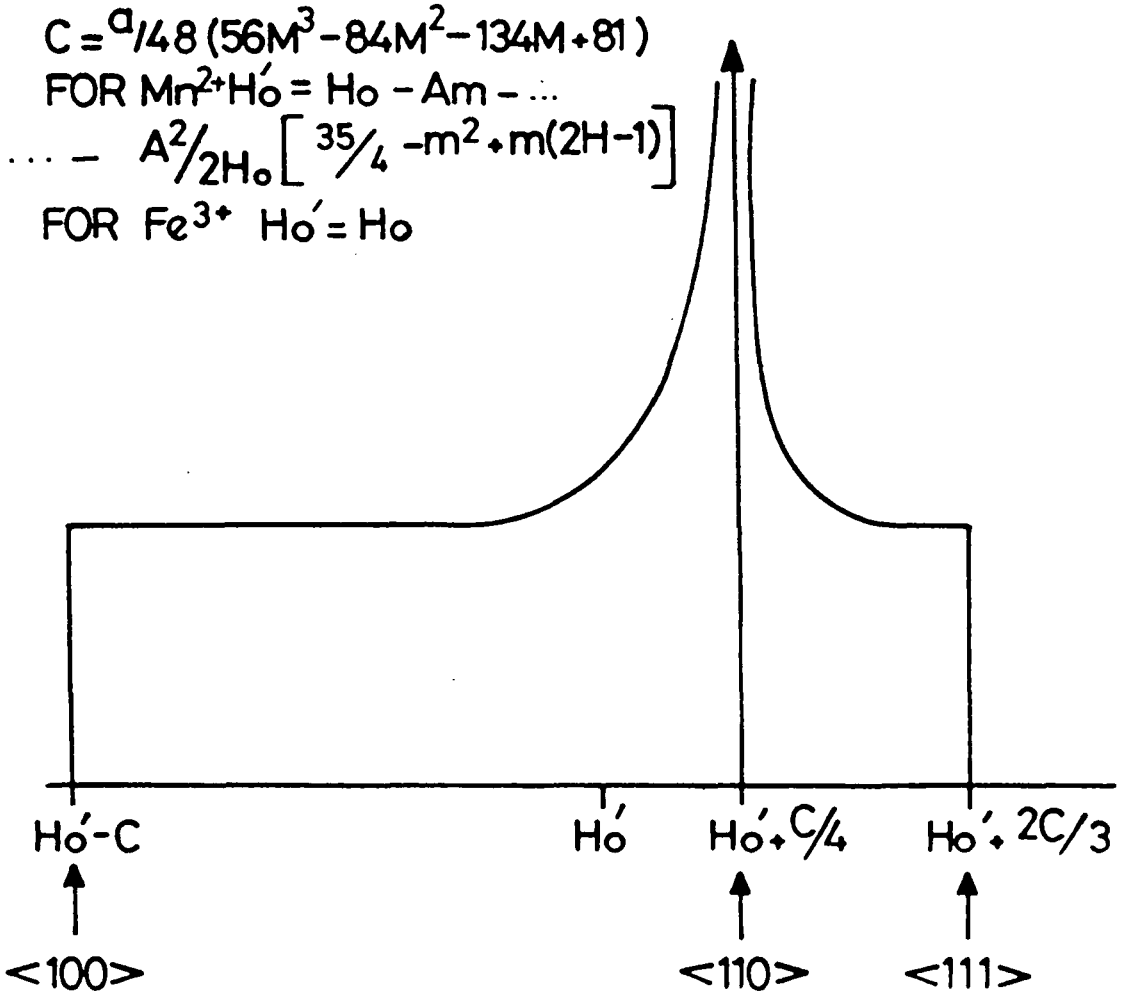

FIGURE 5.1 E.P.R. POWDER ABSORPTION SPECTRUM FOR THE M → M − 1 ($M \neq 1/2$) TRANSITIONS OF A $^6S_{5/2}$ GROUND STATE ION IN CUBIC SYMMETRY (AFTER RUBIO et al.[5.10]).

peaks in the experimental powder spectrum of Mn^{2+} in MgO with those predicted by theory (which are listed in table 5.1), although in some cases not all of the predicted peaks were observed. Measurements may be restricted to the outermost hyperfine groups ($m = {}^{5}/2$ and $m = {}^{-5}/2$) if the superposition of fine structure lines in other groups makes identification of the observed peaks difficult.[5.13] Kakazei and Vlasova[5.13] observed the ($\theta = \pi/2, \phi = \pi/4$) and ($\theta = 54.74^{\circ}, \phi = \pi/4$) absorption peaks of Mn^{2+} in powdered MgO and tried to relate their relative intensities to the observed angular variation of linewidth in single crystal samples. They concluded that since for the $\pm^{5}/2 \leftrightarrow \pm^{3}/2$ transitions in a single crystal the linewidth is equal to 0.28 and 0.15mT for $\theta = \pi/2$ and 54.74° respectively, while for the $\pm^{3}/2 \leftrightarrow \pm^{1}/2$ transitions 0.16 and 0.10mT respectively[5.14] the ($\theta = 54.74^{\circ}, \phi = \pi/4$) absorption peaks should be greater in intensity than the ($\theta = \pi/2, \phi = \pi/4$) absorption peaks.

For the Fe^{3+} ion, the resonant fields for the $M \leftrightarrow M-1$ transitions are given, to first order in a, by equation 4.31 except that the terms in A must be omitted since Fe^{3+} displays no hyperfine structure. The differentiated resonance conditions will be the same for Fe^{3+} as for Mn^{2+} (equations 5.3a&b) because only the term in a is angular dependent. Therefore the stationary values of $H(\theta, \phi)$ for Fe^{3+} are the same as those for Mn^{2+} and occur at the field positions listed in table 5.1 (of course, in the case of Fe^{3+}, the terms in A must be omitted from the constant H_0). The predicted powder absorption spectrum of Fe^{3+} in MgO is

thus identical to that predicted for each of the six hyperfine groups of Mn^{2+}: the central $M = \frac{1}{2} \longleftrightarrow -\frac{1}{2}$ transition is, to first order in a, isotropic (for the same reason that the $(M = \frac{1}{2} \longleftrightarrow -\frac{1}{2}, m)$ transitions of Mn^{2+} are isotropic) and each of the other $M \longleftrightarrow M-1$ fine structure transitions give rise to powder absorption spectra such as that shown in Figure 5.1.

Experimentally, only the $M = \frac{1}{2} \longleftrightarrow -\frac{1}{2}$ transition of Fe^{3+} has been observed in powdered MgO[5.8] and, contrary to expectation, this transition is found to be slightly anisotropic. This is due to second order terms in a which are more important for Fe^{3+} than for Mn^{2+} (for which the $(M = \frac{1}{2} \longleftrightarrow -\frac{1}{2}, m)$ transitions are found to be isotropic in powdered MgO[5.11]) because a is much larger for Fe^{3+} than it is for Mn^{2+}. The other fine structure transitions are probably rendered undetectable because of the large value of a which means that they will be spread over a wide magnetic field range ($^{10a}/_{3} \sim 75mT$ for the $\pm^{5}/_{2} \longleftrightarrow \pm^{3}/_{2}$ transitions and $^{25a}/_{6} \sim 90mT$ for the $\pm^{3}/_{2} \longleftrightarrow \pm^{1}/_{2}$ transitions)

Clearly, to adequately describe the spectrum of Fe^{3+} in powdered MgO the theory developed in this section would need to be revised to include second order terms in a. Although this is a fairly simple operation, it will not be attempted here, mainly because the simulation procedures described in sections 5.3 and 5.4, which do take account of these second order terms, are better suited to solving the problem of accurately predicting the powder spectrum of Fe^{3+} in MgO.

5.3 POWDER SPECTRA SIMULATION USING NUMERICAL INTEGRATION TECHNIQUES.

For a particular transition, in a system containing N_o total spins and assuming that each of the N_o spins produces a spectrum having a delta function lineshape with a negligible variation of intensity with magnetic field orientation, the shape function, S(H), of equation 5.1 may be written as:[5.11]

$$S(H) = \frac{\ell}{N_o}\int_{H}^{H+dH} \frac{dN}{dH} \qquad (5.5)$$

where dN is the number of spins which undergo the transition in question for magnetic fields between H and H + dH and ℓ is the transition probability. The above expression follows directly from equation 5.1 if we assume that in a powder sample the spins are randomly oriented, since under these conditions:

$$dN = \left(\frac{N_o}{4\pi}\right) d\Omega \qquad (5.6)$$

where $d\Omega$ is equivalent to the quantity $d\Omega(H_m)$ of equation 5.1 and is the solid angle containing dN spins.

The three simulation procedures described in this section effectively provide numerical evaluations of the

right-hand-side of equation 5.5. The orientation of the principal axes (three mutually perpendicular [100] directions for MgO) of each individual crystallite in the powder with respect to H may be defined in terms of the Eulerian angles θ and ϕ. For each numerical simulation technique pairs of values for θ and ϕ are used to calculate the resonant fields of all transitions using resonance conditions appropriate to the material being studied. The number of times that this procedure generates a resonance field between H_α and $H_{\alpha+1}$ is then histogrammed on a magnetic field array H_1, $H_2 \longrightarrow H_n$. This histogram represents a graphical solution of the function dN/dH between H_1 and H_n and thus, according to equation 5.5 and ignoring constant factors, also represents the shape function S(H). It is convenient to construct a separate histogram for each transition so that after multiplication by the appropriate transition probabilities (for the $^6S_{5/2}$ ions, Fe^{3+} and Mn^{2+}, the relative intensities of Table 4.3 are used) the individual histograms may be added together to produce a single histogram which represents the shape function, S(H), for the complete spectrum.

All the numerical methods must use at least as many pairs of θ & ϕ values as there are individual crystallites undergoing resonance in the experimental powder since the noise level (both experimentally and in the simulation) directly depends upon the number of individual components contained in the total assembly.[5.3] Experimentally, the volume of powder responsible for the E.P.R. absorption was contained in a cylinder of length 1 cm and diameter 2mm. Since the powder had been sieved through a 185μm mesh, a simple calculation shows that the number of crystallites

undergoing resonance is at least 20,000. Therefore each numerical method must consider at least 20,000 individual pairs of θ and ϕ values if the noise levels in the experimental and simulated traces are to be comparable (of course, if the number of points in the simulation is exactly equal to the number of crystallites undergoing resonance, the noise level in the experimental trace will always be somewhat higher due to instrumental noise).

The features described above are common to all three numerical powder spectrum simulation techniques. In fact, the three methods only differ in that each adopts a slightly different approach to the problem of selecting a set of values for θ and ϕ. Obviously, as θ and ϕ define the orientation of an individual crystallite with respect to the magnetic field, H, in the laboratory frame, they must be consistent with the model assumed, i.e. a random collection of small single crystallites. The procedure must produce a set of θ and ϕ values which, in statistical terms, may be regarded as a "random" set. The ability of each of the numerical methods (and also of the analytical method described in section 5.4) to do this is assessed in section 5.5. Here it is proposed simply to describe the method of θ and ϕ selection adopted in each of the three cases.

Firstly, a true Monte-Carlo technique (which represents the exact analogue of the experimental situation) may be used to select values of θ and ϕ, nominally at random. If k' and k" represent pseudo-random numbers between 0 and 1 (these numbers may be generated in a computer using standard statistical packages) then the angular variables θ and ϕ may be written as:

$$k' = \cos\theta \tag{5.7a}$$

$$k''\left(\frac{\pi}{2}\right) = \phi \tag{5.7b}$$

Equations 5.7a and 5.7b generate values of θ and ϕ corresponding to one octant of a sphere only; since all orientations are equally probable it is statistically valid to constrain the limits of the values of θ and ϕ in this way (a complete sphere, allowing all possible combinations of values of θ and ϕ would truly represent a collection of random crystallites). Of course, the number of points in the simulation is simply equivalent to the number of pairs of pseudo-random numbers, k' and k", generated.

Secondly, we may use a Monte-Carlo type technique which instead of using random numbers to select θ and ϕ values relies on the fact that as all orientations are equally probable we may divide up a sphere into small, equal elements of solid angle, $d\Omega$, (each of which is characterized by its θ and ϕ values) and then calculate the resonant fields of all transitions for each element to produce the simulated powder spectrum. In other words, this method assumes a uniform distribution of θ and ϕ values such as we would expect to find using a true Monte-Carlo technique if a large number of points are taken. To carry out this type of simulation, the surface area of the sphere (or octant) must be divided up into equal elements using a grid system. Each point on the grid represents a particular element of solid angle $d\Omega$: the angular co-ordinates θ and ϕ are used to define the location of each point on the grid (see Figure 5.2)

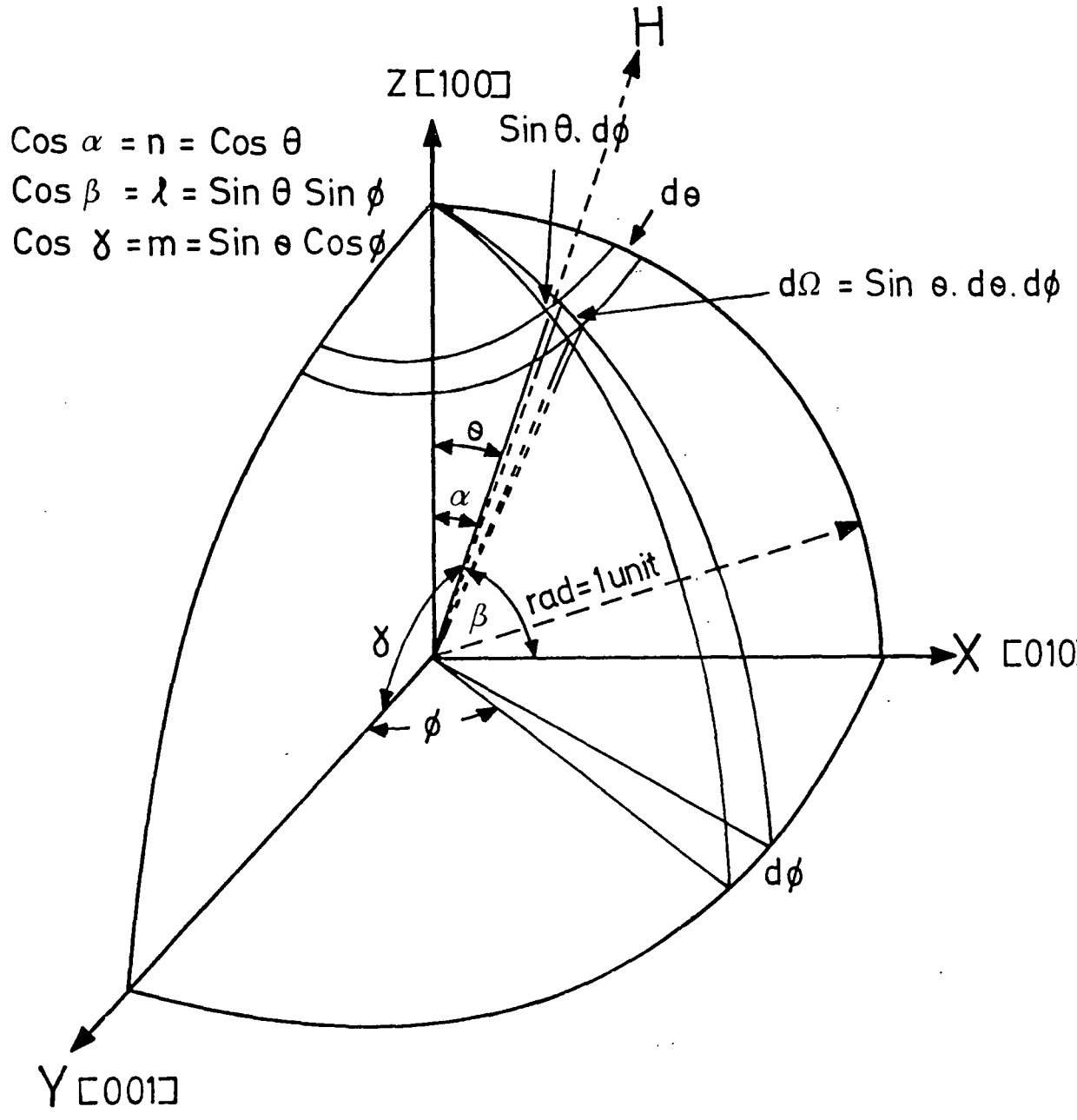

FIGURE 5.2 SPHERICAL GEOMETRY PARAMETERS EMPLOYED IN POWDER PATTERN SIMULATIONS.

The coarseness of the grid determines the number of orientations considered in the simulation. It has been found empirically that simulation procedures employing a uniform grid such as that mentioned give less noise for an equal number of orientations than true Monte-Carlo techniques.[5.3]

Both the other numerical methods to be described here employ different versions of the "uniform grid" technique mentioned above. It must be reiterated that this technique can only be applied if the small elements $d\Omega$ into which the sphere (or octant) representing all possible orientations is divided are equal. Two grid systems which to a great extent obey this condition have been devised.[5.3,5.5 - 5.7]

Firstly, we may divide up the octant (used for all practical simulations instead of a whole sphere) according to the equations:

$$\Delta\theta = k_1 \tag{5.8a}$$

$$\Delta\phi = k_2/\sin\theta \tag{5.8b}$$

where k_1 and k_2 are constants and $\Delta\theta$ and $\Delta\phi$ represent the spacings between grid "lines" in the θ and ϕ directions respectively. In the xy plane (see Figure 5.2) when $\theta = 90^{\circ}$, $\Delta\phi$ is simply equal to k_2. As θ decreases (in steps of k_1) towards zero, $\Delta\phi$ increases and the circumference of the band $\Delta\theta$ (at θ) decreases. Each element of solid angle, $d\Omega$, occupies an area $\sin\theta\Delta\theta\Delta\phi$ on the octant surface and according to equations 5.8a and 5.8b will be equal to

a constant, $(k_1 k_2)$, for all values of θ and ϕ as the condition governing the use of this technique requires.

Secondly, the octant may be divided up using the conditions:

$$\Delta\cos\theta = k_3 \qquad (5.9a)$$

$$\Delta\phi = k_4 \qquad (5.9b)$$

Again, k_3 and k_4 are constants and $\Delta\phi$ represents the spacing between grid "lines" in the ϕ direction. The symbol $\Delta\cos\Theta$ is used to indicate that the grid "lines" in the Θ direction are separated by equal increments of $\cos\Theta$. As θ decreases from 90° to 0° the area of the $\Delta\cos\Theta$ bands increases (there is an equal probability of any given crystallite being oriented in any one of the complete $\Delta\cos\Theta$ bands). Thus each $\Delta\cos\Theta$ band may be divided up equally in the ϕ direction (i.e. $\Delta\phi$ = a constant, k_4) to create elements $d\Omega$ having equal areas and hence there will be an equal probability of a given crystallite being oriented in any one of the elements $d\Omega$. The basis of this method lies in the geometry of Figure 5.2: an element of solid angle, $d\Omega$, is equal to $\sin\Theta.d\Theta.d\phi$ and thus to create equal elements of solid angle the sphere must be divided into equal units of $\sin\theta.d\theta.d\phi$ or equal areas in $d(\cos\theta)d\phi$ space.

Whichever of the three methods available for the selection of θ and ϕ values is adopted, the simulation

process, as explained earlier, eventually leads to a numerical solution of the function $^{dN}/_{dH}$, which represents the powder pattern S(H). However, the powder pattern histogram is constructed assuming that the spectrum contains lines of negligible linewidth: in order to be compared with a real powder spectrum the powder pattern must be convoluted with an isotropic broadening function of a given width (the appropriate lineshape function and linewidth are usually obtained from single crystal data).

Most broadening mechanisms common in E.P.R. result in either a Gaussian or Lorentzian lineshape. Such broadening mechanisms may be simulated using the following convolution functions (which are normalised to give unit area for all values of the linewidth parameters):[5.3]

$$\text{Lorentzian:} \quad F(H-H_o) = \frac{\sigma_L}{2\pi}\left[\frac{1}{\sigma_L^{\,2}/4 + (H - H_o)^2}\right] \qquad (5.10a)$$

$$\text{Gaussian:} \quad G(H-H_o) = \frac{1}{\sigma_G\sqrt{2\pi}} \cdot \exp\left[\frac{-(H-H_o)^2}{2\sigma_G^{\,2}}\right] \qquad (5.10b)$$

The characteristic shapes of the functions, and the significance of the linewidth parameters, σ_L and σ_G, are shown in Figure 5.3.

When two or more independent, Lorentzian, broadening mechanisms are present in a substance, the convolution

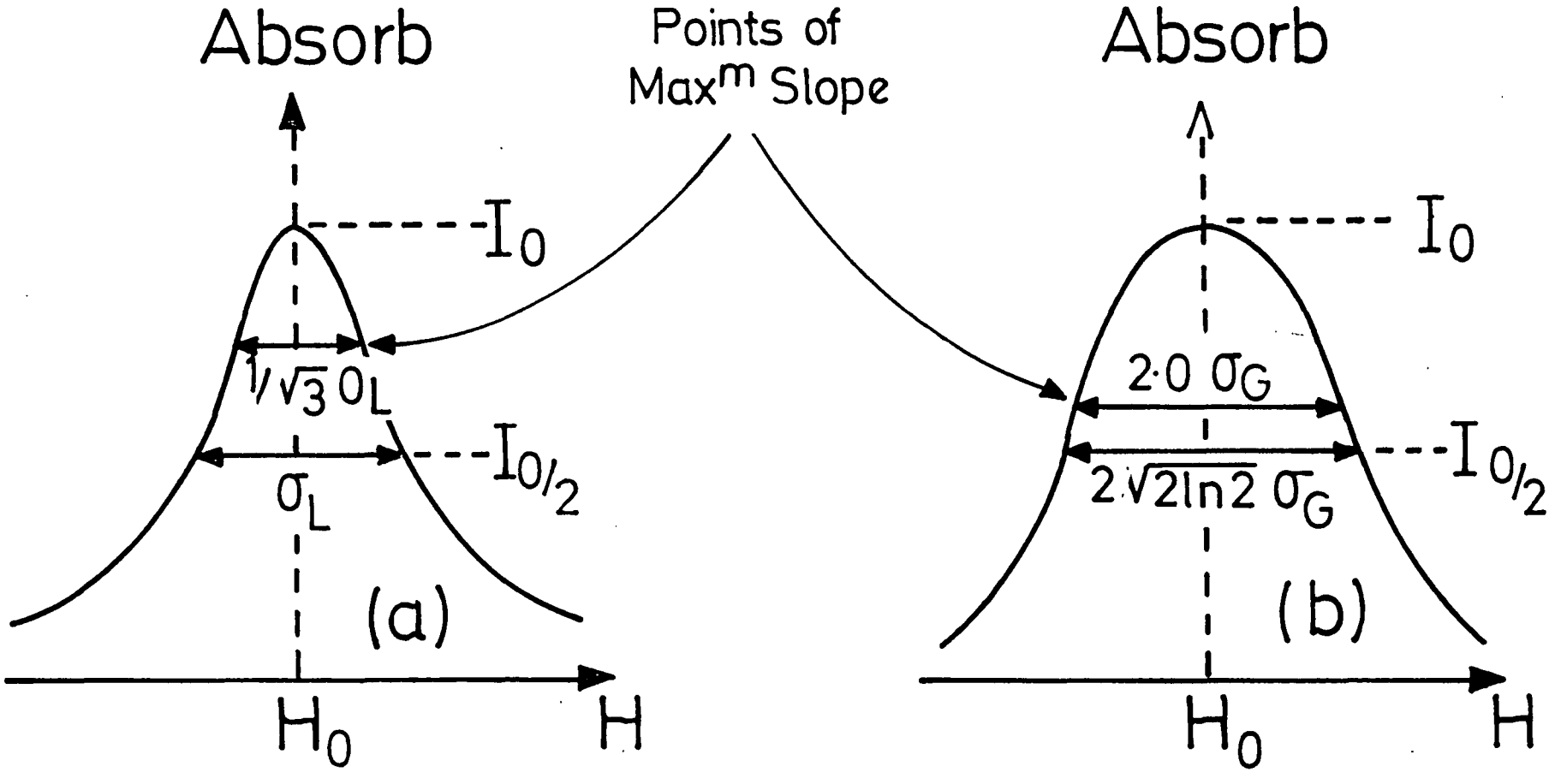

FIGURE 5.3 CHARACTERISTIC (a) LORENTZIAN
(b) GAUSSIAN LINE SHAPES.

process may still be undertaken using equation 5.10a except that the total linewidth used in the equation is now the sum of the component linewidths. When two or more independent, Gaussian, broadening mechanisms are present, the convolution process may be undertaken using equation 5.10b, the total linewidth used in the equation being given by the square root of the sum of the squares of the component linewidths.[5.15] If both Lorentzian and Gaussian broadening mechanisms are important, the powder pattern may be convoluted with both equations 5.10a and 5.10b one after the other; in this case the total "linewidth" is somewhere between the sum and the square root of the sum of the squares of the component linewidths.

For the purpose of explaining how the convolution process is carried out, let us assume that we have a single, dominant broadening mechanism (which is quite a common situation experimentally). The powder pattern histogram information is contained in an array $S(H)_1$, $S(H)_2 \longrightarrow S(H)_n$ where $S(H)_1, S(H)_2 \longrightarrow S(H)_n$ give the number of times that the simulation procedure produces a resonance field between H_α and $H_{\alpha+1}$ The appropriate lineshape function and linewidth (obtained from single crystal data) are then used to construct another array, $I(H)_1, I(H)_2 \longrightarrow I(H)_n$ where $I(H)_1, I(H)_2 \longrightarrow I(H)_n$ give the amplitude of the lineshape function at the magnetic field values $H_1, H_2 \longrightarrow H_n$ which correspond to those of the powder pattern array. As the common lineshape functions are symmetrical about the field of maximum absorption, H_0, (see Figure 5.3) the array $I(H)_1, I(H)_2 \longrightarrow I(H)_n$ is constructed so that it contains only one half of the lineshape (either that part where

$H>H_o$ or that part where $H<H_o$) and also so that H_1 corresponds to the field H_o. The amplitudes $I(H)_1, I(H)_2 \longrightarrow I(H)_n$ are also normalised so that:

$$\sum_i I(H)_i = 1 \qquad (5.11)$$

If an empty array $B(H)_1, B(H)_2 \longrightarrow B(H)_n$ is created into which the results of the convolution process may be placed, then we may instruct the computer to conduct the following calculation:

$$B(H)'_{NEW} = B(H)'_{OLD} + S(H)'' \times I(H + |H'' - H'|) \qquad (5.12)$$

where $(H)'$ and $(H)''$ can both vary between H_1 and H_n. If we first fix H'' at H_1 and vary H' between H_1 and H_n the effect is to "smear out" the contents of the $S(H)_1$ element of the array over all the $B(H)_1, B(H)_2 \longrightarrow B(H)_n$ elements. If the process is now repeated with H'' fixed at H_2 the contents of the $S(H)_2$ element are "smeared out" over all the $B(H)_1, B(H)_2 \longrightarrow B(H)_n$ elements and, in addition, the formalism of equation 5.12 automatically changes the location of the maximum intensity of the convolution function to the H_2 position. If this process is repeated until H'' reaches H_n the convolution process will be

completed and the experimental broadening simulated.

Finally, to properly compare it with experiment, the simulation should be presented in first derivative form. This is achieved simply by taking the difference between the contents of adjacent elements in the $B(H)_1, B(H)_2 \longrightarrow B(H)_n$ array and plotting these values against magnetic field i.e. the final simulation is a plot of $B(H)_\alpha - B(H)_{\alpha-1}$ versus H_α .

5.4 AN ANALYTICAL METHOD FOR CALCULATING THE ABSORPTION FUNCTIONS AND EPR LINESHAPES OF $^6S_{5/2}$ IONS IN CUBIC CRYSTAL FIELDS[5.8]

In common with the numerical simulation techniques described in section 5.3 the right hand side of equation 5.5 is solved, however, in this case, as the heading for this section suggests, an analytical solution is obtained.

The powder absorbed, i(H), when the magnetic field changes dH from H (which, apart from constant factors, is equivalent to the shape function, S(H)) may be written as:

$$i(H) = \frac{dN}{dH} = \frac{dN}{d\Omega} \cdot \frac{d\Omega}{dH} = \frac{N_o}{4\pi} \cdot \frac{d\Omega}{dH} \qquad (5.13)$$

The final form of i(H) given above follows from equation 5.6. In order to proceed with the derivation, $d\Omega/dH$ is split up into two component differential quantities as follows:

$$i(H) = \frac{N_o}{4\pi} \left(\frac{d\Omega}{dS} \Big/ \frac{dH}{dS} \right) \qquad (5.14)$$

The variable S describes the angular variation of the resonance fields of the E.P.R. transitions of $^6S_{5/2}$ ions in cubic crystal fields (S is related to the parameter p of Table 4.3 by the equation $p = 1 - 5S$). The introduction of S allows the resonance fields to be expressed in terms of only a single variable (i.e. $S=S(\theta,\phi)$) and this in turn means that an evaluation of $\Omega(S)$, which is necessary in order to solve equation 5.14, is much simpler than an evaluation of $\Omega(H)$, which is necessary in order to solve equation 5.13. $\Omega(S)$ is obtained by calculating the area of a unit radius sphere enclosed within its intersection with the surface $S = S(\theta,\phi)$.

The projected intersections of $S(\theta,\phi) = (\frac{1}{4})(\sin^2 2\theta + \sin^4\theta \sin^2 2\phi)$ with the unit radius sphere, the projected S curves, are given by:

$$\rho_{\pm} = 2 \left\{ 1 \pm \left\{ 1 - (S/2)(7 + \cos 4\phi) \right\}^{\frac{1}{2}} \right\}^{\frac{1}{2}} (7 + \cos 4\phi)^{-\frac{1}{2}} \ldots \qquad \ldots.(5.15)$$

and are shown in Figures 5.4a and b for various values of S within its range $0 \leq S \leq 1/3$. For the interval $0 \leq S \leq 1/4$ the S curves are six families of roughly circular curves with centres at the intersections of the fourfold (C_4) axes with the sphere. For the rest of the range,

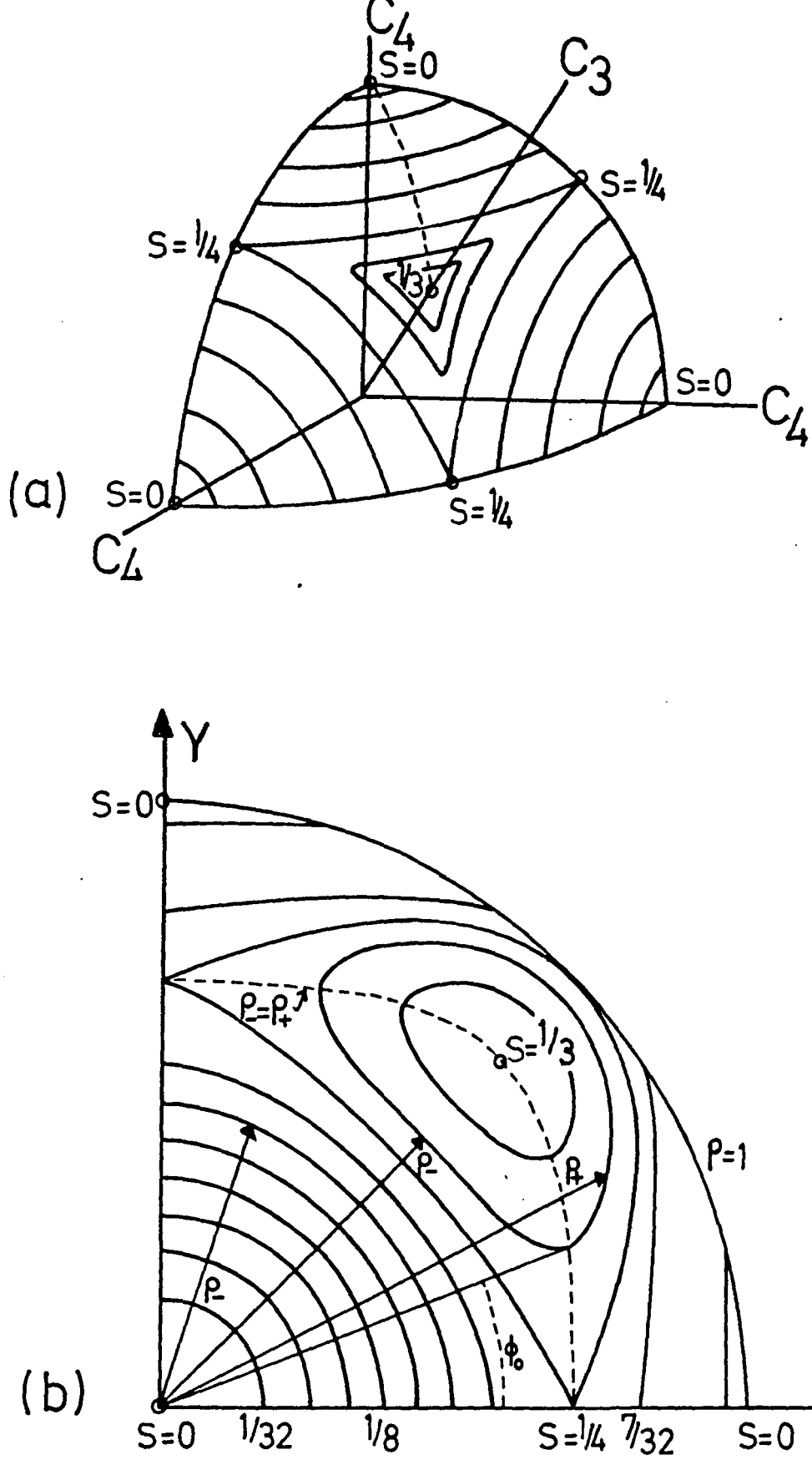

FIGURE 5.4 a) THE INTERSECTIONS OF $S = \frac{1}{4}(\sin^2 2\theta + \sin^4 \theta \sin^2 2\phi)$ WITH A UNIT RADIUS SPHERE.

b) THE PROJECTED INTERSECTIONS OF S WITH THE UNIT RADIUS SPHERE IN THE xy PLANE (AFTER BELTRAN-LOPEZ AND CASTRO-TELLO[5.8]).

$^1/4 \leq S \leq {}^1/3$, the S curves are eight families of pear-shaped curves which, as S increases, progressively diminish in size toward the points of intersection of the sphere with the threefold (C_3) axes.

The solid angle subtended between the points S = 0 and the curves $S \leq {}^1/4$ is calculated from the projected S curves by means of:[5.16]

$$\Omega(S \leqslant {}^1/4) = 48 \int_0^{\pi/4} (1 - \{ 1 - \rho_-^2 \}^{\frac{1}{2}}) d\phi \qquad (5.16)$$

Direct integration of this equation is not possible, but a Taylor expansion of the integrand about the point for which S = 0 yields a series representation of good convergence. Furthermore, since we are more interested in $^{d\Omega}/dS$ than in $\Omega(S)$, we take the derivative of this series before integration and substitute ρ_- to obtain $^{d\Omega}/dS$. For the rest of the range of S, $^1/4 \leq S \leq {}^1/3$, the integrand is expanded about the point for which $S = {}^1/3 (\rho_\pm^2 = {}^2/3, \phi = \pi/4)$.

For both ranges of S, the solutions obtained for $^{d\Omega}/dS$ involve complete elliptic integrals (for details of the solutions see reference 5.8 p447). Since the expressions obtained for $^{d\Omega}/dS$ are complex, it is convenient to use a computer to extract the desired information, namely a plot of $^{d\Omega}/dS$ against S. The graph obtained is shown in Figure 5.5 and from this it is seen that the absorption function for any transition will have two shoulders at the fields

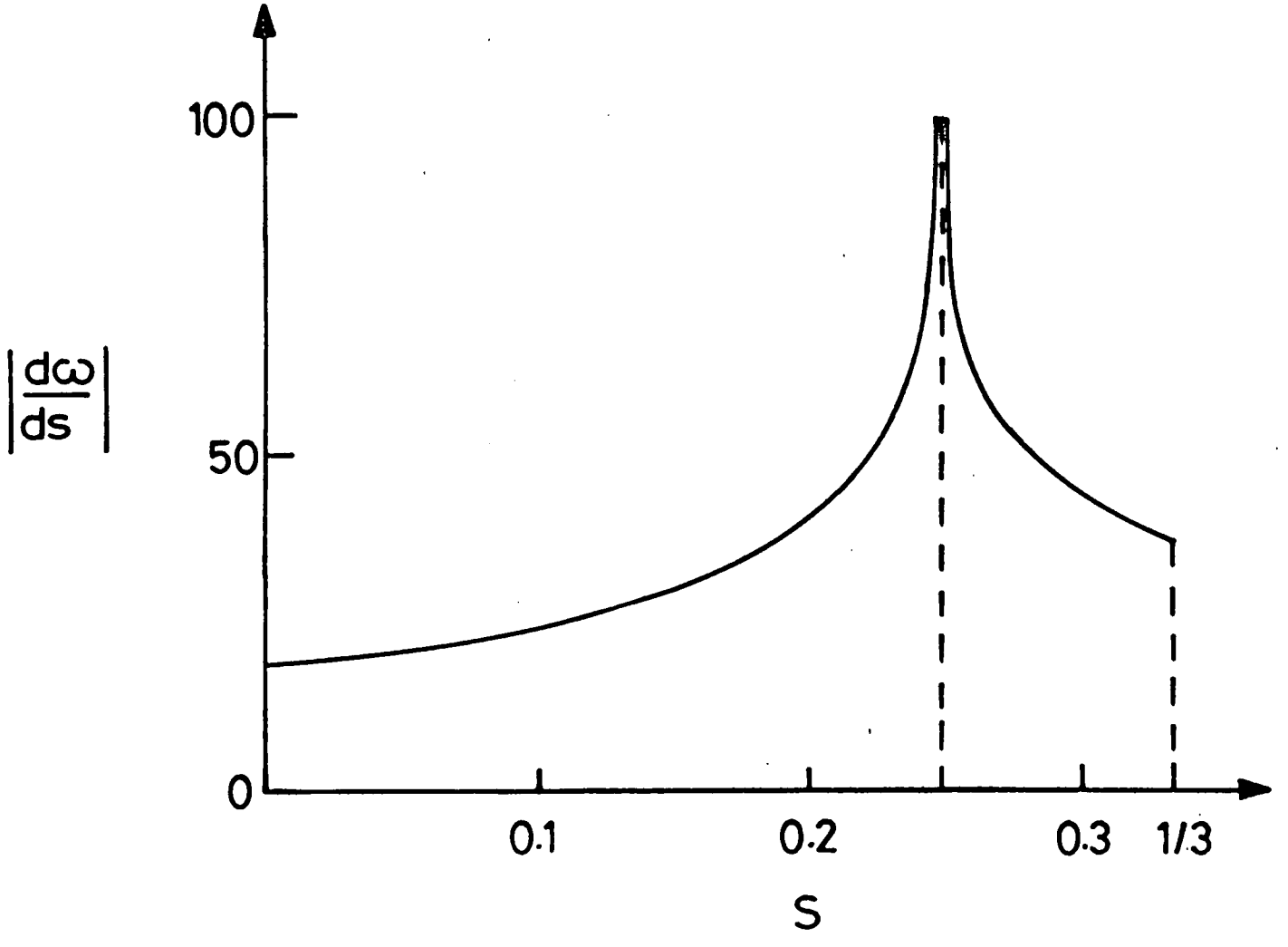

FIGURE 5.5 RATE OF CHANGE OF SOLID ANGLE WITH S AS DEFINED IN FIGURE 5.4 (AFTER BELTRAN-LOPEZ AND CASTRO-TELLO(5.8)).

corresponding to S = 0 and S = $^1/3$ and at least one divergence at the field corresponding to S = $^1/4$.

The complete absorption function, i(H), also involves the differential expression $^{dH}/dS$. The field positions of the angular dependent $\Delta M = \pm 1$, $\Delta m = 0$ transitions of $^6S_{5/2}$ ions in cubic fields are given in Table 4.3; these may be re-expressed in terms of S as follows:

$$H = H_0 \pm 2(1-5S)a + {}^5/3(S-7S^2)\,a^2/H_0 \quad \text{for } M = \pm {}^5/2 \leftrightarrow \pm {}^3/2 \qquad (5.17a)$$

$$H = H_0 \pm {}^5/2(1-5S)a - {}^5/48(3+178S-625S^2)\,a^2/H_0 \quad \text{for } M = \pm {}^3/2 \leftrightarrow \pm {}^1/2 \qquad (5.17b)$$

$$H = H_0 + {}^{10}/3(7S-25S^2)\,a^2/H_0 \quad \text{for } M = +\tfrac{1}{2} \leftrightarrow -\tfrac{1}{2} \qquad (5.17c)$$

where a is the cubic field parameter in magnetic field units. For Fe^{3+}, $H_0 = {}^{h\nu}/g\beta$ and for Mn^{2+}, $H_0 = {}^{h\nu}/g\beta$ plus the isotropic terms of the resonance field expressions (i.e. the hyperfine terms). From the above equations dH/dS is easily obtained for each transition and if at any point $^{dH}/dS$ is zero, a divergence in i(H) will be created at that point (this is in addition to the divergence of i(H) at the field corresponding to S = $^1/4$ resulting from the variation of $^{d\Omega}/dS$ with S).

Inspection of equations 5.17a&b shows that for the fine structure transitions, $M = \pm^{5}/2 \longleftrightarrow \pm^{3}/2$ and $M = \pm^{3}/2 \longleftrightarrow \pm^{1}/2$, $^{dH}/dS$ is not equal to zero for any value of S and therefore the complete absorption function for each of these transitions is essentially linear in $^{d\Omega}/dS$. The corresponding EPR lines are therefore spread over magnetic field ranges of 10a/3 and 25a/6 respectively, and, in general, will not be observed except for the divergences at $H(S=\frac{1}{4})$ and the pairs of shoulders at $H(S=0)$ and $H(S=^{1}/3)$. The magnetic field positions of these features are given in Table 5.2.

For the central $M = +\frac{1}{2} \longleftrightarrow -\frac{1}{2}$ transition $^{dH}/dS$ reduces to zero when $S = ^{7}/50$. This transition will therefore show a divergence at the field corresponding to $S = ^{7}/50$ in addition to the features shown by the outer fine structure transitions. Moreover, the four features shown by the central transition (their field positions are also given in Table 5.2) will only be spread over a relatively small range of field because the expression for the resonance field of this transition contains only a small second order term which is angular dependent. Thus it is often found experimentally that, in a polycrystalline sample, only the $M = +\frac{1}{2} \longleftrightarrow -\frac{1}{2}$ transition can be detected because the resonances contributing to the line are "smeared out" much less in terms of field than in the case of the outer $M = \pm^{5}/2 \longleftrightarrow \pm^{3}/2$ and $M = \pm^{3}/2 \longleftrightarrow \pm^{1}/2$ transitions. In any event, the central transition dominates the powder spectrum and therefore, for the remainder of this section, only this transition will be considered.

The absorption function for the $M = +\frac{1}{2} \longleftrightarrow -\frac{1}{2}$

TRANSITION	S VALUE	SHOULDER	DIVERGENCE
$\pm 5/2 \leftrightarrow \pm 3/2$	0	$H_o \mp 2a$	
	$1/3$	$H_o \pm 4a/3 - 20a^2/27H_o$	
	$1/4$		$H_o \pm a/2 - 5a^2/16H_o$
$\pm 3/2 \leftrightarrow \pm 1/2$	0	$H_o \pm 5a/2 - 5a^2/16H_o$	
	$1/3$	$H_o \mp 5a/3 + 20a^2/27H_o$	
	$1/4$		$H_o \mp 5a/8 - 225a^2/256H_o$
$+\frac{1}{2} \longleftrightarrow -\frac{1}{2}$	0	H_o	
	$1/3$	$H_o - 40a^2/27H_o$	
	$1/4$		$H_o + 5a^2/8H_o$
	$7/50$		$H_o + 49a^2/30H_o$

Table 5.2 Magnetic field positions of shoulders and divergences in the E.P.R. spectrum of $^6S_{5/2}$ ions in randomly oriented cubic crystals (after ref. 5.8)

transition, obtained by substituting $d\Omega/dS$ and dH/dS from equation 5.17c into equation 5.14, is plotted in Figure 5.6 as a function of the dimensionless variable $(H - H_0)H_0/a^2 (= {}^{10}/_3(7S - 25S^2))$. The main features of this function will make the EPR line appear as a split line of approximate peak-to-peak separation $H = a^2/H_0$ with two small shoulders at field values $H = H_0$ and $H = H_0 - 40a^2/27H_0$.

The absorption function of Figure 5.6 may be convoluted numerically with a lineshape function of given linewidth in order to simulate a real powder spectrum using exactly the same procedure as was used for the numerical simulation methods of section 5.3. Finally, the broadened simulation is differentiated (again using the method described in section 5.3) in order to compare it with experiment.

5.5 AN ASSESSMENT OF THE RELIABILITY OF THE SIMULATION TECHNIQUES DESCRIBED.

In this section, a detailed comparison will be made between the powder spectrum simulation techniques described in sections 5.2 to 5.4. The valid methods of simulation will be assumed to be those which, when used to predict a particular powder spectrum, produce absorption functions which agree both in terms of general shape and in terms of the predicted field positions of any distinct features. A simulation procedure will be assumed to be unreliable if its absorption function does not agree with the majority. The trial of the simulation techniques was restricted to a comparison between the powder patterns predicted by each method for ${}^6S_{5/2}$ ions in randomly oriented cubic fields. This particular powder spectrum was chosen for the purpose

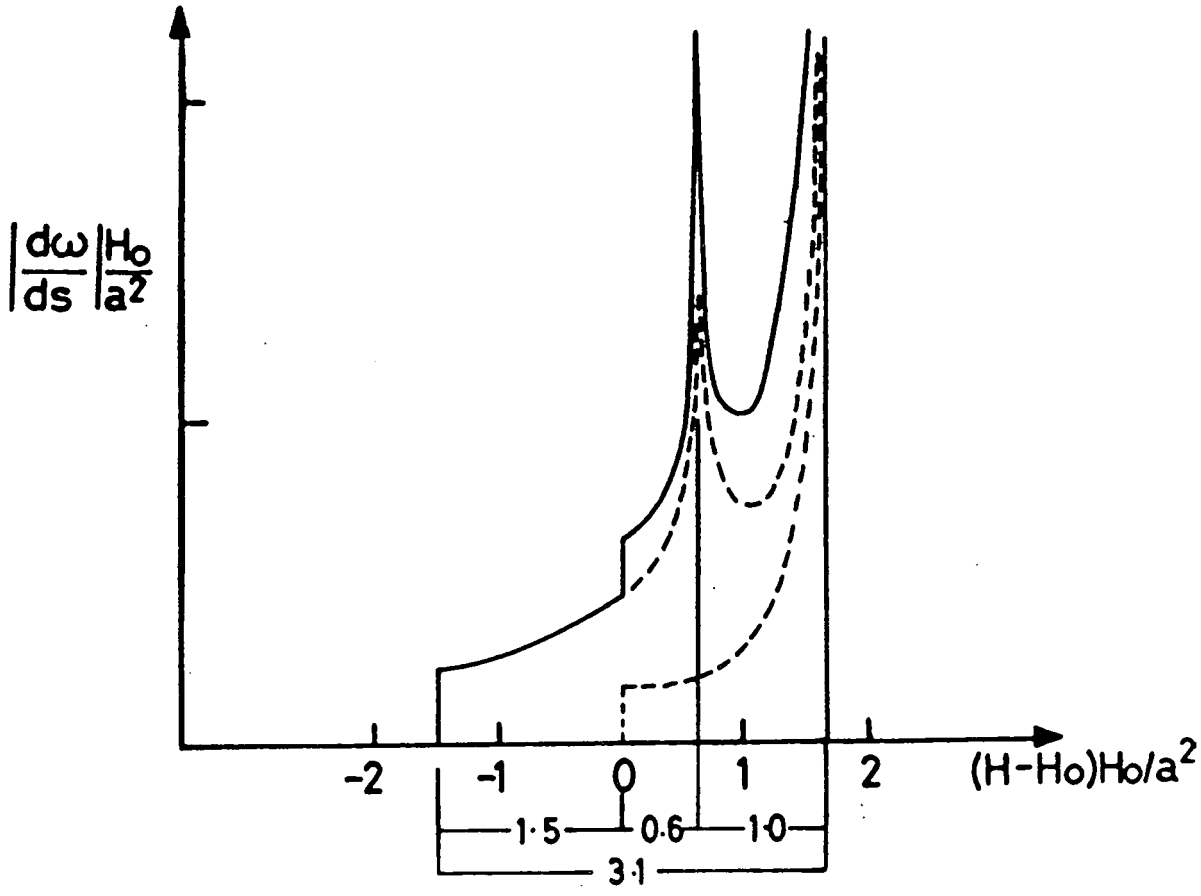

FIGURE 5.6 ABSORPTION FUNCTION FOR THE M = $+^1/_2 \leftrightarrow {}^1/_2$ TRANSITION OF $^6S_{5/2}$ IONS IN A CUBIC FIELD (AFTER BELTRAN-LOPEZ AND CASTRO-TELLO[5.8]).

of testing the simulation procedures against each other because it is the only powder spectrum to which the analytical technique of section 5.4 may be applied and also because the only other powder spectrum of interest to us, that of Cr^{3+} in MgO, is expected to be exactly the same as the single crystal spectrum, since the single crystal spectrum is isotropic.

A close inspection of Tables 5.1 and 5.2 shows that there is good agreement between the analytical technique of section 5.4 and the differential method of section 5.2 concerning the predicted positions of shoulders and divergences in the powder patterns of the fine structure transitions ($M = \pm^{5}/2 \longleftrightarrow \pm^{3}/2$ & $M = \pm^{3}/2 \longleftrightarrow \pm^{1}/2$) of the $^{6}S_{5/2}$ ion. An exact agreement would be found if second order terms in the expressions for the resonance fields (i.e. terms in a^{2}/H_{o}) were included in the calculations undertaken to arrive at Table 5.1. Because of this agreement we may assume that the simulation techniques of sections 5.2 and 5.4 are reliable and if either is compared with the numerical simulation methods of section 5.3 to test their reliability the conclusions drawn from such a comparison will apply to both techniques. The advantage of assessing the numerical methods against the analytical technique is that each produce simulations of the complete lineshape and therefore a more detailed comparison can be made than if the differential method were used for the same purpose (the lineshape shown in Figure 5.1 for the differential method is inferred and, strictly speaking, this method can only be used to find the positions of the shoulders and divergences in the powder pattern).

Both the analytical and numerical methods solve the right hand side of equation 5.5, which may be split up into several component differential quantities as shown in equation 5.14. The analytical method assumes that $dN/d\Omega$ is constant ($dN/d\Omega = N_o/4\pi$) as indeed it should be for a random collection of independent, small single crystals. This assumption is also implied in one of the conditions which must be met in order for the numerical methods to be applied. The condition in question is that which requires the unit radius sphere to be divided up into equal units of solid angle, $d\Omega$, (from which values of θ and ϕ are obtained in order to calculate the resonance fields many times and build up the powder pattern on a histogram). Of course, this condition does not apply to the true Monte-Carlo technique but if the pseudo-random numbers generated in the computer are, indeed, statistically equivalent to a random set then $dN/d\Omega$ will again be equal to a constant. The differential function dH/dS is also identical for the analytical technique and all the numerical methods since it is simply derived from the expressions for the resonance fields of the various transitions.

The analytical and numerical methods will therefore be equivalent if the function $d\Omega/dS$ is the same in both cases. $d\Omega/dS$ has already been evaluated as a function of S for $^6S_{5/2}$ ions in randomly oriented cubic fields using the analytical technique (see Figure 5.5). Since S is an angular function, each numerical simulation technique may be used to calculate values of S from the set of θ and ϕ values that particular numerical method uses to evaluate the powder pattern. For each numerical method, the number of times that this procedure generates a value of S between

S_α and $S_{(\alpha+1)}$ may be histogrammed on an "S array" $S_1, S_2 \longrightarrow S_n$ and in each case the histogram will represent an evaluation of the function $d\Omega/dS$ between S_1 and S_n. The allowed range of S means that we can set $S_1 = 0$ and $S_n = 1/3$. The curves of $d\Omega/dS$ against S obtained in this way for each of the three numerical methods are identical and a representative example is shown in Figure 5.7.

Inspection shows that, in all essential details Figure 5.7 is also identical with the curve of $d\Omega/dS$ against S obtained using the analytical technique (Figure5.6). The only minor difference is that Figure 5.7 displays a certain amount of "noise". By undertaking several trial numerical simulations it was established that the "noise" was reduced if more points were taken. Thus, we may assume that, if enough pairs of values of θ and ϕ are used ($\sim 10^6$) the numerical simulation techniques of section 5.3 produce absorption functions which are identical to those produced by the analytical technique of section 5.4. To demonstrate this point, predictions of the lineshape arising from the $M = +\frac{1}{2} \longleftrightarrow -\frac{1}{2}$ transition of Fe^{3+} in powdered MgO were obtained from the analytical and numerical simulation procedures and are shown in Figures 5.8a&b respectively. The simulations were produced using the value of a (the cubic field splitting constant) appropriate for Fe^{3+} in MgO (i.e. a = 21.6mT) and a Lorentzian lineshape function of peak-to-peak linewidth 0.2 mT.

In conclusion, since it has already been established that the differential and analytical methods of sections 5.2 and 5.4 respectively are equivalent, we may assume that

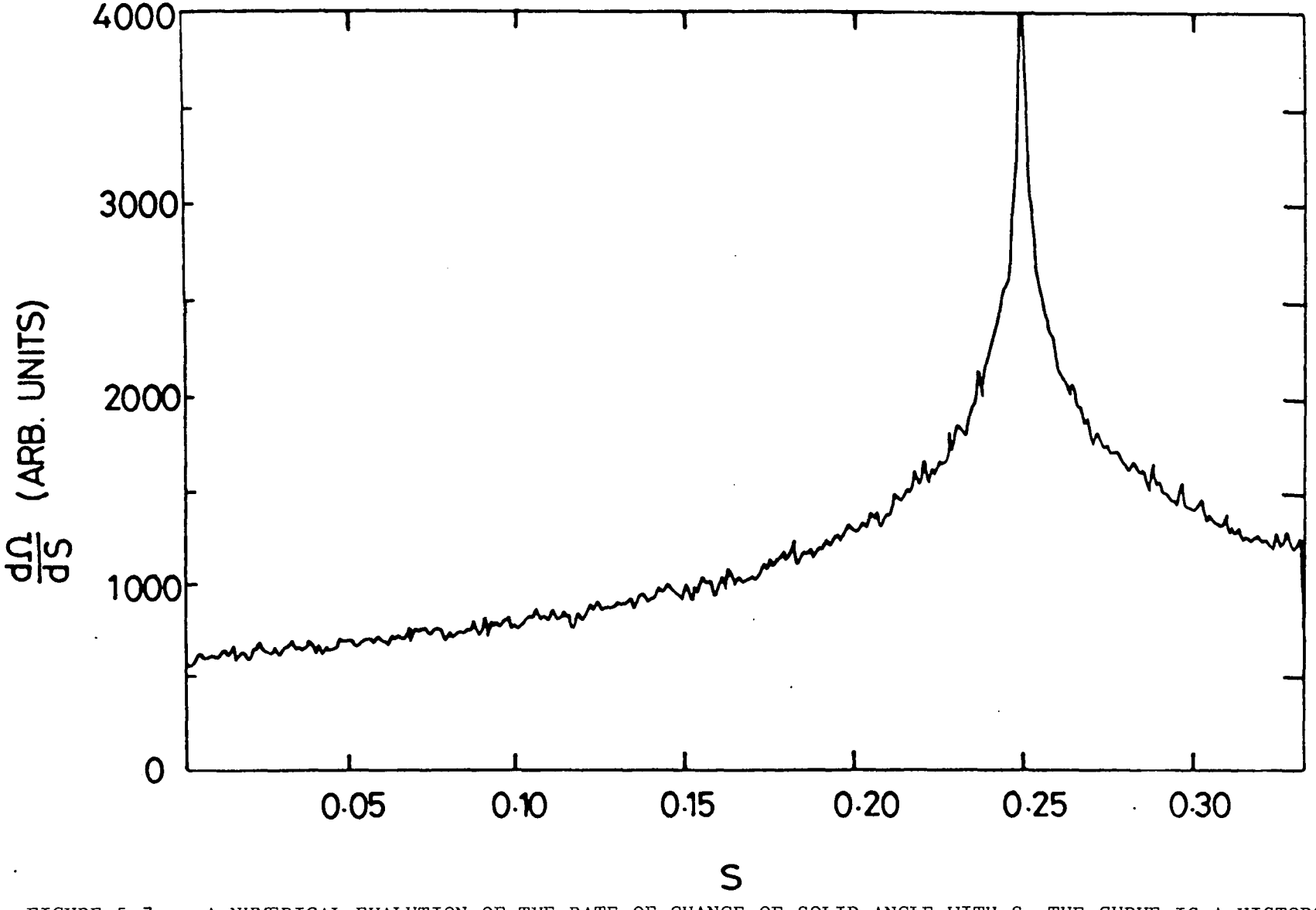

FIGURE 5.7 A NUMERICAL EVALUTION OF THE RATE OF CHANGE OF SOLID ANGLE WITH S; THE CURVE IS A HISTORGRAM OF 4×10^5 POINTS.

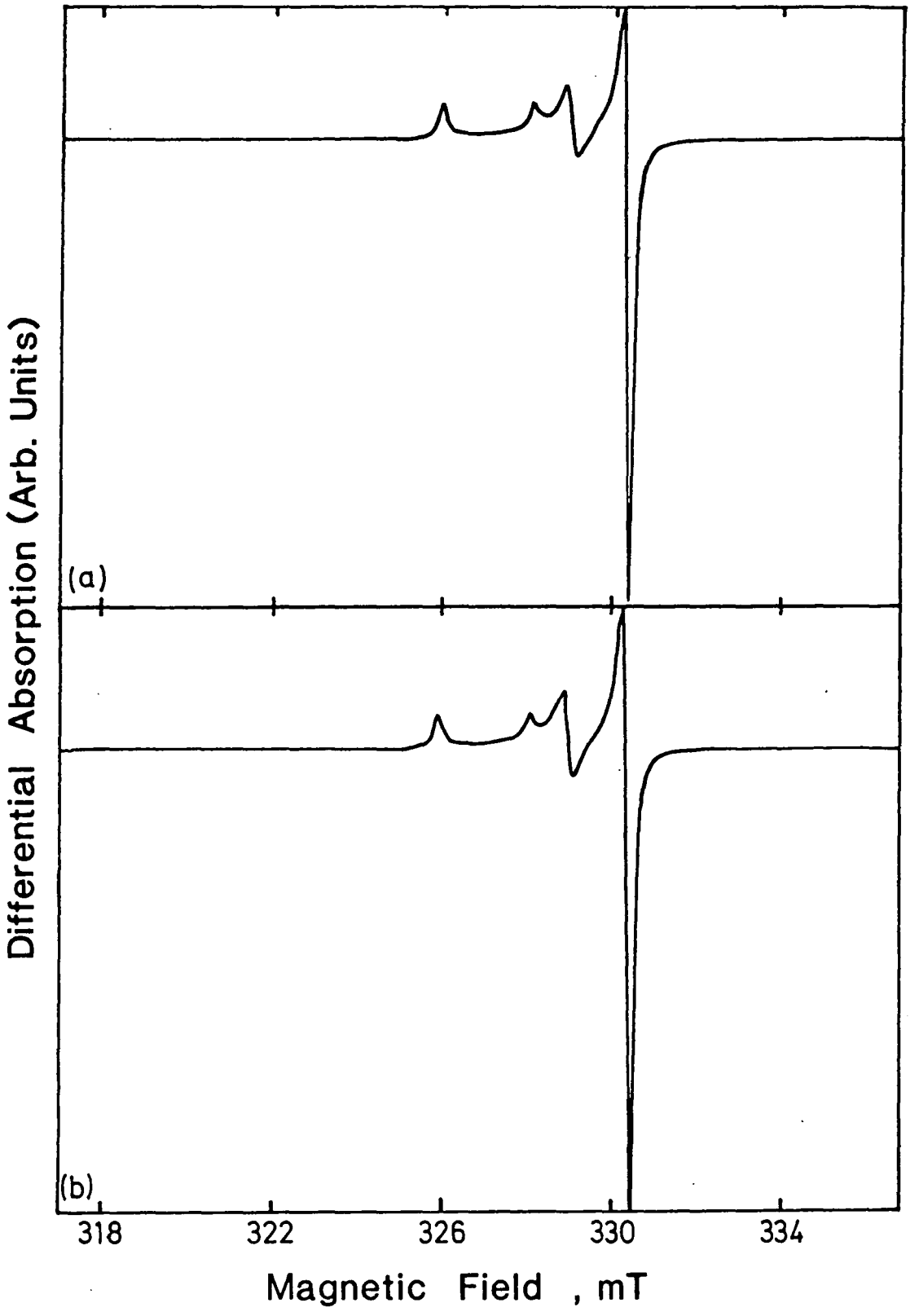

FIGURE 5.8 THEORETICAL E.P.R. LINESHAPE FOR THE M = $-\frac{1}{2} \leftrightarrow +\frac{1}{2}$ TRANSITION OF Fe^{3+} IN POWDERED MgO OBTAINED FROM a) AN ANALYTICAL AND b) A NUMERICAL CALCULATION USING a = 21.6 mT AND A LORENTZIAN LINESHAPE OF PEAK TO PEAK WIDTH 0.2 mT.

all the simulation techniques discussed in this Chapter are equally reliable, although, as discussed in section 5.1, each has its own particular advantages and disadvantages.

REFERENCES

5.1 R.H. Sands Phys. Rev. 99, 1222(1955)

5.2 F.K. Kneübuhl J. Chem Phys 33, 1074(1960)

5.3 P.C. Taylor and P.J. Bray J. Mag. Res. 2, 305(1970)

5.4 R.W. Reynolds, L.A. Boatner, C.B. Finch, A. Chatelain and M.M. Abraham J. Chem. Phys. 56, 5607 (1972).

5.5 W. Hutton "The role of Titania in the formation of $MgO-Al_2O_3-SiO_2$ glass ceramics" Ph.D. thesis, Durham University ( ), unpublished.

5.6 H.S. Eggleston "Electron Paramagnetic resonance of rutile pigments" Ph.D. thesis, Durham University, (1982), unpublished.

5.7 This chapter.

5.8 V. Beltran-Lopez and J. Castro-Tello J. Mag. Res. 39, 437(1980)

5.9 D. Cordischi, R.L. Nelson and A.J. Tench Trans. Faraday Soc. 65, 2740 (1969)

5.10 T. Yamamura, A. Hasegawa, Y. Yamada and M. Miura Bull. Chem. Soc. Japan 43, 3377 (1970)

5.11 J. Rubio.O., E. Munoz P., J Boldu O., Y. Chen and M.M. Abraham J. Chem. Phys. 70, 633 (1979)

5.12 F. Gesmundo and P.F. Rossi J. Solid State Chem. 8, 297(1973)

5.13 N.G. Kakazei and M.V. Vlasova, J. Appl. Spectroc. (U.S.A.) translated from Zhurnal Prikladnoi Spektroskopii 24, 150 (1976)

5.14 E.R. Feher Phys. Rev. 136, A145 (1964)

5.15 D.G. Hughes and D.K.C. MacDonald Proc. Phys. Soc. 78, 75 (1961)

5.16 M.H. Protter and C.B. Morrey Jr, "Modern Mathematical Analysis" p.244, Addison-Wesley, Reading, Mass., 1964.

CHAPTER SIX

THE INTERPRETATION OF E.P.R. SPECTRA III: LINESHAPES AND LINEWIDTHS.

In Chapter Four it was shown that the theoretical interpretation of single crystal E.P.R. line positions and intensities yields important information concerning the nature of the species undergoing resonance. However, the shapes and widths of individual spectral lines were not considered, although a great deal of additional information is available from this source, since line broadening is caused by the relaxation of the spin system, which in turn is caused by the need of spins to dissipate the energy absorbed during resonance. The type of interactions taking place both between the paramagnetic ions and also between individual paramagnetic ions and the surrounding diamagnetic lattice determines the dominant relaxation mechanisms and the strength of these interactions largely determines the linewidth. The experimental characteristics of the E.P.R. lines (such as the lineshape and the dependence of the linewidth on the impurity concentration and the temperature) are compared with those predicted theoretically for each type of broadening mechanism in order to establish the dominant broadening mechanisms in a material.

Four important effects influencing E.P.R. lineshape and linewidth which will be discussed theoretically in this chapter are: spin-spin interactions such as dipolar and exchange effects, spin-lattice relaxation to the surrounding diamagnetic ions, strain broadening due to

lattice distortions and instrumental broadening caused by unfavourable experimental conditions. Experimental evidence (which will be discussed fully in Chapters Seven to Nine) suggests that the dipolar and strain broadening mechanisms largely determine the linewidths and lineshapes of the E.P.R. spectra of iron group ions in magnetically dilute MgO crystals. Broadening due to spin-lattice relaxation, although present, is not a dominant factor in these crystals as will be shown in section 6.4. The major causes of instrumental broadening will be discussed in section 6.5 so that the experimental conditions which enable such sources of broadening to be eliminated may be established. These experimental conditions were rigorously adhered to when the spectra described in Chapters Seven to Nine were recorded.

Other sources of E.P.R. line broadening include: unresolved hyperfine structure, interactions between the paramagnetic ions and the nuclei of surrounding diamagnetic ions and imhomogeneity in the applied magnetic field. Such effects are not important as far as dilute solutions of iron group ions in MgO are concerned and so they will not be discussed in this Chapter. Details of the mechanisms which give rise to these sources of broadening and the effect that they have upon linewidth and lineshape are given in the standard texts[6.1,6.2].

Another experimental parameter which it might be thought would provide important information, particularly regarding the impurity concentration, is the intensity of the absorption spectrum. However, this is very hard to determine in absolute terms, the measured intensity being

heavily dependent upon the characteristics of the instrument used to record the spectrum. In contrast, the shapes and widths of spectral lines are largely independent of instrumental parameters and therefore the conclusions drawn from their examination are more reliable than those drawn from a consideration of line intensities and for this reason line intensities will not be discussed in this Chapter.

6.1 THE DETERMINATION OF LINESHAPE AND LINEWIDTH - A GENERAL SURVEY

The shape of an individual resonance peak is usually described in terms of the moments of the line, particularly the second and fourth moments. The n^{th} moment of a line is defined as:[6.3]

$$M_n = \int_0^\infty (\nu - \nu_0) f(\nu)\, d\nu \qquad (6.1)$$

where ν_0 is the frequency at the point of maximum absorption of the resonance line and $f(\nu)$ is a function describing the lineshape. $f(\nu)$ is normalised so that:

$$\int_0^\infty f(\nu)\, d\nu = 1 \qquad (6.2)$$

If we let $(\nu - \nu_0) = u$ and $f(\nu) = f(\nu_0 + u) = \overline{f}(u)$ then we may redefine M_n as follows:

$$M_n = \int_{-\nu_o}^{\infty} u^n \bar{f}(u)\,du \qquad (6.3)$$

which for narrow lines becomes:

$$M_n = \int_{-\infty}^{\infty} u^n \bar{f}(u)\,du \qquad (6.4)$$

Inspection of equation 6.4 shows that for symmetrical lines the odd moments vanish.

The two most common E.P.R. experimental lineshapes (Lorentzian and Gaussian) were discussed in Chapter Five. If the spectral lineshape is Gaussian, $\bar{f}(u)$ may be replaced by the convolution function of equation 5.10b; if it is Lorentzian $\bar{f}(u)$ may be replaced by the convolution function of equation 5.10a. If, however, the lineshape is imbetween Lorentzian and Gaussian $\bar{f}(u)$ must be replaced by a lineshape function which is an appropriate combination of the Gaussian and Lorentzian functions. In order to correspond with the notation of equations 6.1 to 6.4 the Lorentzian and Gaussian convolution functions of equations 5.10a and b may be rewritten as:

$$\text{Gaussian: } \bar{f}_G(u) = \frac{1}{\sigma\sqrt{2\pi}} \exp\left[\frac{-u^2}{2\sigma^2}\right] \qquad (6.5a)$$

$$\text{Lorentzian: } \bar{f}_L(u) = \frac{\Delta}{2\pi} \cdot \frac{1}{u^2 + \frac{1}{4}\Delta^2} \qquad (6.5b)$$

The linewidth, $\Delta\nu$, is defined according to the equation:

$$\bar{f}(u = \frac{\Delta\nu}{2}) = \tfrac{1}{2}\bar{f}(0) \qquad (6.6)$$

and is given by $\Delta\nu = 2\sigma\sqrt{2\ln 2} = 2.35\sigma$ for Gaussian and $\Delta\nu = \Delta$ for Lorentzian lineshapes.

Evaluation of equation 6.4 with $\bar{f}(u) = \bar{f}_G(u)$ shows that for a Gaussian line the even moments are:

$$\begin{aligned} M_2 &= \sigma^2 \\ M_4 &= 3\sigma^4 \\ M_{2n} &= 1.3.5.....(2n-1)\,\sigma^{2n} \end{aligned} \qquad (6.7)$$

whilst for a Lorentzian line in order to evaluate the moments from equation 6.4 with $\bar{f}(u) = \bar{f}_L(u)$ the line must be truncated at $\nu = \nu_o \pm \alpha$ (where $\alpha >> \Delta$) to ensure that the line has a finite area. For the truncated Lorentzian line the even moments are:

$$\begin{aligned} M_2 &= \alpha\Delta/\pi \\ M_4 &= \alpha^3\Delta/3\pi \\ M_{2n} &= \frac{\Delta}{\pi} \cdot \frac{\alpha^{2n-1}}{2n-1} \end{aligned} \qquad (6.8)$$

In order to examine the similarity between a given

experimental lineshape and either the Gaussian or Lorentzian curve, we need only calculate the ratio M_4/M_2^2. For the Gaussian curve:

$$M_4/M_2^2 = 3 \qquad (6.9)$$

whilst for the Lorentzian curve:

$$M_4/M_2^2 = \pi\alpha/3\Delta >> 1 \qquad (6.10)$$

6.2 SPIN-SPIN INTERACTIONS

Spin-spin interactions are responsible for both dipolar and exchange effects; the dipolar interaction leads to a broadening of the resonance line whereas the exchange interaction narrows the line.

Dipolar broadening is caused by local variations in the magnetic field[6.3,6.4]. Besides the applied magnetic field, H_o, a local field, H_{loc}, created by the surrounding magnetic ions also acts on each paramagnetic centre and thus the resonance condition becomes $h\nu = g\beta\ (H_o + H_{loc})$. Because the dipole moments of the paramagnetic ions are randomly oriented, the value of H_{loc} will vary from site to site and hence the resonance condition will be fulfilled for different values of H_o depending on the value of H_{loc}. The order of magnitude of $H_{loc} \sim \beta / r^3$ where r is the separation of the paramagnetic ions. As the variation in the resonant magnetic field is due entirely to the variation of H_{loc} from site to site, the line broadening, ΔH, caused by the dipolar interaction will simply be equal to H_{loc} i.e. $\Delta H \sim \beta / r^3$.

The exchange interaction is an electrostatic rather than a magnetic effect being due to the overlap of the electron shells of neighbouring ions. In ionic insulators, where one does not expect to find loosely bound hydrogenic-like states, true exchange interactions will be limited to paramagnetic impurity ions which are nearest neighbours because the shells of paramagnetic ions which are any further apart will not overlap. However, exchange coupling can still take place between impurity ions separated by relatively large distances via the electron shells of the intervening diamagnetic ions (this mechanism is known as "superexchange"[6.5]). Nevertheless, both the exchange and superexchange mechanisms have much shorter ranges than the dipolar interaction already mentioned. Under the influence of the exchange interaction the dipole moments of the paramagnetic ions coupled together tend to adopt a common orientation. Hence, if both spin-spin interactions are important, the effect of exchange is to reduce the range of variation of the local field, H_{loc}, responsible for dipolar broadening and consequently the E.P.R. lines are considerably narrower than they would be if dipolar effects alone were present.

Both the exchange and dipolar interactions have been considered in detail by various groups of workers [6.6-6.11] Here, the approach adopted by Van Vleck[6.6] will be discussed, together with the extensions of his method developed by Kittel and Abrahams[6.8] and by de Biasi and Fernandes.[6.11]

Provided that: (i) the paramagnetism is purely spin in nature so that both initial splittings and g-value

anisotropy are absent; (ii) the Zeeman energy is larger than the dipole-dipole interaction; and (iii) the temperature is high enough so that the populations of the levels can be considered equal, the following Hamiltonian may be used to represent the spin-spin interactions:[6.6]

$$\mathcal{H} = Hg\beta\sum_{j} S_{zj} + \sum_{k>j} \tilde{A}_{jk} S_j S_k + \ldots\ldots$$

$$\ldots + g^2\beta^2 \sum_{k>j} [\, r_{jk}^{-3}(S_j \cdot S_k) - 3\, r_{jk}^{-5}(r_{jk} \cdot S_j)(r_{jk} \cdot S_k) \tag{6.11}$$

where the first, second and third terms represent the Zeeman, exchange and dipolar energies respectively. $\tilde{A}_{jk}$ is related to the normal exchange integral by $\tilde{A}_{jk} = -2z^2 J_{jk}$ (z is the number of unpaired electrons each atom possesses). Bearing in mind the assumptions mentioned above, Van Vleck used the Hamiltonian of equation 6.11 to derive expressions for the second and fourth moments of the expected absorption line. He found that only the dipolar interaction contributes towards the second moment whereas the fourth moment equation contains terms due to both the dipolar and the exchange interactions.

In systems where the spin-spin interactions are purely dipolar in nature, the exchange terms in the fourth moment equation disappear and evaluation of the ratio M_4/M_2^2 shows that the lineshape is approximately Gaussian. If a true Gaussian lineshape is assumed, the value of the second moment may be used to calculate a theoretical value

for the linewidth, $\Delta\nu$, since equations 6.6 and 6.7 show that for a Gaussian line $\Delta\nu = 2.35 \sqrt{M_2}$.

The spins may also be coupled together by both dipolar and exchange interactions. In such systems, the second moment is unaltered by the presence of exchange, being dependent upon dipolar interactions alone, but because of the exchange terms in the fourth moment equation the fourth moment becomes larger than it would be in the absence of exchange. Thus, if both spin-spin interactions are important in a material, the ratio M_4/M_2^2 is larger than it is in materials where the spin-spin interactions are purely dipolar in origin. From equations 6.9 and 6.10 we may conclude that exchange forces alter the dipolar lineshape in such a way that as they increase in strength the lineshape moves away from Gaussian towards Lorentzian i.e. the resonance peak is sharpened, the line becoming narrower at the centre and dropping off more rapidly in the wings. The second moment may no longer be used to calculate the linewidth in the manner described when the broadening is due to dipolar interactions alone since such a calculation assumes that the lineshape is Gaussian. However, Anderson and Weiss[6.7] showed that if both exchange and dipolar forces are important, the half width, $\Delta\nu$, is given by:

$$\Delta\nu = M_2/(J''/h) \qquad (6.12)$$

where M_2 is the second moment due to dipolar broadening, and (J''/h) is the exchange energy in frequency units. The overall effect of exchange forces, therefore, is to

reduce the linewidth of dipolar broadened lines and this effect is known as "exchange narrowing".

Van Vleck[6.12] tested his model by comparing the linewidths and lineshapes predicted by dipolar broadening theory with those measured experimentally for various paramagnetic salts and hydrated paramagnetic salts (see Table 6.1) In magnetically concentrated salts (i.e. unhydrated salts) the measured linewidth was much smaller than predicted and the lineshape was Lorentzian or near Lorentzian. Van Vleck concluded that the discrepancies between theory and experiment could be explained by assuming that considerable exchange coupling takes place in such materials. This assumption is borne out by the results for the hydrated salts where the theoretical and experimental linewidths compare well and the lineshape is approximately Gaussian, as expected for dipolar broadened lines. The presence of the water of crystallization dilutes the magnetic ions to the extent that exchange forces are no longer significant.

Although the experimental evidence discussed above seems to vindicate Van Vleck's theory of dipolar broadening it must be remembered that his model only applies to materials such as those listed in Table 4.1 in which all the "spin lattice" sites are populated identically (the "spin lattice" is the lattice formed by <u>all</u> the atomic sites in a crystal which may be occupied by paramagnetic ions). This fact essentially invalidates the recent use of the Van Vleck model to explain the behaviour of the E.P.R. spectra of transition metal ions in lightly doped magnesium oxide crystals [6.13-6.15], since even at the highest impurity

Substance	Linewidth, $\Delta H_{\frac{1}{2}}$,Gauss		M_4/M_2^2
	Experimental	Calculated	
$MnCl_2.4H_2O$	1,410	1,530	2.28
$MnCl_2$	750	2,950	3.84
$MnSO_4.4H_2O$	1,150	1,560	2.69
$MnSO_4.H_2O$	320	2,870	4.54
$MnSO_4$	665	3,520	3.33
$Mn(NO_3)_2.6H_2O$	1,210	1,003	2.92
MnF_2	470	7,020	3.73

Table 6.1 Some of Van Vleck's dipolar line broadening data.[6.12]

concentrations investigated ($\sim$ 15,000ppm) very few of the spin lattice sites are occupied by magnetic ions. Because the experimental E.P.R. lineshapes in these samples were Lorentzian rather than Gaussian and, in addition, the linewidths calculated using dipolar broadening theory were much larger than those observed, it was suggested that the paramagnetic ions were experiencing strong exchange forces. It is hard to reconcile this conclusion with Van Vleck's data (Table 6.1) which shows that exchange forces decrease in magnitude very rapidly as the distance between the magnetic ions increases (according to Table 6.1, in the hydrated salts the intervening water of crystallization separates the paramagnetic ions by a large enough distance to destroy the exchange coupling found in the unhydrated salts).

More applicable to the lightly doped magnesium oxide samples is the theory of dipolar broadening in the absence of exchange developed by Kittel and Abrahams[6.8]. Their approach is basically an extension of Van Vleck's dipolar broadening theory to cover materials in which the paramagnetic ions are diluted and occupy the atomic sites of the host lattice in a random fashion. If f is the probability that a lattice site is occupied by a magnetic system, Kittel and Abrahams find that the second moment, $\langle \Delta \nu^2 \rangle$, in frequency units is given by:

$$\langle \Delta \nu^2 \rangle = [S(S+1)/3h^2]\, f \sum_k B_{jk}^2 \qquad (6.13)$$

where

$$B_{jk} = -3/2g^2\beta^2 r_{jk}^{-3}[1-3\cos^2\theta_{jk}] \qquad (6.14)$$

r_{jk} is the distance between the j^{th} and k^{th} atom and θ_{jk} is the angle between r_{jk} and the applied magnetic field direction. Equation 6.13 is simply equivalent to $M_2 f$ where M_2 is the value of the second moment predicted by Van Vleck's dipolar broadening theory.

If the spin-spin interactions are purely dipolar in nature, the fourth moment, $\langle \Delta \nu^4 \rangle$, in frequency units assumes the form:[6.3]

$$h^4\langle \Delta \nu^4 \rangle = \left\{ f^2[3(\sum_k B_{jk}^2)^2 - 1/3N^{-1} \sum_{j\neq k\neq \ell} B_{jk}^2 (B_{j\ell}-B_{k\ell})^2] + \ldots \right.$$

$$\left. \ldots + f[\left(1.4 + \frac{0.3}{S(S+1)}\right) \sum_k B_{jk}^4] \right\} [1/3S(S+1)]^2 \qquad (6.15)$$

where N is the total number of magnetic ions. For small values of $f(<0.01)$, the term in f^2 can be disregarded so that:

$$\frac{\langle \Delta \nu^4 \rangle}{\langle \Delta \nu^2 \rangle^2} \approx \frac{\sum_k B_{jk}^4}{\left(\sum_k B_{jk}^2\right)^2} \cdot \frac{1}{f} >> 1 \qquad (6.16)$$

and comparison of this result with equations 6.9 and 6.10 shows that the lineshape may be described by a cut-off Lorentzian curve. If f>0.1 the lineshape is approximately Gaussian and if f = 1 equations 6.13 and 6.15 are equivalent to the second and fourth moment equations given by Van Vleck's dipolar broadening theory.

For the doped magnesium oxide samples examined in this work equation 6.16 applies and manipulation of equation 6.8 shows that the full width at half height of the cut-off Lorentzian curve (Δ) may be written as:

$$\Delta = \frac{\pi}{\sqrt{3}} \frac{\langle \Delta \nu^2 \rangle^{3/2}}{\langle \Delta \nu^4 \rangle^{1/2}} \qquad (6.17)$$

For a Lorentzian line, the peak-to-peak linewidth in magnetic field units, ΔH_{pp}, is given by:

$$\Delta H_{pp} = \frac{\Delta}{\sqrt{3}} \left(\frac{\mu_o}{4\pi} \cdot \frac{h}{g\beta} \right) \qquad (6.18)$$

($\mu_o/4\pi$. $h/g\beta$) converts the units of Δ from Hertz to Teslas.

Hence, Kittel and Abrahams' model of dipolar broadening in dilute magnetic materials predicts that the peak-to-peak linewidth ΔH_{pp}, is given by

$$\Delta H_{pp} = \frac{\pi}{(3)^{3/2}} f . \frac{\left(\sum_k B_{jk}^2 \right)^{3/2}}{\left(\sum_k B_{jk}^4 \right)^{1/2}} \left[\frac{S(S+1)}{1.4+0.3/S(S+1)} \right]^{1/2} \left(\frac{\mu_o}{4\pi g \beta} \right) \qquad (6.19)$$

and that the lineshape is a truncated Lorentzian with cut-off fields, H_c, given by:

$$H_c = H_o \pm (1.4S(S+1)+0.3)^{1/2} \left[\frac{\sum_k B_{jk}^4}{\sum_k B_{jk}^2} \right]^{1/2} \left(\frac{\mu_o}{4\pi g \beta} \right) \qquad (6.20)$$

where $H_o = h\nu / g\beta$

Recently, de Biasi and Fernandes[6.11] have modified Kittel and Abrahams' expressions to include the effect of exchange interations. It is necessary to recognise that in dilute solid solutions the effect of exchange is quite different from its effect in concentrated solutions i.e. in substances where all or almost all of the cationic sites are populated by paramagnetic ions. In the latter case, the exchange interaction leads to "exchange narrowing"[6.6,6.7] which was discussed earlier in this Chapter. In dilute solutions, the probability that several ions are coupled together by exchange forces is very low. On the other hand, there is a significant number of pairs of exchange coupled ions. These pairs do not contribute to the broadening of the main resonance line, since the ground state of such a pair (assuming antiferromagnetic coupling, as is usually the case) is a singlet. Ions which are too far apart to be exchange coupled only interact with each other via the dipolar mechanism. Therefore, the aim of de Biasi and Fernandes' approach is to quantify the number of exchange coupled pairs in a dilute solid solution and to exclude the

ions so coupled together from the summation terms in the expressions for the dipolar linewidth and cut-off fields of the truncated Lorentzian lineshape (equations 6.19 and 6.20).

Modification of equations 6.19 and 6.20 to take into account the exchange interaction leads to the following general expressions:

$$\Delta H_{pp} = (\pi/2\sqrt{3})A(S)f_e[S_{1\theta}(r_e)]^{3/2}[S_{2\theta}(r_e)]^{-1/2} \qquad (6.21)$$

$$H_c = H_o \pm (3/2)B(S)[S_{2\theta}(r_e)/S_{1\theta}(r_e)]^{1/2} \qquad (6.22)$$

A(S) and B(S) are constants which depend upon the parameters characterizing the paramagnetic ion and the host lattice i.e.:

$$A(S) = \frac{\mu_o g \beta}{4\pi a^3}\left(\frac{S(S+1)}{1.4 + 0.3(S^2+S)^{-1}}\right)^{\frac{1}{2}} \qquad (6.23)$$

$$B(S) = \frac{\mu_o g \beta}{4\pi a^3}[0.3 + 1.4S(S+1)]^{\frac{1}{2}} \qquad (6.24)$$

Here a is the nearest neighbour distance in the host lattice. The other components of equations 6.21 and 6.22 are defined as follows:

$$f_e = f(1-f)^{z(r_e)} \tag{6.25}$$

$$S_{1\theta}(r_e) = a^6 \sum_{r_{jk}>r_e} r_{jk}^{-6}(1-3\cos^2\theta_{jk})^2 \tag{6.26}$$

$$S_{2\theta}(r_e) = a^{12} \sum_{r_{jk}>r_e} r_{jk}^{-12}(1-3\cos^2\theta_{jk})^4 \tag{6.27}$$

Here f_e is the concentration of substitutional ions not coupled by the exchange interaction, r_e is the effective range of the exchange interaction and $z(r_e)$ is the number of cationic sites included in a sphere of radius r_e.

For powdered samples, the powers of the direction cosines in equations 6.26 and 6.27 can be replaced by their averages over a sphere ($\overline{(1-3\cos^2\theta_{jk})^2} = 4/5$ and $\overline{(1-3\cos^2\theta_{jk})^4} = 48/35$). The peak-to-peak linewidth and the cut off fields are then given by:

$$\Delta H_{pp} = C_1 A(S) \tag{6.28}$$

$$\left|H_c - H_o\right| = C_2 B(S) \tag{6.29}$$

where

$$C_1 = (\pi\sqrt{7}/15) f_e [S_1(r_e)]^{3/2} [S_2(r_e)]^{-\frac{1}{2}} \quad (6.30)$$

$$C_2 = (3\sqrt{21}/7) [S_2(r_e)/S_1(r_e)]^{\frac{1}{2}} \quad (6.31)$$

$$S_1(r_e) = a^6 \sum_{r_{jk}>r_e} r_{jk}^{-6} \quad (6.32)$$

$$S_2(r_e) = a^{12} \sum_{r_{jk}>r_e} r_{jk}^{-12} \quad (6.33)$$

The values of the coefficients C_1 and C_2 are independent of the parameters of the paramagnetic ion and the host lattice. C_1 is a function of the total concentration of the paramagnetic ion, the range of the exchange interaction and the lattice geometry. C_2 depends only on the lattice geometry and the range of the exchange interaction.

To apply de Biasi and Fernandes' theory to impurity ions distributed in magnesium oxide powders we need to compute the values of C_1 and C_2 for an FCC lattice. C_1 and C_2 are readily determined once the values of the summations $S_1(r_e)$ and $S_2(r_e)$ defined by equations 6.32 and 6.33 are known. As the convergence of these summations is relatively slow, their evaluation becomes much easier if they are written in the form:

$$S_1(r_e) = a^6 \left[S_1(\infty) - \sum_{r_{jk}<r_e} r_{jk}^{-6} \right] \quad (6.34)$$

$$S_2(\ r_e) = a^{12}\left[S_2(\infty) - \sum_{r_{jk}<r_e} r_{jk}^{-12}\right] \qquad (6.35)$$

The values of $S_1(\infty) = \sum r_{jk}^{-6}$ & $S_2(\infty) = \sum r_{jk}^{-12}$ for an F.C.C. lattice are given in the literature[6.16]. If we assume that the paramagnetic ions occupy cationic sites in the host lattice then the radius vectors, r_{jk}, may be determined using simple trigonometry. Hence the sums

$$\sum_{r_{jk}<r_e} r_{jk}^{-6} \quad \& \quad \sum_{r_{jk}<r_e} r_{jk}^{-12}$$

are readily calculated for different values of r_e and the results of such calculations for a general F.C.C. lattice are shown in Table 6.2, where n is the number of the order of each coordination (n = 1 includes no neighbouring sites, n = 2 the nearest neighbour sites and so on), $r = r_{jk}/a$ is the radius of the corresponding sphere and N is the number of cationic sites on the surface of the n^{th} coordination sphere. The summations $S_1(\ r_e)$ and $S_2(\ r_e)$ are thus truncated at the surface of a particular coordination sphere, depending on the range of the exchange interaction.

The values of C_1 and C_2 computed with the aid of Table 6.2 and equations 6.25, 6.30 and 6.31 are shown in Figure 6.1 and Table 6.3 respectively. The concentration dependence of C_1, illustrated in Figure 6.1 for ten different ranges of the exchange interaction, shows that,

n	r	N	Nr^{-6}	Nr^{-12}	$S_1(r_e)$	$S_2(r_e)$
2	$\sqrt{2}/2$	12	96.000	768.000	19.631	8.440
3	$\sqrt{3}/2$	6	6.000	6.000	13.631	2.440
4	1	24	7.104	2.102	6.527	0.338
5	$\sqrt{2}$	12	1.500	0.187	5.027	0.151
6	$\sqrt{10}/2$	24	1.536	0.098	3.491	0.053
7	$\sqrt{3}$	8	0.296	0.011	3.195	0.042
8	$\sqrt{14}/2$	48	1.104	0.024	2.091	0.018
9	2	6	0.096	0.002	1.995	0.016
10	$3\sqrt{2}/2$	36	0.396	0.004	1.599	0.012

Table 6.2 Calculated Values of $S_1(r_e)$ and $S_2(r_e)$ for the F.C.C. lattice.

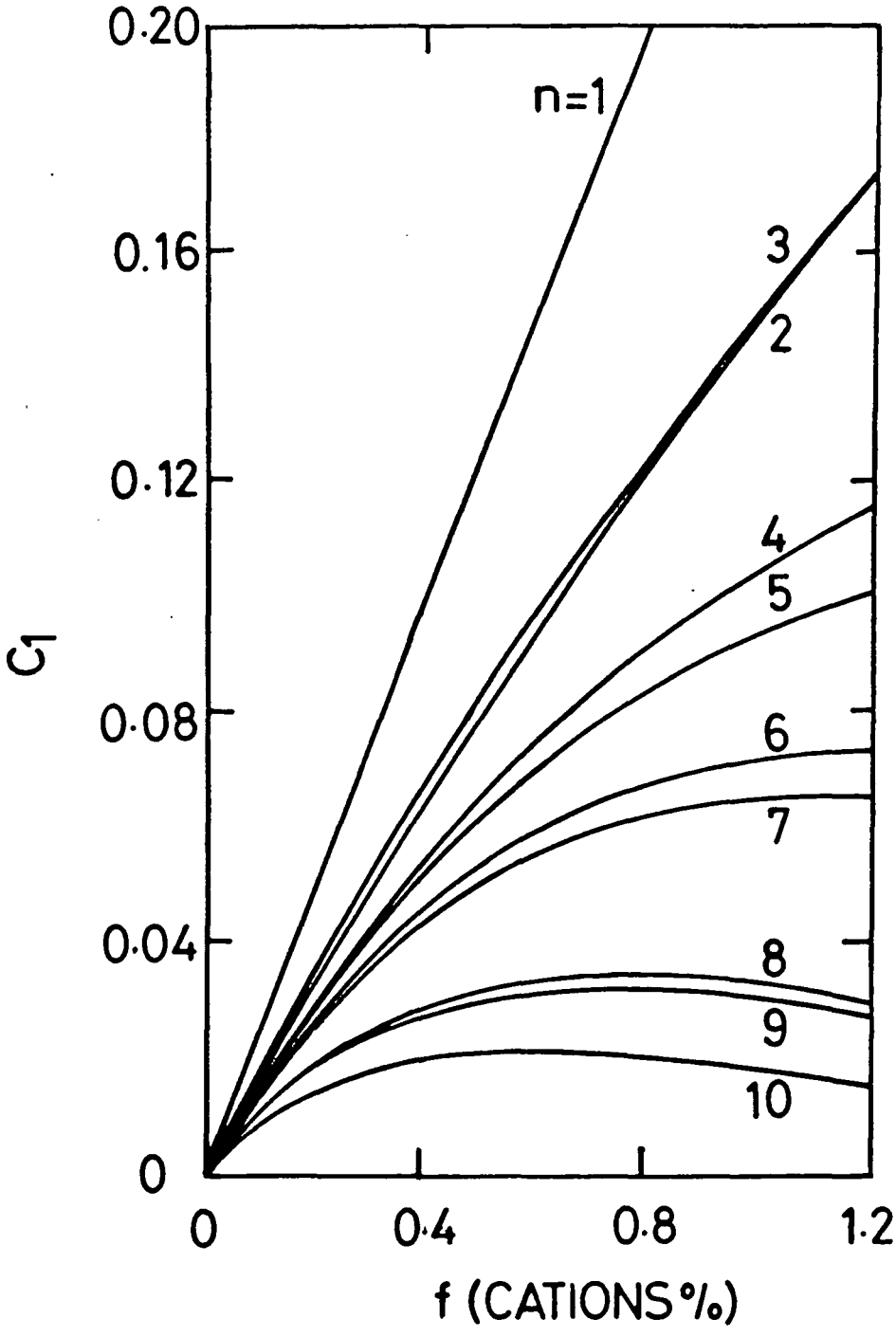

FIGURE 6.1 CONCENTRATION DEPENDENCE OF THE LINEWIDTH COEFFICIENT C_1 FOR A FACE-CENTRED CUBIC LATTICE AND SEVERAL RANGES OF THE EXCHANGE INTERACTION.

n	C_2	$z(r_e)$
1	5.089	0
2	1.288	12
3	0.831	18
4	0.447	42
5	0.340	54
6	0.242	78
7	0.225	86
8	0.182	134
9	0.176	140
10	0.172	176

Table 6.3 Calculated values of C_2 and $z(r_e)$ for the F.C.C. lattice.

for the same impurity concentration, the value of C_1, and hence the linewidth, tends to decrease as the range of the exchange interaction is increased. Table 6.3 demonstrates that the coefficient C_2, and thus the value of $|H_c - H_0|$, decreases as the range of the exchange interaction is increased.

If clustering effects are important the model can still be used provided that the equation:

$$f_e = f(1 - pf)^{Z(r_e)} \qquad (6.36)$$

is used in place of equation 6.25[6.17] (p is known as the "clustering factor" and is defined as the ratio of the actual probability that a neighbouring cationic site is occupied to the probability of occupation if the distribution were random).

In Chapters Seven to Nine the experimental variation of E.P.R. linewidth with concentration for Cr^{3+}, Mn^{2+} and Fe^{3+} in magnesium oxide will be interpreted in terms of de Biasi and Fernandes' model. The major steps in the analysis are:

i) The theoretical dependence of the peak-to-peak linewidth upon dopant concentration for various values of n is calculated from equation 6.28. To carry out this calculation C_1 and A(S) must be evaluated. A(S) is a numerical constant which simply depends upon the parameters characterizing the dopant ion and is given by equation 6.23. C_1 may be determined for various values of n and at a number of different dopant concentrations with the aid of Tables 6.2

and 6.3 and equations 6.25 and 6.30.

ii) A graph of experimental peak-to-peak linewidth against concentration is then constructed which is compared with the theoretical curves obtained in (i) to determine n.

iii) Finally the values of r_e and C_2 corresponding to n are obtained from Tables 6.2 and 6.3 (r_e characterizes the exchange forces in the material and C_2 gives the cut-off fields of the E.P.R. line which, according to theory, has a truncated Lorentzian shape).

To develop his dipolar broadening theory, Van Vleck[6.6] assumed that there is no hyperfine interaction or zero-field splitting of the spin energy levels. Unfortunately, these assumptions also restrict the range of application of the theory. As Kittel and Abrahams'[6.8] and de Biasi and Fernandes'[6.11] models are both based on Van Vlecks' original theory the same restrictions apply i.e. their theories only hold for ions with $S = \frac{1}{2}$ in any symmetry or for ions with $S<2$ in cubic symmetry. On the other hand, Pryce and Stevens[6.18] demonstrated that Van Vlecks' dipolar broadening theory (and therefore we may assume Kittel and Abrahams' and de Biasi and Fernandes' models) can be applied in the presence of hyperfine interactions to each of the lines of the hyperfine structure, provided that the hyperfine splitting is larger than the linewidth of the individual lines.

Hence de Biasi and Fernandes' model is directly applicable to Cr^{3+} ions in magnesium oxide and we shall assume that it may also be applied to the $M = \frac{1}{2} \longleftrightarrow -\frac{1}{2}$ transitions of Mn^{2+} and Fe^{3+} in magnesium oxide because the splitting of the spin energy levels of these ions is

small and the $M = \frac{1}{2} \leftrightarrow -\frac{1}{2}$ transition is free, to first order, of strain broadening (see section 6.3). In addition, the hyperfine splitting of the Mn^{2+} ion conforms to the condition governing the use of dipolar broadening theory in the presence of hyperfine interactions laid down by Pryce and Stevens.

6.3 STRAIN BROADENING

In real crystals lattice distortions are always present. They may arise from a variety of causes including strain, such as that created when the impurity ion and the cation of the host lattice differ in size, point defects, such as vacancies and interstitial ions, planar defects such as stacking faults and dislocations. The combined effect of all types of crystal imperfections is to create a strain field, the magnitude of which at a particular point in the crystal is determined by the distribution of defects throughout the crystal. The strain field may either change the point symmetry at the paramagnetic ion or preserve the point symmetry but change the crystal field parameters slightly. Any change in the symmetry of the site occupied by a paramagnetic ion will dramatically alter its E.P.R. spectrum and this effect of strain will not be considered in this section.

If the strain field causes a change in the values of the crystal field parameters for an individual paramagnetic ion then the resonant field of that ion will also be altered. As the amount of strain to which individual paramagnetic ions are subjected is variable, the resonant fields of the assembly of ions will be distributed over a

range of values and hence the absorption lines will be broadened, although the overall form of the spectrum will remain unaltered. A theoretical model which allows us to quantify the broadening caused by this mechanism will now be discussed.

In cubic crystals, the components of the stress tensor are related to the tensor D (which represents the effect of deformations of the system on the Spin Hamiltonian) by two independent constants of proportionality, C_{11} and C_{44}, known as stress coefficients. If the stresses are due to crystal imperfections, let us assume that the probability of the components of the stress tensor related to D by the constant C_{11} taking on a particular value is given by a Gaussian curve of full width at half height 2.35α and that the probability of the components of the stress tensor related to D by the constant C_{44} taking on a particular value is given by a Gaussian curve of full width at half height 2.35γ . If it is also assumed that the components of the stress tensor at different paramagnetic sites in the crystal are uncorrelated then it may be shown that the increase in the second moment due to strain broadening, $<\delta H^2>$, is given by:[6.19]

$$<\delta H^2>_{M\rightarrow M-1} = (2M-1)^2.3/4 \left\{ (3/2C_{11})^2(\alpha/2)^2(1-3F) + \ldots \right.$$

(6.37)

$$\left. \ldots + C_{44}{}^2\,\gamma^2 3F \right\} \left[h^2c^2/g^2\beta^2 \right]$$

where $F = (\sin^2\theta\cos^2\theta + \sin^2\phi\cos^2\phi\sin^4\theta)$

α and γ characterize the distribution of internal stresses in the crystal and their values are obviously sample dependent, as the internal stresses in a sample will depend upon its history. The angular dependence of equation 6.37 allows us to determine the amount of strain broadening for the most important high symmetry directions in the crystal. Thus,

$$\text{if } H//\langle 100\rangle \text{ then } \langle \delta H^2\rangle = (2M-1)^2(27/8)\,\alpha^2 C_{11}^2\left[h^2c^2/g^2\beta^2\right] \quad \ldots. \quad (6.38a)$$

$$\text{if } H//\langle 111\rangle \text{ then } \langle \delta H^2\rangle = (2M-1)^2 3\,\gamma^2 C_{44}^2\left[h^2c^2/g^2\beta^2\right] \quad \ldots. \quad (6.38b)$$

$$\text{if } H//\langle 110\rangle \text{ then } \langle \delta H^2\rangle = (2M-1)^2.3.\left\{(9/32)\,\alpha^2 C_{11}^2 + \ldots \right. \quad (6.38c)$$

$$\left. \ldots + 3/4\,\gamma^2 C_{44}^2\right\}\left[h^2c^2/g^2\beta^2\right]$$

Let us assume that the observed linewidth, ΔH_{obs}, contains a component due to random internal stresses, ΔH_s, and a component which would be present in the absence of such stresses, ΔH_i. ΔH_i includes the contributions to line broadening from all sources other than strain broadening and will be referred to as the intrinsic linewidth. As the

E.P.R. lines of the doped magnesium oxide samples examined in this work were found to be Lorentzian in shape we may assume that the total linewidth is given by the sum of the individual components of the linewidth so that:

$$\Delta H_{obs} = \Delta H_i + \Delta H_s \qquad (6.39)$$

As ΔH_{obs} was measured experimentally as a peak-to-peak linewidth, ΔH_i and ΔH_s in equation 6.39 must also represent peak-to-peak linewidths. Therefore, if the applied magnetic field is parallel to one of the cubic axes, ΔH_s is given by the peak-to-peak linewidth corresponding to the second moment of equation 6.38a, i.e.:

$$\Delta H_s = \frac{\pi \langle \delta H^2 \rangle}{\sqrt{3}\,|H_c - H_o|} = \frac{\pi (2M-1)^2}{\sqrt{3}\,|H_c - H_o|} \left[\frac{27}{8}\right] \alpha^2 C_{11}^2 \left[\frac{h^2 c^2}{g^2 \beta^2}\right] \qquad (6.40)$$

This expression applies for any impurity ion and thus if $H \,//\, \langle 100 \rangle$ the observed linewidth for the $M = \frac{1}{2} \longleftrightarrow -\frac{1}{2}$ transition is given by:

$$\Delta H_{obs} = \Delta H_i \qquad (6.41a)$$

while for the $M = \pm\, ^3/_2 \leftrightarrow \pm\, ^1/_2$ transitions:

$$\Delta H_{obs} = \Delta H_i + \frac{27\pi}{2\sqrt{3}\,|H_c - H_o|}\,\alpha^2 C_{11}^2\left[\frac{h^2c^2}{g^2\beta^2}\right] = \Delta H_i + \Delta H_s' \qquad (6.41b)$$

and for the $M = \pm 5/2 \longleftrightarrow \pm 3/2$ transitions:

$$\Delta H_{obs} = \Delta H_i + \frac{54\pi}{\sqrt{3}\,|H_c - H_o|}\,\alpha^2 C_{11}^2\left[\frac{h^2c^2}{g^2\beta^2}\right] = \Delta H_i + 4\Delta H_s' \qquad (6.41c)$$

where $\Delta H_s' = \frac{27\pi}{2\sqrt{3}|H_c - H_o|}\,\alpha^2 C_{11}^2\left[\frac{h^2c^2}{g^2\beta^2}\right]$

If spin-spin interactions are the major source of the intrinsic broadening, ΔH_i, then the cut-off fields of the Lorentzian curve, $|H_c - H_o|$, may be determined using the method developed by de Biasi and Fernandes[6.11], which was described in the previous section. C_{11} is given in the literature[6.19] and hence the parameter α, characterizing the stresses in the sample, may be determined from the observed linewidths with the aid of equations 6.41a to c.

The most important prediction of the theory outlined above is that the strain broadening for a given transition is proportional to $(2M-1)^2$ where M is the quantum label of the transition. Hence, for any given impurity ion, to first order the $M = \frac{1}{2} \longleftrightarrow -\frac{1}{2}$ transition is not broadened by strain whereas the broadening observed for the $M = \pm 3/2 \longleftrightarrow \pm 1/2$ transitions is one quarter of that observed for the $M = \pm 5/2 \longleftrightarrow \pm 3/2$ transitions.

6.4 SPIN-LATTICE RELAXATION

Spin-Lattice relaxation processes are caused by interactions between paramagnetic impurity ions and lattice vibrations (phonons). These interactions transfer the energy absorbed during resonance to the lattice in order to reestablish the thermal equilibrium populations of the spin energy levels.

If two spin levels j and k have energies E_j and E_k and populations at thermal equilibrium of N^o_j and N^o_k particles per unit volume, then, assuming Boltzmann statistics, we may write:

$$\frac{N^o_k}{N^o_j} = \exp\left[\frac{-(E_k-E_j)}{kT}\right] \tag{6.42}$$

If the probability of a transition being induced from level j to level k by lattice vibrations is P_{jk} then under thermal equilibrium conditions:

$$N^o_k P_{kj} = N^o_j P_{jk} \tag{6.43}$$

With the aid of equation 6.42 it can be shown that this relationship may assume the form:

$$P_{jk} = P_{kj} \exp\left[\frac{-(E_k - E_j)}{kT}\right] \qquad (6.44)$$

If $E_k > E_j$ then $P_{kj} > P_{jk}$, so that lattice vibrations induce more transitions from upper levels to lower levels than from lower levels to upper levels. Thus during paramagnetic resonance the oscillating R.F. field stimulates transitions mainly from lower to higher energy levels whereas lattice vibrations give rise to transitions mainly in the opposite direction; the overall effect is to convert the R.F. energy into heat.

Because there are transitions continually taking place between the spin levels due to the action of lattice vibrations the lifetimes of the paramagnetic ions in these levels are shortened. This causes broadening of the spin levels and consequently the E.P.R. lines will also be broadened. The linewidth due to spin-lattice relaxation processes of the E.P.R. line related to the pair of spin levels E_j and E_k is given by:

$$2\pi\Delta\nu = \sum_{m \neq j} P_{jm} + \sum_{n \neq k} P_{kn} = {}^{1}/T_1 \qquad (6.45)$$

Thus the spin-lattice broadening, $\Delta\nu$, can be used to determine the spin-lattice relaxation time, T_1, which is defined as the time taken for an excess of energy given to

the spins to fall to $^1/e$ or 0.368 of its initial value.

The most effective spin-phonon coupling is achieved when the crystal field is modulated through motion of the electrically charged ions under the action of the lattice vibrations.[6.20,6.21] Transitions between the spin levels may occur via three main relaxation processes and the transition probabilities P_{jm} and P_{kn} for each relaxation process under the influence of the spin-phonon coupling mechanism mentioned were calculated by Van Vleck[6.22] and Orbach.[6.23] The probabilities P_{jm} and P_{kn} for each spin-lattice relaxation process are temperature dependent and theory predicts that the combined influence of all three relaxation processes will cause T_1 to vary with temperature in the following manner:[6.22,6.23]

$$^1/T_1 = AT + BT^n + C \exp(-E/kT) \qquad (6.46)$$

Here A,B and C are constants and T is the absolute temperature.

The first term in equation 6.46 represents the sum of the probabilities P_{jm} and P_{kn} for the so called "direct process". This involves the exchange of a phonon between the relaxing spin and the lattice vibration modes, the phonon having an energy equal to the difference in energy between the levels involved in the spin-relaxation transition.

The probability for Raman relaxation transitions varies with temperature according to the second term in

equation 6.46. In the Raman process the relaxing spin interacts with two phonons. There are two possible routes by which this type of relaxation may proceed. Firstly, the transition between the spin levels E_k and E_j may be accompanied by the creation of two phonons with energies $h\nu_1$ and $h\nu_2$ which obey the condition $E_k - E_j = h\nu_1 + h\nu_2$. Secondly, the spin may relax by the process of Raman scattering which involves the virtual absorption of a phonon of energy $h\nu_1$ and the emission of a phonon of energy $h\nu_2$. The difference in energy between the phonons is equal to the change in energy of the relaxing spin i.e. $E_k - E_j = h\nu_2 - h\nu_1$. However, the number of pairs of phonons for which $h\nu_1 + h\nu_2 = E_k - E_j$ is negligible compared with those for which $h\nu_2 - h\nu_1 = E_k - E_j$ so that only the Raman scattering mechanism need be considered (the process involving the creation of two phonons will be disregarded in the rest of this section).

The Raman scattering mechanism is a two phonon process which is much less probable than a one phonon process (such as the direct process). On the other hand, the probability of Raman scattering is increased compared to that of direct phonon emission by the fact that in the direct process only phonons of energy $E_k - E_j$ can take part and these are very few in number, whereas phonons of many energies can take part in the two phonon Raman scattering process (provided that the combined values of $h\nu_1$ and $h\nu_2$ satisfy the condition $E_k - E_j = h\nu_2 - h\nu_1$). The overall effect of these two competing factors is that the constant A (related to the direct process) is greater than the constant B (related to the Raman scattering process)

but not by many orders of magnitude ($B \sim 10^{-6}A$). When the temperature dependences of the probabilities for both relaxation processes are taken into account (the probability of Raman-type relaxation increases according to a T^5 or T^7 or T^9 law depending upon the type of energy level system possessed by the paramagnetic species being investigated [6.1]) it can be seen that the direct process will tend to dominate at low temperatures so that $^1/T_1 \alpha T$ whereas at higher temperatures the Raman scattering process will tend to dominate so that $^1/T_1 \alpha T^n$ (where n=5, 7 or 9). A change in the dominant relaxation mechanism at a certain temperature has been observed in many materials.

The third term in equation 6.46 represents the probability of the Orbach process. This involves the relaxing spin absorbing a phonon by a direct process to excite it to a much higher level. The spin then relaxes to a lower spin energy level by emitting a phonon of slightly higher energy. The overall change is to transfer the spin to a lower energy level. This relaxation mechanism can only occur if there is another energy level at $E < k\theta_D$ (where θ_D is the Debye temperature) so that phonons are available to cause the initial transition.

The Raman scattering mechanism takes place via a virtual intermediate level which can take on any value of energy and hence phonons of many different energies may be involved in the relaxation process. In contrast, the phonons which may contribute to the Orbach process are restricted to those located in a narrow band of energy at $h\nu = E$ and therefore the Orbach process is much less probable than Raman scattering of phonons. However, should

the Orbach relaxation mechanism dominate in a particular temperature range then $^1/T_1$ will increase exponentially as the temperature increases.

The measured linewidths of the E.P.R. spectral lines of Cr^{3+}[6.14], Fe^{3+}[6.13] and Mn^{2+}[6.24] in MgO are independent of temperature over the range 77K to 300K. This experimental data provides qualitative evidence that there is no substantial contribution to the linewidth from spin-lattice relaxation processes in these crystals since equations 6.45 and 6.46 show that the linewidth would be heavily dependent upon temperature if the major part of it were attributable to spin-lattice broadening.

For the Fe^{3+} ion, quantitative evidence which supports the qualitative evidence already discussed is provided by a study of the temperature dependence of the spin-lattice relaxation time of Fe^{3+} in MgO carried out in this Department.[6.25] It was found that at temperatures below 25K the direct spin-lattice relaxation mechanism dominates and $^1/T_1 \alpha T$. Above 25K a Raman-type relaxation mechanism dominates and $^1/T_1$ varies with temperature according to a T^7 law. Vasquez's[6.25] data only covers the temperature range 4.2K to 35K but if we assume that the Raman relaxation mechanism will continue to dominate at higher temperatures, then extrapolation of the data to the temperature of the experiments conducted in this work (293K) shows that $T_1 = 3.35 \times 10^{-7}$ seconds.

Equation 6.45 may be written as:

$$\Delta H = \frac{h}{2\pi g \beta T_1} \qquad (6.47)$$

where ΔH is the spin-lattice broadening in magnetic field units. Theory predicts that lines broadened by spin-lattice relaxation processes will be Lorentzian in shape[6.1,6.26] (as indeed the experimental lines of Fe^{3+} in MgO are) and thus the spin-lattice contribution to the peak-to-peak linewidth is given by:

$$\Delta H_{pp}(\text{spin-lattice}) = \frac{h}{2\sqrt{3}\,\pi\, g\,\beta\, T_1} \qquad (6.48)$$

since $\Delta H_{pp}(\text{spin-lattice}) = \Delta H/\sqrt{3}$.

Substituting $T_1 = 3.35\times10^{-7}$ seconds we find that at 293K $\Delta H_{pp}(\text{spin-lattice}) = 9.8\times10^{-3}$mT and since the total peak-to-peak linewidth of Fe^{3+} in MgO at this temperature is $\sim$ 1mT, the spin-lattice contribution is negligible ($\sim$1%). Although appropriate T_1 data could not be found in the literature to show quantitatively that there is no substantial contribution to the linewidth from spin-lattice relaxation processes for the Cr^{3+} and Mn^{2+} ions in MgO, the qualitative evidence is sufficient to conclude that this is the case. Therefore, spin-lattice broadening mechanisms will not be considered when the linewidth data for all three ions is discussed in Chapters Seven to Nine.

6.5 INSTRUMENTAL BROADENING AND LINESHAPE DISTORTION.

There are four common instrumental effects which may lead to distortion of the E.P.R. lineshape and a corresponding increase in linewidth if care is not taken setting up the spectrometer. The first is known as "saturation broadening." This occurs when the microwave power incident on the sample is too high, which causes the populations of the upper and lower states between which transitions are induced to approach each other. The incident radiation is then able to stimulate almost as many emissive transitions as absorptive ones which leads to a reduction in the amplitude of the absorption line and an increase in its width. It is necessary to use a power level well below that needed to saturate the system in order to observe an unbroadened and undistorted lineshape.

The second source of instrumental distortion is "modulation broadening" which will occur if the amplitude of the modulation field is of a comparable size to the width of the absorption line. Modulation broadening diminishes the amplitude, distorts the lineshape and increases the linewidth of the true E.P.R. signal. It may be avoided by keeping the amplitude of the modulation field, H_{mod}, well below the natural width of the line, ΔH. However, the intensity of the line increases with H_{mod} if its amplitude is below the level at which broadening occurs and so a practical condition which will maximise the intensity of the line while avoiding distortion is:

$$H_{mod} \leqslant \Delta H/5 \qquad (6.49)$$

The third common error which causes E.P.R. line distortion is scanning the line too quickly. Distortion arises because the rate of change of the E.P.R. absorption is faster than the time constant of the instrument. In other words, the spectrometer is unable to follow the rapid changes in absorption faithfully as the line is scanned.

Finally, a fourth source of E.P.R. line distortion may be avoided if the modulation field frequency, f_{mod}, is less than the linewidth, ΔH, expressed in frequency units i.e. if

$$f_{mod} < \frac{g\beta}{h} \Delta H \qquad (6.50)$$

Thus, for the 100kHz modulating field used by the Varian V4502-15 spectrometer, lines with widths as small as 0.01mT may be recorded without distortion.

Figure 6.2 illustrates an undistorted E.P.R. line and also how this line is affected by the various types of instrumental distortion described in this section. Since every precaution was taken to avoid the effects outlined above when the spectra described in Chapters Seven to Nine were recorded, instrumental distortion of E.P.R. lines will be disregarded when the factors influencing the lineshapes and linewidths of these spectra are considered.

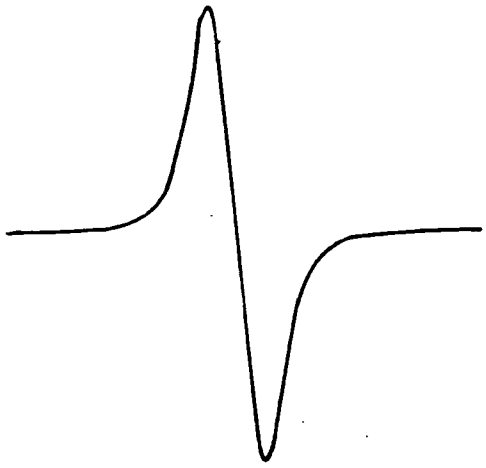

a

a) undistorted line

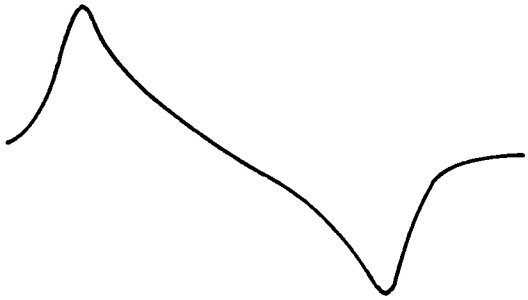

b

b) modulation distortion

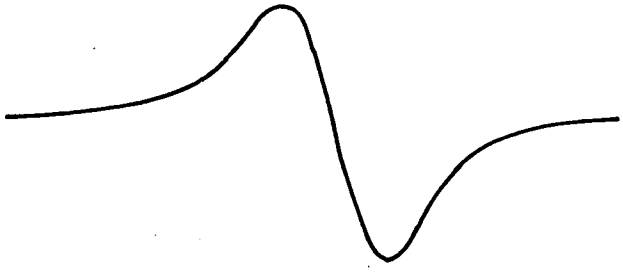

c

c) saturation broadening

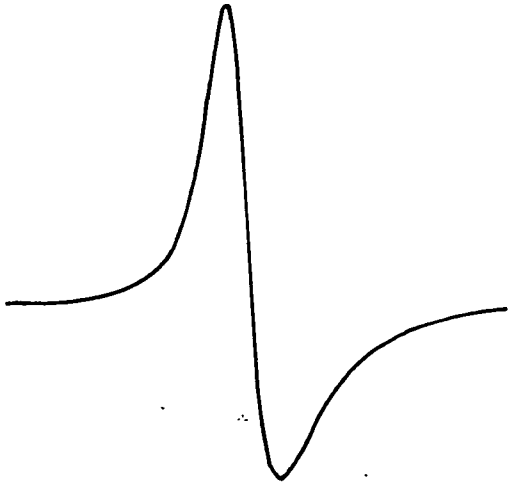

d

d) scan rate too high

FIGURE 6.2 THE EFFECT OF SEVERAL COMMON TYPES OF INSTRUMENTAL DISTORTION UPON THE TRUE E.P.R. LINESHAPE.

REFERENCES

6.1 A. Abragam and B. Bleaney "Electron Paramagnetic Resonance of Transition Ions" Clarendon Press, Oxford (1970).

6.2 C.P. Poole and H.A. Farach "Relaxation in Magnetic Resonance" Academic Press, N.Y. (1971).

6.3 S.A. Al'tshuler and B.M. Kozyrev "Electron Paramagnetic Resonance in Compounds of Transition Elements" 2nd Ed., 1974. (U.K. Distributors, J. Wiley and Sons, Chichester).

6.4 An Elementary Discussion of Theory and Experiments in Electron Paramagnetic Resonance" by Members of the Scientific Staff of Alpha Scientific Laboratories, Berkeley, California.

6.5 P.W. Anderson Phys. Rev. 79, 350 (1950).

6.6 J.H. Van Vleck Phys. Rev. 74, 1168 (1948).

6.7 P.W. Anderson and P.R. Weiss Rev. Modern Phys. 25, 269 (1953).

6.8 C. Kittel and E. Abrahams Phys. Rev. 90, 238 (1953)

6.9 W.J.C. Grant and M.W.P. Strandberg Phys. Rev. 135, A715 (1964).

6.10 B.I. Kochelaev, R. Kh. Sabirov and G.G. Khaliullin Sov. Phys. Solid State 19, 86 (1977).

6.11 R.S. de Biasi and A.A.R. Fernandes J. Phys. C. 16, 5481 (1983).

6.12 J.H. Van Vleck Nuovo Cimento Supp. 6, 993 (1956).

6.13 J.S. Thorp, R.A. Vasquez, C. Adcock and W. Hutton J. Mat. Sci. 11, 89 (1976)

6.14 J.S. Thorp, M.D. Hossain, L.J.C. Bluck J. Mat. Sci. 14, 2853 (1979).

6.15 J.S. Thorp, M.D. Hossain, L.J.C. Bluck, T.G. Bushell J. Mat. Sci. 15, 903 (1980).

6.16 J.E. Jones and A.E. Ingham Proc. Roy. Soc. A107, 636 (1925).

6.17 R.S. de Biasi Magn. Lett 1, 103 (1978).

6.18 M.H.L. Pryce and K.W.H. Stevens Proc. Phys. Soc. 63, 36 (1950).

6.19 E.R. Feher Phys. Rev. 136, A 145 (1964).

6.20 W. Heitler and E. Teller Proc. Roy. Soc. A155, 629 (1936).

6.21 R.L. Kronig Physica 6, 33 (1939).

6.22 J.H. Van Vleck Phys. Rev. 57, 426 (1940)

6.23 R. Orbach Proc. Roy. Soc. A264, 458, 485 (1961).

6.24 M.D. Hossain, J.S. Thorp and A.D. Inglis "E.S.R. Linewidths in Mn^{2+}/MgO" (unpublished).

6.25 R.A. Vasquez "Magnetic Resonance in Iron-Doped Magnesium Oxide" M.Sc. Thesis, Durham University, (1975), Unpublished.

6.26 C.P. Poole and H.A. Farach "The Theory of Magnetic Resonance" Wiley-Interscience, N.Y. (1972).

CHAPTER SEVEN

E.P.R. AND RHEED INVESTIGATIONS OF CHROMIUM DOPED MAGNESIUM OXIDE SINGLE CRYSTALS AND POWDERS: EVIDENCE FOR LATTICE STRAIN AND SPINEL ($MgCr_2O_4$) FORMATION

7.1 EXPERIMENTAL RESULTS FOR MgO:Cr SINGLE CRYSTALS

7.1.1 CHARACTERISATION OF THE SAMPLES

a) E.P.R. SPECTRA

The E.P.R. spectra of the MgO:Cr single crystals were recorded on the Varian V4205-15 spectrometer at room temperature with the magnetic field parallel to one of the cubic axes. In all, five different samples were examined, in which the nominal concentration of the chromium dopant ranged from 800 p.p.m. to 15,100 p.p.m. by weight (see Table 7.1 for the complete list of nominal chromium concentrations).

A typical recording of the most intense group of spectral lines found in each of the specimens examined is shown in Figure 7.1 (the particular spectrum illustrated here was obtained from a sample with a nominal chromium concentration of 800 p.p.m. by weight). The spectrum shown in Figure 7.1 consists of a single, intense line with a g-factor of approximately 1.9800 and four less intense lines which are centred on the main line and are equally spaced, successive components being separated by approximately 1.8 mT. The intensity of each line of the quartet is about one fortieth of that of the main line.

This spectrum is well known and is due to Cr^{3+} ions occupying sites of octahedral symmetry. It was first

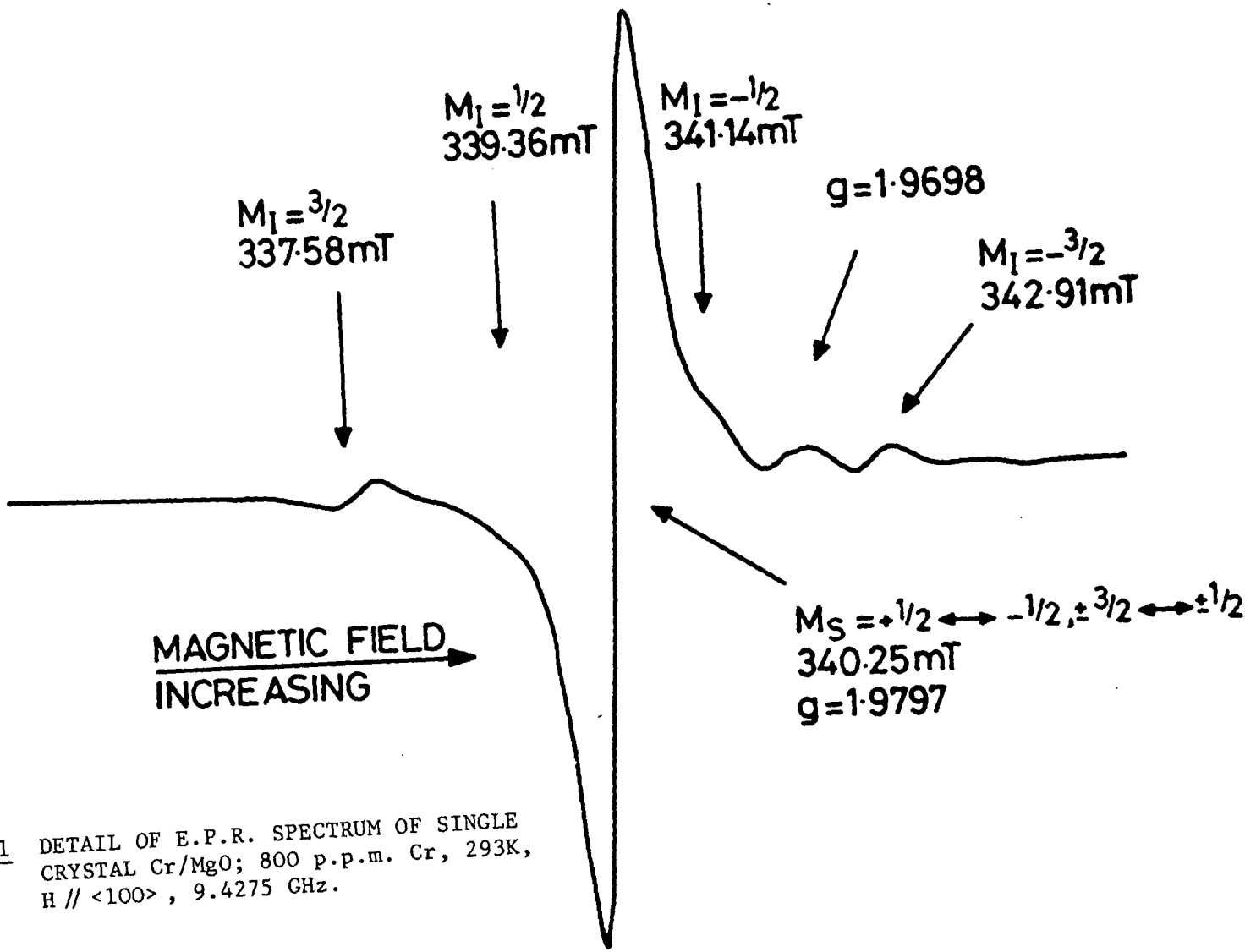

FIGURE 7.1 DETAIL OF E.P.R. SPECTRUM OF SINGLE CRYSTAL Cr/MgO; 800 p.p.m. Cr, 293K, H // <100> , 9.4275 GHz.

reported by Low[7.1] and his analysis, which has been described in detail in section 4.5, is appropriate. Figure 7.1 also shows a line at g = 1.9698. This line was only observed for the sample containing 800 p.p.m. by weight of chromium and the paramagnetic centre responsible for it was not identified.

The intense central line arises from the M = +3/2$\longleftrightarrow$+1/2, M = +1/2$\longleftrightarrow$-1/2 and M = -1/2$\longleftrightarrow$-3/2 transitions of the isotopes of chromium with no nuclear spin (Cr^{50}, Cr^{52} and Cr^{54}) which are coincident (i.e. they occur at the same value of magnetic field) because the four electronic energy levels of these isotopes are equally spaced and, in strong magnetic fields, diverge linearly as the applied magnetic field increases.

The four less intense lines are hyperfine transitions due to the only other naturally occuring isotope of chromium, Cr^{53}, which has a nuclear spin, I, of 3/2. The experimentally observed relationship between the hyperfine lines (i.e. that they are equally spaced and centred upon the single line at g $\sim$ 1.9800) is accurately predicted by equation 4.22. In addition, from this equation it may be deduced that the separation between successive hyperfine lines is equal to A, the hyperfine structure constant. The natural abundance of the Cr^{53} isotope is 9.55% and since all four hyperfine lines are equally intense, each hyperfine line is expected to have an intensity of about 1/42 of that of the main line. The observed intensity ratio of 1/40 is in close agreement with this prediction.

The parameters characterizing the E.P.R. spectrum of

the Cr^{3+} ions in sites of octahedral symmetry (the g-factor, the peak-to-peak linewidth of the central line and A, the hyperfine structure constant identified with the hyperfine transitions of the Cr^{53} isotope) were measured for each of the chromium doped magnesium oxide single crystals and the values obtained are given in Table 7.1 together with the microwave frequencies at which the measurements were taken. The g-factors and hyperfine structure constants listed in Table 7.1 are in close agreement with each other and also with previously published data[7.1-7.3]. The variation of the linewidth of the central line in the spectrum with chromium concentration will be discussed in section 7.1.2. For the sample containing 9,500 p.p.m. by weight of chromium the hyperfine structure constant could not be measured because the hyperfine lines were obscured by the high level of background noise.

The Cr^{3+} ions giving rise to the E.P.R. spectrum described occupy sites of octahedral symmetry and it is likely that they substitute for Mg^{2+} ions in the magnesium oxide host lattice. In addition, the spectrum described is characteristic of Cr^{3+} ions that are isolated from each other which implies that the Cr^{3+} ions are not clustered together and do not co-operate magnetically (in contrast, for example, to ions that are exchange coupled which do co-operate in such a way that their spins become partially or fully aligned and the ions so coupled together act as a single unit). The only interactions taking place between the isolated Cr^{3+} ions are dipolar in nature.

The angular variation of the cubic Cr^{3+} spectrum was investigated for the sample containing 800 p.p.m. of

CHROMIUM CONCENTRATION (p.p.m.)	LINEWIDTH ΔHpp (mT)	g-FACTOR	HYPERFINE STRUCTURE CONSTANT A($\times 10^{-4}$ cm^{-1})	FREQUENCY (GHz)
800	0.506	1.9797	16.44	9.4275
3600	0.921	1.9799	16.61	9.4295
7400	0.645	1.9794	16.68	9.4290
9500	0.493	1.9794	-	9.4285
15100	0.564	1.9806	16.48	9.4280

TABLE 7.1 E.P.R. PARAMETERS FOR SINGLE CRYSTAL Cr/MgO SAMPLES: H// <100>, 293K.

chromium. Our measurements were restricted to one dopant concentration because it was assumed that the general characteristics displayed by the angular variation of the spectrum at one particular dopant concentration would be common to all the samples, whatever the dopant concentration. This is a reasonable assumption to make, since the Cr^{3+} centre responsible for the spectrum should have identical properties in each of the five chromium doped magnesium oxide samples examined.

E.P.R. spectra were recorded at 10^{o} intervals as the crystal doped with 800 p.p.m. of chromium was rotated in a [100] plane. An additional spectrum was recorded when the crystal had been rotated through 45^{o} as at this point the magnetic field was parallel to a <110> type direction in the crystal. Figure 7.2 shows the variation of the resonant magnetic fields of three transitions of the cubic Cr^{3+} spectrum with polar angle θ_H (which is the angle between the <100> type direction with which the magnetic field is initially aligned and the magnetic field). The three transitions in question are the central one (which arises from the superimposed $M = +1/2 \leftrightarrow -1/2$ and $M = \pm 3/2 \leftrightarrow \pm 1/2$ transitions of the isotopes of chromium with no nuclear spin) and the two outermost hyperfine transitions ($M_I = +3/2$ and $M_I = -3/2$) of the Cr^{53} isotope. The resonant magnetic fields of the inner hyperfine transitions ($M_I = +1/2$ and $M_I = -1/2$) of the Cr^{53} isotope could not be determined because these transitions were not fully resolved from the outer wings of the main line in the spectrum.

Although the microwave frequency at which the spectra

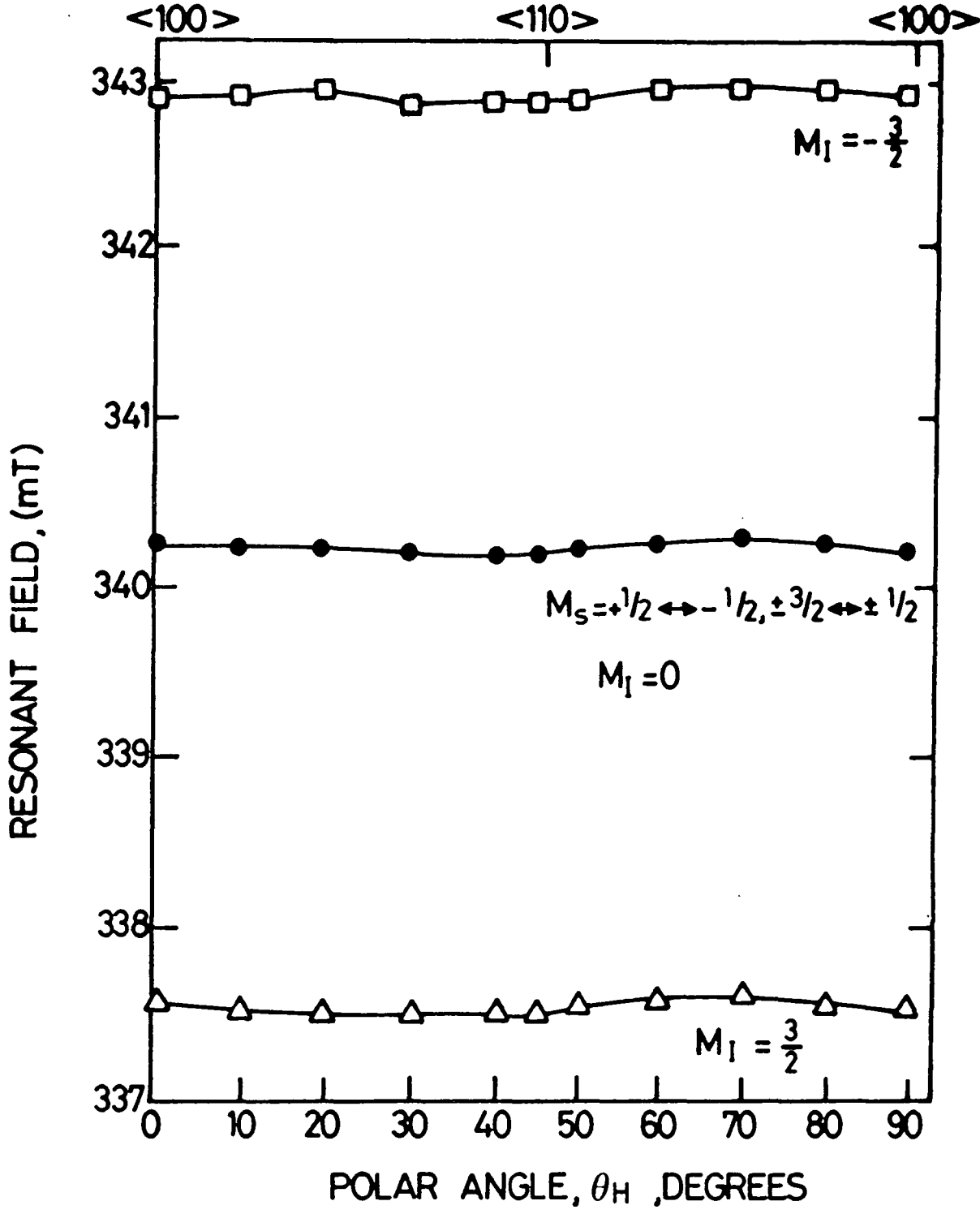

FIGURE 7.2 VARIATION OF RESONANT FIELD WITH POLAR ANGLE. SINGLE CRYSTAL Cr/MgO, 800p.p.m. Cr, [100] PLANE, 293 K, 9.4275 GHz.

were recorded varied slightly as the crystal was rotated (see Table 7.2), the resonant magnetic fields plotted in Figure 7.2 are those which would be found at a constant microwave frequency of 9.4275GHz. Conversion of the measured resonant magnetic fields to the corresponding values at 9.4275GHz is achieved using the following relationship:

$$H_1 = \frac{9.4275}{\nu_2} . H_2 \qquad (7.1)$$

where H_1 = the resonant magnetic field at 9.4275GHz

H_2 = the measured resonant magnetic field.

& ν_2 = the microwave frequency at which the spectrum was recorded.

Figure 7.2 shows that, in agreement with previously published data,[7.1-7.3] the cubic Cr^{3+} spectrum is largely isotropic, although the fluctuations in the resonant magnetic fields of all three transitions shown in the figure follow a similar pattern. It may be deduced that, due to its isotropic nature, the Cr^{3+} spectrum has the same form in both single crystal and powdered magnesium oxide (the powder spectrum of chromium doped MgO will be discussed in detail in section 7.2).

The g-factor, hyperfine structure constant (A) and peak-to-peak linewidth of the central transition (ΔH_{MS}) were determined for each of the spectra recorded at 10^o intervals from the sample doped with 800 p.p.m. of chromium. These are listed in Table 7.2 (along with the microwave

frequencies and relative gains used when the measurements were taken) and are plotted against polar angle in Figure 7.3. This figure shows that there is no significant variation of g or A with polar angle (which is to be expected as g and A should both be isotropic for ions located in sites of cubic symmetry). In contrast, between $\theta_H = 30^o$ and $\theta_H = 50^o$ ΔH_{HS} drops markedly below the almost constant value of ~ 0.505 mT it has over the remaining range of θ_H values.

The full E.P.R. spectra of the chromium doped samples provided no evidence that any fraction of the chromium dopant exists in any valency state other than the trivalent (Cr^{3+}) state. The Cr^+ ion has a $3d^5$ electronic configuration and therefore, in sites of cubic symmetry, its E.P.R. spectrum is similar to that of Fe^{3+} in sites of the same symmetry (see section 4.6). The five $\Delta M = 1$ transitions form a symmetric pattern and with the magnetic field parallel to a <100> direction the $\pm 3/2 \longleftrightarrow \pm 1/2$ transitions are located at $\pm 5/2a$ and the $\pm 5/2 \longleftrightarrow \pm 3/2$ transitions at $\mp 2a$ from the central $+1/2 \longleftrightarrow -1/2$ transition. In addition, each of the $\Delta M = 1$ transitions is at the centre of a quartet of weaker lines which are equally spaced and are due to the hyperfine transitions of the Cr^{53} isotope. It is not surprising that the Cr^+ ion is not present in our samples, since it has only been observed (using E.P.R. techniques) in magnesium oxide single crystals which have been subjected to γ-ray irradiation.[7.4]

The Cr^{2+} ion presents a more difficult problem. In magnesium oxide, it has not been observed using normal E.P.R. methods, although it has been detected using acoustic

POLAR ANGLE Θ (DEGREES)	ΔHpp (mT)	g - factor	HYPERFINE STRUCTURE CONSTANT A($\times 10^4$ cm^{-1})	FREQUENCY (GHz)	GAIN (ARBITRARY UNITS)
0	0.506	1.9797	16.44	9.4275	320
10	0.505	1.9798	16.59	9.4275	400
20	0.505	1.9798	16.68	9.4275	400
30	0.471	1.9799	16.50	9.4275	500
40	0.483	1.9800	16.49	9.4275	500
45	0.493	1.9800	16.53	9.4280	500
50	0.509	1.9798	16.44	9.4280	500
60	0.509	1.9796	16.50	9.4280	500
70	0.497	1.9794	16.52	9.4280	400
80	0.509	1.9796	16.58	9.4275	320
90	0.509	1.9799	16.59	9.4280	320

TABLE 7.2 E.P.R. PARAMETERS FOR ISOFREQUENCY PLOT FOR SINGLE CRYSTAL Cr/MgO (800 p.p.m. Cr, 10^o intervals, 293K).

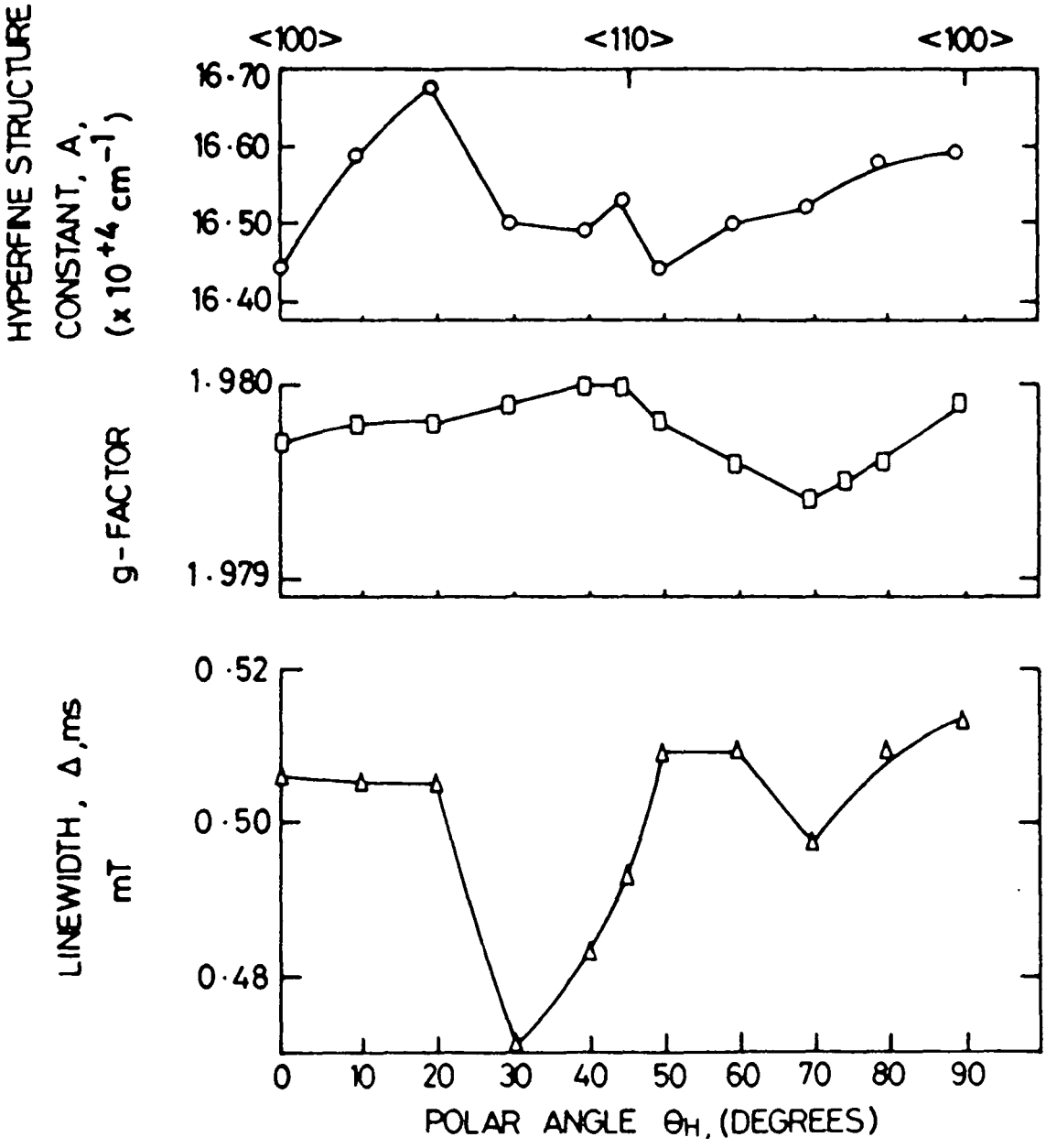

FIGURE 7.3 VARIATION OF A, g-FACTOR AND ΔH_{ms} WITH POLAR ANGLE IN THE [100] PLANE; SINGLE CRYSTAL Cr/MgO, 800 p.p.m. Cr, 293K.

paramagnetic resonance (A.P.R.).[7.5-7.8] However, although x-irradiation of chromium doped magnesium oxide samples causes the intensity of the cubic Cr^{3+} spectrum to diminish (due to the formation of Cr^{2+} ions), after irradiation the intensity of the cubic Cr^{3+} spectrum recovers.[7.3,7.9] In addition, the intensity of the Cr^{3+} spectrum increases on heating the sample in vacuum, indicating that Cr^{2+} ions are being converted to Cr^{3+} ions [7.3,7.9] Taken together, these two pieces of evidence show that the Cr^{3+} state is far more stable at room temperature than the Cr^{2+} state.

Direct evidence that Cr^{3+} is the most stable valency state of chromium in MgO comes from the A.P.R. spectra. [7.5,7.6] In nominally pure MgO the Cr^{3+} spectrum was detected using normal E.P.R. methods but the Cr^{2+} spectrum could only be detected (using A.P.R.) after the sample was irradiated with x-rays. In MgO samples deliberately doped with chromium Cr^{3+} ions were again present, but in this case the Cr^{2+} ion could be observed without the need for x-irradiation, indicating that some fraction of the chromium dopant naturally exists in the (+2) valency state.

Chemical analysis showed that the Cr^{2+} content in the x-irradiated undoped crystals could not be more than 2 p.p.m. Comparison of the intensities of the Cr^{2+} A.P.R. spectrum in the doped and undoped crystals showed that the concentration of Cr^{2+} ions in the doped crystals (which is the natural concentration of the Cr^{2+} ions since these crystals were not x-irradiated) was of the same order as in the undoped crystals. Since the total chromium content in the doped crystals was 1,000 p.p.m. we may assume

that the fraction of the chromium dopant in our samples existing as Cr^{2+} is very small.

The E.P.R. spectrum of Cr^{4+} in MgO has not been reported in the literature and this is presumably because Cr^{4+} is too unstable to exist in the host lattice. It is therefore safe to assume that no fraction of the chromium dopant in our samples exists in this valency state.

For each of the five chromium doped MgO samples the complete E.P.R. spectrum was recorded and a typical example is shown in Figure 7.4. The particular spectrum illustrated was obtained from the sample doped with 800 p.p.m. of chromium with the magnetic field parallel to a <100> direction.

The lines labelled A_o, B_o and C_o and A_{90}, B_{90} and C_{90} are due to Cr^{3+} ions in sites of axial symmetry. The labels given to the lines correspond to those of Wertz and Auzins[7.3] who first observed the axial Cr^{3+} spectrum. The pattern of the spectral lines allowed Wertz and Auzins to conclude that the sites occupied by the Cr^{3+} ions responsible for the spectrum are axially symmetric about the principal crystal axes and they deduced that this [100]-type axial symmetry is caused by a vacancy at one of the magnesium positions next-nearest to the chromium ions. The line labelled C_o is not fully resolved from the central line of the cubic Cr^{3+} spectrum, the peaks of which extend off the scale in Figure 7.4 (showing that the cubic Cr^{3+} spectrum is far more intense than the axial Cr^{3+} spectrum).

Towards the high magnetic field end of the spectrum illustrated in Figure 7.4 there are some very low intensity lines which were first observed by Marguglio and Kim.[7.10]

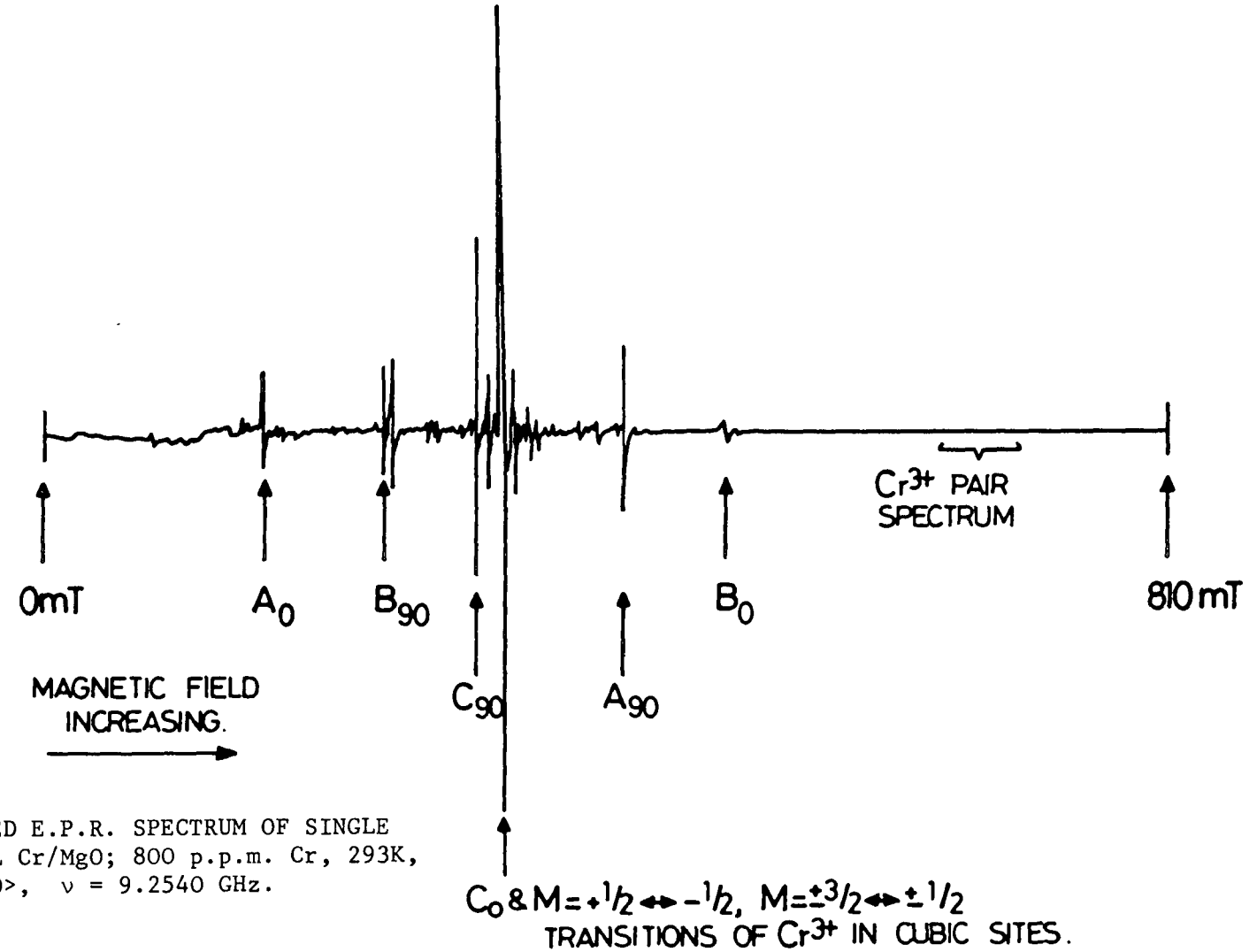

FIGURE 7.4 EXTENDED E.P.R. SPECTRUM OF SINGLE CRYSTAL Cr/MgO; 800 p.p.m. Cr, 293K, H// <100>, ν = 9.2540 GHz.

These lines have been labelled on the diagram as being due to Cr^{3+} pairs and in making this identification we have followed the analysis of Marguglio and Kim, who attributed them to transitions within the S = 1 and S = 2 multiplets of the complex (Cr^{3+} - O - Cr^{3+}). Marguglio and Kim were also able to conclude from their measurements that the two Cr^{3+} ions in the (Cr^{3+} - O - Cr^{3+}) complex are in a straight line.

The gain used to record the spectrum shown in Figure 7.4 was approximately 150 times greater than that used to record the portion of this spectrum shown in Figure 7.1 which is attributable to Cr^{3+} ions in sites of cubic symmetry. Since the spectra illustrated in Figures 7.1 and 7.4 were both recorded from the sample doped with 800 p.p.m. of chromium we may conclude that less than 1% of the Cr^{3+} ions occupy sites of axial symmetry and that an even smaller proportion exist as Cr^{3+} pairs in the (Cr^{3+} - O - Cr^{3+}) complex. The remainder of the Cr^{3+} ions detectable by E.P.R. occupy sites of cubic symmetry.

In conclusion, all of the chromium dopant in the samples examined which is detectable by E.P.R. exists in the trivalent Cr^{3+} state. Although Cr^{2+} ions cannot be observed using normal E.P.R. methods, A.P.R. measurements [7.5,7.6] enable us to conclude that if this ion is present in our samples, its concentration is very low compared to that of the Cr^{3+} ion. Cr^{+} and Cr^{4+} are detectable using normal E.P.R. methods and no evidence could be found for the presence of these ions in the samples examined here. Of the Cr^{3+} ions, the vast majority occupy sites of cubic symmetry while small numbers exist in sites of axial

symmetry and as Cr^{3+} pairs in the complex (Cr^{3+}-O-Cr^{3+}).

b) E.D.A.X. SPECTRA

Energy Dispersive Analysis by x-rays (E.D.A.X.) spectra were recorded from all five chromium doped magnesium oxide samples in the as received state. The samples were bombarded by the high energy electron beam of a Cambridge Stereoscan 600 scanning electron microscope (S.E.M.). This bombardment caused them to emit x-rays, a representative portion of which were collected by a detector attached to the sample chamber of the S.E.M. The detected x-rays were then analysed in terms of their energies by a LINK Systems 860 series 2 E.D.A.X. energy spectrum analyser. The processed data was presented as a plot of the variation of x-ray intensity with x-ray energy: this plot is the E.D.A.X. spectrum of the sample under investigation.

The samples were mounted, in powder form, on aluminium stubs by means of double sided adhesive tape and coated with a thin layer of gold. This prevented electrical charge accumulating on the sample surface when bombarded by the electron beam of the S.E.M. As the area of the sample on the stub was much greater than that of the S.E.M. electron beam, E.D.A.X. spectra were recorded from several different regions of each sample. Since all the spectra obtained from a given sample were equivalent, we may regard any one of them as being typical of that sample. In addition, the lack of variation in the E.D.A.X. spectra recorded from an individual specimen tends to suggest that

all five chromium doped MgO samples are homogenous in composition. Typical examples of the E.D.A.X. spectra obtained from the samples doped with 800 p.p.m. and 15,100 p.p.m. of chromium are shown in Figures 7.5(a) and (b) respectively.

Any E.D.A.X. spectrum (including those shown in Figures 7.5(a) and (b)) consists of two distinct parts: a continuous background, which is due to the rapid decelleration of the electrons in the S.E.M. beam on striking the sample, and a number of sharp peaks superimposed on the continuous background. These peaks occur when an incident electron knocks an electron out of one of the inner shells of an atom in the sample. This leaves the atom in an excited high energy state and one of the outer electrons of the atom immediately fills the vacancy created in the inner shell. As it falls the outer electron emits energy of a specific wavelength (typically in the x-ray region) and this highly monochromatic radiation gives rise to an E.D.A.X. peak. Since, as will be clear from the above discussion, the energy of an emitted x-ray depends upon the spacings between the energy levels of the atom producing it, it will be characteristic of that atom. Accordingly, the peaks of the E.D.A.X. spectra shown in Figures 7.5(a)&(b) have been labelled with the symbols of the elements and the electronic transitions within those elements responsible for them.

The E.D.A.X. spectra obtained from the five chromium doped samples all displayed the MgK_{α}, AuL, AuM and CrK_{α} peaks. In addition, for the more heavily doped samples

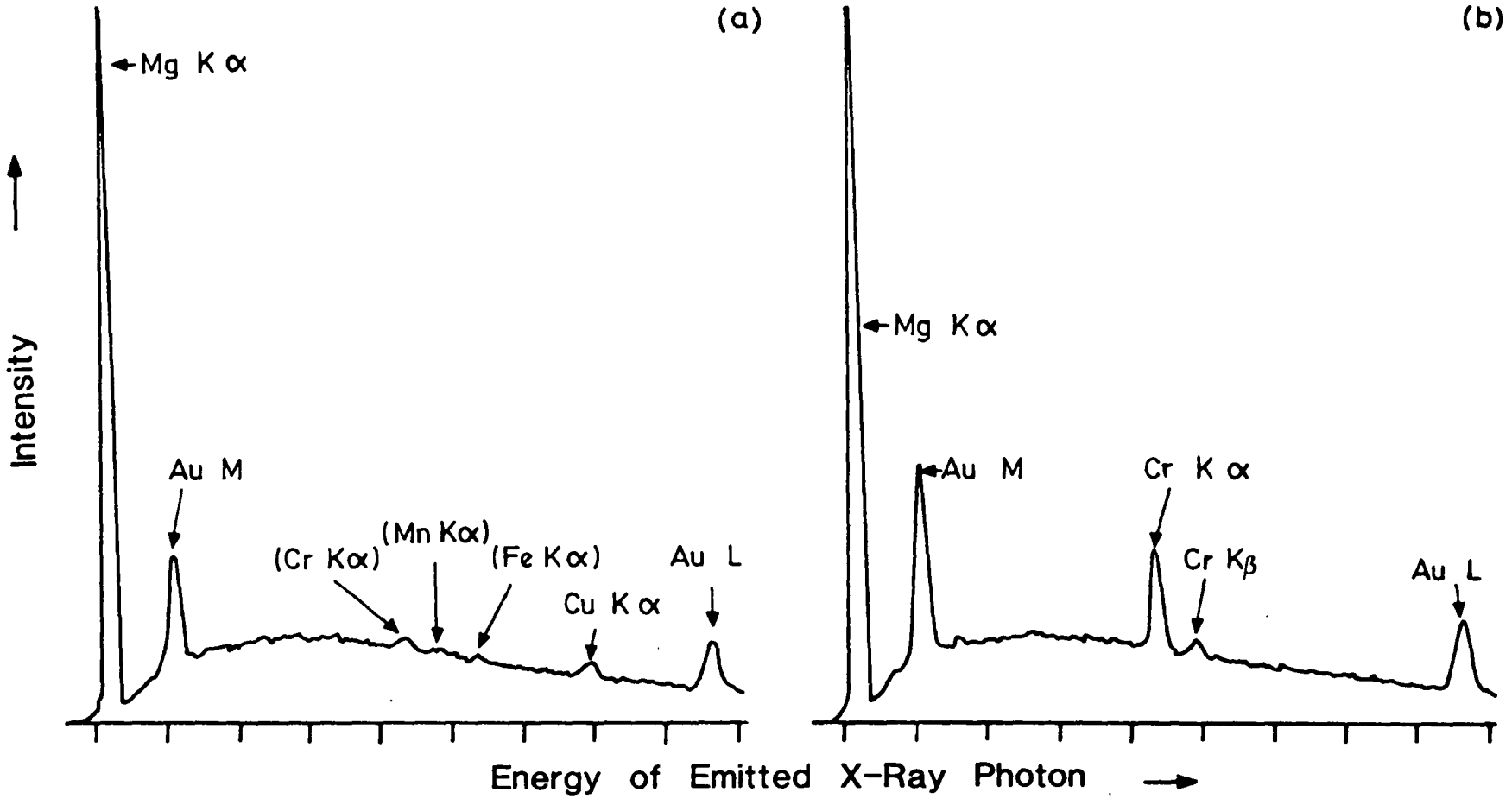

FIGURE 7.5 TYPICAL E.D.A.X. SPECTRA OF MgO DOPED WITH (a) 800 p.p.m. AND (b) 15,100p.p.m. of CHROMIUM.

(those containing 9,500 p.p.m. and 15,100 p.p.m. of chromium) a CrK_{β} peak was present and for the more lightly doped samples (those containing 800 p.p.m., 3,600 p.p.m. and 7,400 p.p.m. of chromium) MnK_{α} , FeK_{α} and CuK_{α} peaks were present.

The MgK_{α} peak is obviously due to the magnesium atoms of the host lattice. No E.D.A.X. peak due to the oxygen atoms of the host lattice was observed because this peak has an energy outside the range covered by the x-ray energy analyser.

The CrK_{α} and CrK_{β} peaks are due to different x-ray transitions within the chromium dopant atoms; the CrK_{β} peak only shows up in the spectra of the more heavily doped samples because its intensity is low in relation to that of the CrK_{α} peak.

The MnK_{α} and FeK_{α} peaks, which show the presence of manganese and iron respectively, are observed because it is impossible to prepare magnesium oxide free from unwanted transition metal impurities. These peaks are only prominent in the spectra of the more lightly doped samples, possibly showing that as the concentration of the deliberately introduced dopant is increased, the inclusion of unwanted impurities is suppressed. A similar conclusion has been drawn from the variation of the relative intensities of the E.P.R. spectra of various transition metal impurities in iron doped MgO with iron concentration.[7.11,7.12]

An E.D.A.X. spectrum recorded from double sided adhesive tape coated with gold and mounted on an aluminium stub is shown in Figure 7.6. This spectrum clearly demonstrates that the CuK_{α} peak observed in the E.D.A.X.

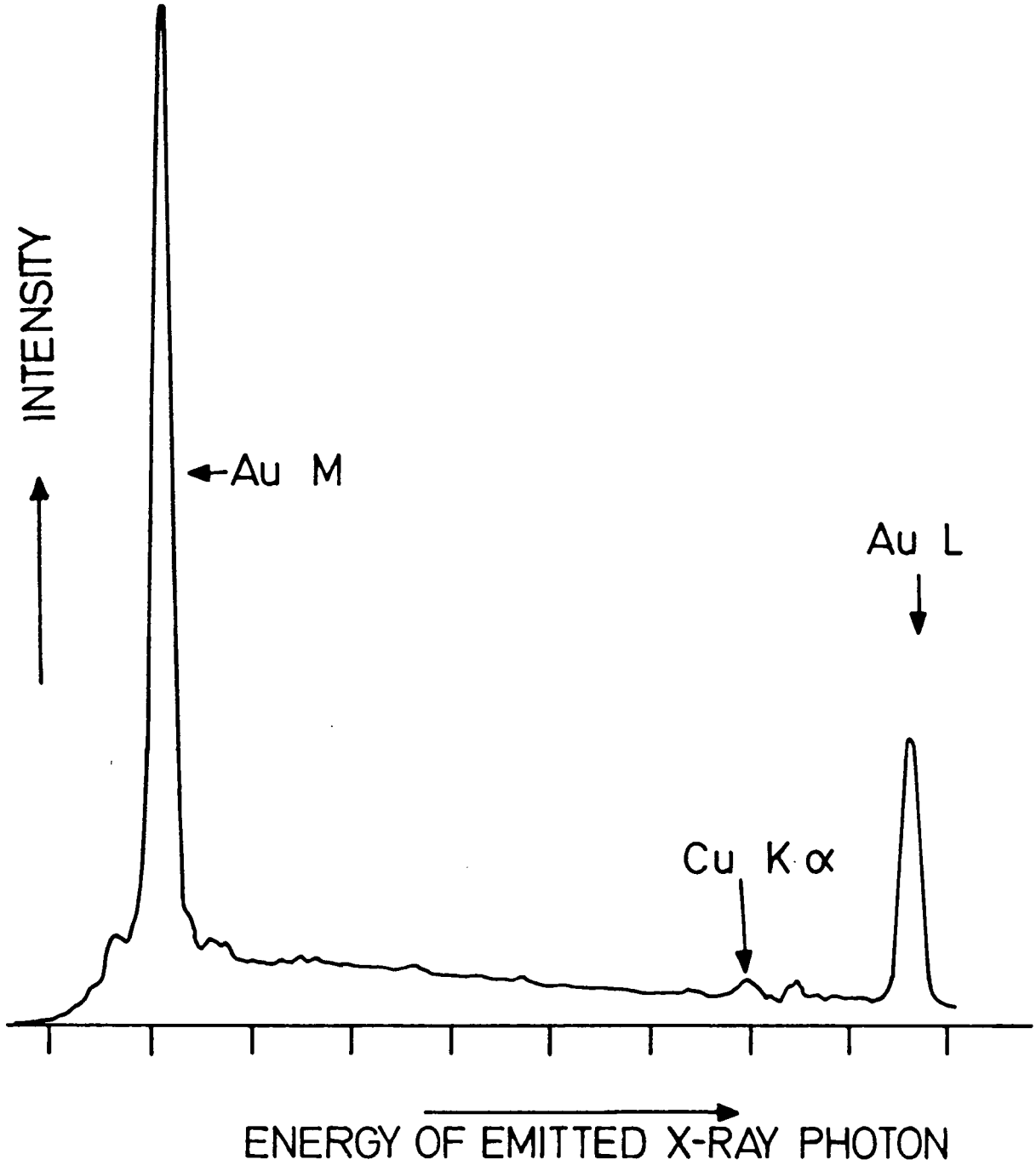

FIGURE 7.6 E.D.A.X. SPECTRUM FROM GOLD COATED DOUBLE-SIDED ADHESIVE TAPE ON AN ALUMINIUM STUB.

spectra of some of the chromium doped MgO samples does not arise from copper atoms in these samples but rather from copper atoms in the mountings used to fix these samples in place in the S.E.M. It is also clear from Figure 7.6 that, as expected, the AuL and AuM peaks are due to different x-ray transitions within the gold atoms of the thin film put down to prevent charging of the samples during electron bombardment.

Since the concentration of magnesium atoms in all five doped samples is approximately the same and may be taken as constant, the E.D.A.X. spectra were normalized so that the MgK_{α} peak was of the same height in each case. Having normalized the spectra, we may compare the heights above the background of the E.D.A.X. peaks due to any given element among the five E.D.A.X. spectra in order to determine the relative concentration of that element in each of the chromium doped MgO samples. This procedure was carried out for the CrK_{α} peak which, in general, increased in intensity as the nominal chromium concentration increased. Only the sample doped with 9,500 p.p.m. of chromium did not follow this trend: for this sample the CrK_{α} peak in the E.D.A.X. spectrum was abnormally large, larger in fact than that in the spectrum of the sample nominally doped with 15,100 p.p.m. of chromium.

The anomalous nature of the sample nominally containing 9,500 p.p.m. of chromium is not only indicated by its E.D.A.X. spectrum but also be its E.P.R. spectrum. As described earlier, the cubic Cr^{3+} E.P.R. spectrum of this sample has such a high level of background noise that, in contrast to the spectra of the other chromium doped

samples, the hyperfine transitions of the Cr^{53} isotope are obscured.

It is important to realise that because E.D.A.X. transitions involve the lower electron shells of atoms, properties which influence the outer electronic structure have no bearing on the E.D.A.X. spectrum. Thus although Cr^{3+} was detected in three different environments by E.P.R. (in cubic sites, in axial sites and as Cr^{3+} pairs) the relative concentration of Cr^{3+} in each of these environments estimated from the E.P.R. spectra could not be confirmed using the E.D.A.X. data. This is because all chromium atoms, whatever their valency state or local surroundings, contribute towards the CrK_{α} peak and hence we may only determine the relative concentration of the element chromium in each doped sample from this peak.

Thus the E.D.A.X. data allows us to conclude that, with the exception of the sample nominally doped with 9,500 p.p.m. of chromium, the true total chromium content of the MgO samples increases in line with the nominal total chromium content quoted by the manufacturers. It should be noted that, unfortunately, our assessment of the chromium content of each doped MgO sample from their E.D.A.X. spectra is purely qualitative; the E.D.A.X. data cannot be used to check the nominal chromium concentrations quantitatively.

7.1.2 RHEED INVESTIGATIONS: EVIDENCE FOR SPINEL FORMATION

Five as received single crystals of MgO:Cr with different dopant concentrations covering the whole range given in Table 7.1 were examined using Reflection High

Energy Electron Diffraction (RHEED). The work was carried out on a JEM-120 electron microscope operating at 100kV. The electron beam of the microscope impinged upon the large face of the sample under investigation (which had typical dimensions of 10mm x 5mm x 1mm) at a glancing angle (one or two degrees) and was diffracted by the crystal lattice. The diffracted beam represents the RHEED pattern, which for each sample was recorded on a photographic plate located in the final stage of the microscope.

Since the wavelength of the electrons is very small ($\sim 0.04\text{Å}$) and, typically, the interplanar spacing, $d_{hk\ell}$, is of the order of 2Å, the Bragg equation ($\lambda = 2d_{hk\ell}\sin\theta$) shows that for diffraction to occur the Bragg angle, θ, is approximately 1^{o}. Thus only planes which are virtually parallel to the sample surface will contribute towards the RHEED diffraction pattern. Figure 7.7 is a diagrammatic representation of the RHEED process. It is clear from this Figure that:

$$R_{hk\ell} = L\tan 2\theta \qquad (7.2)$$

and since θ is small we may approximate and combine equation 7.2 with the Bragg equation to obtain:

$$\lambda L = R_{hk\ell}\ d_{hk\ell} \qquad (7.3)$$

L is a constant for any given microscope and may be found by first examining a material of known interplanar spacing. Determination of the electron wavelength, λ, and the distance from any diffracted spot to the undeviated beam

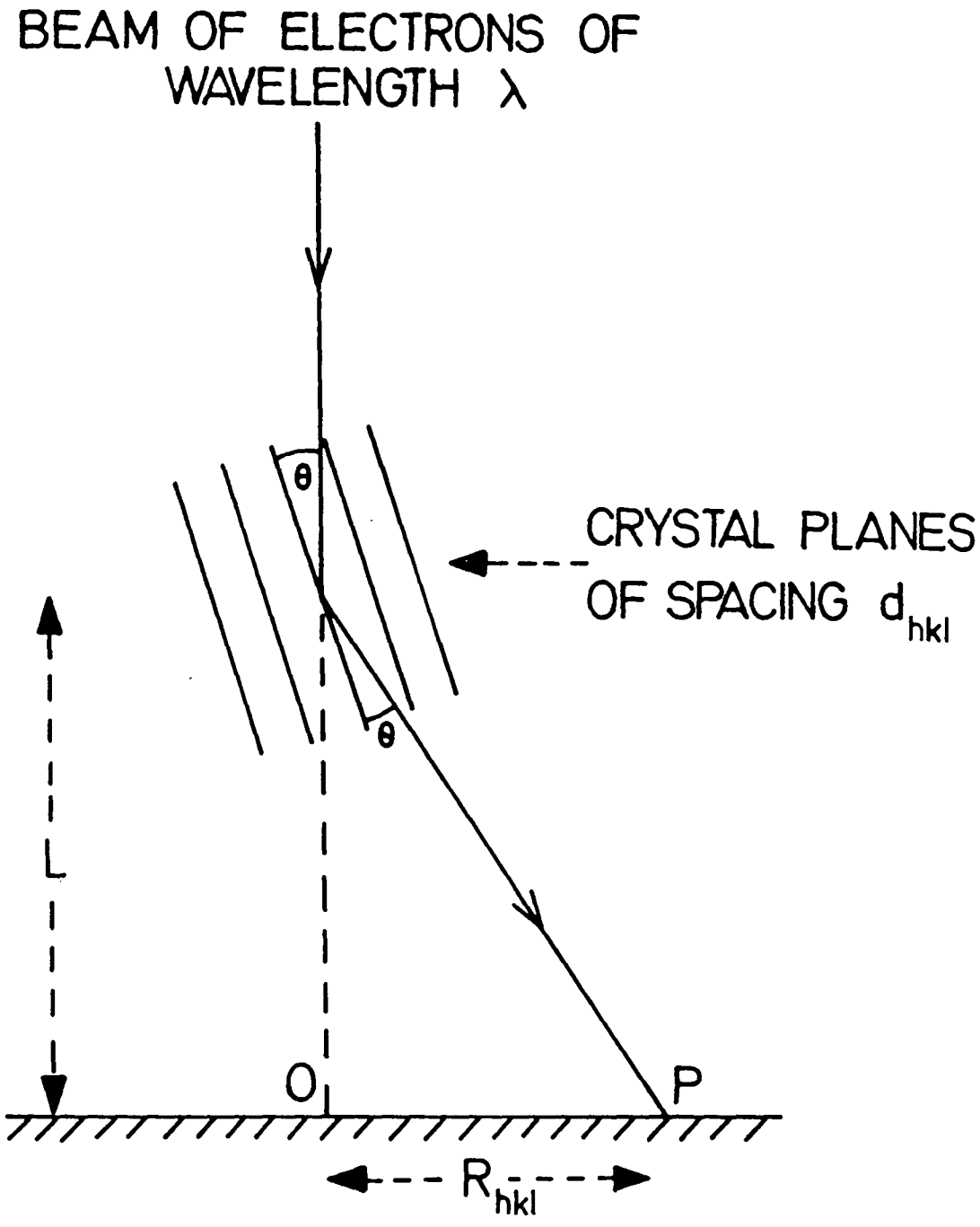

FIGURE 7.7 SCHEMATIC REPRESENTATION OF R.E.D.

on the photographic plate ($R_{hk\ell}$) then allows the inter-planar spacing, $d_{hk\ell}$, to be calculated by substituting L, $R_{hk\ell}$ and λ into equation 7.3.

The concept of the reciprocal lattice is very important in solving RHEED patterns. Diffraction from a set of planes ($hk\ell$) will only occur if the point in the reciprocal lattice which represents that set of planes intersects with the Ewald sphere. Because of the short wavelength of the electrons, the Ewald sphere for RHEED will have a very large radius ($r \alpha {}^{1}/\lambda$), and hence the sphere approximates to a plane section through the reciprocal lattice. The RHEED diffraction spots therefore correspond to reciprocal lattice points in this plane section, which is perpendicular to the direction of the incident beam. In fact, the spots in a RHEED pattern represent the reciprocal lattice points of reflecting planes which all belong to the same zone, the zone axis having the same Miller indices as the crystallographic direction along which the beam of the electron microscope was travelling when the diffraction pattern was recorded. For more comprehensive accounts of the RHEED technique the reader is referred to articles by Bauer[7.13] and by Russell.[7.14] Further experimental and theoretical details which are particularly relevant to the RHEED work reported in this section are given by Inglis,[7.12] who, using a similar approach to that adopted by the present author, investigated the formation of the spinel magnesioferrite ($MgFe_2O_4$) in iron doped MgO.

The samples to be investigated were cleaned in acetone, dried in air and then etched in fuming nitric acid for

varying lengths of time. The etchant attacks MgO much more rapidly than it attacks the spinel precipitates;[7.15] this results in the formation of etch hillocks on the sample surface with spinel phase material at the peaks. Thus, etching in this way will cause the electron beam to preferentially sample spinel precipitates when it is glanced off the surface. The spots in the diffraction pattern arising from the precipitates are therefore artificially increased in intensity compared with those arising from the MgO host material, thereby increasing the sensitivity of RHEED to the presence of the spinel phase.

The RHEED patterns shown in Figures 7.8(a) and (b) were obtained from the sample doped with 800 p.p.m. of chromium after it had been etched for 1 minute . Both patterns are due to the MgO host lattice; that of Figure 7.8(a) was obtained with the electron beam almost parallel to a <100> direction, and that of Figure 7.8(b) was obtained with the electron beam almost parallel to a <110> direction. As described in Chapter Two, the MgO lattice is face centred cubic and, as illustrated in Figures 7.8(a) and (b), the diffraction spots may be indexed with reciprocal lattice points corresponding to the reflecting planes producing the spots which are consistent with this type of lattice.[7.16] Furthermore, the spacings of the diffraction spots in Figures 7.8(a) and (b) allow us to confirm that the face centred cubic lattice producing these RHEED patterns has a lattice parameter equal to that of MgO.

Similar patterns were obtained from the samples doped with 3,600 p.p.m. and 7,400 p.p.m. of chromium. Variation

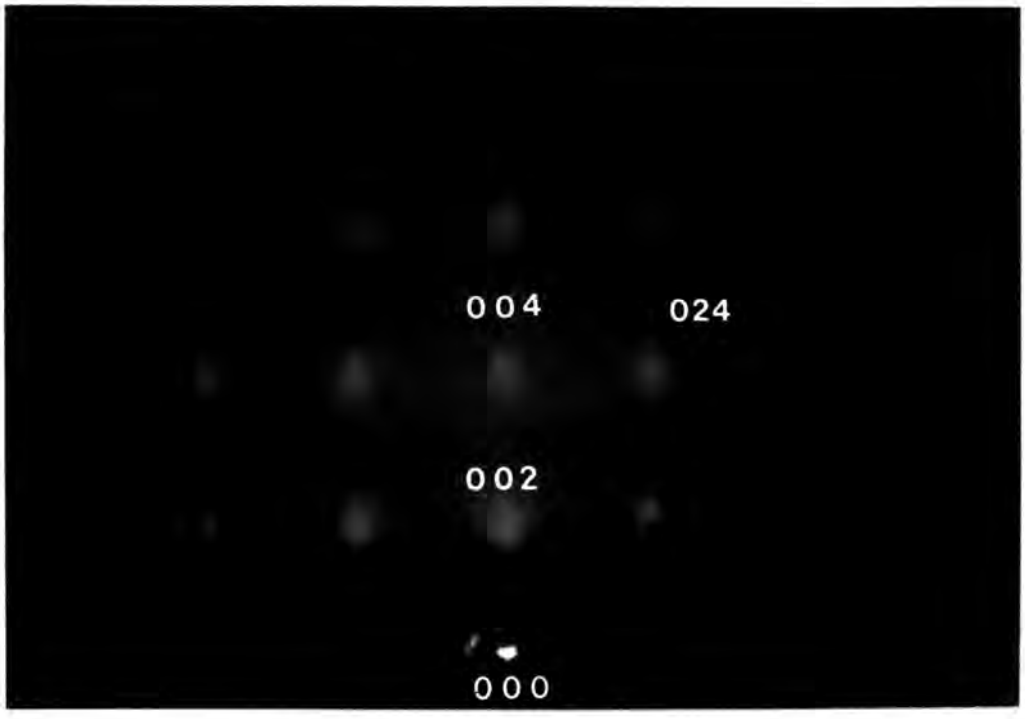

Fig. 7.8(a)

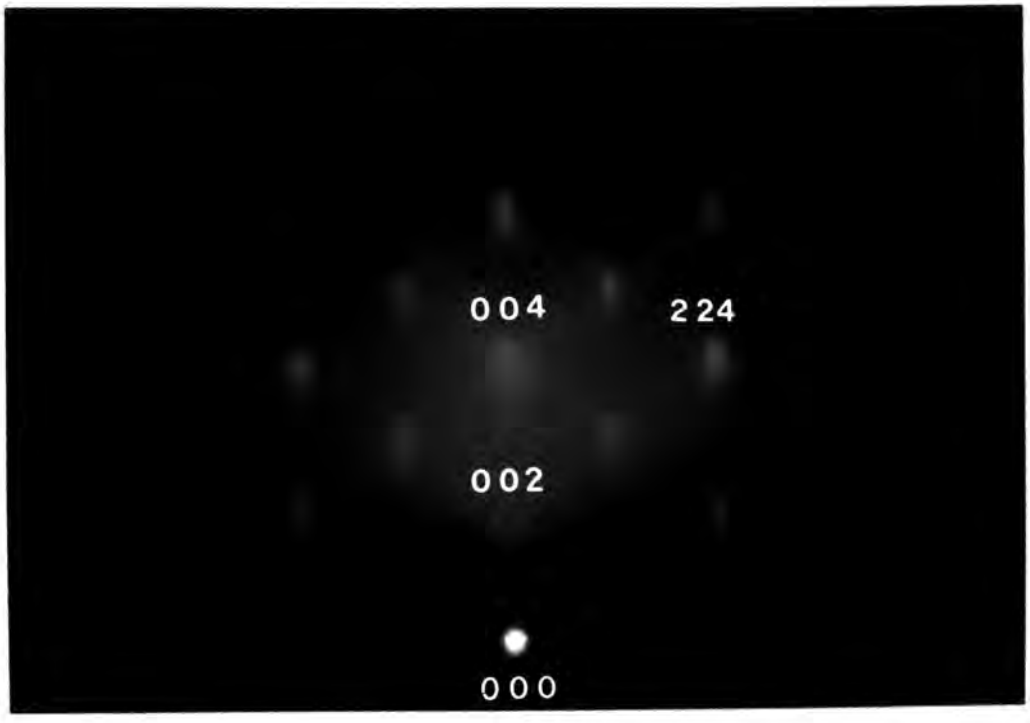

Fig. 7.8(b)

Figure 7.8 RHEED. patterns recorded from single crystal MgO:Cr with (a) the electron beam // <100> & (b) the electron beam // <110> ; dopant concentration = 800p.p.m.; etching time = 1 minute.

of the etching time did not produce any changes in the patterns observed.

Figures 7.9(a) and (b) are RHEED patterns obtained with the same electron beam alignments as in Figures 7.8(a) and (b) respectively. These patterns were recorded from the sample doped with 15,100 p.p.m. of chromium after it had been etched for one minute. The spots which are wholly or partially due to MgO may be determined by comparing Figures 7.8(a) and (b) with Figures 7.9(a) & (b) (the MgO spots are more intense than the rest in the patterns of Figures 7.9(a) and (b)). The additional spots which appear in Figures 7.9(a) and (b) arise from a second cubic lattice which is in alignment with the MgO host lattice and which has a lattice parameter equal to twice that of MgO. It is thought that the additional spots are caused by precipitates of the spinel magnesiochromite ($MgCr_2O_4$) which, in the bulk, has a lattice parameter of 8.333Å - almost exactly twice that of MgO (a_{MgO} = 4.2112Å). The indices given to the diffraction spots in Figures 7.9(a) and (b) refer to the Miller indicies of the reflecting planes in the $MgCr_2O_4$ lattice which are responsible for them.

Evidence that our assignment of the additional spots to $MgCr_2O_4$ is reasonable is provided by the information given on the x-ray ASTM index card of this material, which, although it refers to x-ray diffraction, is equally applicable to RHEED data. Firstly, of the reflections which the ASTM index indicates are allowed, then all are either present, or would be present at positions which

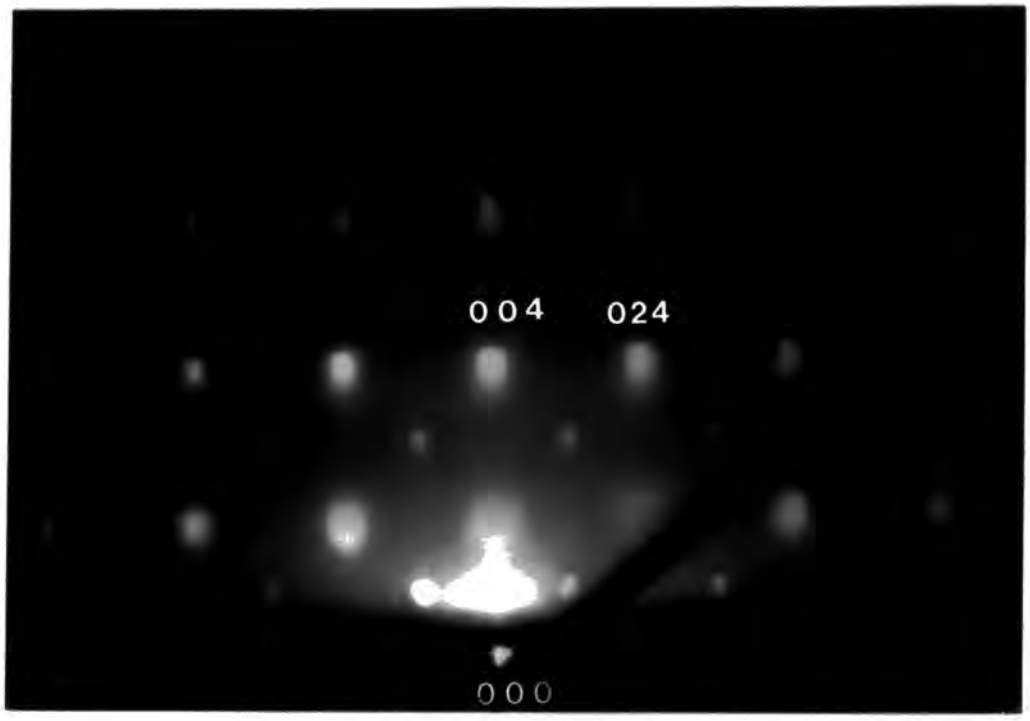

Fig. 7.9(a)

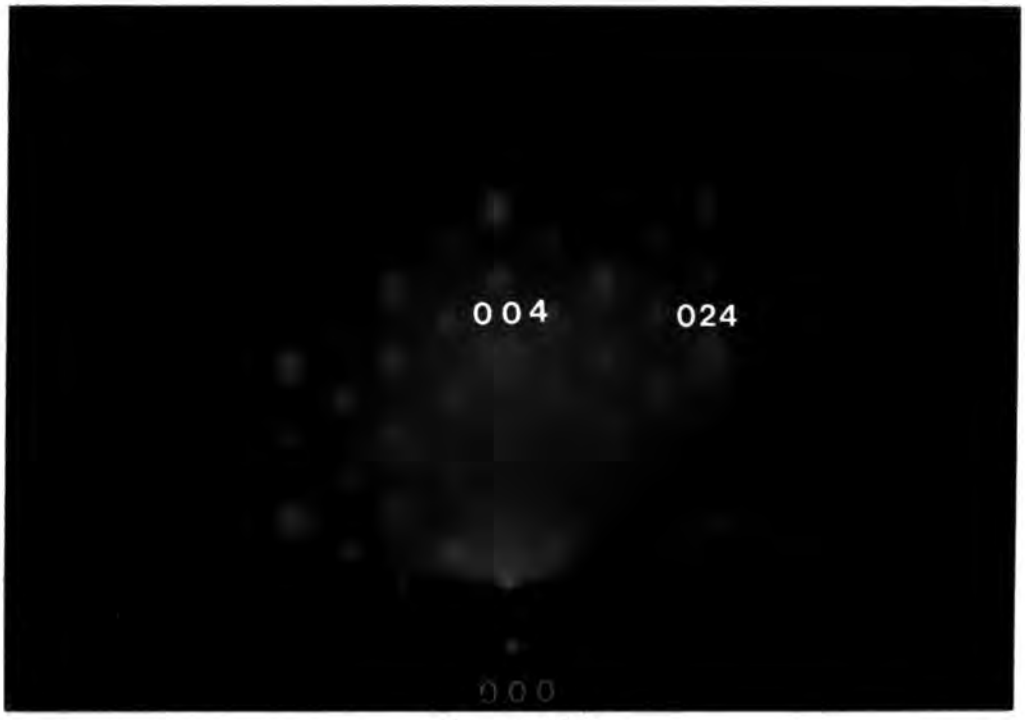

Fig. 7.9(a)

Figure 7.9 RHEED. patterns recorded from single crystal MgO:Cr with (a) the electron beam // <100> & (b) the electron beam // <110> ; dopant concentration = 15,100 p.p.m.; etching time = 1 minute.

overlap with the spots due to MgO reflections, in Figures 7.9(a) and (b). Secondly, the reflections which the ASTM index predicts will be absent are, as far as Figure 7.9(a) is concerned, either absent or overlap with host lattice reflections, so that it is not possible to determine whither there are spinel spots at these positions or not.

However, in Figure 7.9(b), spots are found at some of the positions where absences are expected (for example, the (200) $MgCr_2O_4$ reflection is present but is predicted to be absent). Nonetheless they cannot be due to genuine lattice reflections because spots attributable to lattice reflections which should be absent are not observed when the electron beam is parallel to a <100> type direction (Figure 7.9(a)). The presence of diffraction spots at positions where absences are expected in Figure 7.9 (b) is thought to be due to the phenomenon of "double diffraction".[7.17] This arises when part of the primary beam which has already been diffracted is incident upon a second spinel precipitate and is diffracted again. This second diffraction produces a RHEED pattern similar in form to that produced by the main primary beam but displaced from it.

The above discussion shows that the RHEED patterns of Figures 7.9(a) and (b) are consistent with the proposal that a second phase with a spinel structure and a lattice parameter twice that of MgO has been precipitated out in register with the host lattice. Such patterns were also observed for the sample containing 9,500 p.p.m. of chromium

but, as with its E.P.R. and E.D.A.X. spectra, the RHEED patterns of this sample are somewhat anomalous in that the spinel spots and the MgO spots are of equal intensity. The RHEED patterns of the sample doped with 15,100 p.p.m. of chromium follow the expected behaviour, namely that the spinel spots are much weaker than the MgO spots.

The etching time did have an effect upon the RHEED patterns of the samples for which spinel spots were observed. For etching times greater than one minute rings were also observed, as shown in Figures 7.10(a) and (b) which illustrate the RHEED patterns recorded with the electron beam parallel to a <100> and a <110> direction respectively for the sample doped with 15,100 p.p.m. of chromium after it had been etched for 25 minutes.

The pattern of rings is consistent with them being due to the spinel precipitate and not the MgO host. As rings are an indication of polycrystallinity, the spinel precipitates responsible for the rings are not aligned with the MgO host lattice but have random orientations. It is thought that excessive etching causes the base of the etch hillocks which is composed of MgO to be dissolved away, thereby depositing the insoluble spinel precipitates, located at the peaks of the etch hillocks, onto the sample surface. The precipitates will obviously be deposited on the surface with random orientations and hence give rise to a "powder" diffraction pattern composed of rings. That only very faint rings were observed in iron doped MgO after etching times as long as five minutes[7.12] seems to indicate that $MgCr_2O_4$ is much less soluble in fuming nitric acid than $MgFe_2O_4$.

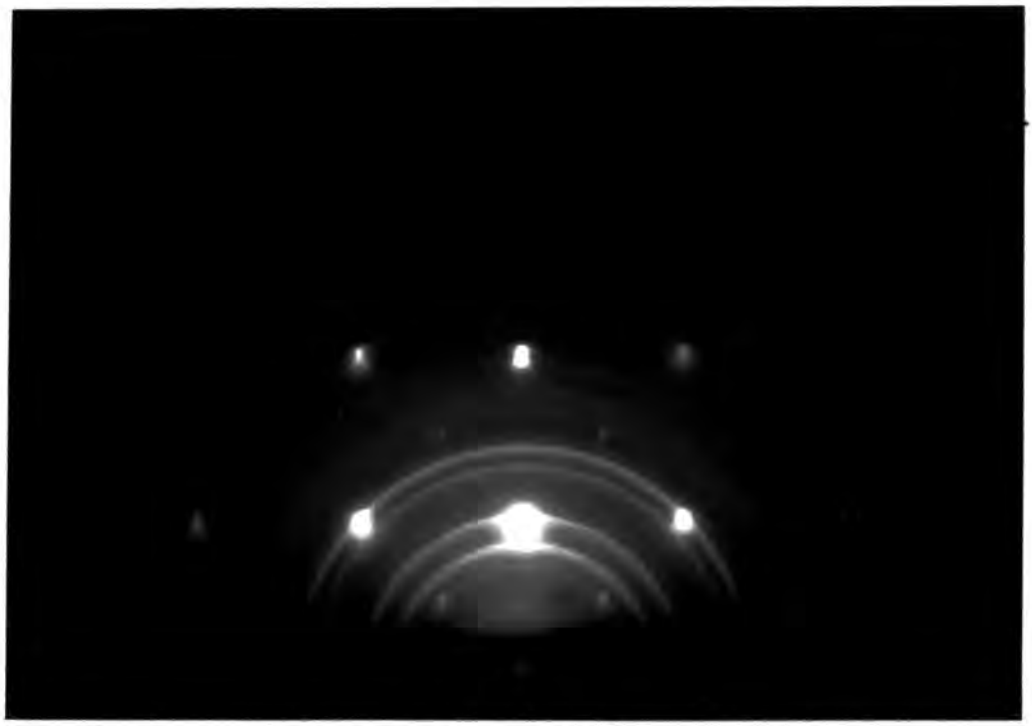

Fig. 7.10(a)

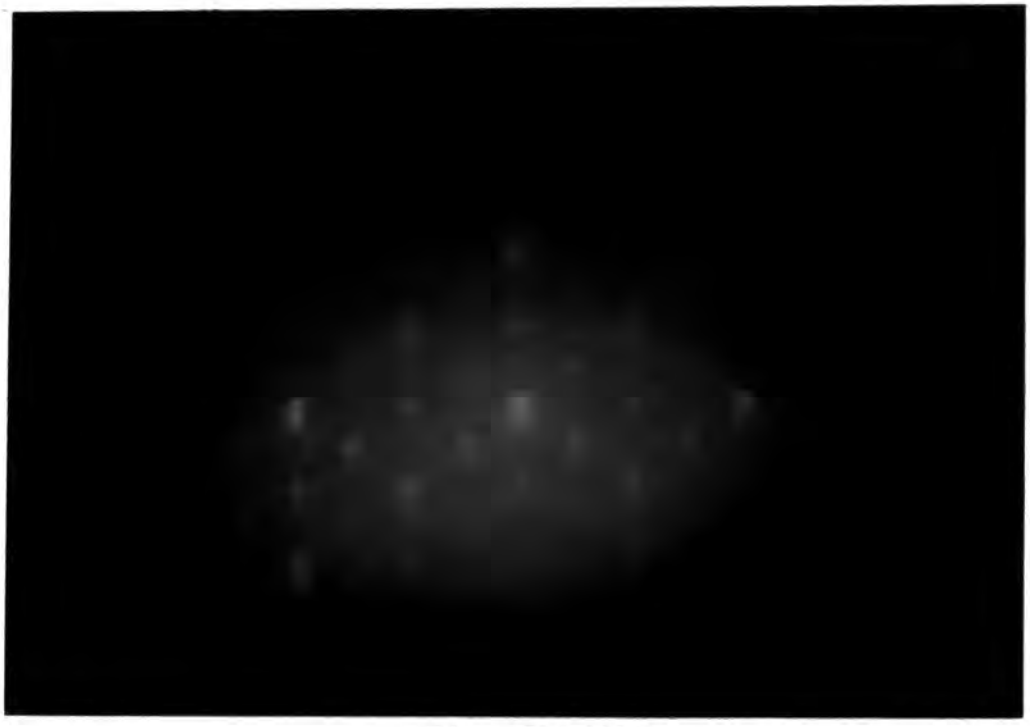

Fig. 7.10(b)

Figure 7.10 RHEED. patterns recorded from single crystal MgO:Cr with (a) the electron beam // <100> & (b) the electron beam // <110> ; dopant concentration = 15,100 p p.m.; etching time = 25 minutes.

The lightly doped samples (those containing 800 p.p.m., 3,600 p.p.m. and 7,400 p.p.m. of chromium), whose RHEED patterns did not show the presence of magnesiochromite were heat treated at 800^{o}C for 10 hours in an oxygen atmosphere in order to try to induce growth of the spinel phase. Re-examination by RHEED showed that only in the sample doped with 7,400 p.p.m. of chromium had any spinel precipitates been formed. Since all three heat treated samples had been etched for one minute, only the spinel spots were seen in the RHEED patterns of the sample doped with 7,400 p.p.m. of chromium, the short etching period preventing spinel precipitates with random orientations from being deposited on the sample surface which would have given rise to diffraction rings.

Summing up, the RHEED investigations show that precipitates of a cubic compound with a spinel-like structure which is in register with the host lattice and which has a lattice parameter twice that of MgO are present in the as received samples doped with 9,500 p.p.m. and 15,100 p.p.m. of chromium. This compound has been identified as magnesiochromite, $MgCr_2O_4$. That heat treatment readily induces magnesiochromite formation in the sample containing 7,400 p.p.m. of chromium suggests that in this sample it is possible that either:

(i) spinel precipitates are present in the as received crystal but their concentration is too low for them to be observed using the RHEED technique (the heat treatment induces them to grow to sizes which are detectable using RHEED).

or that:

(ii) a disordered phase of clustered chromium ions is present in the as received sample which, because it has no regular crystal structure, does not produce a RHEED pattern; heat treatment allows the clustered chromium ions to rearrange and form, in conjunction with the ions of the host lattice, the spinel $MgCr_2O_4$ which, because of its regular crystal structure, is detectable on re-examination by RHEED.

Precipitates of spinel or a clustered chromium phase may also be present in the as received crystals with the lowest chromium concentrations (those containing 800 p.p.m. and 3,600 p.p.m. of chromium). However, if this is so, we must conclude that, because precipitate growth will be more difficult to achieve the lower the total chromium content, then the 10 hour heat treatment is not long enough to grow precipitates in the two most lightly doped samples in sufficient concentrations for them to be detected using the RHEED technique.

7.1.3 THE VARIATION OF E.P.R. LINEWIDTH WITH CHROMIUM CONCENTRATION

The peak-to-peak linewidth of the central transition of the cubic Cr^{3+} spectrum (which represents three coincident lines corresponding to the $M = +\frac{1}{2} \longleftrightarrow -\frac{1}{2}$ and $M = \pm 3/2 \longleftrightarrow \pm 1/2$ transitions) was measured with the magnetic field parallel to a <100> direction in the crystal for each doped sample (see Table 7.1). The values obtained are plotted against total nominal chromium concentration in Figure 7.11. The least squares method was used to fit the experimental points to the cubic equation:

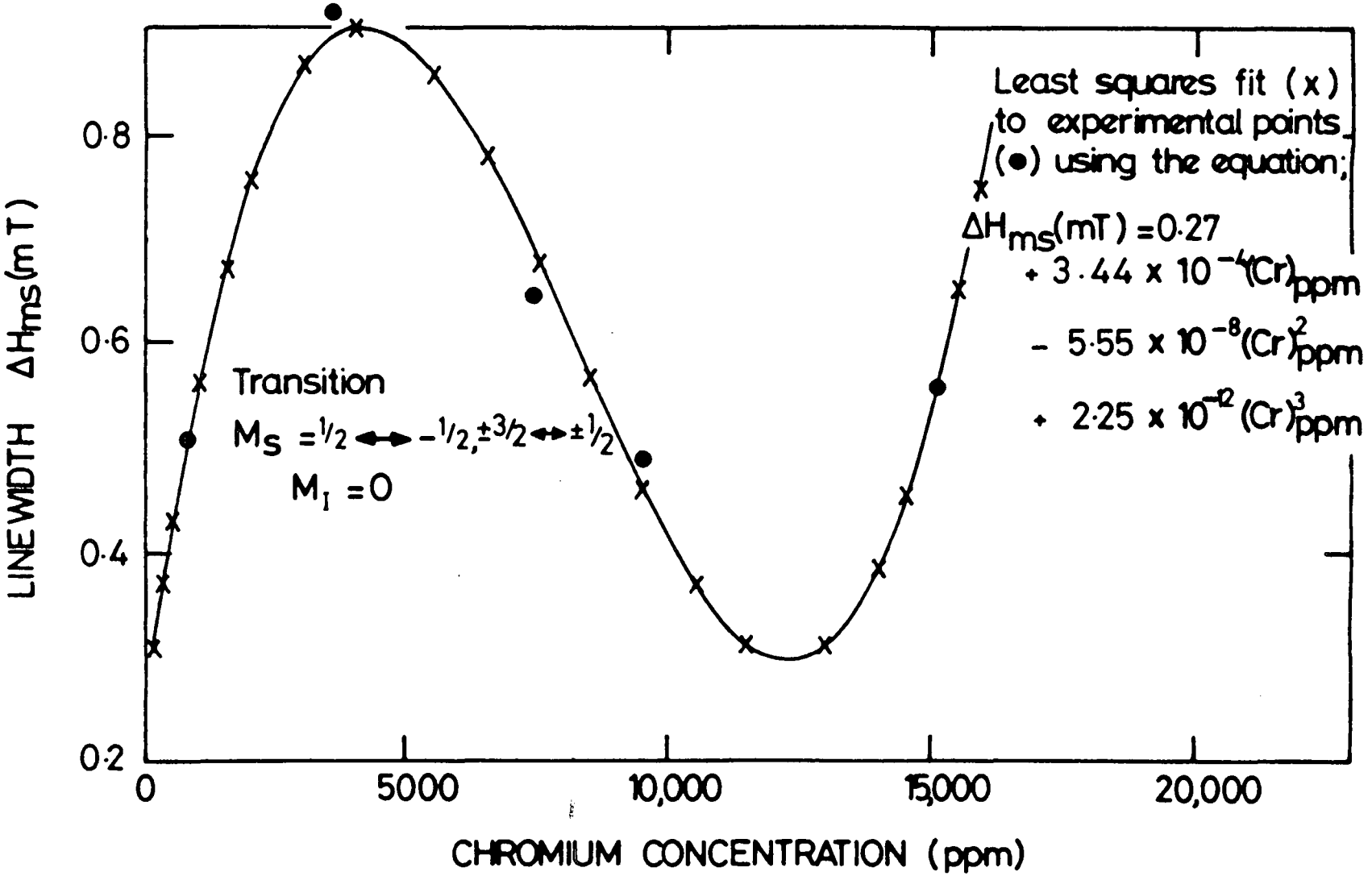

FIGURE 7.11 VARIATION OF LINEWIDTH WITH CHROMIUM CONCENTRATION FOR SINGLE CRYSTAL Cr/MgO (293K, H// <100>).

$$\Delta H_{MS}(mT) = 0.27 + 3.44 \times 10^{-4}[Cr] - 5.55 \times 10^{-8}[Cr]^2 + 2.25 \times 10^{-12}[Cr]^3 \quad (7.4)$$

where [Cr] is the nominal chromium concentration in p.p.m. by weight.

It is clear from Figure 7.11 that the experimental dependence of E.P.R. linewidth upon chromium concentration does not agree with that predicted by the dipolar broadening theory of de Biasi and Fernandes.[7.18] The measured linewidths are much smaller than expected and the form of the experimental curve does not correspond with that of any one of the theoretical curves calculated for different ranges of the exchange interaction using de Biasi and Fernandes' model. Indeed, the measured linewidths are so much smaller than those predicted by dipolar broadening theory, it has been assumed in the past, quite reasonably, that the central transition linewidth is independent of the chromium concentration.[7.2]

This discrepancy between theory and experiment is not due to the fact that de Biasi and Fernandes' model is, strictly speaking, only valid for powders since the variation of the E.P.R. linewidth of the central transition in the cubic Cr^{3+} spectrum with chromium concentration for powdered samples is very similar to that shown in Figure 7.11 for single crystal samples (see section 7.2.4). Nor is the discrepancy due to any misapplication of de Biasi and Fernandes' theory; in fact, the theory is particularly applicable to Cr^{3+} in a cubic environment because there is no zero-field splitting of the spin energy levels.

As was shown in section 7.1.1, the vast majority of isolated chromium atoms exist in the trivalent state in octahedral symmetry sites. However, assuming that dipolar interactions are the major factor in determining the magnitude of the linewidth in the cubic Cr^{3+} spectrum, we must conclude that only a small fraction of the total number of chromium atoms (which is equal to the nominal dopant concentration) contribute towards this spectrum. This apparent contradiction may be resolved by recalling that the RHEED investigations, at least for the samples with the higher chromium contents, showed that a substantial number of the dopant ions are not isolated but instead cluster together to form precipitates of the spinel phase $MgCr_2O_4$. It is also possible that spinel formation takes place in the more lightly doped samples but if this is the case, then the precipitate concentration is too low for them to be detected using the RHEED technique. Therefore, it is proposed that the nominal dopant concentration is approximately equal to the concentration of isolated Cr^{3+} ions in cubic sites plus the concentration of clustered Cr^{3+} ions in the spinel phase magnesiochromite i.e.

$$[Cr]_{nominal} \simeq [Cr^{3+}]_{\substack{isolated,\\ cubic\ sites}} + [Cr^{3+}]_{spinel} \quad (7.5)$$

The above relationship excludes the concentrations of isolated Cr^{3+} ions in non-cubic sites and of chromium atoms not in the (+3) valency state but, as already mentioned and as was shown in section 7.1.1, these are extremely small and may be ignored without seriously affecting the accuracy

of equation 7.5.

Evidence which supports the above interpretation is provided by the literature, in that formation of $MgCr_2O_4$ has been observed in MgO:Cr samples with chromium concentrations comparable to those in the samples examined here using a variety of analytical techniques such as magnetic susceptibility measurements, E.P.R., x-ray diffraction and diffuse reflectance spectroscopy[7.19 -7.23] It has been noted that the solubility of Cr^{3+} ions in MgO is considerably increased if an equal number of Li^+ ions are also added. This is because no charge compensation is required for Cr^{3+}-Li^+ pairs; if only Cr^{3+} is introduced into the MgO lattice the excess positive charge of this ion with respect to the Mg^{2+} ion it replaces cannot be easily compensated for either by valency variation or by cation vacancies and hence its solubility is limited.[7.20,7.21] This lack of solubility encourages the chromium dopant ions to cluster because in the spinel phase, $MgCr_2O_4$, the charges of the ions balance and therefore charge compensation by one of the mechanisms just mentioned is not required.

The RHEED evidence for spinel formation is purely qualitative i.e. using this technique we may only discover whether magnesiochromite is present or absent in any given sample. The E.P.R. linewidth data is important mainly because it may be used in conjunction with dipolar broadening theory to determine the concentration of isolated Cr^{3+} ions in cubic sites. Equation 7.5 then allows us to calculate the concentration of Cr^{3+} ions in the separate magnesiochromite phase. However, since de Biasi and Fernandes' dipolar broadening theory only applies to powders,

the best estimate of the concentration of isolated Cr^{3+} ions in octahedral sites may be determined from the linewidth of the central transition in the cubic Cr^{3+} spectrum of a powder sample. Therefore, the linewidth data relating to the cubic Cr^{3+} spectra of the powder samples which is reported in section 7.2.4, will be used to calculate $[Cr^{3+}]_{\substack{\text{isolated} \\ \text{cubic sites}}}$ and $[Cr^{3+}]_{spinel}$ for each doped sample and details of the calculation will also be given in the same section.

Although magnesiochromite is antiferromagnetic, at room temperature it is above its Néel temperature and therefore displays paramagnetic behaviour so that it should give rise to a characteristic E.P.R. spectrum. In fact, a symmetrical broad line, of approximate peak-to-peak width 40mT which is centred on the cubic Cr^{3+} isolated ion spectrum (i.e. its g-value is 1.9800) has been detected in chromium doped MgO samples and identified with magnesiochromite.[7.21] There is some indication that a line of this nature is present in the extended E.P.R. spectrum of the sample doped with 15,100 p.p.m. of chromium shown in Figure 7.12. No broad line with a g-value of 1.9800 is seen in the full E.P.R. spectrum of the sample containing 800 p.p.m. of chromium (Figure 7.4). These E.P.R. observations are consistent with the RHEED results reported in the previous section since they indicate that spinel precipitates are only present in detectable quantities in the samples with the highest dopant concentrations. However, neither the RHEED nor the E.P.R. data conclusively proves that magnesiochromite precipitates are not present

FIGURE 7.12 EXTENDED E.P.R. SPECTRUM OF SINGLE CRYSTAL Cr/MgO; 15,100 p.p.m. Cr, 293K, H// <100>, ν = 9.2540 GHz.

in the more lightly doped samples; it is possible that neither technique has sufficient sensitivity to show their presence at the low concentration levels they are expected to have in these samples. Furthermore, it is reasonable to conclude that, using E.P.R., we will be unable to detect the presence of magnesiochromite precipitates if their concentration in the MgO host lattice is low because the line associated with this material is broad. It is well known that broad lines are less readily detected than narrow lines (such as those belonging to the cubic Cr^{3+} spectrum).

7.1.4 EVIDENCE FOR LATTICE STRAIN

The relative gains used to record cubic Cr^{3+} spectra of equal peak heights from the sample doped with 800 p.p.m. of chromium as it was rotated relative to the magnetic field in a [100] plane are shown in Table 7.2. The relative gain is at a minimum when H is parallel to a cubic axis and steadily increases to reach its maximum value when H is parallel to a <110> -type direction. This indicates that, for a fixed relative gain, the peak height is maximum when H // <100> and minimum when H // <110>.

Similar variations in the intensity of the cubic Cr^{3+} spectrum with the angle between the magnetic field and the crystal axes have been noted in the literature and explained in terms of a spread in the values of the crystal field parameters.[7.24] That the crystal field parameters are not equal for all Cr^{3+} ions is in turn indicative of the presence of strain in the regions of the lattice surrounding the sites occupied by the paramagnetic impurity

ions.

The $M = \pm 3/2 \longleftrightarrow \pm 1/2$ lines are broadened and their width is anisotropic (having its maximum value when $H \,//\, \langle 110 \rangle$ and its minimum value when $H \,//\, \langle 100 \rangle$) if random internal stresses are present in the crystal, whereas the $M = +\frac{1}{2} \longleftrightarrow -\frac{1}{2}$ line is not affected by lattice strain, and it is narrow and isotropic as it would be in a strain-free sample. Thus, the effect of strain on the widths of the lines corresponding to the various transitions explains the variation of the peak height with the angle between the magnetic field and the crystal axes which is found experimentally.

Unfortunately, the strain broadening theory discussed in section 6.3 cannot be applied to the cubic Cr^{3+} spectrum. To use this theory to assess the degree of strain in the regions of the host lattice immediately surrounding the paramagnetic ions, it must be possible to measure individually the widths of lines with different values of the electronic magnetic quantum number, M.[7.25] In the cubic Cr^{3+} spectrum the lines corresponding to the $M = +1/2 \longleftrightarrow -1/2$ and $M = \pm 3/2 \longleftrightarrow \pm 1/2$ transitions all coincide at the same value of magnetic field and therefore their individual widths cannot be determined. If the Cr^{3+} ions occupy axially symmetric sites then the $M = +1/2 \longleftrightarrow -1/2$ and $M = \pm 3/2 \longleftrightarrow \pm 1/2$ transitions are resolved and it has been shown that the angular variation of their linewidth is consistent with that predicted by the strain broadening theory described in section 6.3, which was also used to calculate the line broadening due to strain in the samples examined.[7.26]

The effect of heat treatment upon the linewidth of the central transition in the cubic Cr^{3+} spectrum of the single crystal doped with 3,600 p.p.m. of chromium provides further evidence for lattice strain. The heat treatments were carried out for various lengths of time at 500^{o}C in an oxygen atmosphere and after each annealing period the sample was allowed to cool down gradually to room temperature over a period of 10 hours. That similar spectrometer gains were used to record similar intensity spectra from the sample after each heat treatment suggests that the 'annealing' process does not appreciably change the concentration of isolated Cr^{3+} ions in octahedral symmetry sites. This evidence seems to verify the conclusion (which was arrived at with the aid of the $MgO-MgCr_2O_4$ phase diagram) that the particular conditions chosen for the heat treatment would optimize the reduction in lattice strain whilst maintaining the room temperature distribution of the chromium dopant between the isolated Cr^{3+} ion and clustered Cr^{3+} ion ($MgCr_2O_4$) phases (see Chapter 2).

The cubic Cr^{3+} spectrum was recorded from the single crystal containing 3,600 p.p.m. of chromium at room temperature with the magnetic field parallel to a cubic axis after it had been subjected to 0, 12, 35, 83 and 155 hours of the 'annealing' heat treatment described above. The g-factor, hyperfine structure constant, A, and peak-to-peak linewidth of the central transition, ΔH_{MS}, were measured for each spectrum (using the procedures described in section 7.1.1.) and the values obtained are shown in Table 7.3 together with the microwave frequencies at which the measurements were taken.

'ANNEALING' TIME (HRS)	LINEWIDTH (mT)	g - FACTOR	HYPERFINE STRUCTURE CONSTANT A($\times 10^4$ cm^{-1})	FREQUENCY (GHz)
0	0.921	1.9799	16.61	9.4295
12	0.586	1.9795	16.46	9.3820
35	0.530	1.9793	16.42	9.3820
83	0.482	1.9795	16.38	9.3825
155	0.463	1.9793	16.39	9.3825

TABLE 7.3 E.P.R. PARAMETERS AT 293K FOR 3600 p.p.m. Cr/MgO SINGLE CRYSTAL SAMPLE 'ANNEALED' FOR VARIOUS TIMES.

Not surprisingly, the heat treatment has no noticable effect on the crystal field parameters A and g, which retain the values characteristic of Cr^{3+} ions in octahedral symmetry even after an annealing period of 155 hours. However, the peak-to-peak linewidth, ΔH_{MS}, steadily decreases as the annealing time increases. This is shown graphically in Figure 7.13(a). The decrease of ΔH_{MS} with increasing annealing time appears from Figure 7.13(a) to follow an exponential decay and might therefore be expected to obey an equation of the form:

$$[\Delta H_{MS}]_t = [\Delta H_{MS}]_o e^{-\alpha t} \qquad (7.6)$$

where $[\Delta H_{MS}]_o$ and $[\Delta H_{MS}]_t$ are the peak-to-peak linewidths before heat treatment and after a heat treatment of t hours respectively and α is a constant. α may be determined from the slope of the plot of $\ln[\Delta H_{MS}]$ against annealing time, t, which is illustrated in Figure 7.13(b).

A decrease in the concentration of isolated Cr^{3+} ions in cubic sites would result in a reduction of ΔH_{MS}, simply because the degree of line broadening arising from dipolar interactions would decrease. However, it has already been demonstrated that the annealing process is unlikely to bring about a reduction in the concentration of these ions. Therefore, it is proposed that the linewidth decreases after annealing because internal strains in the crystal, which lead to E.P.R. line broadening, are removed or at least reduced in magnitude as a result of heat treatment.

In fact, Figure 7.13(b) would seem to indicate that there are two sources of strain in the crystal. One source

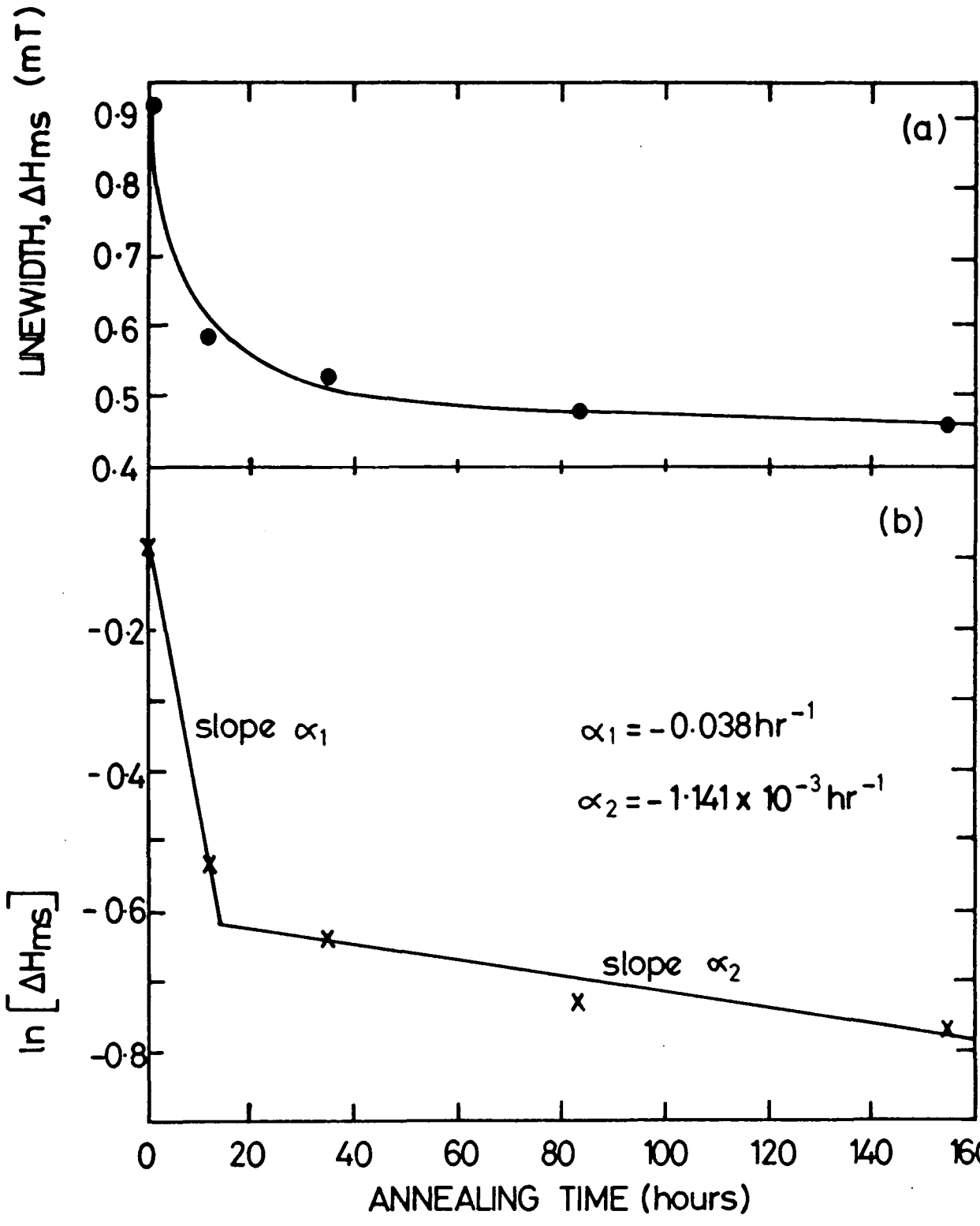

FIGURE 7.13 VARIATIONS OF (a) LINEWIDTH ΔH_{ms} AND (b) ln $[\Delta H_{ms}]$ WITH ANNEALING TIME; SINGLE CRYSTAL Cr/MgO, 3,600 p.p.m. Cr, H// <100>, 293K.

of lattice strain is readily removed by the heat treatment and consequently the initial decrease in linewidth (up to t = 14 hours) is rapid (the exponential decay in linewidth is characterized by α = -0.038 hr^{-1}). The other source of strain is not relieved so rapidly by the annealing process and hence when t exceeds 14 hours the exponential decay of the linewidth is less rapid (α = -1.141 x 10^{-3} hr^{-1}).

The change in the rate of decrease of the linewidth at t = 14 hours is not likely to be due to the physical shape of the sample i.e. it is not because the strain in the regions of the lattice surrounding paramagnetic ions near the surface is relieved faster than the strain in the regions of the lattice surrounding paramagnetic ions in the bulk. This may be deduced from a similar plot of ln[linewidth] versus annealing time for the powdered sample of MgO:Cr containing 3,600 p.p.m. of chromium (see section 7.2.3). Although the ratio of surface area to volume is much greater for the powder than for the single crystal, this does not seem to influence the effect of the heat treatment upon the linewidth. As Figures 7.13(b) and 7.16(b) show, both the single crystal and powder curves have the same form: in each case there are two distinct rates at which the linewidth decreases, the annealing times at which the change in rate occurs are similar (t(single crystal) = 14 hours, t(powder) = 18 hours) and the magnitudes of the decrease in the linewidth brought about by the annealing process are also similar.

Each isolated Cr^{3+} ion in octahedral symmetry has a

cation vacancy associated with it and although both types of point defect will distort the lattice in the regions where they are located (both cause local extensional strains because the lattice 'collapses in' on them - see section 2.2) the strain fields surrounding them will be different. Therefore, it is proposed that, of the two different rates of decrease in the linewidth, one is associated with strain relief in the regions of the lattice surrounding the cationic vacancies and that the other is associated with removal of lattice strain in the regions where the isolated Cr^{3+} ions are located in substitutional sites. The rapid decay in the linewidth (characterized by $\alpha = -0.038\ hr^{-1}$) is probably a result of cationic vacancy strain relief and therefore the slower decay in the linewidth (characterized by $\alpha = -1.141 \times 10^{-3}\ hr^{-1}$) is probably caused by the removal of lattice distortion originally brought about when Mg^{2+} ions are replaced by Cr^{3+} dopant ions in the host material.

7.2 EXPERIMENTAL RESULTS FOR MgO:Cr POWDERS

7.2.1 CHARACTERIZATION OF THE E.P.R. SPECTRA

Powders were prepared from single crystal chippings of all five chromium doped MgO samples. The chippings were crushed with a mortar and pestle and the powders thus produced were sieved through a 185 μm mesh. This ensured that at least 20,000 individual crystallites were absorbing microwave power during resonance, a sufficient number to yield a powder spectrum with a low level of background noise.

Spectra were recorded from all five powders on the

Varian V4205-15 E.P.R. spectrometer at room temperature. The traces obtained were very similar and a typical example is shown in Figure 7.14 (this particular spectrum was recorded from the powder with a nominal chromium concentration of 800 p.p.m. by weight). Comparison of Figures 7.1 and 7.14 shows that these spectra are almost identical. The spectrum illustrated in Figure 7.14 may therefore be identified with isolated Cr^{3+} ions in sites of octahedral symmetry.

That the cubic Cr^{3+} spectrum survives in the powder samples is not surprising since it is isotropic (that this is so is clearly demonstrated by the isofrequency plot of Figure 7.2).Hence, although a powder is a collection of randomly oriented crystallites, whatever the orientation of any given crystallite with respect to the external field, H, the magnetic field values at which resonance occurs will always be the same i.e. the resonant magnetic fields of the various transitions are independent of angle.

The cubic Cr^{3+} spectra obtained from the powder samples were analysed using exactly the same procedures as were used to analyse the corresponding spectra in the case of the single crystal samples (see section 7.1.1). The values obtained for g, A and the linewidth of the central transition between points of maximum slope, ΔH, are shown in Table 7.4 together with the microwave frequencies at which the measurements were taken. Because the spectrum is isotropic, g and A are also isotropic and, not surprisingly, the values given in Table 7.4 for these parameters agree well (within experimental error) with those obtained from the single crystal samples (Table 7.1) and

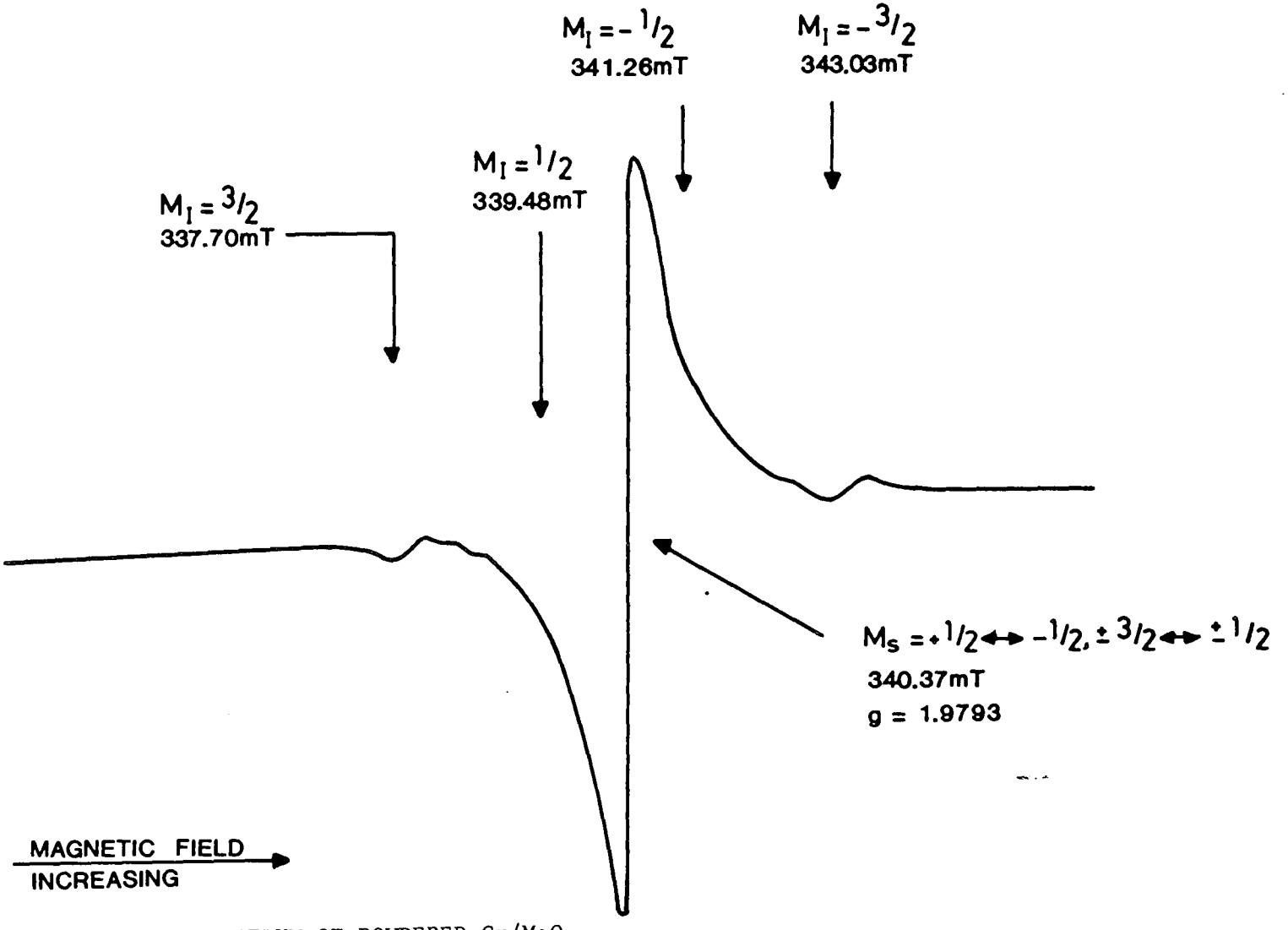

FIGURE 7.14 DETAIL OF E.P.R. SPECTRUM OF POWDERED Cr/MgO SINGLE CRYSTAL; 800p.p.m. Cr, 293K, 9.4290 GHz.

CHROMIUM CONCENTRATION (p.p.m.)	LINEWIDTH (mT)	g - FACTOR	HYPERFINE STRUCTURE CONSTANT $A(\times 10^{4}\ cm^{-1})$	FREQUENCY (GHz)
800	0.568	1.9793	16.43	9.4290
3600	0.929	1.9804	16.41	9.4275
7400	0.721	1.9797	16.31	9.4280
9500	0.587	1.9793	16.42	9.4270
15100	0.674	1.9791	16.59	9.4275

TABLE 7.4 E.P.R. PARAMETERS FOR POWDERED Cr/MgO SAMPLES (SIEVED THROUGH 185 μm MESH), 293K.

also with those published in the literature.[7.1 - 7.3] It is noticable that, for each doped sample, ΔH in the powder is greater than ΔH_{MS} in the corresponding single crystal. That the linewidth increases on powdering a single crystal sample will be discussed in terms of strain broadening theory in section 7.2.3.

Only the cubic Cr^{3+} spectrum is observed for the powder samples. The axial Cr^{3+} spectrum and the Cr^{3+} pair spectrum, both of which were observed for the single crystal samples, are not seen. This is because these spectra are highly anisotropic and therefore the transitions associated with them will be spread over a wide range of magnetic field when the MgO:Cr sample is in powder form. Thus, the intensities of the transitions will also be spread over a wide range of magnetic field. For the axial Cr^{3+} and Cr^{3+} pair spectra the "smearing out" of the intensities of the transitions must be quite substantial since they are rendered undetectable by this effect.

Thus, in a way, the powder spectra are much 'cleaner' than the single crystal spectra in that the number of lines observed is greatly reduced. This is particularly true for the sample containing 9,500 p.p.m. of chromium. In the single crystal spectrum of the sample doped at this level, the degree of background noise is so great that the hyperfine transitions due to the Cr^{53} isotope cannot be observed. In the powder spectrum of the same sample the background noise has almost completely disappeared; the Cr^{53} hyperfine transitions are clearly visible and from their field positions, as Table 7.4 shows, a value for the hyperfine structure constant, A, was deduced. We must

conclude that much of the background noise in the spectrum of the single crystal sample doped with 9,500 p.p.m. of chromium in fact consists of low intensity, anisotropic E.P.R. transitions associated with unknown impurities which, like the transitions of the axial Cr^{3+} and Cr^{3+} pair spectra, are "smeared out" in the spectrum of the powder sample and rendered undetectable.

7.2.2 COMPUTER SIMULATION OF THE POWDER SPECTRA

Computer simulations of the powder spectrum of Cr^{3+} in octahedral sites in MgO were undertaken using all three numerical methods described in section 5.3. At any given dopant concentration, the spectra predicted by the various methods were identical and typical examples of the simulations obtained for the powders containing 800 p.p.m. and 15,100 p.p.m. of chromium are shown in Figures 7.15(a) and 7.15(b) respectively.

The variables in the simulation procedure are the crystal field parameters (A and g), the microwave frequency, the lineshape function and the linewidth. At any given dopant concentration, the powder spectrum was simulated using a Lorentzian lineshape function whose peak-to-peak width corresponded with that of the central transition in the single crystal spectrum of the sample doped at the same level (ΔH_{MS} in Table 7.1). A Lorentzian lineshape function was chosen for the purposes of the simulation because analysis of the central transition in the single crystal cubic Cr^{3+} spectra showed that it had this shape.

The values of A and g determined experimentally from the single crystal spectrum at a particular dopant

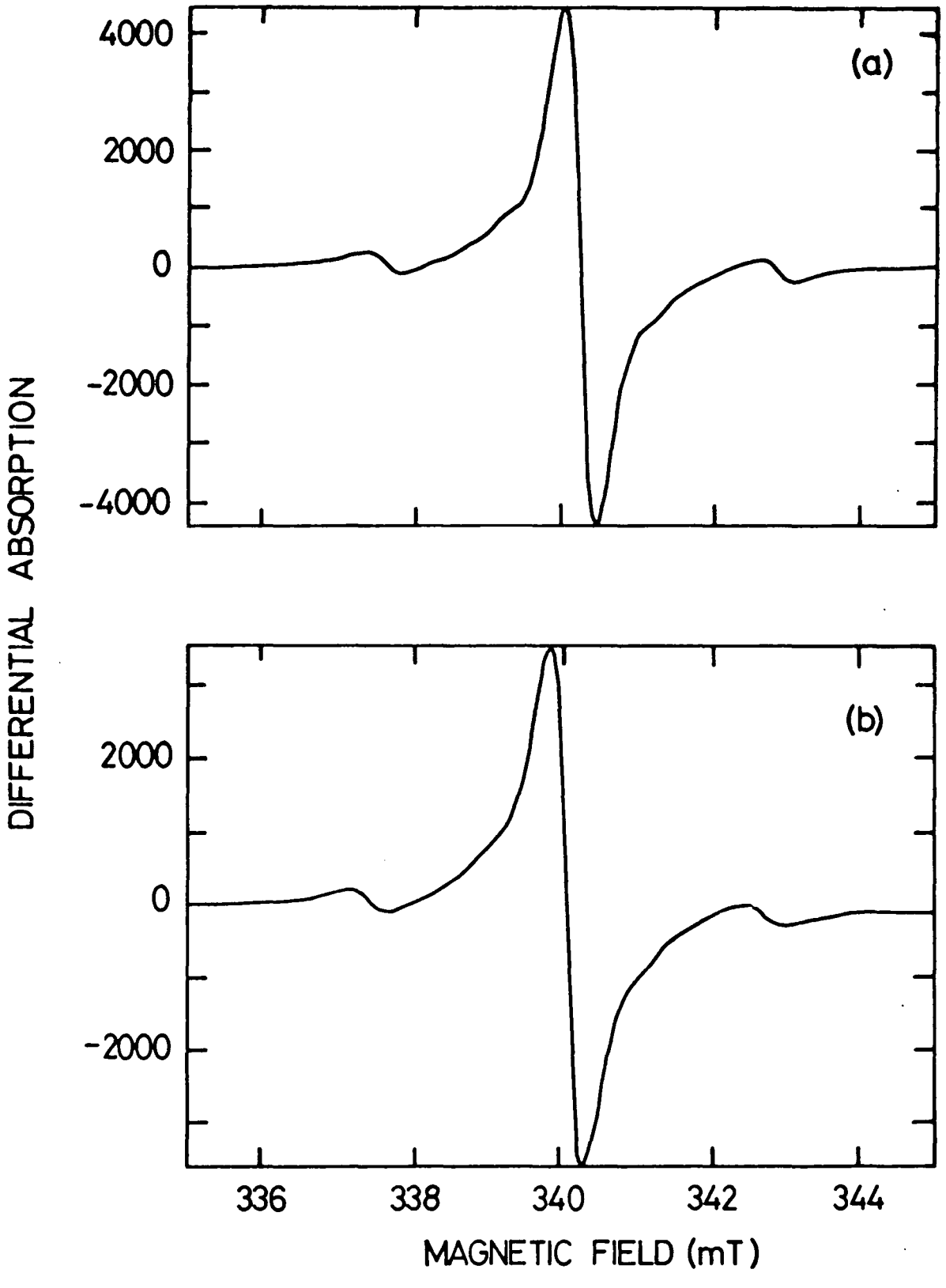

FIGURE 7.15 COMPUTER SIMULATED POWDER SPECTRA FOR Cr/MgO
(a) 800p.p.m. Cr
(b) 15,100 p.p.m. Cr USING CORRESPONDING SINGLE CRYSTAL LINEWIDTHS.

concentration were used to simulate the powder spectrum at the same dopant concentration. Since A could not be determined from the single crystal spectrum of the sample doped with 9,500 p.p.m. of chromium, the powder spectrum was simulated at this dopant concentration using the average of the A values obtained from the other single crystal spectra (i.e. $A_{9,500} = 16.55 \times 10^{-4} cm^{-1}$).

At any given doping level, the powder spectrum was simulated at the microwave frequency used to record the experimental powder spectrum so that the field positions of spectral lines in the simulated and experimental powder spectra could be directly compared. Thus, the powder spectra of the five MgO:Cr powders examined were simulated at the microwave frequencies given in Table 7.4.

Since single crystal parameters were used in the simulation procedure and the cubic Cr^{3+} spectrum is isotropic, the computed powder spectrum at any given dopant concentration should, if the simulation procedure is valid, be identical to the experimental single crystal spectrum at the same dopant concentration except that the magnetic field values at which the transitions occur will be shifted to those appropriate for the microwave frequency at which the experimental powder spectrum was recorded. Therefore, g, A and the linewidth between points of maximum slope were determined from the computed spectra and it was found that they agreed well, at all dopant concentrations, with the corresponding single crystal values. This agreement shows that the numerical simulation methods described in section 5.3 are valid and it may be assumed that, if the appropriate single crystal resonance conditions are used, the numerical

simulation methods will accurately predict the powder spectrum of any paramagnetic species. For $^6S_{5/2}$ ions in cubic sites, if the spectrum computed using the numerical methods of section 5.3 agrees with the spectrum computed using the analytical method of section 5.4, then the analytical method may also be assumed to be valid.

7.2.3 STRAIN BROADENING OF THE CENTRAL TRANSITION IN THE CUBIC Cr^{3+} POWDER SPECTRA

At any given dopant concentration, the linewidth of the central transition of the cubic Cr^{3+} spectrum measured for the single crystal sample is comparable to its width in the computer simulated powder spectrum, although this line is broader in the experimental powder spectrum. At all dopant concentrations, the powder spectrum was simulated assuming that the linewidth was independent of the crystallite orientation and equal to the single crystal value when the magnetic field, H, is parallel to a <100>-type direction in the crystal. Therefore it might be thought that the discrepancy between the width of the central transition in the experimental and simulated powder spectra is due to the variation of dipolar linewidth with the orientation of the magnetic field to the crystal axes. Calculations using dipolar theory have shown that, in the [100] plane, a plot of dipolar linewidth against the angle θ between a reference <100> direction in the crystal and the magnetic field is symmetrical about $\theta = 45^{o}$ and that the dipolar linewidth is minimum when H // <100> and maximum when H is oriented along the <110> direction.[7.2]

However, it has been reported in the literature[7.2]

that, at all the dopant concentrations examined here, the width of the central transition in the cubic Cr^{3+} spectrum is independent of the angle θ between the magnetic field and the crystal axes. Evidence which supports this conclusion is provided by the plot of linewidth against polar angle in the [100] plane for the single crystal doped with 800 p.p.m. of chromium shown in Figure 7.3, which demonstrates that the linewidth is approximately constant at all values of θ. Thus it appears that dipolar effects cannot explain the increase in the width of the central line in the cubic Cr^{3+} spectrum when a single crystal is powdered.

We propose that the linewidth of the $M = +1/2 \longleftrightarrow -1/2$, $\pm 3/2 \longleftrightarrow \pm 1/2$ transitions is greater in the powder than in the single crystal due to the effects of lattice strain. Two experiments were undertaken which provided evidence supporting this suggestion.

Firstly, a similar annealing experiment to that conducted for the single crystal doped with 3,600 p.p.m. of chromium (which was reported in section 7.1.4) was undertaken for the powder doped with 3,600 p.p.m. of chromium. Table 7.5 shows the values of g, A and linewidth between points of maximum slope, ΔH, measured from the cubic Cr^{3+} spectra which were recorded after the powder had been subjected for various lengths of time to the "annealing" heat treatment described in section 7.1.4 (the annealing times and microwave frequencies at which the spectra were recorded are also given in Table 7.5). A plot of the linewidth of the central transition against annealing time is illustrated in Figure 7.16(a) and Figure 7.16(b) shows

'ANNEALING' TIME (hrs)	LINEWIDTH (mT)	g - FACTOR	HYPERFINE STRUCTURE CONSTANT A(x 10^4 cm^{-1})	FREQUENCY (GHz)
0	0.929	1.9804	16.41	9.4275
12	0.772	1.9791	16.60	9.3800
24	0.690	1.9796	16.42	9.3790
35	0.699	1.9792	16.56	9.3800
83	0.646	1.9791	16.58	9.3805
155	0.617	1.9790	16.50	9.3800

TABLE 7.5 E.P.R. PARAMETERS AT 293K for 3600 p.p.m. Cr/MgO POWDER SAMPLES 'ANNEALED' FOR VARIOUS TIMES.

the relationship between ln(linewidth) and the annealing time.

As in the single crystal case, A and g are unaffected by the annealing process. The decrease of the linewidth and the natural log of the linewidth with the annealing time is also similar in form for the single crystal and powdered samples doped with 3,600 p.p.m. of chromium. However, for the powdered sample the decrease of the linewidth (and consequently the natural log of the linewidth) is less rapid than for the single crystal.

That Figures 7.13(a) and 7.16(a) and also Figures 7.13(b) and 7.16(b) are virtually identical indicates that the sources of strain in the single crystal and powder samples are the same. Thus the comments of section 7.1.4 concerning the effects that the specified heat treatment has upon the strain broadened central transition in the cubic Cr^{3+} spectrum of the single crystal doped with 3,600 p.p.m. of chromium may equally well be applied to the corresponding powder sample. Therefore, the sources of strain in the powder which produce two different rates of decrease in the linewidth are associated with lattice distortion in:

a) the regions immediately surrounding the cationic vacancies
b) the regions immediately surrounding isolated Cr^{3+} ions in substitutional sites.

The exponential decay of the powder linewidth with increasing annealing time follows equation 7.6. In the two different regions of Figure 7.16(b) the values obtained for the parameter, α , were:

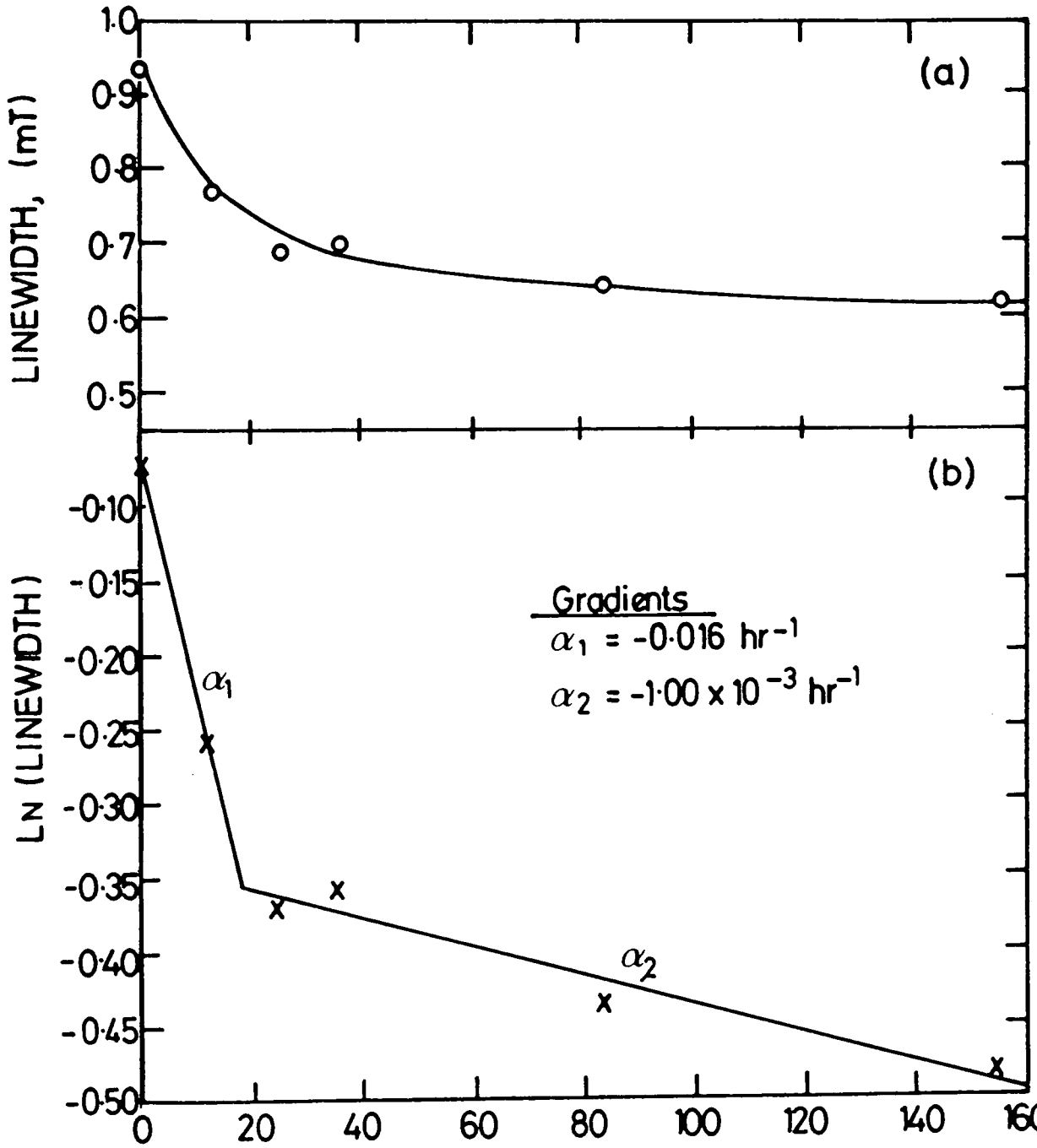

FIGURE 7.16 GRAPHS OF (a) LINEWIDTH AND (b) ln (LINEWIDTH) VERSUS ANNEALING TIME FOR 3,600 p.p.m. Cr/MgO POWDER SAMPLE 293K.

$$\alpha_1(t<18 \text{ hours}) = 0.016 hr^{-1} \quad \alpha_2(t>18 \text{ hours}) = -1.00 \times 10^{-3} hr^{-1}.$$

As the corresponding values for the single crystal sample are $\alpha_1 = -0.038\ hr^{-1}$ and $\alpha_2 = -1.141 \times 10^{-3}\ hr^{-1}$ it is clear that both types of lattice strain (one associated with vacancies, the other with isolated Cr^{3+} ions in substitutional sites) are relieved by the annealing process at a slower rate in the powder than in the single crystal.

It is proposed that this is because the grinding process used to create the powders increases the lattice distortion in the regions surrounding each cationic vacancy and each isolated Cr^{3+} ion located at a substitutional site. Thus in these regions the lattice strain is less easily removed by the annealing process than in the single crystal case and consequently the linewidth of the central transition of the cubic Cr^{3+} spectrum decreases less rapidly in the powder than in the single crystal.

A fact which supports this point of view is that the annealing time at which the rapid decrease in the linewidth ceases is greater in the case of the powder than in the case of the single crystal. This indicates that there is more of the strain associated with the rapid decrease in the linewidth (assumed to be due to the lattice distortion in the regions surrounding cation vacancies) in the powder sample doped with 3,600 p.p.m. of chromium than in the single crystal sample doped at the same level.

Secondly, all five chromium doped MgO powders were "annealed" for 24 hours using the heat treatment described

in section 7.1.4. Cubic Cr^{3+} spectra were recorded and the values obtained for the crystal field parameters (A & g) and the linewidth between points of maximum slope at each dopant concentration are given in Table 7.6 together with the microwave frequencies at which the measurements were taken. Once again, g and A are unaffected by the annealing process whilst, at each dopant concentration, the linewidth of the cubic Cr^{3+} central transition is less in the spectrum of the heat treated powder than in the spectrum of the powder before heat treatment.

Comparison of Tables 7.4 and 7.6 shows that, although not true in every case, in general "annealing" has the greatest effect on the powders which have the largest linewidths before heat treatment. This seems to indicate that the greater the initial amount of strain in a powder sample, the greater will be the reduction in lattice distortion for a given period of heat treatment. In addition, comparison of Tables 7.1 and 7.4 shows that the increase in the linewidth of the $M = +1/2 \longleftrightarrow -1/2, \pm 3/2 \longleftrightarrow \pm 1/2$ transition in the cubic Cr^{3+} spectrum upon powdering a single crystal sample is, in general, greater the smaller the initial single crystal linewidth. This leads us to conclude that powdering a single crystal sample introduces lattice distortion more readily if the single crystal is relatively strain free than if the single crystal is highly strained. Thus it appears there is a maximum amount of lattice distortion (i.e. a "saturation" level of strain) which the host lattice can support.

CHROMIUM CONCENTRATION (p.p.m.)	LINEWIDTH (mT)	g - FACTOR	HYPERFINE STRUCTURE CONSTANT A(x 10^4 cm^{-1})	FREQUENCY (GHz)
800	0.556	1.9795	16.48	9.3805
3600	0.690	1.9796	16.42	9.3790
7400	0.437	1.9793	16.38	9.3790
9500	0.416	1.9795	16.11	9.3790
15100	0.442	1.9793	16.49	9.3790

TABLE 7.6 E.P.R. PARAMETERS AT 293K for 'ANNEALED' Cr/MgO POWDER SAMPLES ('ANNEALED' AT 500°C FOR 24 HRS AND COOLED SLOWLY (OVER ∿10 HRS))

7.2.4 THE VARIATION OF E.P.R. LINEWIDTH WITH CHROMIUM CONCENTRATION: EVIDENCE FOR SPINEL FORMATION

The linewidth between points of maximum slope, ΔH, of the central transition in the cubic Cr^{3+} spectrum was measured for each powder sample and each "annealed" powder sample (see Tables 7.4 and 7.6) and the values obtained are showed plotted against total nominal chromium concentration in Figures 7.17 and 7.18 respectively. The data points lie on curves described by cubic equations. Using the least squares method, the equation giving the best fit to the experimental points for the powder samples was found to be:

$$\Delta H_{MS}(mT) = 0.36 + 2.98 \times 10^{-4}[Cr] - \ldots \ldots -4.74 \times 10^{-8}[Cr]^2 + 1.92 \times 10^{-12}[Cr]^3 \quad (7.7)$$

whilst for the annealed powder samples the best fit was obtained for the equation:

$$\Delta H_{MS}(mT) = 0.49 + 1.18 \times 10^{-4}[Cr] - \ldots \ldots -2.33 \times 10^{-8}[Cr]^2 + 1.01 \times 10^{-12}[Cr]^3 \quad (7.8)$$

where [Cr] is the nominal total chromium concentration in p.p.m.

The variation of linewidth with chromium concentration for the powder samples and also for the "annealed" powder samples is very similar in form to that for the single

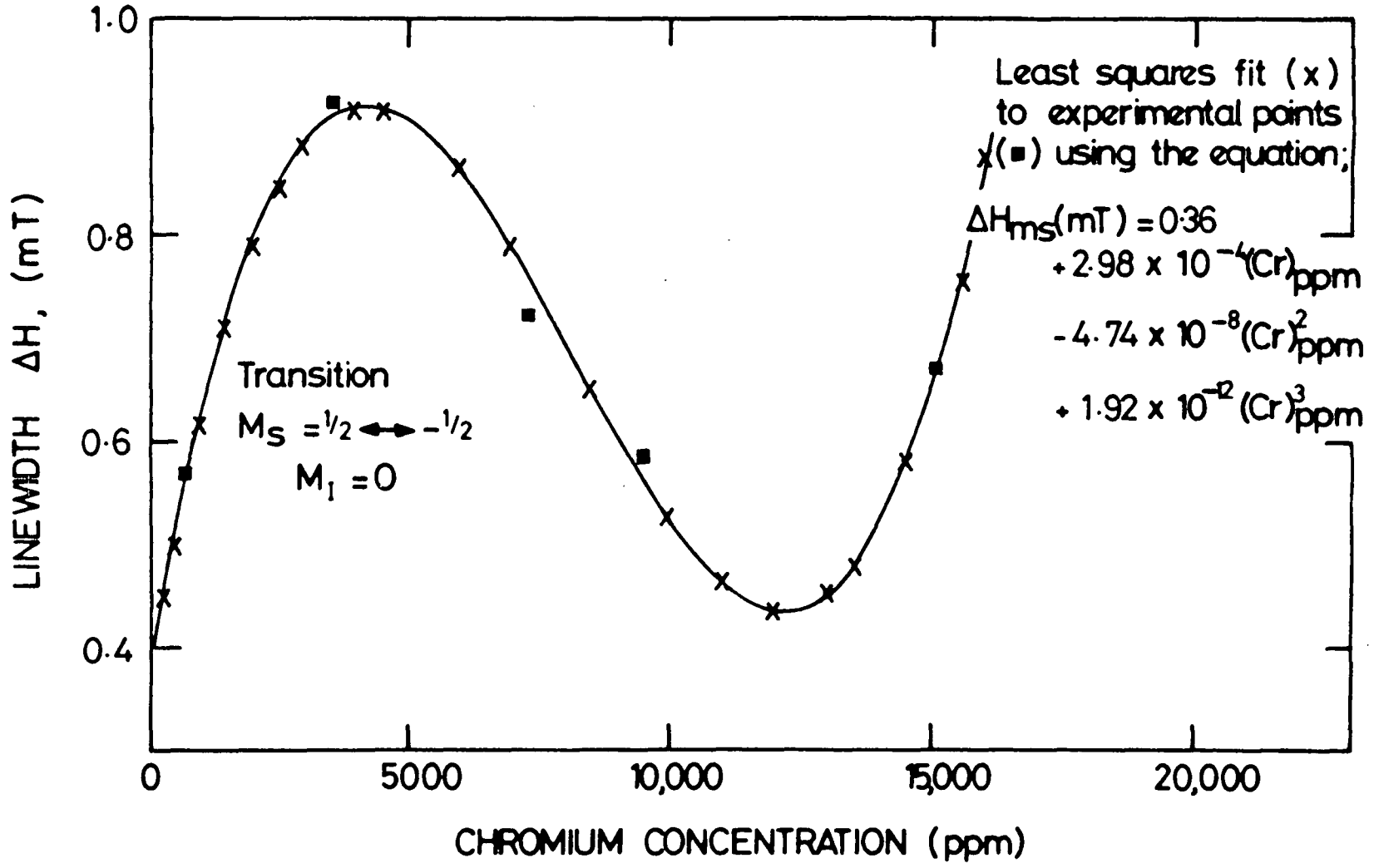

FIGURE 7.17 VARIATION OF LINEWIDTH WITH CHROMIUM CONCENTRATION FOR POWDERED Cr/MgO; 293K.

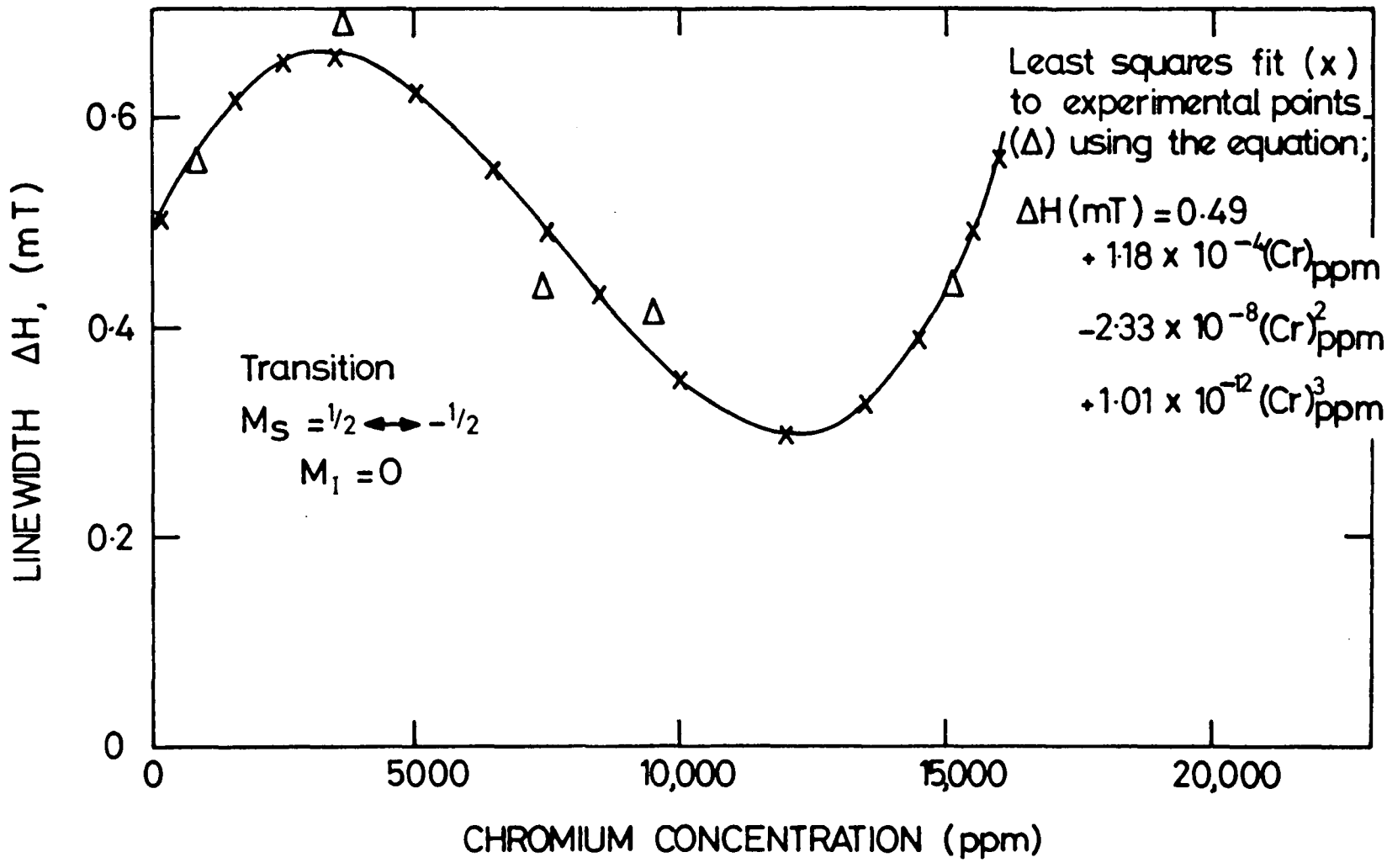

FIGURE 7.18 VARIATION OF LINEWIDTH WITH CHROMIUM CONCENTRATION FOR ANNEALED Cr/MgO POWDERS; 293K.

crystal samples when H is parallel to a <100> direction in the crystal (see Figure 7.11). Thus, for the reasons given in section 7.1.3, the experimental dependence of linewidth upon nominal chromium concentration for both the powder and annealed powder samples cannot be explained in terms of de Biasi and Fernandes' dipolar broadening theory[7.18] although MgO:Cr is an ideal system to which their theory may be applied. As described in section 7.1.3, we propose that the discrepancy between theory and experiment is due to the fact that a significant proportion of the chromium dopant exists in precipitates of the spinel phase $MgCr_2O_4$.

That MgO:Cr powders are particularly suitable for the application of de Biasi and Fernandes' model is demonstrated by the fact that they used experimental data obtained from such powders to test out their theoretical results. In disagreement with the present work, they found that the linewidths of the central transitions in the cubic Cr^{3+} spectra recorded from their samples laid on the theoretical curve for n = 5 (see Figure 6.1). Substituting the constants appropriate for chromium and n = 5 into equation 6.28, it follows that the dependence of the linewidth between points of maximum slope upon chromium concentration for de Biasi and Fernandes' samples obeys the equation:

$$\Delta H_{MS}(mT) = 629f(1-f)^{54} \qquad (7.9)$$

where f is the fractional chromium concentration.

We assume that the discrepancy between de Biasi and

Fernandes' results and ours arises because clustering of the chromium dopant did not take place in their samples. Furthermore de Biasi and Fernandes did not present any evidence for strain broadening of the cubic Cr^{3+} central transition and so we shall assume that their samples were strain free. Our annealed powder samples are relatively strain free and so the difference between the concentration dependence of the linewidth in these samples and de Biasi and Fernandes' can, to a good approximation, be accounted for by the fact that $MgCr_2O_4$ precipitates are present in our annealed powder samples but not in de Biasi and Fernandes'.

Supposing that equation 7.9 represents the concentration dependence of the linewidth when all the chromium dopant is present as isolated Cr^{3+} ions in cubic sites (of course, this equation also takes account of the small number of isolated ions which will, by chance, be close enough to interact via the exchange mechanism). Then we can find the points on the curve of this equation corresponding to the linewidths measured for our samples and read off from the fractional concentration axis the concentrations of chromium existing as isolated Cr^{3+} ions in cubic sites.

This procedure has been carried out for the annealed powder samples and the deduced isolated Cr^{3+} ion concentrations in sites of octahedral symmetry are given in column three of Table 7.7(a) in units of p.p.m. The remainder of the dopant is assumed to exist in the $MgCr_2O_4$ phase and the concentrations of this species (calculated simply by subtracting the isolated ion concentration from the total

TOTAL NOMINAL CHROMIUM CONCENTRATION (p.p.m.)	ΔHpp, mT (EXPERIMENTAL)	Cr^{3+} CONCENTRATION (p.p.m.)			
		ISOLATED ION	SPINEL	ISOLATED ION	SPINEL
3600	0.690	1514	2086	1656	1944
7400	0.437	902	6498	1209	6191
9500	0.416	870	8630	1265	8235
15100	0.442	934	14166	1700	13400

TABLE 7.7(a) DEDUCED CONCENTRATIONS OF Cr^{3+} EXISTING AS ISOLATED IONS AND IN THE SPINEL $MgCr_2O_4$ FOR THE 'ANNEALED' POWDER SAMPLES.

MAXIMUM ISOLATED Cr^{3+} ION CONCENTRATION*	REFERENCE
0	7.20
2.4 - 2.8	7.23
< 5.9	7.22
0.173	7.21
0.098	THIS WORK

* IN UNITS OF NUMBER OF Cr^{3+} IONS PER 100 Mg^{2+} IONS

TABLE 7.7(b) PUBLISHED DATA ON THE LIMITED SOLUBILITY OF ISOLATED Cr^{3+} IONS IN MgO.

nominal dopant concentration - see section 7.1.3) are given, in p.p.m., in column four of Table 7.7(a). The deduced concentrations, while approximately correct, do not take account of the small fraction of the dopant which exists as isolated Cr^{3+} ions in sites of axial symmetry.

Results for the sample doped with 800 p.p.m. of chromium are not presented in Table 7.7(a) because the measured linewidth for this sample is actually greater than that predicted by equation 7.9. Thus it is assumed that for this sample all the chromium dopant exists as isolated Cr^{3+} ions in cubic sites (with, of course a small fraction of the ions existing as exchange coupled pairs and a similarly small fraction existing as isolated Cr^{3+} ions in axial sites).

Alternatively, the concentration of chromium in the spinel phase may be calculated from the equation:

$$[Cr]_{spinel} = \left(1 - \frac{\Delta H_2}{\Delta H_1}\right)[Cr]_{total} \qquad (7.10)$$

where ΔH_1 is the linewidth predicted by equation 7.9 at a given total chromium concentration, $[Cr]_{total}$, ΔH_2 is the experimentally measured linewidth at the same concentration and $[Cr]_{spinel}$ is the spinel concentration (all concentrations being in p.p.m.). Whilst acknowledging that isolated Cr^{3+} ions in sites of axial symmetry and exchange coupled

Cr^{3+} pairs have small but finite concentrations, the remaining fraction of the dopant is assumed to be present as isolated Cr^{3+} ions in sites of cubic symmetry.

The calculated values of $[Cr^{3+}]_{\substack{isolated \\ ion}}$ and $[Cr^{3+}]_{spinel}$ for the annealed powder samples using the method just described are shown in columns five and six respectively of Table 7.7(a). Once again, for the sample doped with 800 p.p.m. of chromium, all the dopant is considered to exist as isolated Cr^{3+} ions in sites of cubic symmetry since for this sample $\Delta H_2 > \Delta H_1$.

A further method of determining $[Cr^{3+}]_{\substack{isolated \\ ions}}$ and $[Cr^{3+}]_{spinel}$ has been proposed by de Biasi and Fernandes.[7.18] If clustering is important, then we can modify equation 7.9 to take account of it as follows: [7.27 - 7.29]

$$\Delta H_{MS}(mT) = 629f(1 - pf)^{54} \qquad (7.11)$$

The "clustering factor", p, is defined as the ratio of the actual probability that a neighbouring cationic site is occupied to the probability of occupation if the distribution were random. It should be possible, by choosing a suitable value for p (which in turn is a measure of the spinel concentration) to fit equation 7.11 to the experimentally determined data for the annealed powder samples shown in Figure 7.18. In the present work, no attempt has been made to determine $[Cr^{3+}]_{\substack{isolated \\ ions}}$ and $[Cr^{3+}]_{spinel}$ using this

method of approach.

Inspection of Table 7.7(a) shows that the isolated Cr^{3+} ion concentration in the annealed powder samples examined lies in the range 870 p.p.m. to 1700 p.p.m. Cordischi et al[7.21] estimated the relative concentrations of isolated Cr^{3+} ions and $MgCr_2O_4$ in their MgO:Cr samples prepared in air by comparing the intensity of the central transition in the cubic Cr^{3+} spectrum to that of the broad line attributed to the spinel phase. They found that the isolated Cr^{3+} ion concentration ranged from approximately 1,800 p.p.m. to 2,700 p.p.m. in the samples examined. Considering the different preparation conditions, one might expect that, as is found experimentally, the degree of solubility of Cr^{3+} in the host lattice differs between Cordischi et al's samples and ours. Even so, both sets of results indicate that the solubility of Cr^{3+} in MgO is limited and, allowing for the difficulty in determining absolute concentrations from E.P.R. data, the degree of agreement between our results and Cordischi et al's concerning the maximum concentration of Cr^{3+} ions which can enter into solid solution is remarkable.

In fact, several groups of workers[7.20 - 7.23] have reported a limited solubility of Cr^{3+} in MgO and their estimates of the maximum amount of chromium which can enter into solid solution are given in Table 7.7(b) in units of [number of Cr atoms per 100 Mg atoms]. For comparison, Table 7.7(b) also shows the average of the isolated Cr^{3+} ion concentrations deduced for the various annealed powder samples (given in Table 7.7(a)) in the same units. It is noticable that our value for the "saturated solid solution"

Cr^{3+} concentration is in reasonable agreement with all but one of those given in Table 7.7.(b). Only the value obtained by Valigi and Cimino[7.23] differs considerably from ours (theirs is, in fact, much larger). This discrepancy possibly reflects the effect of different preparation conditions upon the solubility of Cr^{3+} in MgO. Alternatively, the fact that E.P.R. techniques were not employed by Valigi and Cimino to determine the maximum number of isolated Cr^{3+} ions which can enter into solid solution (they studied the change in the lattice parameter of MgO upon addition of chromium using x-ray diffraction methods) may be significant.

7.3 SUMMARY OF RESULTS FOR THE MgO:Cr SYSTEM

Spectra attributable to isolated Cr^{3+} ions in octahedral symmetry sites were recorded from all the single crystal and powder samples. Two additional spectra, one due to isolated Cr^{3+} ions in sites of [100] axial symmetry and one due to Cr^{3+} pairs in the complex (Cr^{3+} - O - Cr^{3+}) were observed for the single crystal samples. These spectra are not seen for the powder samples because they are highly anisotropic and consequently the lines are "smeared out" and lost because of the random orientation of the crystallites which constitute the powder. There is also some evidence to suggest that a broad line, previously attributed to the spinel $MgCr_2O_4$, is present in the more heavily doped samples.

Overall then, the E.P.R. spectra of several species of chromium are observed in the samples examined in this work. By far the most intense group of spectral lines

are those due to isolated Cr^{3+} ions in sites of cubic symmetry; the lines attributable to the other identified species of chromium have intensities which are approximately equivalent and which are $\leqslant$ 1% of the intensity of the central transition in the cubic Cr^{3+} spectrum.

The RHEED patterns show that, in the samples with the highest dopant concentrations (those containing 9,500 p.p.m. and 15,100 p.p.m. of chromium), precipitation of the spinel phase $MgCr_2O_4$ takes place in the MgO host lattice. That heat treatment induces growth of the spinel phase in the sample doped with 7,400 p.p.m. of chromium indicates that spinel precipitates may also be present in the more lightly doped as received crystals but at concentration levels which are too low for them to be detected using the RHEED technique. Growth of the spinel phase is probably favoured because it removes the need for charge compensation of isolated Cr^{3+} ions by the creation of cation vacancies.

A calculation based on the discrepancy between the measured linewidths of the central transition in the cubic Cr^{3+} spectra of the annealed powder samples and those predicted by de Biasi and Fernandes' dipolar broadening theory for n = 5 (which was found to be the range of the exchange interaction in the MgO:Cr powders examined by de Biasi and Fernandes) has been used to determine the concentration of Cr^{3+} existing both as isolated ions and in the spinel $MgCr_2O_4$ in these samples. For the sample doped with 800 p.p.m. of chromium the dopant exists almost entirely as isolated ions whereas for the other doped samples some fraction of the chromium is always present in

spinel phase material. The fraction of Cr^{3+} ions in the $MgCr_2O_4$ phase increases with the total dopant concentration (ranging from $\sim$ 1600 p.p.m. when $[Cr]_{total}$ = 3,600p.p.m. to $\sim$ 14000 p.p.m. when $[Cr]_{total}$ = 15,100 p.p.m.).

Finally, the variation of the intensity of the central transition in the cubic Cr^{3+} spectrum with polar angle and the decrease in the width of the same line brought about (for both single crystals and powders) by the "annealing" heat treatment described earlier shows that this line (as well as, presumably, the hyperfine lines in the same spectrum) is strain broadened. The plots of linewidth against annealing time indicate that there are two sources of strain in the samples examined. One has been associated with the collapse of the lattice in the regions surrounding cation vacancies and the other has been associated with the collapse of the lattice in the regions surrounding isolated substitutional Cr^{3+} ions. Of course, the cation vacancies must be comparatively close to isolated Cr^{3+} ions if the distrotion of the lattice in the regions where they are located is to cause strain broadening of the lines in the cubic Cr^{3+} spectrum.

REFERENCES

7.1 W. Low Phys. Rev. 105, 801 (1957).

7.2 J.S. Thorp, M.D. Hossain and L.J.C. Bluck J. Mat. Sci. 14, 2853 (1979)

7.3 J.E. Wertz and P. Auzins Phys. Rev. 106, 484 (1957)

7.4 G. Rius and A. Herve Solid State Comm. 11, 795 (1972)

7.5 F.G. Marshall and V.W. Rampton J. Phys. C. 1, 594 (1968)

7.6 J.R. Fletcher, F.G. Marshall, V.W. Rampton, P.M. Rowell and K.W.H. Stevens Proc. Phys. Soc. 88, 127 (1968)

7.7 F.S. Ham Phys. Rev. B 4, 3854 (1971)

7.8 J.R. Fletcher and K.W.H. Stevens J. Phys. C 2, 444 (1969)

7.9 J.E. Wertz, J.W. Orton and P. Auzins J. Appl. Phys. Supplement 33, 322 (1962)

7.10 J. Marguglio and Y.m. Kim J. Chem. Phys. 62, 1497 (1975)

7.11 W.H. Gourdin, W.D. Kingery and J. Driear J. Mat. Sci. 14, 2074 (1979)

7.12 A.D. Inglis "Clustering in iron-doped magnesium oxide" Ph.D. Thesis, Durham University, (1981), unpublished.

7.13 E. Bauer in "Techniques of Metals Research" vol.2 (Ed. R.F. Bunghal), Wiley-interscience, N.Y. (1969)

7.14 G.J. Russell Prog. Crystal Growth and Charact. 5, 291 (1982)

7.15 D.H. Bowen Proc 6th Saclay Metall. Colloq., (1962) p.151.

7.16 P.B. Hirsch et al "Electron Microscopy of thin Crystals" Butterworths, London (1965), p.499.

7.17 W.K. Chen and N.L. Petersen J. Phys. Chem. Solids 41, 335 (1980)

7.18 R.S. de Biasi and A.A.R. Fernandes J. Phys. C: Solid State Phys. 16, 5481 (1983).

7.19 D. Cordischi, D. Gazzoli and M. Valigi J. Sol State Chem. 24, 371 (1978)

7.20 A. Cimino, M. Lo Jacono, P. Porta and M. Valigi Z. Phys. Chem.(Frankfurt), N.F. 51, 301 (1966)

7.21 D. Cordischi, J.C. Vickerman and A. Cimino Trans. Faraday Soc. 66, 1312 (1970)

7.22 M. Valigi Z. Phys. Chem. (Frankfurt), N.F. 97, 241 (1975)

7.23 M. Valigi and A. Cimino Z. Phys. Chem. (Frankfurt), N.F. 99, 131 (1976).

7.24 J.S. van Wieringen and J.G. Rensen Paramagnetic Resonance, Proc. 1st Internat. Conf., Jerusalem, Vol.I, ed. W. Low, Academic Press, (1963).

7.25 E.R. Feher Phys. Rev. 136, A 145 (1964)

7.26 R.A. Serway, S.A. Marshall and R.B. Robinson Phys. Stat. Sol. (B) 56, 319 (1973).

7.27 R.S. de Biasi Magnetism Letters 1, 103 (1978).

7.28 F. Gesmundo and C. de Asmundis J. Phys. Chem. Solids 33, 1861 (1972)

7.29 W.J.C. Grant and M.W.P. Strandberg Phys. Rev. 135, A727 (1964).

CHAPTER EIGHT

E.P.R. STUDIES OF MANGANESE DOPED MAGNESIUM OXIDE SINGLE CRYSTALS AND POWDERS

8.1 EXPERIMENTAL RESULTS FOR MgO:Mn SINGLE CRYSTALS

8.1.1 CHARACTERISATION OF THE E.P.R. SPECTRA

The E.P.R. spectra of the MgO:Mn single crystals were recorded on the Varian V4205-15 spectrometer at room temperature with the magnetic field parallel to one of the cubic axes. In all, three different samples, nominally containing 840, 1,400 and 2,900 p.p.m. by weight of manganese, were examined.

The spectra recorded from the samples doped with 840 p.p.m. and 2,900 p.p.m. by weight of manganese are shown in Figures 8.1(a) and 8.1(b) respectively. Both the spectra illustrated are due to Mn^{2+} ions in sites of octahedral symmetry, although there is a marked difference between them. This difference is a result of the fact that the width of each line in the spectrum increases with the manganese concentration. In the spectrum of the sample doped with 2,900 p.p.m. of manganese many of the lines which are evident in the spectrum of the sample doped with 840 p.p.m. of manganese are broadened to the extent that they overlap and are unresolved. Therefore, Figure 8.1(b) is simply a less well resolved version of Figure 8.1(a). In accordance with the observed relationship between linewidth and dopant concentration, the spectral linewidths

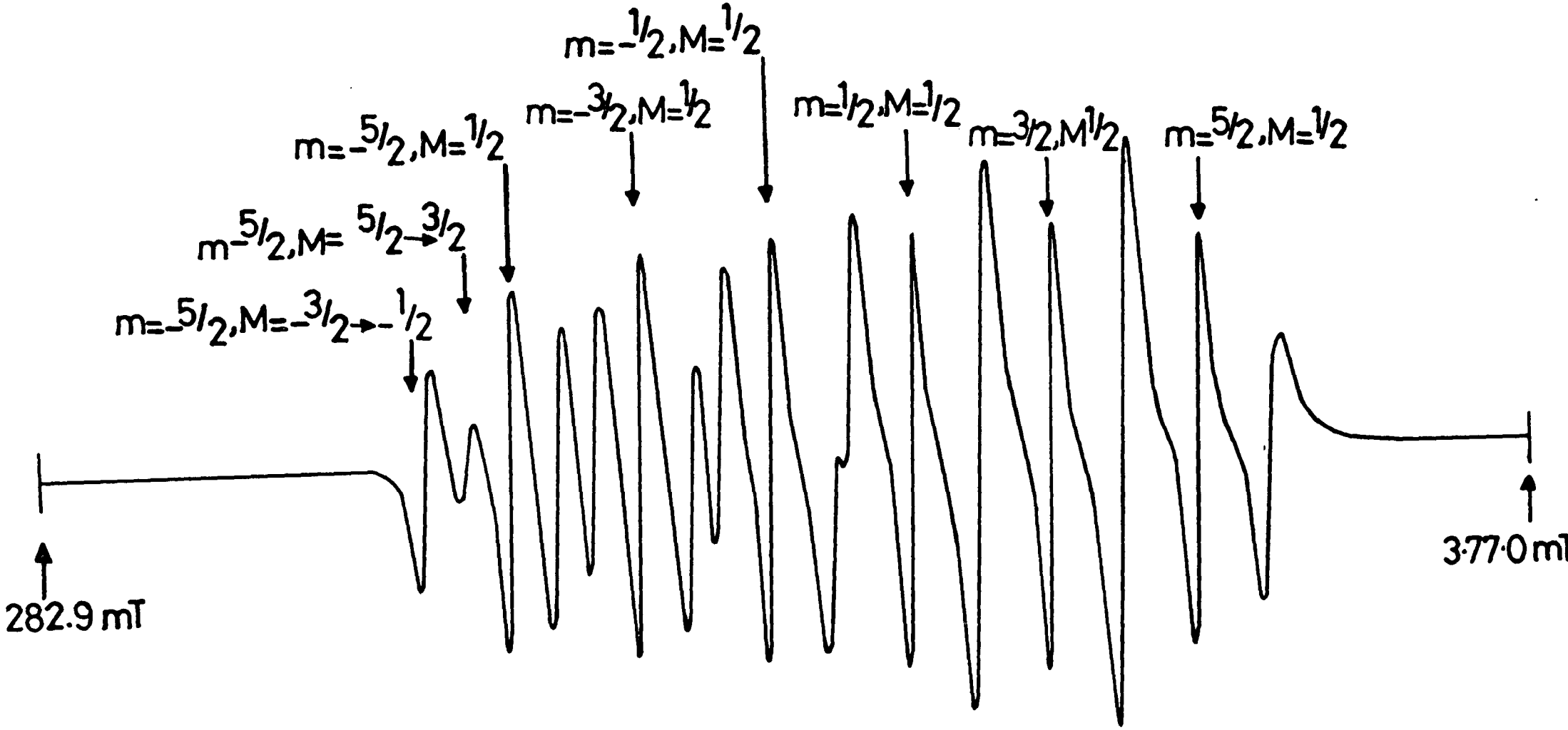

FIGURE 8.1(a) E.P.R. SPECTRUM OF SINGLE CRYSTAL Mn/MgO; 840 p.p.m. Mn, H// <100>, 9.3820 GHz, 293K.

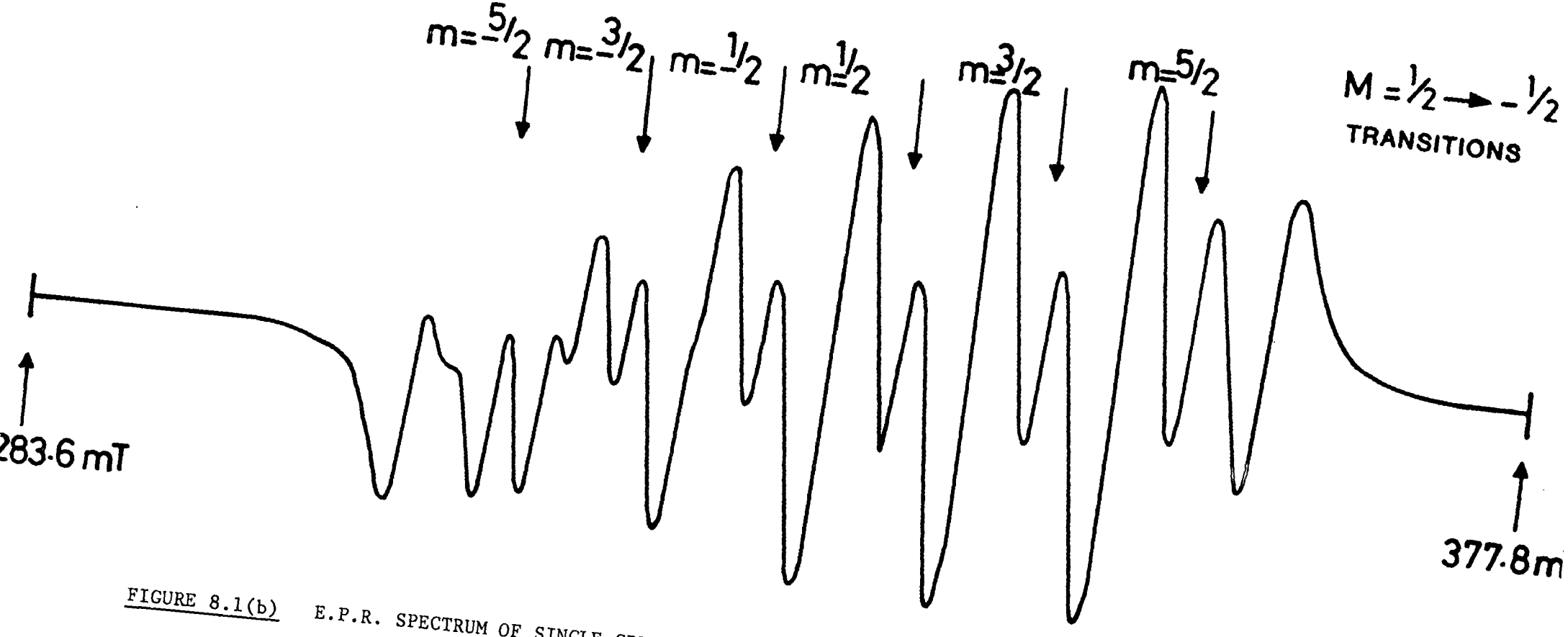

FIGURE 8.1(b) E.P.R. SPECTRUM OF SINGLE CRYSTAL Mn/MgO; 2,900 p.p.m. Mn, H// <100>, 9.3820 GHz, 293K.

of the sample containing 1,400 p.p.m. of manganese lie between those of the samples containing 840 p.p.m. and 2,900 p.p.m. of manganese, but remain small enough for the spectrum to retain the form of Figure 8.1(a) (the dependence of the Mn^{2+} spectral linewidths upon dopant concentration will be considered in detail in section 8.1.2).

The E.P.R. spectrum of Mn^{2+} in cubic sites in MgO was first reported by Low[8.1,8.2] and his analysis showed that the Spin Hamiltonian of equation 4.28 accurately describes the observed spectrum. The resonant magnetic fields of the allowed $\Delta M = \pm 1$, $\Delta m = 0$ transitions predicted by equation 4.28 are given, to first order in a (the fine structure constant) and second order in A (the hyperfine structure constant) by equation 4.31, which was derived by Matarrese and Kikuchi.[8.3] The spectra reported here were analysed following Matarrese and Kikuchi's method, which is described in detail in section 4.7.

The only naturally occurring isotope of manganese, Mn^{55}, has a nuclear spin, I, of 5/2 and since A is larger than a for this ion in MgO[8.1], the $\Delta M = \pm 1$, $\Delta m = 0$ transitions should form a pattern of six hyperfine groups of lines with five fine structure lines in each hyperfine group. For each of the manganese doped crystals examined the absorption lines arising from the six hyperfine $(M = \frac{1}{2} \longleftrightarrow -\frac{1}{2}, m)$ transitions were fully resolved. A and g were calculated by substituting the measured field positions of pairs of lines with the quantum labels $(M=\frac{1}{2} \longleftrightarrow -\frac{1}{2}, m)$ and $(M=\frac{1}{2} \longleftrightarrow -\frac{1}{2}, -m)$ into equations 4.32a and b respectively. Since the $(M=\frac{1}{2} \longleftrightarrow -\frac{1}{2}, m)$ lines consist of three such pairs, the experimental values of A and g quoted in Table 8.1 are

the averages of the three values obtained from each manganese doped sample for each of these parameters. Reference to Table 8.1 shows that the g-factors and hyperfine structure constants measured for the three samples examined are in good agreement both with each other and also with the values reported in the literature.[8.1,8.2]

Previous measurements have shown that a is positive[8.1] and in section 4.7 it was demonstrated that A and a have opposite signs (this was deduced from the observed relative separations of the fine structure lines in the m=+5/2 and m=-5/2 pentads). Therefore in Table 8.1 the hyperfine structure constants have been assigned negative values.

The four remaining fine structure lines in each of the six hyperfine pentads(i.e. the complete spectrum except for the ($M=\frac{1}{2}\longleftrightarrow -\frac{1}{2}m$) lines) were, in general, unresolved so that the pattern of lines characteristic of Mn^{2+} in cubic sites (six groups of five lines) was not observed in the crystals examined here. This lack of resolution is a result of the relatively high doping level in all three samples, which, since the spectral linewidths are dependent upon dopant concentration, causes the fine structure lines to broaden and overlap.

However, for the samples doped with 840 p.p.m. and 1,400 p.p.m. of manganese the two transitions of the m=-5/2 pentad which are lowest in field (the ($M=5/2 \longleftrightarrow 3/2$, m=-5/2) and ($M=-3/2 \longleftrightarrow -1/2$, m=-5/2) transitions) were clearly resolved both from each other and also from the central ($M=\frac{1}{2}\longleftrightarrow -\frac{1}{2}$, m=-5/2) transition of the pentad. All the remaining fine structure transitions, except for the ($M=\frac{1}{2}\longleftrightarrow -\frac{1}{2}$,m) transitions already mentioned, were unresolved in the spectra of these crystals and their field positions

Mn CONCENTRATION (p.p.m.)	SPECTROSCOPIC SPLITTING FACTOR g	HYPERFINE STRUCTURE CONSTANT, A ($\times 10^4$ cm^{-1})	FINE STRUCTURE CONSTANT, a ($\times 10^4$ cm^{-1})	$\overline{\Delta Hpp}$ (Ms = $\frac{1}{2} \leftrightarrow -\frac{1}{2}$, m TRANSITIONS) mT	ΔHpp (Ms = $-\frac{3}{2} \leftrightarrow -\frac{1}{2}$ $m = -\frac{5}{2}$ TRANSITION) mT	ΔHpp (Ms = $\frac{5}{2} \leftrightarrow \frac{3}{2}$ $m = -\frac{5}{2}$ TRANSITION) mT	MICROWAVE FREQUENCY GHz
840	2.0015	-81.16	18.47	0.778	0.953	1.038	9.3820
1400	2.0020	-81.16	18.54	0.896	1.090	1.044	9.3815
2900	2.0003	-81.12	-	1.426	-	-	9.3820

TABLE 8.1 E.P.R. PARAMETERS FOR SINGLE CRYSTAL Mn/MgO SAMPLES:

T = 293K, H//<100> .

could not be measured. Since the fine structure constant is determined by measuring the separations of the fine structure lines within individual hyperfine groups (see section 4.7), such measurements were restricted to the m=-5/2 pentad for the samples doped with 840 p.p.m. and 1,400 p.p.m. of manganese. For the crystal doped with 2,900 p.p.m. of manganese only the central ($M=\frac{1}{2}\leftrightarrow-\frac{1}{2},m$) lines of each hyperfine pentad were fully resolved and therefore a could not be measured for this sample.

The theoretical separations of the two outer fine structure lines from the central ($M=\frac{1}{2}\leftrightarrow-\frac{1}{2},m=-5/2$) line of the m=-5/2 pentad are, for the ($M=5/2\leftrightarrow 3/2,m=-5/2$) transition ($\Delta H=2a-5A^2/H_o$) and for the ($M=-3/2\leftrightarrow-\frac{1}{2},m=-5/2$) transition ($\Delta H = 5a/2 + 5A^2/2H_o$) (see Figures 4.8 a and b). The experimental values of a given in Table 8.1 for the samples containing 840 p.p.m. and 1,400 p.p.m. of manganese were determined by averaging the two values of a which were obtained for each of these samples by substituting the appropriate measured separations and A values from Table 8.1 into the expressions given above. As with the other E.P.R. parameters, the measured values of a agree well both with each other and with the published data.[8.1,8.2]

In Table 8.1 the measured peak-to-peak linewidths of the various transitions are given. As expected for lines with the same electronic quantum number but different nuclear quantum numbers, the fully resolved ($M=\frac{1}{2}\leftrightarrow-\frac{1}{2},m$) transitions were found to have approximately equal linewidths. The average peak-to-peak linewidth of these transitions in each doped crystal is shown in column five of Table 8.1.

The peak-to-peak linewidths of the ($M=-3/2 \leftrightarrow -\frac{1}{2}, m=-5/2$) and ($M=5/2 \leftrightarrow 3/2$, $m=-5/2$) transitions for the samples containing 840 p.p.m. and 1,400 p.p.m. of manganese are given in columns six and seven respectively of Table 8.1. Due to line overlap, the linewidths of the remaining fine structure transitions in the spectra of these samples (except those of the ($M=\frac{1}{2} \leftrightarrow -\frac{1}{2}, m$) transitions) could not be measured. However, because the spectrum of Mn^{2+} in cubic sites is symmetrical, the linewidth of the ($M=-3/2 \leftrightarrow -\frac{1}{2}, m=-5/2$) transition may be regarded as typical of that for all lines with quantum labels of the form ($M=\pm 3/2 \leftrightarrow \pm 1/2, m$) and similarly the linewidth of the ($M=5/2 \leftrightarrow 3/2$, $m=-5/2$)transition may be regarded as typical of that for all lines with quantum labels of the form ($M=\pm 5/2 \leftrightarrow \pm 3/2, m$). Excluding the six ($M=\frac{1}{2} \leftrightarrow -\frac{1}{2}, m$) lines the ($M=\pm 5/2 \leftrightarrow \pm 3/2, m$) and ($M=\pm 3/2 \leftrightarrow \pm \frac{1}{2}, m$) lines constitute the complete cubic Mn^{2+} spectrum and therefore, although the linewidth data of Table 8.1 is incomplete, it provides quantitative estimates for the linewidths of all the unresolved transitions in the spectra of the samples doped with 840 p.p.m. and 1,400 p.p.m. of manganese.

As already described, none of the outer fine structure transitions (the ($M=\pm 5/2 \leftrightarrow \pm 3/2, m$) and ($M=\pm 3/2 \leftrightarrow \pm \frac{1}{2}, m$) transitions) were fully resolved in the spectrum of the crystal containing 2,900 p.p.m. of manganese and so obviously their linewidths could not be measured for this sample. In the final column of Table 8.1 the microwave frequencies at which the spectra were recorded are given.

Although the E.P.R. parameters (g,A&a) which were

measured for the three samples examined agreed well with those reported for Mn^{2+} in cubic sites in MgO[8.1,8.2], it was felt that further evidence was needed to positively identify the spectra of our samples with this species because none of the recorded traces displayed the pattern of lines which is characteristic of Mn^{2+} in octahedral symmetry (six groups of five lines). The theoretical angular dependence of the cubic Mn^{2+} spectrum predicts that with the magnetic field oriented at $\theta = 32^{o}$, $\phi = 0^{o}$ to the <100> axis (θ and ϕ are defined in Figure 4.2) the anisotropic ($M = \pm 5/2 \longleftrightarrow \pm 3/2, m$) and ($M = \pm 3/2 \longleftrightarrow \pm 1/2, m$) fine structure lines overlap with the almost isotropic ($M = +1/2 \longleftrightarrow -1/2, m$) lines so that the overall spectrum at this orientation consists of only six lines.

Spectra were recorded for the samples doped with 840 p.p.m. and 2,900 p.p.m. of manganese with the magnetic field at an angle of 32^{o} to one of the cubic axes and these are shown in Figures 8.2(a) and (b) respectively. The five fine structure lines in each pentad overlap completely in the spectrum of the sample containing 2,900 p.p.m. of manganese, but there is a suggestion of partial resolution among the fine structure lines of the m=-5/2 and m=+5/2 pentads in the spectrum of the sample doped with 840 p.p.m. of manganese. However, as there are essentially a total of only six lines in the illustrated spectra, we may conclude that the spectra recorded from the three manganese doped samples with the magnetic field parallel to one of the cubic axes are due to Mn^{2+} ions in sites of octahedral symmetry. A spectrum very similar to that shown in

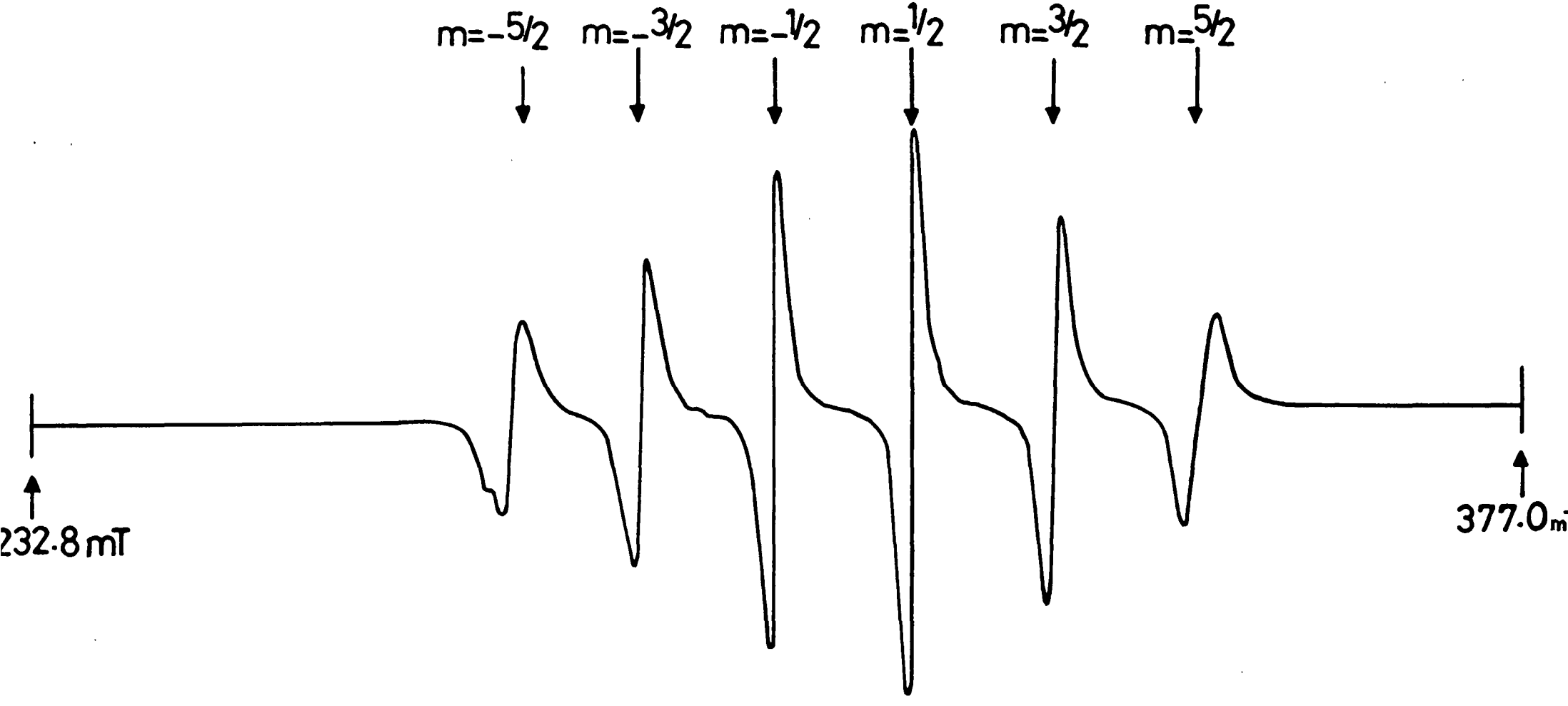

FIGURE 8.2(a) E.P.R. SPECTRUM OF SINGLE CRYSTAL Mn/MgO AT $\theta = 32^{o}$; 840 p.p.m. Mn, 9.3810 GHz, 293K.

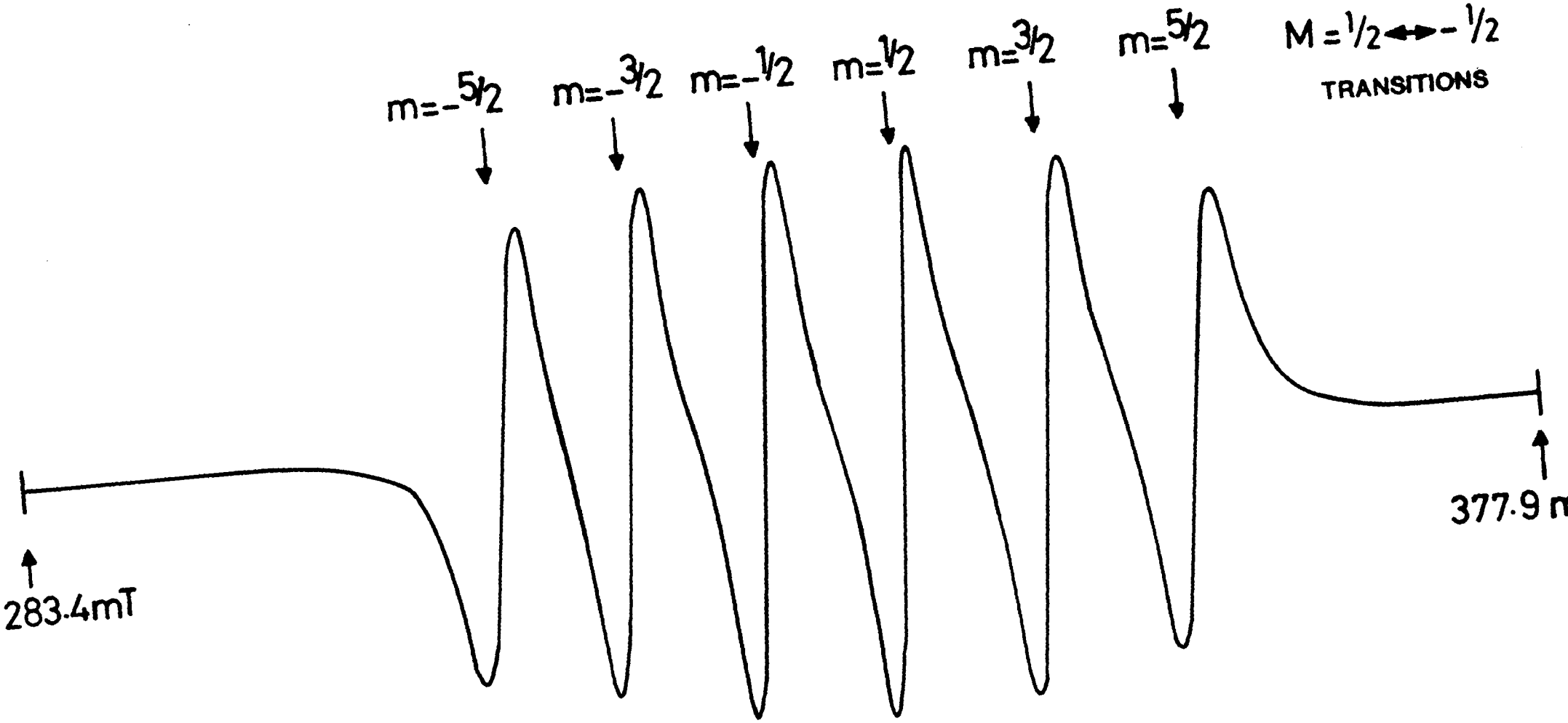

FIGURE 8.2(b) E.P.R. SPECTRUM OF SINGLE CRYSTAL Mn/MgO AT $\theta = 32^{\circ}$; 2,900 p.p.m. Mn, 9.3815 GHz, 293K.

Figure 8.1a has been reported in the literature by Rubio et al[8.4] and attributed by them to Mn^{2+} in cubic sites, thus providing further evidence that our spectra have been correctly assigned.

The six lines of the spectra recorded at $\theta=32^{o}$ occur at the same field positions as do the ($M=\frac{1}{2}\longleftrightarrow-\frac{1}{2}$,m) hyperfine transitions in the spectra recorded with H // <100> since these transitions are very nearly isotropic (all other fine structure transitions seen in the cubic Mn^{2+} spectrum when H // <100> become merged with the ($M=\frac{1}{2}\longleftrightarrow-\frac{1}{2}$,m) transitions when $\theta=32^{o}$). Therefore the surviving six lines in the spectra shown in Figures 8.2a&b were analysed in order to determine the parameters g and A using exactly the same method which was adopted to determine these parameters from the spectra recorded with H // <100>. The values obtained, which are given in Table 8.2, agree well, both with the values calculated for the same samples from the spectra recorded with H //<100>, and also with the published data.[8.1,8.2] This is not surprising, since A and g are both isotropic for the cubic Mn^{2+} spectrum.

The peak-to-peak linewidths of all six lines constituting the spectra illustrated in Figures 8.2 a&b were measured and then averaged to obtain the values given in Table 8.2. It is noticeable that the average linewidth of the lines in the spectra recorded when $\theta=32^{o}$ is larger than the average linewidth of the ($M=\frac{1}{2}\longleftrightarrow-\frac{1}{2}$,m) lines in the spectra recorded when H //<100> for both the samples concerned (those containing 840 p.p.m. and 2,900 p.p.m. of manganese). This increase may be a result of incomplete

MANGANESE CONCENTRATION (p.p.m.)	SPECTROSCOPIC SPLITTING FACTOR g	HYPERFINE STRUCTURE CONSTANT A(x 10^4 cm^{-1})	$\overline{\Delta Hpp}$ OF SIX SURVIVING LINES IN SPECTRUM mT	MICROWAVE FREQUENCY GHz
840	2.0010	-81.25	1.085	9.3810
2900	2.0016	-80.79	2.623	9.3815

TABLE 8.2 E.P.R. PARAMETERS FOR SINGLE CRYSTAL Mn/MgO SAMPLES:

T = 293K, $\theta = 32^{o}$, $\phi = 0^{o}$

overlapping of the fine structure lines in each of the hyperfine pentads in the spectra illustrated in Figures 8.2 a & b. Alternatively, it may be due to the fact that the ($M=\pm5/2 \leftrightarrow \pm3/2, m$) and ($M=\pm3/2 \leftrightarrow \pm1/2, m$) lines both have larger linewidths than the ($M=+\frac{1}{2} \leftrightarrow -\frac{1}{2}, m$) lines (see Table 8.1). Hence, when $\theta = 32^{o}$ and lines with the same value of m merge, the six surviving lines of the spectrum will broaden and therefore have larger widths than those of the ($M=+\frac{1}{2} \leftrightarrow -\frac{1}{2}, m$) lines in the spectrum recorded when H // <100>. The microwave frequencies at which the spectra illustrated in Figures 8.2 a and b were recorded are given in the final column of Table 8.2.

The spectra discussed in this section are due to isolated Mn^{2+} ions in octahedral sites and therefore it is likely that these ions substitute for Mg^{2+} ions in the MgO host lattice. Isolated ions of manganese in all its common valency states (except Mn^{3+}) are detectable using E.P.R. methods as are Mn^{2+} ions in sites of non-cubic symmetry. In addition, it has been shown that Mn^{3+} can only exist in solid solution in MgO if lithium is also added (the number of Mn^{3+} ions formed is equal to the concentration of the Li^{+} ions introduced into the MgO crystal for [Li]/[Mn] ratios of less than one).[8.5,8.6] Since only the cubic Mn^{2+} spectrum was observed in the crystals examined we may conclude that no fraction of the manganese dopant exists as isolated ions in a charge state other than the (+2) state and that none of the isolated Mn^{2+} ions occupy sites of non-cubic symmetry in these crystals. The possibility that some of the manganese

dopant might exist as ions in clusters or in a separate magnetic phase rather than as isolated ions will be considered in the next section.

8.1.2 THE VARIATION OF E.P.R. LINEWIDTH WITH MANGANESE CONCENTRATION

In this section the effect of dipolar broadening upon the linewidths of the MgO:Mn single crystal spectra will be discussed. The discussion will be limited to the linewidths of the transitions in the spectra recorded with H // <100> since the six lines in the spectra recorded with the magnetic field at an angle of 32^{o} to one of the cubic axes are each composed of five overlapping lines whose individual widths cannot be determined.

If dipolar interactions were the only source of line broadening in the cubic Mn^{2+} spectra then all the transitions would have the same linewidth. Reference to Table 8.1 clearly shows that this is not the case: lines for which the magnitude of M differs have different linewidths (at least for the samples doped with 840 p.p.m. and 1,400 p.p.m. of manganese; for the sample containing 2,900 p.p.m. of manganese only the width of the lines corresponding to the $(M=+\frac{1}{2} \leftrightarrow -\frac{1}{2},m)$ transitions could be measured). Assuming that the sample containing 2,900 p.p.m. of manganese follows the trend set by the two most lightly doped crystals, then the average width of the $(M=+\frac{1}{2} \leftrightarrow -\frac{1}{2},m)$ lines is always smaller than that of the other lines (corresponding to the $(M=\pm 5/2 \leftrightarrow \pm 3/2,m)$ and $(M=\pm 3/2 \leftrightarrow \pm 1/2,m)$ transitions) in the spectrum. Since, to first order, the

($M=+\frac{1}{2}\leftrightarrow-\frac{1}{2},m$) lines are not broadened by strain (see section 6.3), it is suggested that the average width of these lines is the "intrinsic" linewidth of all the lines in the spectrum. In addition to possessing this "intrinsic" linewidth the ($M=\pm5/2\leftrightarrow\pm3/2,m$) and ($M=\pm3/2\leftrightarrow\pm1/2,m$) lines are further broadened by random strains in the crystal (this effect will be considered in detail in section 8.1.3).

Figure 8.3 shows a plot of the average width of the ($M=+\frac{1}{2}\leftrightarrow-\frac{1}{2},m$) lines against total nominal manganese concentration (expressed as the percentage fraction of cationic sites occupied by the dopant). The graph includes data taken from the literature[8.7,8.8]; the linewidths given in reference 8.7 were converted to peak-to-peak linewidths assuming a Lorentzian lineshape.

Figure 8.3 also shows the theoretical dependence of the peak-to-peak linewidth upon manganese concentration predicted by de Biasi and Fernandes' dipolar broadening theory[8.9] for ten different ranges of the exchange interaction (see section 6.2). A(S) was determined from equation 6.23 with g = 2.0015, a = 4.2112A[8.10] and S=5/2. For each value of n, C_1 was evaluated at various manganese concentrations using equations 6.25 and 6.30 and the appropriate values of $S_1(r_e)$, $S_2(r_e)$ and $z(r_e)$ given in Tables 6.2 and 6.3. The theoretical curves were then calculated from equation 6.28.

The experimental dependence of the average peak-to-peak width of the ($M=+\frac{1}{2}\leftrightarrow-\frac{1}{2},m$) lines upon manganese concentration does not coincide with any of the theoretical curves. However, it is likely that this discrepancy is

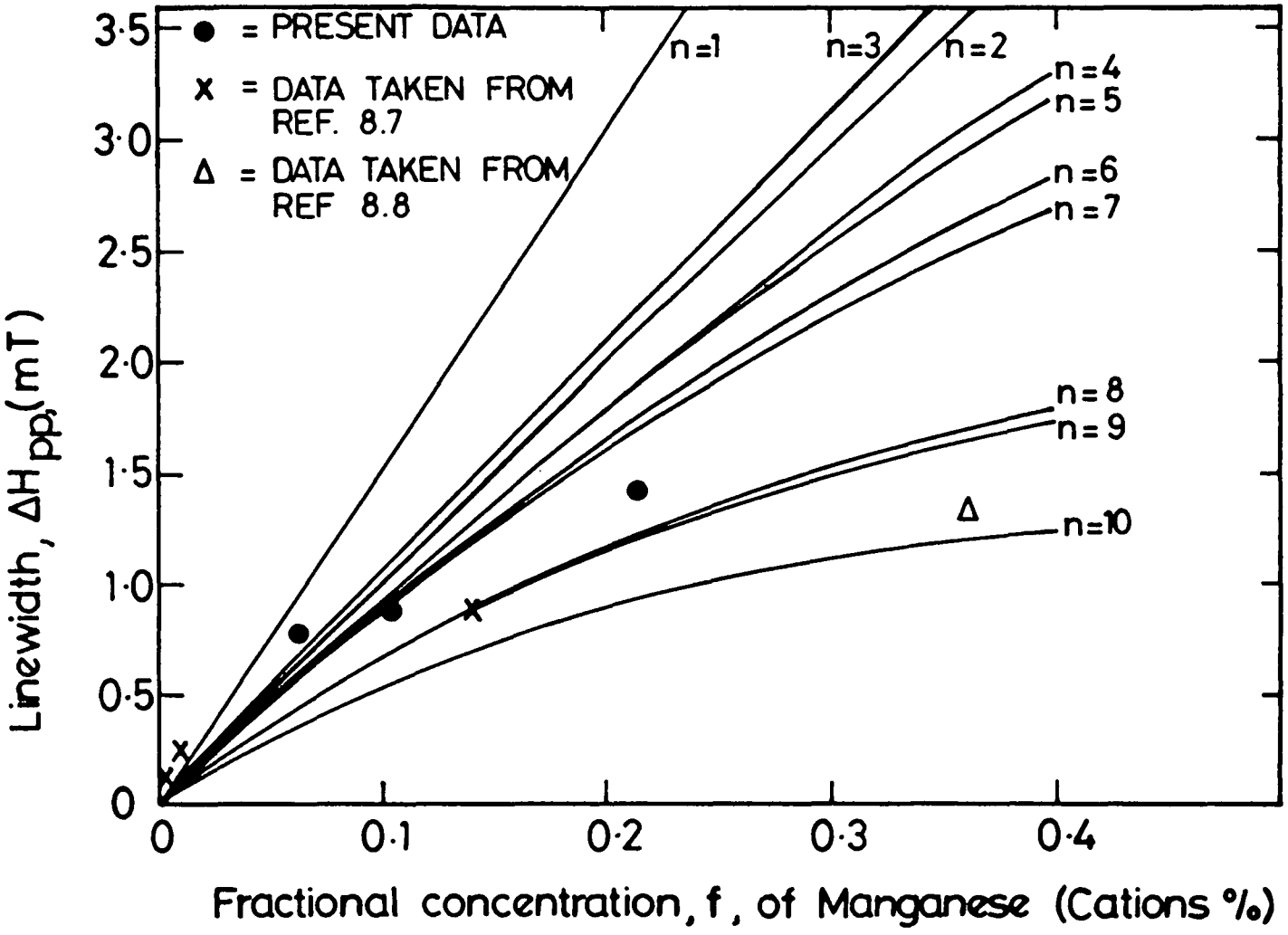

FIGURE 8.3 COMPARISON OF EXPERIMENTAL (SYMBOLS) AND THEORETICAL (FULL LINES) CONCENTRATION DEPENDENCE OF LINEWIDTH IN SINGLE CRYSTAL Mn/MgO.

due to the fact that de Biasi and Fernandes' theory only applies to powdered samples. The experimental dependence of linewidth upon manganese concentration for powdered MgO:Mn samples will be compared with the theoretical curves of Figure 8.3 in section 8.2.2 in order to properly assess whether the application of de Biasi and Fernandes' model to the MgO:Mn system is valid.

Nonetheless, it is safe to conclude from the single crystal data that the experimentally observed average peak-to-peak width of the ($M=+\frac{1}{2}\leftrightarrow-\frac{1}{2},m$) lines is concentration dependent and is of the right order of magnitude at all manganese concentrations examined to be explained in terms of de Biasi and Fernandes' dipolar broadening theory. Recalling the model upon which this theory is based and that the total nominal manganese concentration was used to plot the experimental points shown in Figure 8.3, the evidence suggests that the major portion of the manganese dopant exists as isolated Mn^{2+} ions, which only interact via the dipolar mechanism, and that the remaining dopant forms Mn^{2+} pairs (which do not contribute to the cubic Mn^{2+} spectrum).

Therefore it appears that clustering effects are absent in the MgO:Mn single crystals although such effects were seen in both the chromium and iron doped MgO samples (see Chapters 7 and 9) with the formation of the spinel phase $MgCr_2O_4$ and a clustered iron phase (which may be the spinel $MgFe_2O_4$) respectively. The low solubility of Cr^{3+} and Fe^{3+} in MgO and the consequent formation of clustered phases is due to the fact that these ions have excess charge

with respect to the Mg^{2+} ions of the host lattice which cannot be easily compensated for either by valency variation or by cation vacancies.[8.11,8.12] Obviously, no such problems arise when Mn^{2+} ions are incorporated into the lattice in place of Mg^{2+} ions since they both have the same valency state. Therefore the solubility of this ion in MgO is likely to be much greater than that of both Fe^{3+} and Cr^{3+} thereby reducing the probability of clustering.

Clustered manganese ions in MgO (the clustered ions are often found to exist as Mn^{4+} in the phase Mg_6MnO_8[8.5,8.6]) have an E.P.R. spectrum which consists of a single, large Lorentzian line and this line overlaps with and completely swamps the isolated ion spectrum.[8.6,8.13,8.14] The absence of a line of this nature from the spectra of all the single crystal MgO:Mn samples examined provides further evidence that clustering of the manganese dopant does not take place in these samples.

8.1.3 THE EFFECT OF STRAIN UPON LINEWIDTH IN THE CUBIC Mn^{2+} SPECTRUM

According to the theory discussed in section 6.3, if a material contains random internal stresses then the contribution of strain broadening towards the total linewidth of any given line is proportional to $(2M-1)^2$. Therefore, in strained MgO:Mn samples the observed linewidths of the $(M=\pm 5/2 \leftrightarrow \pm 3/2, m)$ and $(M=\pm 3/2 \leftrightarrow \pm 1/2, m)$ transitions in the cubic Mn^{2+} spectrum ($\Delta H_{obs}(M=\pm 5/2 \leftrightarrow \pm 3/2, m)$ and $\Delta H_{obs}(M=\pm 3/2 \leftrightarrow \pm 1/2, m)$ respectively) will both contain components due to random internal stresses and according to

the theory of section 6.3 the ratio of the magnitudes of these components is given by:

$$\frac{\Delta H_{obs}(M=\pm 5/2 \leftrightarrow \pm 3/2, m) - \Delta H_i}{\Delta H_{obs}(M=\pm 3/2 \leftrightarrow \pm 1/2, m) - \Delta H_i} = \frac{4\Delta H_s'}{\Delta H_s'} = 4 \qquad (8.1)$$

$\Delta H_s'$ is a constant characteristic of the strain broadening in the particular sample being investigated whose magnitude was defined in section 6.3. ΔH_i is the "intrinsic" linewidth of all the lines in the cubic Mn^{2+} spectrum and is the linewidth which arises from the effects of all broadening mechanisms other than the strain broadening mechanism. The width of the $(M=+\frac{1}{2} \leftrightarrow -\frac{1}{2}, m)$ lines is simply ΔH_i (for these lines $(2M-1)^2 = 0$), the magnitude of which was explained in terms of dipolar broadening theory in the previous section.

Applying equation 8.1 to the linewidth data given in Table 8.1 we obtain for the sample doped with 840 p.p.m. of manganese:

$$\frac{\Delta H_{obs}(M=\pm 5/2 \leftrightarrow \pm 3/2, m) - \Delta H_i}{\Delta H_{obs}(M=\pm 3/2 \leftrightarrow \pm 1/2, m) - \Delta H_i} = 1.49$$

where $\Delta H_i = 0.778$ mT, and for the sample doped with 1,400 p.p.m. of manganese:

$$\frac{\Delta H_{obs}(M=\pm 5/2 \leftrightarrow \pm 3/2, m) - \Delta H_i}{\Delta H_{obs}(M=\pm 3/2 \leftrightarrow \pm 1/2, m) - \Delta H_i} = 0.76$$

where $\Delta H_i = 0.896$ mT.

When the manganese concentration is increased to 2,900 p.p.m. the $(M=\pm 5/2 \leftrightarrow \pm 3/2, m)$ and $(M=\pm 3/2 \leftrightarrow \pm 1/2, m)$ lines are unresolved so that their widths cannot be measured. Therefore for this sample equation 8.1 cannot be applied and information is only available concerning the intrinsic linewidth, ΔH_i (given by the average peak-to-peak width of the resolved $(M=+\frac{1}{2} \leftrightarrow -\frac{1}{2}, m)$ lines).

Clearly, the theoretically predicted ratio of equation 8.1 does not agree with those measured experimentally for the samples doped with 840 p.p.m. and 1,400 p.p.m. of manganese. However, the strain broadening theory discussed in section 6.3 was developed on the assumption that the observed linewidth, ΔH_{obs}, is given by the sum of the individual linewidth components ΔH_i and ΔH_s. This assumption is valid provided that ΔH_i and ΔH_s are the linewidth components arising from two independent, Lorentzian broadening mechanisms. If, however, two independent Gaussian broadening mechanisms are responsible for ΔH_i and ΔH_s, then we obtain for the linewidth due to stress and for the intrinsic linewidth, respectively:[8.15]

$$\Delta H_s^2 = 1/3[\Delta H_{obs}^2(M=\pm 5/2 \leftrightarrow \pm 3/2, m) - \Delta H_{obs}^2(M=\pm 3/2 \leftrightarrow \pm 1/2, m)] \quad \ldots\ldots\ldots(8.2)$$

and

$$\Delta H_i^2 = \Delta H_{obs}^2(M=\pm 3/2 \leftrightarrow \pm 1/2, m) - \Delta H_s^2 \qquad (8.3)$$

where

$$\Delta H_s = 2\sqrt{3}\left\{(3/2C_{11})^2(\alpha/2)^2(1-3F)+C_{44}^2\gamma^2 3F\right\}^{\frac{1}{2}}$$

and

$$F = (\sin^2\theta\cos^2\theta + \sin^2\phi\cos^2\phi\sin^4\theta)$$

The Gaussian model predicts that the width of the $(M=+\frac{1}{2} \leftrightarrow -\frac{1}{2}, m)$ lines in the cubic Mn^{2+} spectrum is given by:

$$\Delta H_{obs}(M=\tfrac{1}{2} \leftrightarrow -\tfrac{1}{2}, m) = \Delta H_i \qquad (8.4)$$

whilst for the $(M=\pm 3/2 \leftrightarrow \pm 1/2, m)$ lines of the spectrum:

$$\Delta H_{obs}(M=\pm 3/2 \leftrightarrow \pm 1/2, m) = (\Delta H_i^2 + \Delta H_s^2)^{\frac{1}{2}} \qquad (8.5)$$

and for the $(M=\pm 5/2 \leftrightarrow \pm 3/2, m)$ lines of the spectrum:

$$\Delta H_{obs}(M=\pm 5/2 \leftrightarrow \pm 3/2, m) = (\Delta H_i^2 + 4\Delta H_s^2)^{\frac{1}{2}} \qquad (8.6)$$

Equations 8.2 and 8.3 were evaluated for the samples doped with 840 p.p.m. and 1,400 p.p.m. of manganese using the linewidth data given in Table 8.1 On substituting the values of ΔH_i and ΔH_s thus obtained into equations 8.4 to 8.6 it was found that the linewidths predicted by the Gaussian model for the various transitions in the cubic Mn^{2+} spectrum did not compare well with those observed experimentally.

Quantitatively then, the linewidths observed experimentally in the spectra of the MgO:Mn samples examined do not compare well with the predictions of either the Lorentzian or the Gaussian strain broadening models. However, the qualitative agreement between theory and experiment is much better. Both models predict that the width of the $(M=+\frac{1}{2} \leftrightarrow -\frac{1}{2}, m)$ lines is smaller than that of the other lines in the spectrum and this was observed experimentally when such measurements were possible (i.e. for the samples doped with 840 p.p.m. and 1,400 p.p.m. of manganese). In addition, for the sample doped with 840 p.p.m. of manganese the width of the spectral lines increases with the magnitude of M which is also predicted by both the Lorentzian and Gaussian strain broadening models.

The good qualitative agreement between theory and experiment suggests that the $(M=\pm 5/2 \leftrightarrow \pm 3/2, m)$ & $(M=\pm 3/2 \leftrightarrow \pm 1/2, m)$ lines are broader than the $(M=+\frac{1}{2} \leftrightarrow -\frac{1}{2}, m)$ lines in the cubic

Mn^{2+} spectra of the samples doped with 840 p.p.m. and 1,400 p.p.m. of manganese because random internal stresses in these crystals produce strain broadening. If time had allowed the MgO:Mn single crystals would have been annealed in order to test the validity of this interpretation. Any reduction in the widths of the $(M=\pm 5/2 \leftrightarrow \pm 3/2, m)$ and $(M=\pm 3/2 \leftrightarrow \pm 1/2, m)$ lines after annealing would confirm that they are strain broadened whereas annealing would have no effect upon the widths of these lines if some other broadening mechanism were responsible for them having larger widths than the $(M=+\frac{1}{2} \leftrightarrow -\frac{1}{2}, m)$ lines.

The degree of agreement between theory and experiment appears to depend upon the magnitude of the "intrinsic" linewidth, ΔH_i. In samples where all the spectral lines of the cubic Mn^{2+} spectrum are fully resolved (i.e. for samples with very low manganese concentrations), the experimentally observed linewidths are in good quantitative agreement with those predicted by the Gaussian strain broadening model.[8.15] The qualitative predictions of both the Lorentzian and the Gaussian strain broadening models are the same and, as already stated, accurately describe the relationships between the widths of the lines in the spectrum of the sample doped with 840 p.p.m. of manganese. When the manganese concentration is increased to 1,400 p.p.m. the qualitative agreement between theory and experiment is not so good since the width of the $(M=\pm 3/2 \leftrightarrow \pm 1/2, m)$ lines is greater than that of the $(M=\pm 5/2 \leftrightarrow \pm 3/2, m)$ lines.

Taken as a whole, the evidence suggests that the Gaussian strain broadening model is quantitatively valid for the MgO:Mn system provided that the dopant concentration (and hence ΔH_i) is not excessive. Presumably, the agreement between theory and experiment becomes less good as the manganese concentration increases because of partial line overlap which prevents us from measuring the "true" widths of the lines corresponding to the ($M=\pm 5/2 \leftrightarrow \pm 3/2, m$) and ($M=\pm 3/2 \leftrightarrow \pm 1/2, m$) transitions of the Mn^{2+} ions. According to this interpretation, the magnitude of the "intrinsic" linewidth of the sample doped with 840 p.p.m. of manganese is such that a relatively small amount of line overlap takes place, leading to good qualitative but not quantitative agreement between theory and experiment. When the manganese concentration is increased to 1,400 p.p.m. the amount of line overlap is greater due to the increase in ΔH_i and consequently the discrepancy between the observed and "true" linewidths of the ($M=\pm 5/2 \leftrightarrow \pm 3/2, m$) and ($M=\pm 3/2 \leftrightarrow \pm 1/2, m$) transitions is also greater. Therefore, for this sample even good qualitative agreement between theory and experiment is not found.

The source of the random internal stresses in the MgO:Mn single crystals is likely to be the size mismatch between the dopant Mn^{2+} ions (Goldschmidt radius 0.91Å[8.5]) and the Mg^{2+} ions (Goldschmidt radius 0.78Å[8.5]) of the host lattice. Since these ions have the same valency, the concentration of cation vacancies is presumably low so that the amount of lattice distortion arising from this source will be negligible.

8.2 EXPERIMENTAL RESULTS FOR MgO:Mn POWDERS

8.2.1 COMPARISON OF EXPERIMENTAL AND COMPUTED E.P.R. POWDER SPECTRA

Single crystal chippings of samples nominally doped with 840 p.p.m., 1,400 p.p.m. and 2,900 p.p.m. by weight of manganese were crushed using a mortar and pestle. The powders thus produced were sieved through a 185 μm mesh in order to produce samples with a reasonably uniform particle size and to ensure that the number of particles contained in the volume of powder undergoing resonance (at least 20,000) was sufficient to yield a powder spectrum with a low level of background noise.

E.P.R. spectra were recorded from all three powders on the Varian V4205-15 spectrometer at room temperature. Those obtained from the samples doped with 840 p.p.m. and 2,900 p.p.m. of manganese are shown in Figures 8.4(a) and 8.4(b) respectively. Both the illustrated spectra are due to the same paramagnetic centre, that of the sample doped with 2,900 p.p.m. of manganese simply being a less well resolved version of that of the sample doped with 840 p.p.m. of manganese. The resolution of the spectrum becomes progressively worse as the manganese concentration is increased because the spectral linewidths of the MgO:Mn powders (and hence the degree of line overlap) also increase with manganese concentration (this behaviour will be discussed in terms of dipolar broadening theory in the next section). The observed linewidths of the powder doped with 1,400 p.p.m. of manganese lie between those of

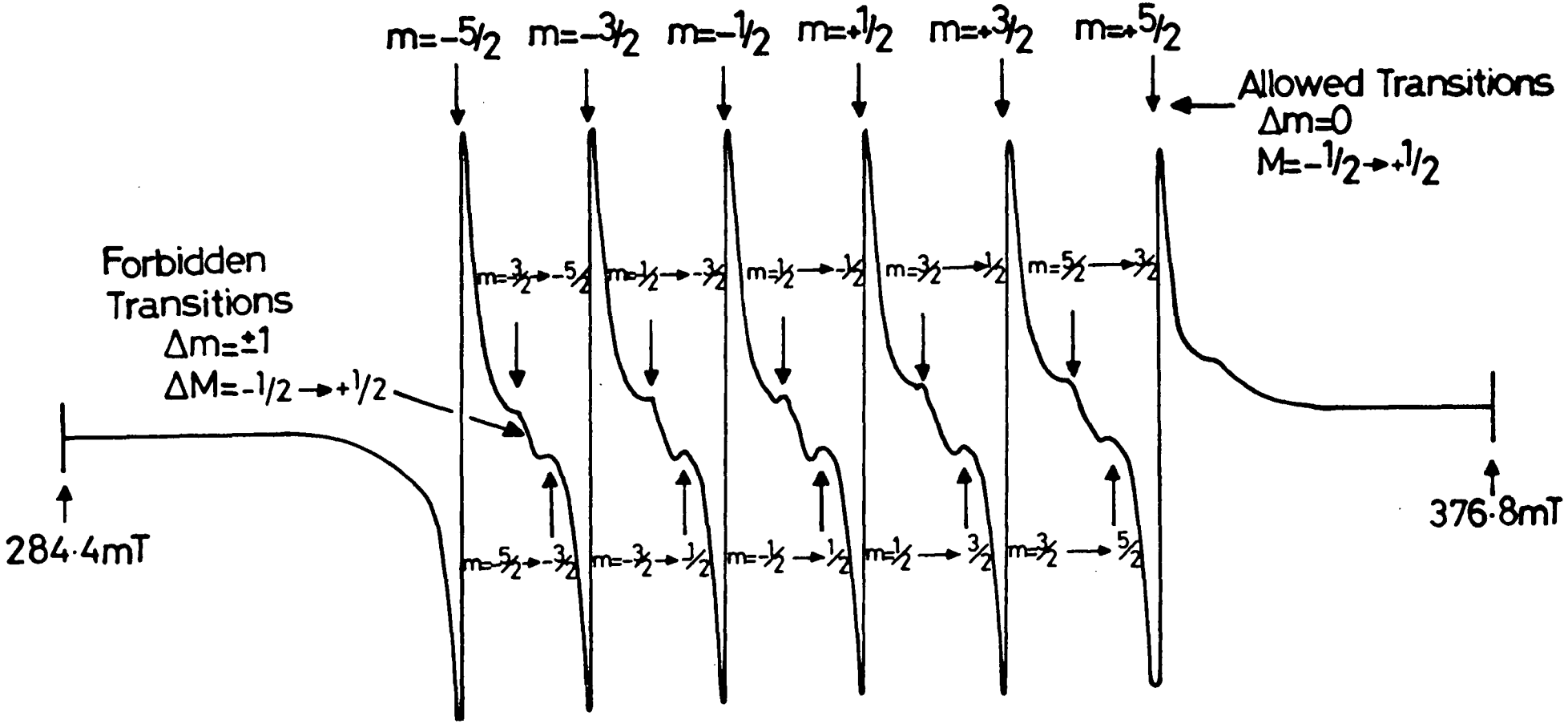

FIGURE 8.4(a) EXPERIMENTAL E.P.R. SPECTRUM OF POWDERED Mn/MgO; 840 p.p.m. Mn, 9.3795 GHz, 293K.

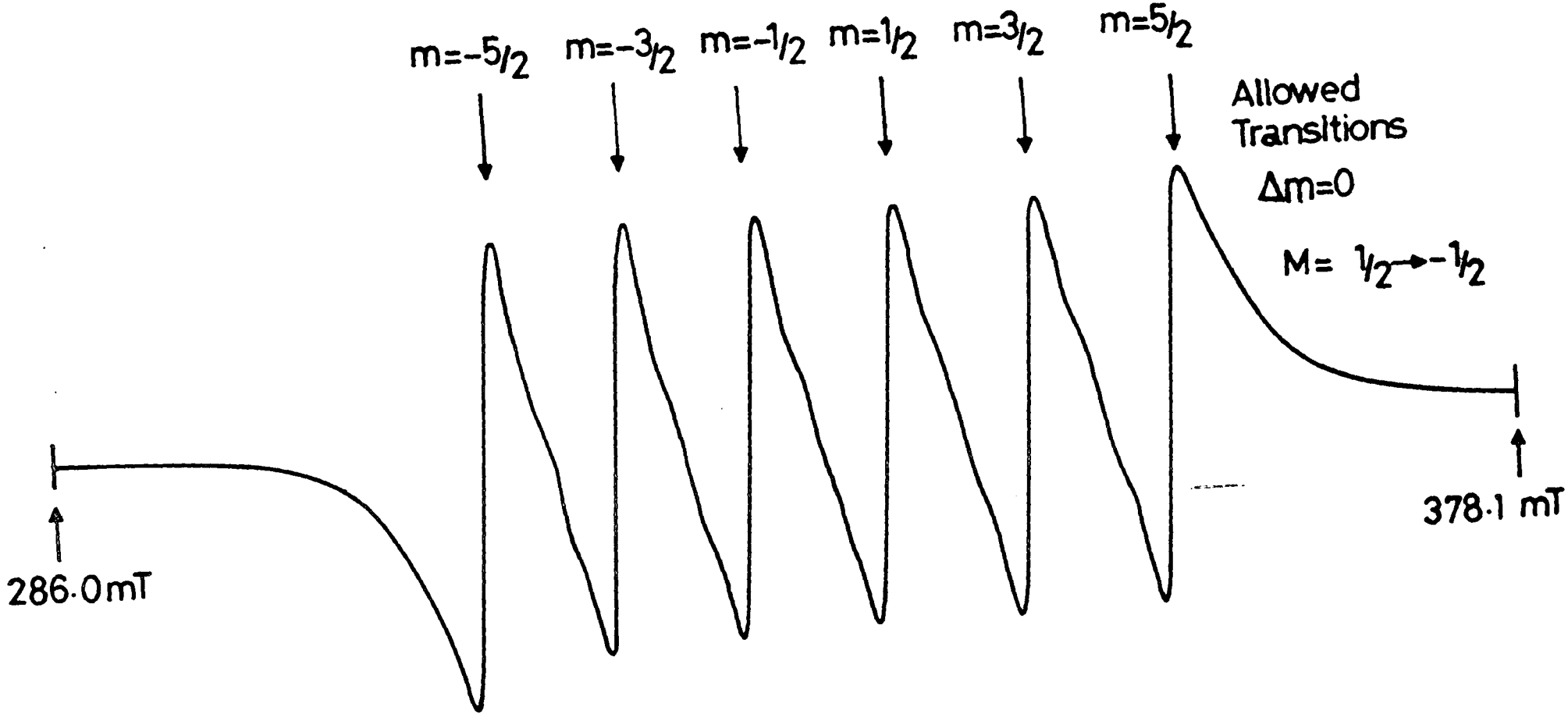

FIGURE 8.4(b) EXPERIMENTAL E.P.R. SPECTRUM OF POWDERED Mn/MgO; 2,900 p.p.m. Mn, 9.3800 GHz, 293K.

the powders containing 840 p.p.m. and 2,900 p.p.m. of manganese but remain small enough for the spectrum to retain the form of Figure 8.4(a).

The spectra illustrated in Figures 8.4(a) & (b) may also be attributed to Mn^{2+} ions in sites of octahedral symmetry but many of the lines observed in the corresponding single crystal spectra of Figures 8.1(a) & (b) are not seen in the powder spectra. However, the six most intense lines in the powder spectra, which are almost equally spaced, may be identified with the six almost isotropic lines observed in the single crystal spectra which correspond to the allowed $(M=+\frac{1}{2}\longleftrightarrow-\frac{1}{2},m)$ transitions (the appropriate quantum labels have been assigned to these lines in Figures 8.4(a) & (b)). The crystal field parameters A & g were calculated from the separations of the $(M=+\frac{1}{2}\longleftrightarrow-\frac{1}{2},m)$ lines using exactly the same method which was used to calculate these parameters from the separations of the same lines in the single crystal spectra (this method was described in section 8.1.1). The values obtained are given in Table 8.3 together with the average peak-to-peak width of the $(M=+\frac{1}{2}\longleftrightarrow-\frac{1}{2},m)$ lines and the microwave frequencies at which the measurements were taken. As expected, the measured g-factors and hyperfine structure constants are in good agreement with data reported for single crystal samples (Tables 8.1 & 8.2 and references 8.1 & 8.2) since both A & g & also the $(M=+\frac{1}{2}\longleftrightarrow-\frac{1}{2},m)$ lines are, to a good approximation, isotropic for the cubic Mn^{2+} spectrum.

Computer simulations of the powder spectrum of Mn^{2+}

MANGANESE CONCENTRATION (p.p.m.)	SPECTROSCOPIC SPLITTING FACTOR g	HYPERFINE STRUCTURE CONSTANT $A(\times 10^4\ cm^{-1})$	$\overline{\Delta Hpp}$ (Ms = $^1/_2 \leftrightarrow -^1/_2$, m TRANSITIONS) mT	MICROWAVE FREQUENCY GHz
840	2.0008	-81.03	0.893	9.3795
1400	2.0015	-80.98	1.227	9.3795
2900	2.0008	-80.84	1.929	9.3800

TABLE 8.3 E.P.R. PARAMETERS FOR POWDERED Mn/MgO SAMPLES (SIEVED THROUGH 185μm MESH): T = 293K.

in cubic sites in MgO were undertaken using all four methods described in sections 5.3 & 5.4. The predicted spectrum at any given dopant concentration was the same for each method and typical examples of the simulations obtained for the powders containing 840 p.p.m. and 2,900 p.p.m. of manganese are shown in Figures 8.5(a) and 8.5(b) respectively.

The variables in the simulation procedure are the crystal field parameters A, a and g, the microwave frequency, the lineshape function and the linewidth. For all these variables (except the microwave frequency) the values which were determined experimentally from the single crystal spectrum at a given dopant concentration were used to simulate the powder spectrum at the same dopant concentration. However, the parameter a could not be determined from the single crystal spectrum of the sample containing 2,900 p.p.m. of manganese and so the literature value of 1.996 mT[8.1] was used to conduct the simulation of the powder spectrum at this concentration.

The convolution process which constitutes part of the simulation procedure and which endeavours to imitate the line broadening in the real powder was carried out using a Lorentzian lineshape function since the single crystal cubic Mn^{2+} spectral lines had this shape. The peak-to-peak width of the Lorentzian lineshape function used to simulate the powder spectrum at any given dopant concentration was made equal to the intrinsic linewidth ΔH_i (Table 8.1 column five) determined from the spectrum of a single crystal doped at the same level.

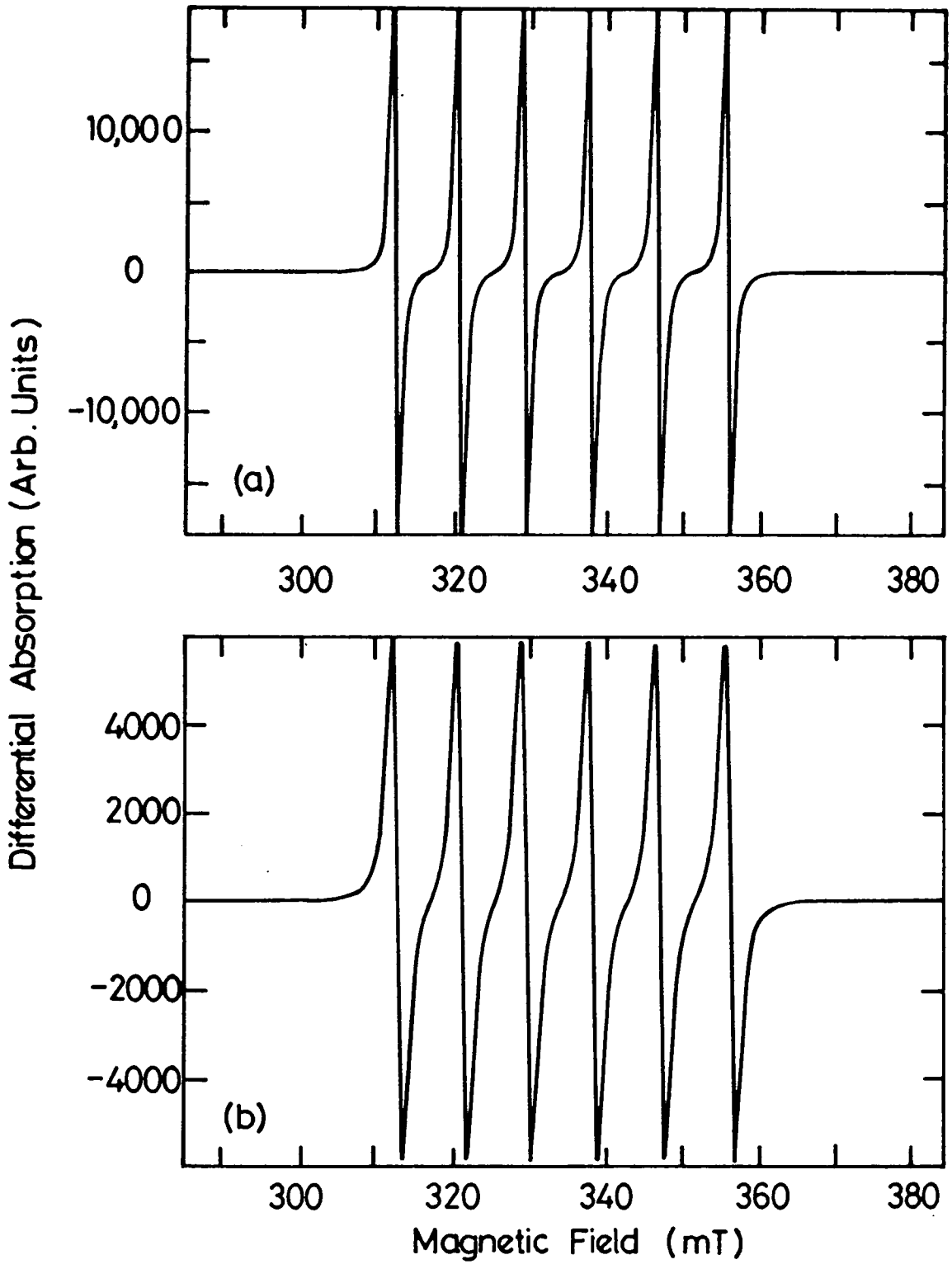

FIGURE 8.5 COMPUTER SIMULATION OF POWER SPECTRUM;
(a) 840 p.p.m. Mn,
(b) 2,900 p.p.m. Mn.

Adjustment of the microwave frequency simply shifts the simulated spectrum along the magnetic field axis. Obviously in order to compare the field positions of similar features in the simulated and experimental powder spectra the microwave frequency chosen for the simulation should be the same as that used to record the experimental spectrum. Hence the powder spectra of the three MgO:Mn powders examined were simulated at the microwave frequencies given in Table 8.3.

The six main lines which are observed in the experimental powder spectra (and which have been attributed to the $(M=+\frac{1}{2}\longleftrightarrow-\frac{1}{2},m)$ transitions) are also seen in the simulated powder spectra. Moreover, the field positions of these lines in the experimental and simulated powder spectra agree well. However, the slight variation in the peak height of the $(M=+\frac{1}{2}\longleftrightarrow-\frac{1}{2},m)$ lines which was observed in the experimental powder spectra is not present in the simulated powder spectra for which all six $(M=+\frac{1}{2}\longleftrightarrow-\frac{1}{2},m)$ transitions have the same peak height.

The other features which are present in the experimental powder spectra are not seen in the simulated powder spectra which only display the six $(M=+\frac{1}{2}\longleftrightarrow-\frac{1}{2},m)$ lines. This is not surprising in the case of the ten lines which occur as five pairs between the $(M=+\frac{1}{2}\longleftrightarrow-\frac{1}{2},m)$ lines in the experimental powder spectra because the measured field positions of these lines show that they are due to "forbidden" hyperfine transitions of the type $M=+\frac{1}{2}\longleftrightarrow-\frac{1}{2}$, $\Delta m=\pm 1$ whereas only the allowed $\Delta M=\pm 1, \Delta m=0$ transitions were included in the simulation procedure

undertaken to predict the powder spectrum of Mn^{2+} in cubic sites in MgO.

The origin of the shoulders to the low field side of the ($M=+\frac{1}{2}\leftrightarrow-\frac{1}{2}, m=-5/2$) transition and to the high field side of the ($M=+\frac{1}{2}\leftrightarrow-\frac{1}{2}, m=+5/2$) transition in the experimental powder spectra is not certain. It may be that they correspond to unresolved shoulders and divergences arising from the singularities in the powder patterns of the anisotropic ($M=\pm5/2\leftrightarrow\pm3/2, m=\pm5/2$) and ($M=\pm3/2\leftrightarrow\pm1/2$, $m=\pm5/2$) transitions, the theoretical positions of which were discussed in Chapter Five (see Tables 5.1 and 5.2) Resolved peaks arising from such singularities have been observed in powdered MgO:Mn by several groups of workers [8.4,8.14,8.16] and their field positions were found to compare well with those predicted by theory. However, no discrete peaks could be discerned from the shoulders observed in the experimental spectra of the three MgO:Mn powders examined which prevented any analysis of the type reported in references 8.4, 8.14 and 8.16 from being undertaken.

The above discussion demonstrates that the general agreement between the experimental powder spectra and those simulated for Mn^{2+} ions in cubic sites in MgO is very good. This agreement, together with the experimentally determined values of A and g given in Table 8.3, provides strong evidence that the experimental powder spectra are due to Mn^{2+} ions in cubic sites.

The six ($M=+\frac{1}{2}\leftrightarrow-\frac{1}{2}, m$) lines in both the experimental and simulated powder spectra are single lines. This fact

is clearly demonstrated for the simulated powder spectra by Figures 8.6(a) and 8.6(b) which show the ($M=+\frac{1}{2}\leftrightarrow-\frac{1}{2}$,$m=-5/2$) transition of the spectra predicted for the powders doped with 840 p.p.m. and 2,900 p.p.m. of manganese respectively in isolation on an expanded magnetic field scale (the other ($M=+\frac{1}{2}\leftrightarrow-\frac{1}{2}$,m) transitions are identical to the ($M=+\frac{1}{2}\leftrightarrow-\frac{1}{2}$, $m=-5/2$) transition.)

The fact that the ($M=+\frac{1}{2}\leftrightarrow-\frac{1}{2}$,m) lines are unsplit seems to be at variance with the prediction made by all the simulation techniques discussed in sections 5.3 and 5.4 that the central transition of a $^6S_{5/2}$ ion in a powder sample will be split into four separate features (two shoulders and two divergences) as shown in Figures 5.8(a) and (b). For Mn^{2+} the central transition is split into six components by the hyperfine interaction and each of these components (the ($M=+\frac{1}{2}\leftrightarrow-\frac{1}{2}$,m) lines) should behave in the manner predicted for the central transition of a $^6S_{5/2}$ ion.

However, the apparently contradictory evidence may be shown to be consistent when the relatively small value of the fine structure constant, a, for the cubic Mn^{2+} spectrum in MgO is taken into account. The two features of the central transition of a $^6S_{5/2}$ ion which are furthest apart in the powder spectrum in terms of magnetic field are the shoulder at the field corresponding to S=1/3 and the divergence at the field corresponding to S=7/50. Reference to Table 5.2 shows that these features are separated in magnetic field units by ($841a^2/270H_0$). At 9GHz, typical values of a and H_0 for the cubic Mn^{2+} spectrum

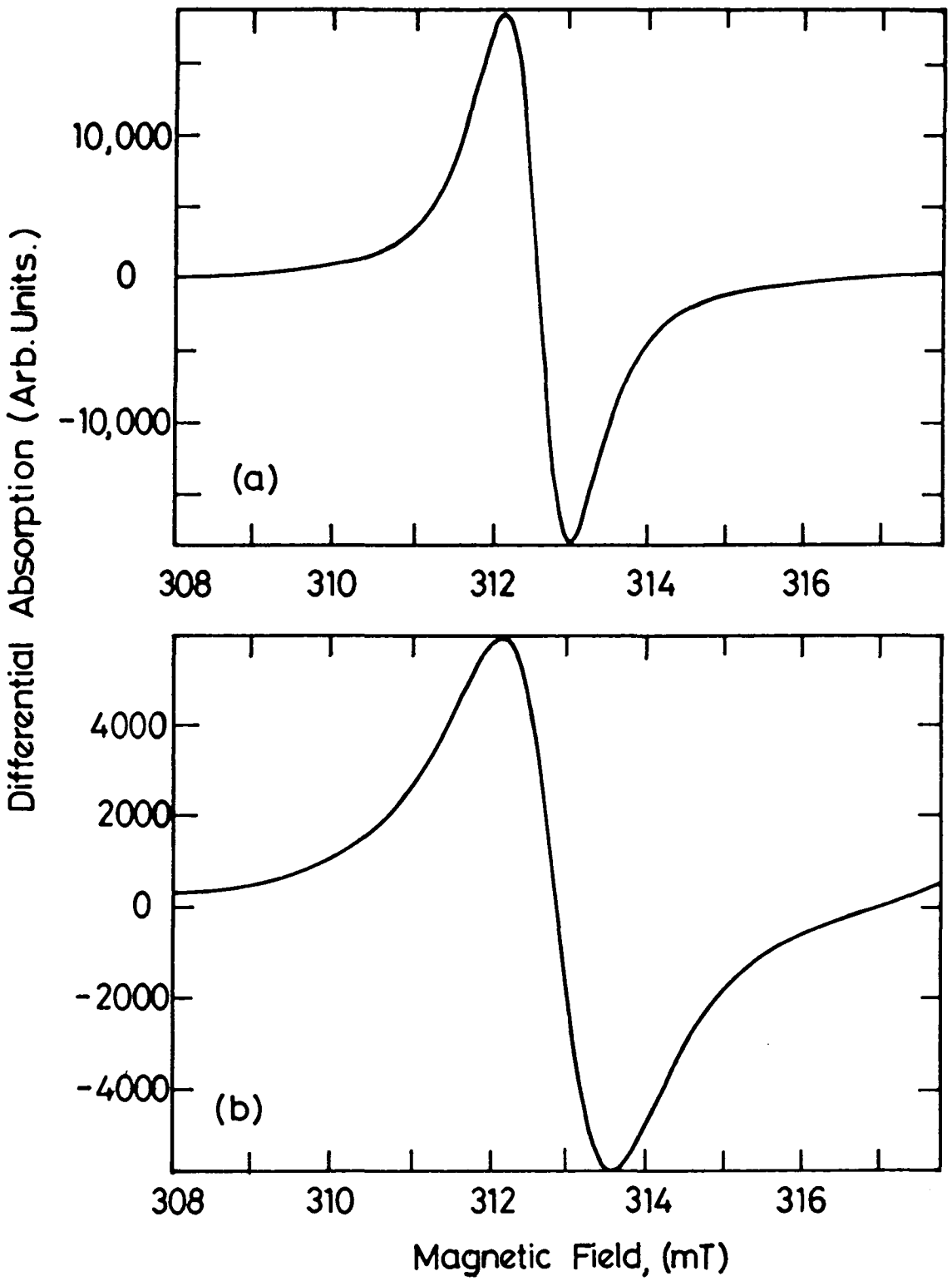

FIGURE 8.6 COMPUTER SIMULATION OF m = $-5/2$ SPECTRUM;
(a) 840 p.p.m. Mn,
(b) 2,900 p.p.m. Mn.

in MgO are a $\sim$ 2mT and $H_o \sim$ 335mT. Substituting these values into the above expression we find that the separation of the outermost features of the $(M=+\frac{1}{2} \leftrightarrow -\frac{1}{2}, m)$ transitions in the cubic Mn^{2+} spectrum in MgO is $\sim$0.04mT. This separation is much less than the average peak-to-peak width of the $(M=+\frac{1}{2} \leftrightarrow -\frac{1}{2}, m)$ lines in the single crystal spectrum at any of the dopant concentrations examined. Therefore, in the powder spectrum, when the $(M=+\frac{1}{2} \leftrightarrow -\frac{1}{2}, m)$ lines each become split into four separate components, these components will remain unresolved. As already noted, this is observed for both the experimental and simulated powder spectra.

However, the slight separation of the components of the $(M=+\frac{1}{2} \leftrightarrow -\frac{1}{2}, m)$ transitions in the powder spectrum does cause the width of these lines in the powder to be greater than in the single crystal if both are doped at the same level. The size of this effect is approximately 0.1mT as may be seen by comparing the linewidths given in Table 8.4 (which are the average peak-to-peak widths of the $(M=+\frac{1}{2} \leftrightarrow -\frac{1}{2}, m)$ lines for the simulated spectra of the three MgO:Mn powders examined) with the average peak-to-peak widths of the $(M=+\frac{1}{2} \leftrightarrow -\frac{1}{2}, m)$ lines in the single crystal spectra (given in Table 8.1).

Table 8.4 also shows that the splitting of the $(M=+\frac{1}{2} \leftrightarrow -\frac{1}{2}, m)$ lines produces slightly less broadening in the simulated powder spectrum as the manganese concentration increases. This is because the splitting of the $(M=+\frac{1}{2} \leftrightarrow -\frac{1}{2}, m)$ lines in the powder spectrum is independent of the manganese concentration (its magnitude is determined

Mn CONCENTRATION (p.p.m.)	$\overline{\Delta H}pp$ ($M = +\frac{1}{2} \leftrightarrow -\frac{1}{2}$, m TRANSITIONS) mT
840	0.908
1400	1.011
2900	1.506

TABLE 8.4 AVERAGE PEAK-TO-PEAK WIDTHS OF THE ($M = +\frac{1}{2} \leftrightarrow -\frac{1}{2}$, m) TRANSITIONS FOR THE SIMULATED POWDER SPECTRA OF Mn^{2+} IN CUBIC SITES IN MgO.

MANGANESE CONCENTRATION (p.p.m.)					
840			1400		
m	ΔH OBSERVED mT	ΔH CALCULATED mT	m	ΔH OBSERVED mT	ΔH CALCULATED mT
$\frac{5}{2}$	2.535	2.454	$\frac{5}{2}$	2.522	2.451
$\frac{3}{2}$	2.379	2.309	$\frac{3}{2}$	2.389	2.305
$\frac{1}{2}$	2.201	2.163	$\frac{1}{2}$	2.268	2.160
$-\frac{1}{2}$	2.035	2.018	$-\frac{1}{2}$	2.113	2.015
$-\frac{3}{2}$	1.956	1.872	$-\frac{3}{2}$	2.057	1.870

TABLE 8.5 THE CALCULATED AND OBSERVED SEPARATIONS, ΔH, OF THE "FORBIDDEN" HYPERFINE DOUBLETS IN THE POWDER SPECTRA OF THE SAMPLES DOPED WITH 840 p.p.m. AND 1400 p.p.m. OF MANGANESE.

solely by the magnitudes of the constants a and H_o) and therefore influences the overall width of these lines (which is concentration dependent, its magnitude being mainly determined by dipolar interactions) to a lesser extent as the manganese concentration increases.

The broadening effect that the splitting of the $(M=+\frac{1}{2}\leftrightarrow-\frac{1}{2},m)$ lines has in the experimental powder spectrum at any given doping level is accurately reflected by the increase in the width of these lines in the simulated powder spectrum compared to their width in the experimental single crystal spectrum at the same doping level. Comparison of Tables 8.3 and 8.4 shows that, for the sample doped with 840 p.p.m. of manganese, the simulated and experimental powder linewidths are, to within experimental error, equivalent. However, for the samples containing 1,400 p.p.m. and 2,900 p.p.m. of manganese the experimental powder linewidths are much larger than those of the simulated spectra. Therefore it appears that if the manganese concentration is low (840 p.p.m.) the powder linewidth is greater than the single crystal linewidth by an amount which is attributable to the splitting of the $(M=+\frac{1}{2}\leftrightarrow-\frac{1}{2},m)$ lines in the powder spectrum but at higher manganese concentrations (1,400 p.p.m. and 2,900 p.p.m.) broadening in addition to that expected from the splitting of the $(M=+\frac{1}{2}\leftrightarrow-\frac{1}{2},m)$ takes place, although the splitting of the $(M=+\frac{1}{2}\leftrightarrow-\frac{1}{2},m)$ lines still contributes towards their width in the powder spectra of these samples. The source of the additional broadening in the more heavily doped samples will be discussed in the next section.

The ten "forbidden" hyperfine lines appear in the experimental powder spectra as five pairs and are due to transitions of the type $M=+\frac{1}{2}\longleftrightarrow-\frac{1}{2},\Delta m=\pm 1$ (the specific quantum label for each of these lines is given in Figure 8.4(a)). The theoretical separation of the two lines in a "forbidden" hyperfine doublet is given by:[8.17]

$$\Delta H_f\ (m) = \frac{17A^2}{2H_o} - \frac{25A^3}{2H_o^2}\ (2m-1) + 2g_n H_o \qquad (8.7)$$

where m is the nuclear magnetic quantum number of the allowed $(M=+\frac{1}{2}\longleftrightarrow-\frac{1}{2},m)$ transition to the high field side of the doublet and g_n is the nuclear spectroscopic splitting factor.

Using $g_n=3.775\times10^{-4}$[8.17] and the values of A and H_o $(=h\nu/g\beta)$ determined from the allowed $(M=+\frac{1}{2}\longleftrightarrow-\frac{1}{2},m)$ transitions in the experimental powder spectra of the samples doped with 840 p.p.m. and 1,400 p.p.m. of manganese, the theoretical separations, ΔH_f (m), were calculated for these two powders and are compared with those observed experimentally in Table 8.5. For the powder containing 2,900 p.p.m. of manganese the wings of the allowed $(M=+\frac{1}{2}\longleftrightarrow-\frac{1}{2},m)$ transitions overlapped with the forbidden hyperfine lines so that their field positions could not be determined. Inspection of Table 8.5 shows that the agreement between the theoretical and experimental separations, ΔH_f (m), is good. Moreover, the field positions of the

five doublets observed in the experimental powder spectra did not agree with any of those predicted for the singularities in the powder absorption curve arising from the ($M=\pm 5/2 \leftrightarrow \pm 3/2, m$) and ($M=\pm 3/2 \leftrightarrow \pm 1/2, m$) transitions of Mn^{2+} in cubic sites in MgO thereby confirming that these lines correspond to "forbidden" hyperfine transitions.

The "forbidden" hyperfine lines can also be seen in the single crystal spectrum of the sample doped with 840 p.p.m. of manganese when the magnetic field is at an angle of 32^{o} to the <100> direction (Figure 8.2(a)) In the corresponding spectrum for a manganese concentration of 2,900 p.p.m. (Figure 8.2(b)) the $M=+\frac{1}{2} \leftrightarrow -\frac{1}{2}, \Delta m=\pm 1$ transitions are not observed because they overlap with the wings of the allowed ($M=+\frac{1}{2} \leftrightarrow -\frac{1}{2}, m$) transitions. The "forbidden" hyperfine lines have zero intensity in the single crystal spectrum when H // <100>[8.18] and therefore they are not seen in Figures 8.1(a) and (b) (in any case, the ($M=\pm 5/2 \leftrightarrow \pm 3/2, m$) and ($M=\pm 3/2 \leftrightarrow \pm 1/2, m$) lines would overlap with and obscure the "forbidden" transitions at this orientation).

It is noticeable that the relative intensities of the "forbidden" to the allowed transitions are much larger in the powder spectrum than in the single crystal spectrum. The observed enhancement of the $M=+\frac{1}{2} \leftrightarrow -\frac{1}{2}, \Delta m=\pm 1$ transitions in the powder spectrum has led to the suggestion that, in powdered MgO, the manganese ions are located in sites of <100> axial symmetry.[8.17,8.19-8.21] Since Mn^{2+} ions exist in a cubic environment in single crystal MgO the site symmetry would have to change in the powder. This has been explained by assuming that the axial distortion in the

powder is either due to strains created during the preparation[8.17] or due to the increased ratio of near-to-the-surface to bulk paramagnetic ions.[8.22]

According to this model, the admixture of states necessary for the observation of the forbidden transitions is due to the existence of higher order cross terms between the A and D terms of the Spin Hamiltonian appropriate for Mn^{2+} ions in sites of <100> axial symmetry. Applying the theory of Bleaney and Rubins,[8.23] Wolga and Tseng[8.17] concluded that in order to explain the enhancement of the forbidden transitions in their powder samples $D \sim 5mT$ (the value of D provides a measure of the degree of axial distortion).

It has been shown in this section that the observed powder spectra may be attributed to Mn^{2+} ions in cubic sites. Nonetheless, the proposal that the site symmetry is axial in the powder is reasonable because the cubic and axial powder spectra of Mn^{2+} ions in MgO may be analysed using an identical procedure since both spectra have the same general form (the number of lines (both allowed and "forbidden") and the theoretical expressions for their field positions are the same in each case). However, there are important differences between the cubic and axial powder spectra (apart from the increase in the relative intensities of the forbidden hyperfine lines in an axial crystal field), as was pointed out by Cordischi, Nelson and Tench[8.22] who observed the spectra of Mn^{2+} ions in both types of symmetry site in MgO powders.

In an axial crystal field the peak height of the

allowed ($M=+\frac{1}{2}\leftrightarrow-\frac{1}{2},m$) lines decreases and their width increases as m varies from -5/2 to +5/2 (i.e. as the magnetic field increases). This is because the axial field splits the allowed lines observed in the cubic powder spectrum into two components (the splitting increases with the absolute value of m) but because D is small ($\sim 5mT$[8.17]) the two components of each line are separated by an amount which is much less than the linewidth and therefore remain unresolved i.e. the axial field broadens the allowed lines observed in the cubic powder spectrum and the broadening increases with the absolute value of m (the axial field broadens, but does not split, the "forbidden" lines observed in the cubic powder spectrum). In a cubic crystal field the ($M=+\frac{1}{2}\leftrightarrow-\frac{1}{2},m$) lines are almost equal in height and linewidth and are closely Lorentzian (in axial symmetry the lineshapes of the ($M=+\frac{1}{2}\leftrightarrow-\frac{1}{2},m$) transitions are considerably distorted).

The characteristics of the allowed transitions in the powder spectra recorded from the three MgO:Mn powders examined closely resemble those mentioned above which are observed when the Mn^{2+} ions are located in sites of cubic symmetry. The variation in the intensities of the ($M=+\frac{1}{2}\leftrightarrow-\frac{1}{2},m$) lines in the experimental powder spectra already mentioned is slight and similar to that observed by Cordeschi et al[8.22] in the spectrum of Mn^{2+} in cubic sites in MgO. A much greater variation in the intensities of these lines was observed by the same authors in the spectrum of Mn^{2+} in axially symmetric sites in MgO. In addition, Eidels-Dubovoi and Beltran-Lopez[8.24] have shown

that an axially symmetric field is not the cause of the intensity variation of the ($M=+\frac{1}{2} \leftrightarrow -\frac{1}{2}, m$) lines in the spectrum of Mn^{2+} in a low-surface-area MgO powder (Cordischi et al [8.22] attributed the spectra they observed from this type of sample to Mn^{2+} in cubic sites).

Furthermore, Drumheller and Rubins[8.18] showed that the intensities of the forbidden transitions in the E.P.R. spectrum of Mn^{2+} in single crystals of MgO were proportional to $(\sin 4\theta)^2$ (θ is the angle between the magnetic field and a reference <100> direction in the crystal). In axial symmetry the intensities of these transitions would be proportional to $(\sin 2\theta)^2$. Drumheller and Rubins established that the $(\sin 4\theta)^2$ intensity variation of the $M=+\frac{1}{2} \leftrightarrow -\frac{1}{2}, \Delta m=\pm 1$ lines is consistent with the Mn^{2+} ions being located in sites of cubic symmetry and that the "forbidden" lines are observable in cubic fields because of the admixture of the cubic zero-field splitting parameter a with the off-diagonal hyperfine terms in the Spin Hamiltonian. However, the relative intensities of the "forbidden" to the allowed transitions for Mn^{2+} in single crystals of MgO reported by Drumheller and Rubins ($\sim 1/100$) are much smaller than those observed in the spectra of the three MgO:Mn powders examined in this work.

Cordischi, Nelson and Tench[8.22] also found that the spectrum of Mn^{2+} in low-surface-area powders was characteristic of a cubic environment whereas in high-surface-area powders the Mn^{2+} ions occupy axially symmetric sites (the finer powder shows a spectrum characteristic of axial symmetry because of the increased ratio of near-to-

the-surface to bulk paramagnetic ions). In terms of Cordischi, Nelson and Tench's definition our powders have low surface areas and therefore the powder spectrum observed should be that of Mn^{2+} in a cubic crystal field. In addition, single crystals of MgO:Mn such as ours which display the cubic Mn^{2+} spectrum have been shown, when crushed (as our samples were, to prepare the powders), to display features in the powder absorption curve characteristic of Mn^{2+} ions in cubic sites.[8.4]

On the whole then, the bulk of the evidence indicates that the powder spectra reported here are due to Mn^{2+} ions in cubic sites. However, the enhancement of the forbidden transitions in the powder spectrum requires that we acknowledge the possibility that in the powder the Mn^{2+} ions are located in sites of <100> axial symmetry.

8.2.2 THE DEPENDENCE OF E.P.R. LINEWIDTH UPON MANGANESE CONCENTRATION

A plot of the average peak-to-peak width of the allowed ($M=+\frac{1}{2}\leftrightarrow-\frac{1}{2}$,m) lines against total nominal manganese concentration (expressed as the percentage fraction of cationic sites occupied by the dopant) is shown in Figure 8.7. The solid curves in the Figure were calculated using the same values of the constants g, a and S and the same method which were employed to determine the curves for n=1 to n=4 in the single crystal case (see section 8.1.2 and Figure 8.3). They represent the theoretical dependence of the peak-to-peak linewidth upon manganese concentration predicted by de Biasi and Fernandes' dipolar broadening

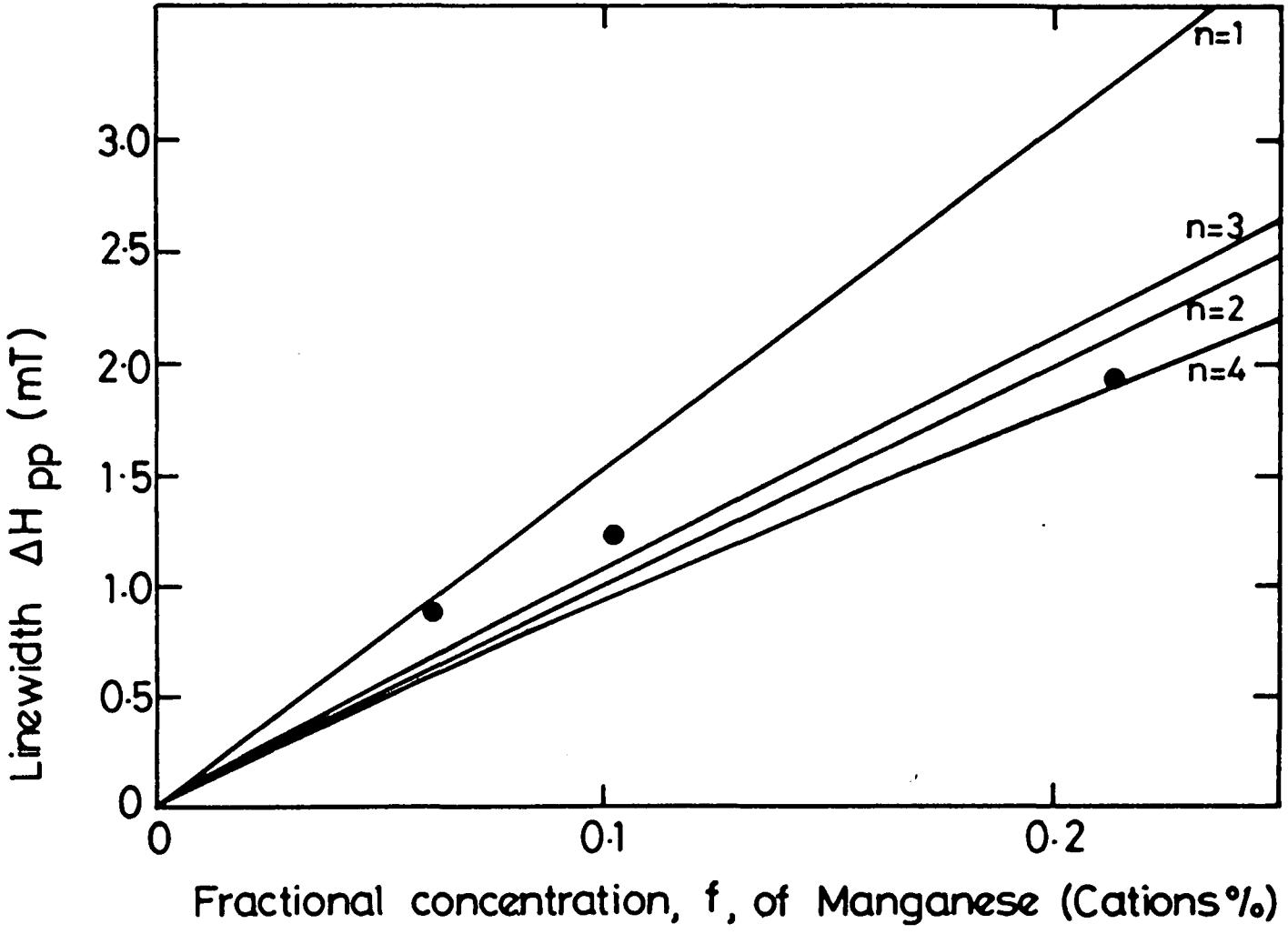

FIGURE 8.7 VARIATION OF LINEWIDTH WITH CONCENTRATION IN POWDERED Mn/MgO; (FULL LINES) THEORY, (DOTS) EXPERIMENTAL.

theory[8.9] for four different ranges of the exchange interaction.

The experimental points do not coincide exactly with any of the theoretical curves. This discrepancy between theory and experiment is not due to strain broadening increasing the width of the ($M=+\frac{1}{2}\leftrightarrow-\frac{1}{2},m$) lines since these lines are not, to first order, broadened by strain fields present in the host lattice. Nor is it due to broadening of the ($M=+\frac{1}{2}\leftrightarrow-\frac{1}{2},m$) lines as a result of line overlap because all the other fine structure lines (corresponding to the ($M=\pm5/2\leftrightarrow\pm3/2,m$) and ($M=\pm3/2\leftrightarrow\pm1/2,m$) transitions) are "smeared out" in the powder spectrum.

The disagreement between the linewidths predicted by de Biasi and Fernandes' model and those observed experimentally for the ($M=+\frac{1}{2}\leftrightarrow-\frac{1}{2},m$) transitions of the MgO:Mn^{2+} powders is likely to be due to the fact that the model only holds in the absence of fine structure splitting of the spin energy levels.[8.25,8.26] Therefore it can only be directly applied to ions with $S<2$ in cubic symmetry and to ions with $S=\frac{1}{2}$ in any other symmetry. Hence, whether the Mn^{2+} ions occupy cubic sites (most of the evidence suggests that this is the case) or whether they occupy axial sites (indicated by the enhancement of the "forbidden" hyperfine transitions in the powder spectrum) in the MgO:Mn powders examined, de Biasi and Fernandes' theoretical results are not, strictly speaking, applicable to this system as Mn^{2+} has a spin, S, of 5/2.

Nonetheless, the experimental points are reasonably close to the theoretical curves for n=2 and n=3. Therefore,

the divergence between de Biasi and Fernandes' model and experiment is not serious enough to invalidate the application of the theory to the MgO:Mn^{2+} system (presumably because the zero field splitting of the Mn^{2+} energy levels is small) although it is sufficient to prevent us from accurately determining the range of the exchange interaction. However, we may conclude from the experimental data that the range of the exchange interaction for Mn^{2+} in MgO is either $a.\sqrt{2}/2 = 2.98\mathring{A}$ (corresponding to n=2) or $a.\sqrt{3}/2 = 3.65\mathring{A}$ (corresponding to n=3, see Table 6.2).

According to di Biasi and Fernandes' model Figure 8.7 shows that Mn^{2+} ions which are either nearest neighbours (for which n=2) or next-to-nearest neighbours (for which n=3) form exchange coupled pairs whilst the vast majority of the Mn^{2+} ions are isolated and only interact via the dipolar mechanism. The combined concentrations of the isolated Mn^{2+} ions and the Mn^{2+} pairs for any given powder are equivalent to the total nominal manganese content of that powder.

Further evidence which supports the above interpretation of the linewidth data is provided by the fact that only the spectra discussed in the previous section were observed in the MgO:Mn powders examined. Therefore, as in the single crystal case, and for similar reasons, we may conclude that in our powder samples the dopant ions do not form large clusters, that they do not exist in a charge state other than the (+2) state and that the Mn^{2+} ions are all located in the same type of symmetry site (probably cubic but possibly axial). Although the

E.P.R. spectrum of nearest neighbour Mn^{2+} pairs in MgO has been reported in the literature[8.27] it was not observed in the samples examined here, probably because the pair concentration is much lower than the isolated ion concentration in these samples (pairs are only formed when, by chance, two Mn^{2+} ions occupy nearest neighbour or next-to-nearest neighbour sites; the probability of this situation arising in dilute solid solution is very low).

The average width of the $(M=+\frac{1}{2}\longleftrightarrow-\frac{1}{2},m)$ lines is considerably larger in the powder spectrum than in the single crystal spectrum at any given manganese concentration. This is not likely to be due to the influence of an axial crystal field, splitting each of the $(M=+\frac{1}{2}\longleftrightarrow-\frac{1}{2},m)$ lines in the Mn^{2+} powder spectrum into two components and thereby broadening them, since, as was shown in the previous section, the characteristics of the $(M=+\frac{1}{2}\longleftrightarrow-\frac{1}{2},m)$ lines in the powder spectrum strongly suggest that these lines correspond to the allowed transitions of Mn^{2+} ions in cubic symmetry.

Assuming that the Mn^{2+} ions occupy cubic sites, then at low manganese concentration (840 p.p.m.) the larger powder linewidth may be attributed to the splitting of the $(M=+\frac{1}{2}\longleftrightarrow-\frac{1}{2},m)$ lines into four components in the powder spectrum but at high manganese concentration (1,400 p.p.m. and 2,900 p.p.m.) only part of the linewidth increase in the powder spectrum ($\sim$ 0.1mT) is explained by this effect (see section 8.2.1). In addition, the discrepancy between the linewidths of the $(M=+\frac{1}{2}\longleftrightarrow-\frac{1}{2},m)$ transitions in the experimental and simulated powder spectra is greater for the sample doped

with 2,900 p.p.m. of manganese than for the sample doped with 1,400 p.p.m. of manganese.

Therefore it appears that the broadening in addition to that expected from the splitting of the ($M=+\frac{1}{2} \leftrightarrow -\frac{1}{2}$,m) lines in the experimental powder spectrum is concentration dependent but is negliglible for manganese concentrations up to at least 840 p.p.m. It is proposed that the source of the additional broadening is the dipolar mechanism, which has already been shown to be responsible for the widths of the non-strain broadened ($M=+\frac{1}{2} \leftrightarrow -\frac{1}{2}$,m) transitions.

The dipolar linewidth varies with the orientation of the magnetic field to the crystal axes; in the [100] plane it has a minimum value when H // <100> and a maximum value when H is oriented along the <110> direction (in the [100] plane a plot of dipolar linewidth against the angle, θ, between a reference <100> direction in the crystal and the magnetic field is symmetrical about $\theta = 45^{o}$).[8.28-8.30] In a powder sample the crystallites are randomly oriented and therefore the dipolar linewidth for individual crystallites will not be constant.

The powder spectra were simulated assuming that the linewidth was independent of the crystallite orientation and equal to the single crystal value when H // <100>. Therefore in the simulations the dipolar linewidth was underestimated at many crystallite orientations and it is suggested that this accounts for the fact that the ($M=+\frac{1}{2} \leftrightarrow -\frac{1}{2}$,m) lines are narrower in the simulations than in the experimental powder spectra for the more heavily doped samples.

The variation of the dipolar linewidth with crystallite orientation is also concentration dependent, being greater at higher paramagnetic concentrations.[8.28-8.30] Hence it is assumed that at a manganese concentration of 840 p.p.m. the dipolar linewidth does not change with crystallite orientation to a large enough extent to have any effect upon the experimental powder linewidth.

The change in dipolar linewidth with crystallite orientation is implicitly taken into account in de Biasi and Fernandes' dipolar broadening theory by replacing the powers of the direction cosines in equations 6.26 and 6.27 by their averages over a sphere.

8.3 SUMMARY OF RESULTS FOR THE MgO:Mn SYSTEM

Both the single crystal and powdered MgO:Mn samples examined have spectra which may be attributed to Mn^{2+} ions in cubic symmetry. In the case of the single crystal specimens the identification of the paramagnetic species responsible for the spectra with Mn^{2+} in cubic sites is certain. However, the large intensities of the forbidden hyperfine transitions relative to those of the allowed transitions in the powder spectra suggests that there is a slight possibility that the Mn^{2+} ions occupy sites of <100> axial symmetry in the powder specimens. Nevertheless, a large body of evidence points to the fact that the Mn^{2+} ions occupy cubic sites in the powder and, on balance, it seems reasonable to suppose that this is the case.

The linewidth data shows that all of the manganese dopant effectively exists as isolated Mn^{2+} ions; in dilute

solid solution a small number of Mn^{2+} ions will, by chance, be located close enough together (i.e. within the range of the exchange interaction) to form exchange coupled pairs. Although the range of the exchange interaction cannot be determined accurately, we can conclude from the linewidth data that it is either 2.98Å (if so, the Mn^{2+} ions must be nearest neighbours to form a pair) or 3.65Å (in which case the Mn^{2+} ions can be located either on nearest neighbour or on next-to-nearest neighbour sites to form a pair).

The observed widths of the (M=5/2$\longleftrightarrow$3/2,m=-5/2) and (M=-3/2$\longleftrightarrow$-1/2,m=-5/2) transitions in the single crystal spectra point to these lines being strain broadened. The likely source of the strain is the size mismatch between the Mn^{2+} dopant ions of the host lattice.

Summing up, the recorded single crystal and powder spectra and the linewidth data obtained from them allow us to conclude that:

(i) The manganese dopant does not aggregate to form large clusters of ions.

(ii) No fraction of the dopant exists in a charge state other than the (+2) state.

(iii) The vast majority of the Mn^{2+} ions are isolated and the remainder form exchange-coupled pairs.

(iv) All the Mn^{2+} ions occupy cubic symmetry sites in the single crystal samples.

(v) The Mn^{2+} ions all occupy the same type of symmetry site in the powder samples which is probably cubic but possibly <100> axial.

(vi) The host lattice is strained in the region of the site occupied by a Mn^{2+} ion, probably because the Mn^{2+} dopant ion is larger than the Mg^{2+} ion which normally occupies the site.

REFERENCES

8.1 W. Low Phys. Rev. 105, 793 (1957)

8.2 W. Low Ann. N.Y. Acad. Sci. 72, 69 (1958)

8.3 L.M. Matarrese and C. Kikuchi J. Phys. Chem. Solids 1, 117 (1956)

8.4 J. Rubio O., E. Munoz P., J.Boldu O., Y. Chen and M.M. Abraham J. Chem. Phys. 70, 633 (1979)

8.5 A. Cimino, M. Lo Jacono, P. Porta and M. Valigi Z. Phys. Chem. (Frankfurt), N.F. 59, 134 (1968)

8.6 D. Cordischi and M. Lo Jacono Z. Phys. Chem. (Frankfurt), N.F. 74, 93 (1971)

8.7 P.R. Solomon Phys. Rev. 152, 452 (1966)

8.8 M.D. Hossain, J.S. Thorp and A.D. Inglis "E.S.R. Linewidths in Mn^{2+}/MgO" (unpublished)

8.9 R.S. de Biasi and A.A.R. Fernandes J. Phys. C:Sol. State Phys. 16, 5481 (1983)

8.10 R.G.W. Wyckoff "Crystal Structures" Vol. 1, Wiley Interscience, N.Y. (1965).

8.11 A. Cimino, M. Lo Jacono, P. Porta and M. Valigi Z. Phys. Chem.(Frankfurt), N.F. 51, 301 (1966)

8.12 M. Valigi, F. Pepe and M. Schiavello J. Chem. Soc. Faraday I 71, 1631 (1975)

8.13 R.A. Weeks and A. Chatelain J. Am. Cer. Soc. 61, 297 (1978)

8.14 F. Gesmundo and P.F. Rossi J. Sol. State Chem. 8, 297 (1973)

8.15 E.R. Feher Phys. Rev. 136, A145 (1964)

8.16 N.G. Kakazei and M.V. Vlasova, J. Appl. Spectroc. (U.S.A.) translated from Zhurnal Prikladnoi Spektroskopii 24, 150 (1976)

8.17 G.J. Wolga and R. Tseng Phys. Rev. 133, A1563 (1964)

8.18 J.E. Drumheller and R.S. Rubins Phys. Rev. 133, A1099 (1964)

8.19 J. Castro and V. Beltran Bull. Rev. Mex. Fis. 4, 3 (1974)

8.20 J. Castro and V. Beltran Bull. Rev. Mex. Fis. 4, 174 (1975)

8.21 J. Castro and V. Beltran Bull. Rev. Mex. Fis. 4, 54 (1976)

8.22 D. Cordischi, R.L. Nelson and A.J. Tench Trans. Faraday Soc. 65, 2740 (1969)

8.23 B. Bleaney and R.S. Rubins Proc. Phys. Soc. 77, 103 (1961)

8.24 S. Eidels-Dubovoi and V. Beltran-Lopez J. Mag. Res. 32, 441 (1978)

8.25 K.W.H. Stevens Proc. Roy. Soc. A214, 237 (1952)

8.26 A. Abragam and K. Kambe Phys. Rev. 91, 894 (1953)

8.27 E.A. Harris J. Phys.C:Solid State Phys. 5, 338 (1972)

8.28 J.S. Thorp, R.A. Vasquez, C. Adcock and W. Hutton J. Mat. Sci. 11, 89 (1976)

8.29 J.S. Thorp, M.D. Hossain and L.J.C. Bluck J. Mat. Sci. 14, 2853 (1979)

8.30 J.S. Thorp, M.D. Hossain, L.J.C. Bluck and T.G. Bushell J. Mat. Sci. 15, 903 (1980)

CHAPTER NINE

E.P.R. INVESTIGATIONS OF MgO:Fe SINGLE CRYSTALS AND POWDERS

9.1 EXPERIMENTAL RESULTS FOR SINGLE CRYSTAL MgO:Fe

9.1.1 CHARACTERIZATION OF THE E.P.R. SPECTRA

Spectra were recorded from all six iron doped MgO single crystals on the Varian V4205-15 spectrometer at room temperature with the magnetic field parallel to a <100>-type direction in the crystal. The dopant concentrations in the samples examined were 310 p.p.m., 2,300 p.p.m., 4,300 p.p.m., 8,500 p.p.m., 11,900 p.p.m. and 12,900 p.p.m. by weight.

A typical trace is shown in Figure 9.1 (this particular example was recorded from the sample containing 310 p.p.m. of iron). The illustrated spectrum is well known, being first reported by Low[9.1], and since then by several other groups of workers[9.2 - 9.6]. It is due to the $\Delta M = \pm 1$ transitions of isolated Fe^{3+} ions in sites of octahedral symmetry.

The cubic Fe^{3+} spectrum consists of a central $M = +\frac{1}{2} \longleftrightarrow -\frac{1}{2}$ transition symmetrically surrounded by two pairs of fine structure lines. When H // <100>, the inner pair of fine structure lines (corresponding to the $M = \pm 5/2 \longleftrightarrow \pm 3/2$ transitions) are located at $\mp 2a$ from the central transition and the outer pair of fine structure lines (corresponding to the $M = \pm 3/2 \longleftrightarrow \pm 1/2$ transitions) are located at $\pm 5/2a$ from the central transition (where a

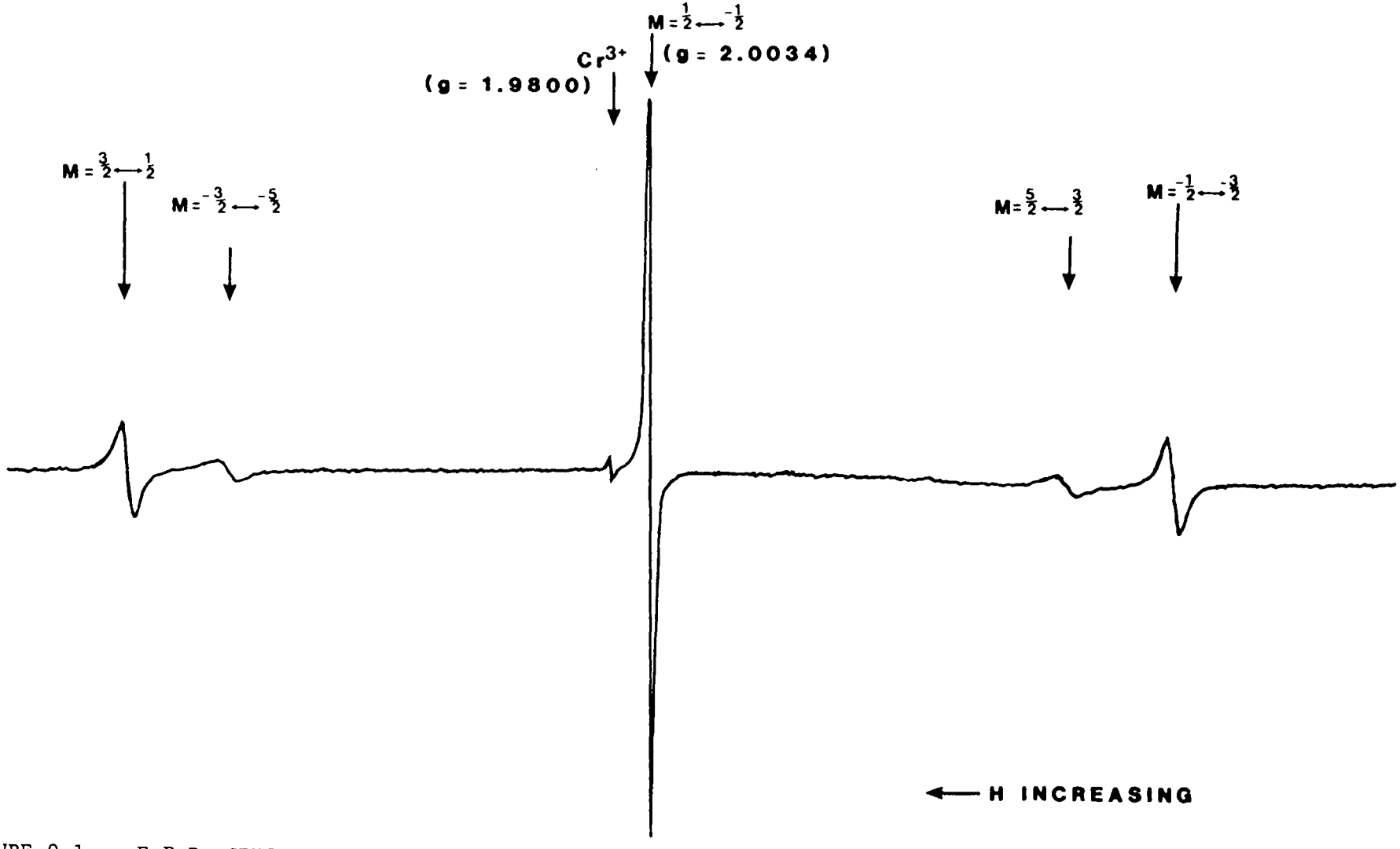

FIGURE 9.1 E.P.R. SPECTRUM WITH H//<100> OF SINGLE CRYSTAL MgO:Fe; IRON CONCENTRATION = 310p.p.m.; T = 293K; ν = 9.3815 GHz.

is the cubic crystalline field splitting parameter).

For all samples, the M = $+\frac{1}{2} \longleftrightarrow -\frac{1}{2}$ line was recorded seperately using an expanded magnetic field scale in order to measure its peak-to-peak width and the g-value (simply equal to $h\nu / \beta\ H_{M=+\frac{1}{2} \longleftrightarrow -\frac{1}{2}}$) accurately. The values of g and peak-to-peak linewidth, $\Delta H_{M=+\frac{1}{2} \longleftrightarrow -\frac{1}{2}}$, obtained at each dopant concentration are given in Table 9.1.

Unfortunately, the proton resonance frequencies corresponding to the magnetic field values at which the Fe^{3+} fine structure lines occur were outside the frequency range of our particular magnetometer. Therefore, since a line at $g \sim 1.9800$ was present in the spectra of all the samples examined, in each case the magnetic field scale of the Fe^{3+} spectrum was calibrated from the separation of this line and the Fe^{3+} $M = +\frac{1}{2} \longleftrightarrow -\frac{1}{2}$ transition. Presumably, the line at g = 1.9800 arises from the coincident $M = +\frac{1}{2} \longleftrightarrow -\frac{1}{2}$ and $M = \pm 3/2 \longleftrightarrow \pm 1/2$ transitions of the spectrum due to Cr^{3+} ions in an octahedral environment (see section 7.1.1). In general, the intensity of the cubic Cr^{3+} central transition relative to that of the cubic Fe^{3+} central transition increased with iron concentration.

With H // <100>, two indpendent values of a were determined for the sample doped with 310 p.p.m. of iron from the separations of the inner and outer pairs of fine structure lines respectively. These two values were then averaged in order to obtain the experimentally determined value of a quoted for this sample in Table 9.1.

For all the other samples, the lines corresponding to the $M = \pm 5/2 \longleftrightarrow \pm 3/2$ transitions were so broad and of such low intensity that their field positions and width could

IRON CONCENTRATION (p.p.m. by weight)	SPECTROSCOPIC SPLITTING FACTOR g	FINE STRUCTURE CONSTANT, a, ($\times 10^4$ cm^{-1})	ΔHpp ($\frac{1}{2} \leftrightarrow -\frac{1}{2}$) TRANSITION mT	$\overline{\Delta Hpp}$ ($\pm \frac{1}{2} \leftrightarrow \pm \frac{3}{2}$) TRANSITIONS mT	$\overline{\Delta Hpp}$ ($\pm \frac{3}{2} \leftrightarrow \pm \frac{5}{2}$) TRANSITIONS mT	MICROWAVE FREQUENCY GHz
310	2.0034	202.1	0.508	1.268	2.155	9.3810
2300	2.0038	198.0	0.518	2.220	-	9.3810
4300	2.0032	194.4	0.536	2.868	-	9.3805
8500	2.0039	196.7	0.557	3.019	-	9.3810
11900	2.0027	199.2	0.587	3.582	-	9.3805
12900	2.0028	198.7	0.566	3.151	-	9.3810

TABLE 9.1 E.P.R. PARAMETERS FOR AS RECEIVED SINGLE CRYSTAL Fe/MgO: MEASUREMENTS TAKEN FROM SPECTRA RECORDED AT 293K WITH H//<100> .

not be measured accurately. Therefore, for these samples, the experimentally determined values of a quoted in Table 9.1 were simply determined from the separations of the lines corresponding to the M = $\pm 3/2 \longleftrightarrow \pm 1/2$ transitions with H //<100>.

Also listed in Table 9.1 are the average widths of the M = $\pm 3/2 \longleftrightarrow \pm 1/2$ lines at each dopant concentration and the average width of the M = $\pm 5/2 \longleftrightarrow \pm 3/2$ lines for the sample doped with 310 p.p.m. of iron. As already stated, the linewidths of the M = $\pm 5/2 \longleftrightarrow \pm 3/2$ transitions could not be determined from the spectra of the samples containing more than 310 p.p.m. of iron. Since the two lines in a fine structure pair are supposedly identical, by averaging their individual widths we obtain the best estimate of the width characteristic of the lines comprising the pair.

Finally, Table 9.1 gives the microwave frequencies at which the measurements were taken. It should be noted that the a and g values listed in Table 9.1 are in close agreement both with each other and also with previously published data.[9.1 - 9.6]

Figure 9.2 shows the spectrum recorded (with H //<100>) from the sample doped with 12,900 p.p.m. of iron. The figure illustrates the point that the M = $\pm 5/2 \longleftrightarrow \pm 3/2$ lines are heavily depressed in the cubic Fe^{3+} spectra of all the samples except that containing 310 p.p.m. of iron. The line corresponding to the coincident M = $+1/2 \longleftrightarrow -1/2$ and M = $\pm 3/2 \longleftrightarrow \pm 1/2$ transitions of Cr^{3+} ions in octahedral symmetry present in the spectra of all the single crystals examined, is also clearly visible in Figure 9.2.

The measured separations of the five other lines in

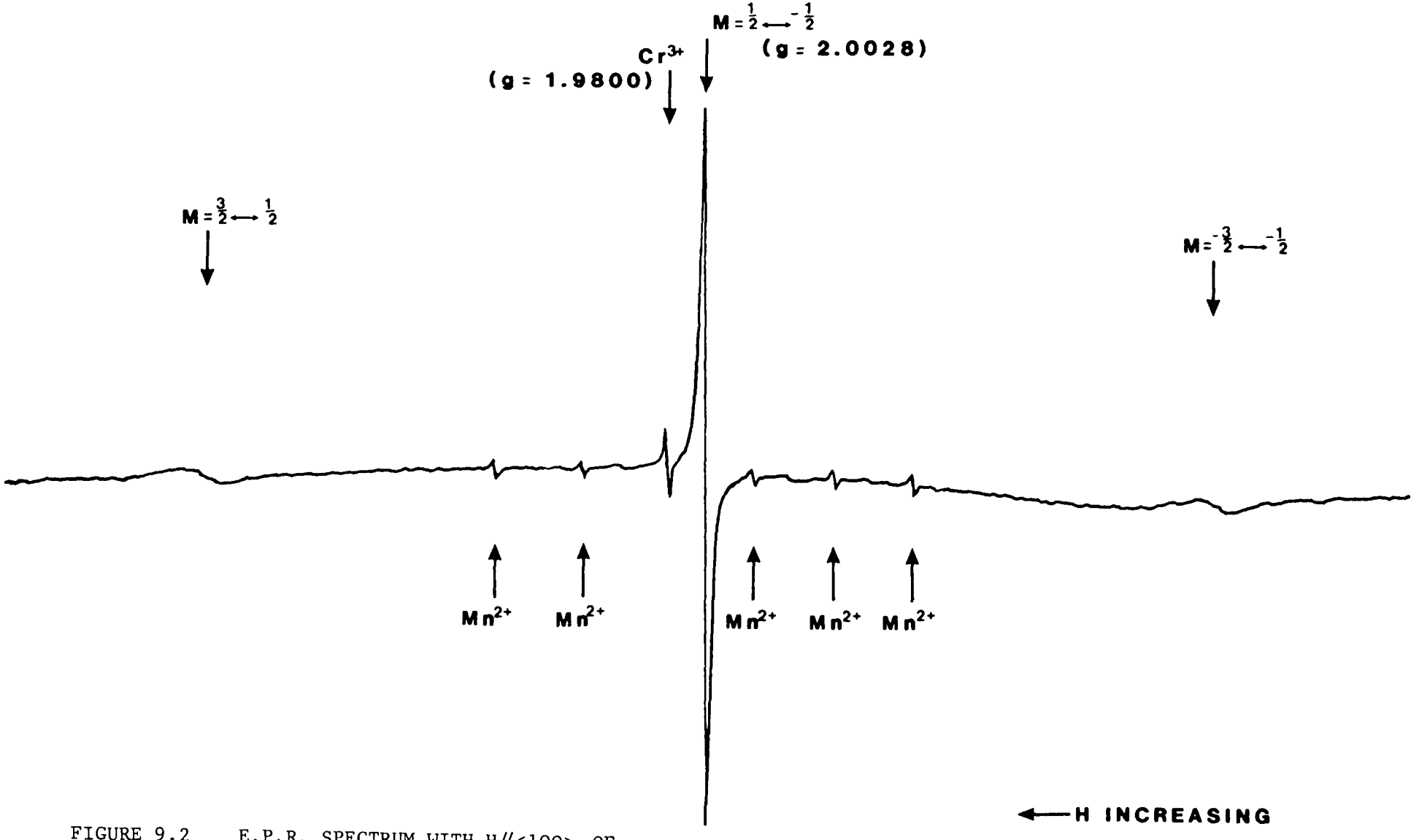

FIGURE 9.2 E.P.R. SPECTRUM WITH H//<100> OF SINGLE CRYSTAL MgO:Fe; IRON CONCENTRATION = 12,900p.p.m.; T = 293K; ν = 9.3810 GHz.

the spectrum illustrated in Figure 9.2 not previously mentioned show that they are attributable to the M = $+\frac{1}{2} \longleftrightarrow -\frac{1}{2}$, m transitions of Mn^{2+} ions in octahedral sites. Although there are six such lines in the cubic Mn^{2+} spectrum, approximately equally spaced, by an amount corresponding to the hyperfine structure constant, A, (see section 8.1.1), that corresponding to the M = $+\frac{1}{2} \longleftrightarrow -\frac{1}{2}$, m = $+\frac{1}{2}$ transition overlaps with, and is obscured by, the cubic Cr^{3+} central transition. The five transitions attributed to Mn^{2+} ions in cubic sites are also seen in the spectrum of the single crystal doped with 11,900 p.p.m. of iron.

A broad line of very low amplitude centred on the cubic Fe^{3+} spectrum was also observed in the spectra of all the samples examined. The intensity of this line relative to that of the M = $+\frac{1}{2} \longleftrightarrow -\frac{1}{2}$ line in the cubic Fe^{3+} spectrum was greater for the more heavily doped samples (those containing 8,500 p.p.m., 11,900 p.p.m. and 12,900 p.p.m. of iron) than for the more lightly doped samples (those containing 310 p.p.m., 2,300 p.p.m. and 4,300 p.p.m. of iron).

We attribute the broad line to "clusters" of Fe^{3+} ions i.e. regions in the MgO crystal where several Fe^{3+} ions are much closer together than they would be if all the dopant ions were randomly distributed over the total number of cationic sites available. The clustered iron phase could be paramagnetic or ferrimagnetic in nature: paramagnetic ions in close proximity would give rise to broad E.P.R. spectral lines because of strong dipolar interactions whereas a broad line associated with precipitates of the ferrimagnetic spinel phase $MgFe_2O_4$ in iron doped MgO has

been reported by several groups of workers.[9.7 - 9.11] Unfortunately, the experimental dependence of the width of the broad line upon the temperature of the sample when the spectrum was recorded, which would enable us to establish whether this line arose from a paramagnetic or ferrimagnetic species (ferrimagnetic lines decrease in width whereas paramagnetic lines increase in width as the sample temperature is increased), was not determined.

RHEED patterns obtained from etched as received single crystals (for the etching treatment see section 7.1.2) displayed only the diffraction spots attributable to MgO. Therefore we assume that the clustered iron phase is not the spinel $MgFe_2O_4$ or any other compound of iron with a regular crystal structure.

Despite extensive and repeated investigations at low temperatures (in the liquid helium range) the E.P.R. spectrum attributable to Fe^{2+} ions in sites of octahedral symmetry in MgO[9.2, 9.12, 9.13] was not observed in any of the samples examined. In addition, although an E.P.R. spectrum due to Fe^{+} in MgO has been reported in the literature,[9.13, 9.14] no evidence was found for the existence of this species in our crystals, which is not surprising, since it has only been found in samples after they have been subjected to ionizing radiations.

Finally, spectra due to isolated Fe^{3+} ions located at sites with non-cubic symmetry have been reported[9.11, 9.15, 9.16] but none of these were observed in our iron doped magnesia single crystals.

Thus we may conclude that, in the single crystals

examined, the dopant exists entirely in the (+3) valency state, either as isolated ions located at sites of cubic symmetry (such ions probably occupy cationic sites normally occupied by Mg^{2+} ions in the MgO host lattice) or as ions in "clusters". The "clusters" do not have a well defined crystal structure or composition and in addition it is not known whether the Fe^{3+} ions in such a cluster are coupled together by exchange forces or whether they simply interact via the dipolar mechanism.

9.1.2 THE VARIATION OF THE LINEWIDTH OF THE CUBIC Fe^{3+} CENTRAL TRANSITION WITH IRON CONCENTRATION

Line broadening due to both spin-lattice relaxation processes and also (to first order) to the effects of lattice strain are unimportant for the $M = +\frac{1}{2} \longleftrightarrow -\frac{1}{2}$ transition in the cubic Fe^{3+} spectrum (see sections 6.4 and 6.3 respectively). Therefore it is reasonable to assume that dipolar interactions largely determine the magnitude of the width of this line in the spectra of the single crystals examined.

The peak-to-peak linewidths of the central transitions in the cubic Fe^{3+} spectra of the six as received single crystals examined were measured (see Table 9.1) and are shown plotted against total nominal iron concentration in Figure 9.3. The variation of linewidth with iron concentration is negligible and therefore the experimental data does not agree with the predictions of de Biasi and Fernandes' dipolar broadening theory [9.17] for any value of n. Although the theory is, strictly speaking, only applicable to powders this cannot account for the wide

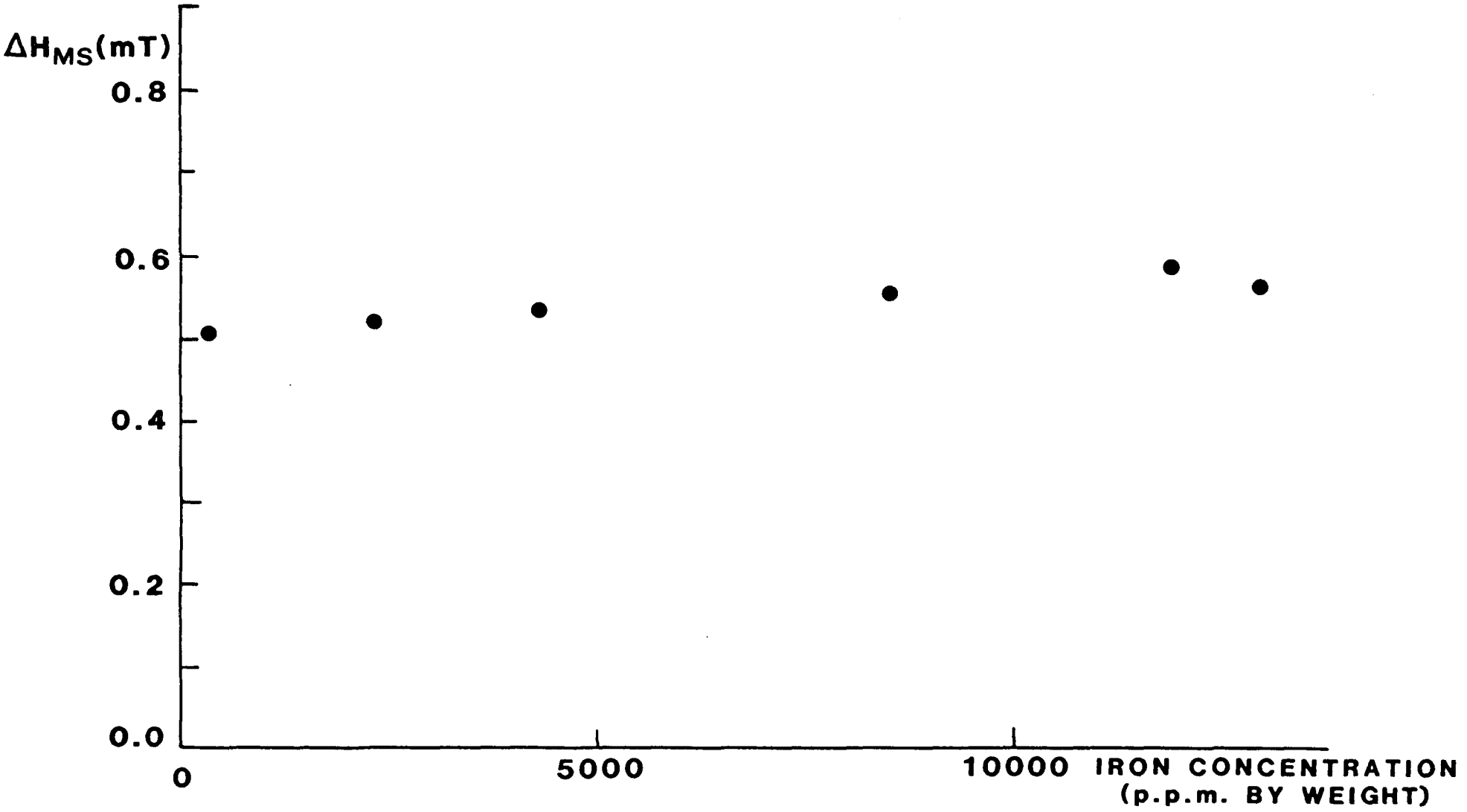

FIGURE 9.3 VARIATION OF THE PEAK-TO-PEAK LINEWIDTH, ΔH_{MS}, OF THE $M = +1/2 \leftrightarrow -1/2$ TRANSITION OF THE CUBIC Fe^{3+} SPECTRUM WITH IRON CONCENTRATION FOR SINGLE CRYSTAL MgO:Fe; THE MEASUREMENTS WERE TAKEN WITH H//<100> AT 293K.

divergence between the theoretical predictions and the experimental results for the MgO:Fe single crystals examined.

The discrepancy between theory and experiment arises because only a fraction of the dopant exists as isolated Fe^{3+} ions in cubic sites. Agreement between de Biasi and Fernandes' model and our experimental results would only be achieved if this fraction were plotted against the widths of the central transition measured from the spectra of the various samples.

Evidence that some fraction of the dopant does not exist as isolated Fe^{3+} ions in cubic sites is provided by the presence of the broad line in the spectra of all the samples examined which was mentioned in the previous section. Attempts have been made[9.5,9.7] to quantitatively estimate the concentration of isolated Fe^{3+} ions in cubic sites in Spicers MgO samples similar to those studied in this work (and with the same total nominal iron concentrations) using the method known as "spin-counting"[9.18]. Unfortunately, even using Inglis et als[9.5] spin-count data we could not reconcile the experimentally determined single crystal linewidths with de Biasi and Fernandes' model for any given range of the exchange interaction (determined by the parameter n). That a plot of Inglis et als measurements of the concentrations of isolated Fe^{3+} ions in cubic sites in their MgO samples against our experimentally determined linewidths does not produce a curve which can be interpreted in terms of de Biasi and Fernandes' dipolar broadening theory is probably due to the unreliable nature of spin-count data.

It is well establshed that counting spins of unknown concentration in a sample by comparing the linewidths of the spectrum due to this sample with those of a sample for which the spin concentration is known is quite inaccurate. In our particular case it might be thought that the presence of isolated Cr^{3+}, "clustered" Fe^{3+} and, in some cases, isolated Mn^{2+} ions in the MgO:Fe crystals will further increase the inaccuracy of the spin-counting method because these impurities will also broaden the lines in the cubic Fe^{3+} spectrum. However, the isolated Cr^{3+} and Mn^{2+} concentrations are much less than the Fe^{3+} isolated ion concentration in all the crystals examined and also the dipolar interaction between unlike ions is much less than between like ions.[9.19] Moreover, any given isolated Fe^{3+} ion in a cubic site is unlikely to be in close proximity to more than one Fe^{3+} "cluster." Therefore the presence of species other than isolated Fe^{3+} ions in cubic sites will have a minimal effect on the accuracy of the spin-count data.

On the other hand, a possible source of error in Inglis et als spin-count data is the fact that their MgO:Fe samples were calibrated against a Varian "pitch in KCl" standard.Unless the line broadening mechanisms in the standard are identical to those in the MgO:Fe doped crystals then determining the concentration of isolated Fe^{3+} spins in an MgO crystal by comparing the intensity of the central transition in the cubic Fe^{3+} spectrum with that of the resonance line of the standard is not really valid. Ideally, an MgO:Fe crystal for which the concentration of Fe^{3+} ions is known should be used as a standard if the

spin-counting technique is to be employed to determine the isolated Fe^{3+} concentration in an iron-doped MgO crystal for which this parameter is unknown.

Assuming the magnitude of the cubic Fe^{3+} central transition linewidth to be determined mainly by dipolar interactions, the fact that it is approximately constant at all the dopant concentrations examined indicates that there is a maximum or "saturation" concentration of isolated Fe^{3+} ions which the MgO host lattice can support. It is assumed that the rest of the dopant exists in the "clustered" iron phase. This interpretation is supported by the fact that the intensity of the broad line associated with the clustered iron phase increases relative to that due to the cubic Fe^{3+} central transition as the total iron concentration increases.

In Chapter Seven it was shown that there is a saturation concentration of isolated Cr^{3+} ions which the MgO lattice can support. That Fe^{3+} and Cr^{3+} behave similarly as regards their solubility in MgO is because both ions have a valency of (+3). The excess positive charge which these ions have relative to the Mg^{2+} ions of the host lattice cannot be easily compensated for either by valency variation or by cation vacancies and hence their solubility is limited.[9.20-9.22] This lack of solubility encourages clustering of the (+3) ions into complexes that internally compensate their excess positive charge. In the case of Cr^{3+} the complex is the spinel $MgCr_2O_4$, in the case of Fe^{3+}, formation of a complex, or perhaps several different types of complex without any definite crystal structure takes place.

9.1.3 INTERPRETATION OF THE LINEWIDTHS OF THE FINE STRUCTURE TRANSITIONS IN THE CUBIC Fe^{3+} SPECTRA

Reference to Table 9.1 shows that in the cubic Fe^{3+} spectra of all the as received single crystals of MgO:Fe examined, the transition linewidths increase with the absolute values of the quantum labels characterizing the transitions. This experimentally observed trend is in qualitative agreement with that predicted by the strain broadening model outlined in section 6.3.

According to the theory of section 6.3, the contribution of strain broadening towards the width of any given line is proportional to $(2M - 1)^2$. Therefore, the width of the $M = +\frac{1}{2} \longleftrightarrow -\frac{1}{2}$ line is unaffected by the presence of random internal stresses in the crystal ($(2M - 1)^2 = 0$ for this transition) and the magnitude of the width of this line, discussed in the previous section, is attributed to the effects of dipolar interactions between the isolated Fe^{3+} ions in cubic sites. It is proposed that in addition to the line broadening attributable to the effects of dipolar interactions (this source of broadening contributes a component towards the total linewidth equal to the width of the $M= +\frac{1}{2} \longleftrightarrow -\frac{1}{2}$ line) the $M = \pm 3/2 \longleftrightarrow \pm 1/2$ and $M = \pm 5/2 \longleftrightarrow \pm 3/2$ lines are further broadened because of the presence of random internal strains in the crystals examined (for these lines $(2M - 1)^2 \neq 0$).

Quantitative analysis of the experimentally observed linewidths in terms of the strain broadening theory discussed in section 6.3 was restricted to the spectrum of the sample doped with 310 p.p.m. of iron because only for this sample could the widths of the $M = \pm 5/2 \longleftrightarrow \pm 3/2$

transitions be measured. Unfortunately, for both the Gaussian and the Lorentzian strain broadening models (see section 8.1.3 and reference 9.23), it was found that quantitative agreement between theory and experiment was lacking. Nevertheless, in the light of the good qualitative agreement already mentioned it seems reasonable to suppose that the fine structure transitions in the cubic Fe^{3+} spectra of the as received MgO:Fe single crystals examined are strain broadened.

It is also interesting to note from the data listed in Table 9.1 that as the width of the $M = +\frac{1}{2} \longleftrightarrow -\frac{1}{2}$ transition increases there is a corresponding increase in the average width of the $M = \pm 3/2 \longleftrightarrow \pm 1/2$ transitions. As discussed in the previous section, an increase in the width of the $M = +\frac{1}{2} \longleftrightarrow -\frac{1}{2}$ transition implies an increase in the concentration of isolated Fe^{3+} ions in cubic sites. This in turn will lead to an increase in the concentration of cation vacancies required to provide electrical compensation for the single excess positive charge which each Fe^{3+} ion has with respect to the Mg^{2+} ion of the host lattice which it replaces. Increasing the cation vacancy concentration will also increase the degree of lattice distortion in the crystal thereby enhancing the contribution of strain broadening towards the width of the fine structure lines. The above interpretation implies that the compensating cation vacancies must be located quite near to isolated Fe^{3+} ions in cubic sites in order to produce distortion in the regions of the lattice occupied by these ions but not so close that they alter the symmetry of the sites occupied by the Fe^{3+} ions. .

In an attempt to confirm our interpretation concerning the sources of broadening contributing to the fine structure linewidths, as received single crystals of the three most lightly doped samples (those containing 310 p.p.m., 2,300 p.p.m. and 4,300 p.p.m. of iron) were "annealed" at 500^{o}C for 24 hours in an oxygen atmosphere and then cooled down gradually to room temperature over a period of 10 hours. Cubic Fe^{3+} spectra were recorded from the annealed crystals at room temperature with H // <100> and analysed using the procedures described in section 9.1.1. The parameters characterizing the spectra are given in Table 9.2.

As expected, the annealing procedure has no effect on the parameters g and a, the values in Table 9.2 being in good agreement both with those measured for the corresponding as received single crystals and also with those reported in the literature.[9.1-9.6] However, in all cases the width of the M = $+\frac{1}{2} \longleftrightarrow -\frac{1}{2}$ transition is greater whilst the average widths of the fine structure transitions are less in the spectrum of the annealed single crystal than in the spectrum of the corresponding as received single crystal.

The increase in the width of the central transition caused by the annealing procedure suggests that the particular heat treatment chosen leads to partial dissolution of the Fe^{3+} "clusters" and a corresponding increase in the concentration of isolated Fe^{3+} ions in cubic sites. The increase in the concentration of isolated Fe^{3+} ions in cubic sites necessarily leads to an increase in the concentration of compensating cation vacancies.

Earlier in this section it was proposed that an increase in the concentration of compensating cation

IRON CONCENTRATION (p.p.m. by weight)	SPECTROSCOPIC SPLITTING FACTOR g	FINE STRUCTURE CONSTANT, a, ($\times 10^4$ cm^{-1})	ΔHpp ($\frac{1}{2} \leftrightarrow \frac{1}{2}$) TRANSITION mT	$\overline{\Delta Hpp}$ ($\pm \frac{1}{2} \leftrightarrow \pm \frac{3}{2}$) TRANSITIONS mT	$\overline{\Delta Hpp}$ ($\pm \frac{3}{2} \leftrightarrow \pm \frac{5}{2}$) TRANSITIONS mT	MICROWAVE FREQUENCY GHz
310	2.0041	200.9	0.532	1.220	1.858	9.3820
2300	2.0025	207.9	0.554	2.181	-	9.3825
4300	2.0028	204.1	0.556	2.511	-	9.3820

TABLE 9.2 E.P.R. PARAMETERS FOR "ANNEALED" SINGLE CRYSTAL Fe/MgO:

MEASUREMENTS TAKEN FROM SPECTRA RECORDED AT 293K WITH H//<100> .

vacancies causes broadening of the fine structure transitions. However, the fine structure transitions are actually narrower in the spectra of the annealed single crystals than in the spectra of the corresponding as received single crystals. This behaviour may be explained in terms which would tend to confirm our suggestion that the fine structure transitions are strain broadened i.e. the relaxation of the host lattice caused by the annealing procedure more than compensates for the increase in lattice distortion which is also brought about by the heat treatment as a result of the increase in the concentration of compensating cation vacancies. In other words, the annealing process produces an overall reduction in the amount of lattice distortion in the regions immediately surrounding isolated Fe^{3+} ions in cubic sites, thereby leading to an overall reduction in the widths of the fine structure transitions.

9.2 EXPERIMENTAL RESULTS FOR POWDERED MgO:Fe

9.2.1 COMPARISON OF EXPERIMENTAL AND COMPUTER SIMULATED POWDER SPECTRA FOR THE LIGHTLY DOPED SAMPLES

Single crystal chippings of the three most lightly doped MgO samples (those containing 310 p.p.m., 2,300 p.p.m. and 4,300 p.p.m. of iron) were crushed with a mortar and pestle and sieved through a 185 μm mesh. This ensured that in the powders thus produced at least 20,000 individual crystallites were absorbing microwave power at resonance.

E.P.R. spectra were recorded at room temperature from the three powder samples prepared in the manner

described above on the Varian V4205-15 E.P.R. spectrometer. A typical trace is shown in Figure 9.4 (the particular spectrum illustrated was recorded from the MgO powder doped with 2,300 p.p.m. of iron).

A line at a magnetic field value corresponding to g = 1.9800 was clearly visible in all the recorded spectra. This line is due to the isotropic $M = +\frac{1}{2} \longleftrightarrow -\frac{1}{2}$ and $M = \pm 3/2 \longleftrightarrow \pm 1/2$ transitions of Cr^{3+} ions in cubic sites which are coincident (it is labelled "Cr^{3+}" in Figure 9.4).

Five almost equally spaced lines which are also visible in all the recorded spectra have been attributed to the $M = +\frac{1}{2} \longleftrightarrow -\frac{1}{2}$, m transitions of isolated Mn^{2+} ions in sites of octahedral symmetry and are labelled accordingly in Figure 9.4. Although there are six such lines in the cubic Mn^{2+} spectrum the $M = +\frac{1}{2} \longleftrightarrow -\frac{1}{2}, m = +\frac{1}{2}$ transition overlaps with and is obscured by the cubic Cr^{3+} central transition.

The features labelled S_1, S_2, D_1 and D_2 in Figure 9.4 are all attributable to the $M = +\frac{1}{2} \longleftrightarrow -\frac{1}{2}$ transition of isolated Fe^{3+} ions located in cubic symmetry sites. S_1 and S_2 are shoulders and D_1 and D_2 are divergences in the powder absorption curve of this transition. The shoulders and divergences attributable to the fine structure transitions of Fe^{3+} ions in cubic sites are not observed. This is probably because these transitions are highly anisotropic and so their total intensity is spread out over a wide range of magnetic field. Thus, the features (shoulders and divergences) in the powder absorption curves of these transitions will be of very low amplitude and it is likely that they are lost in the background noise

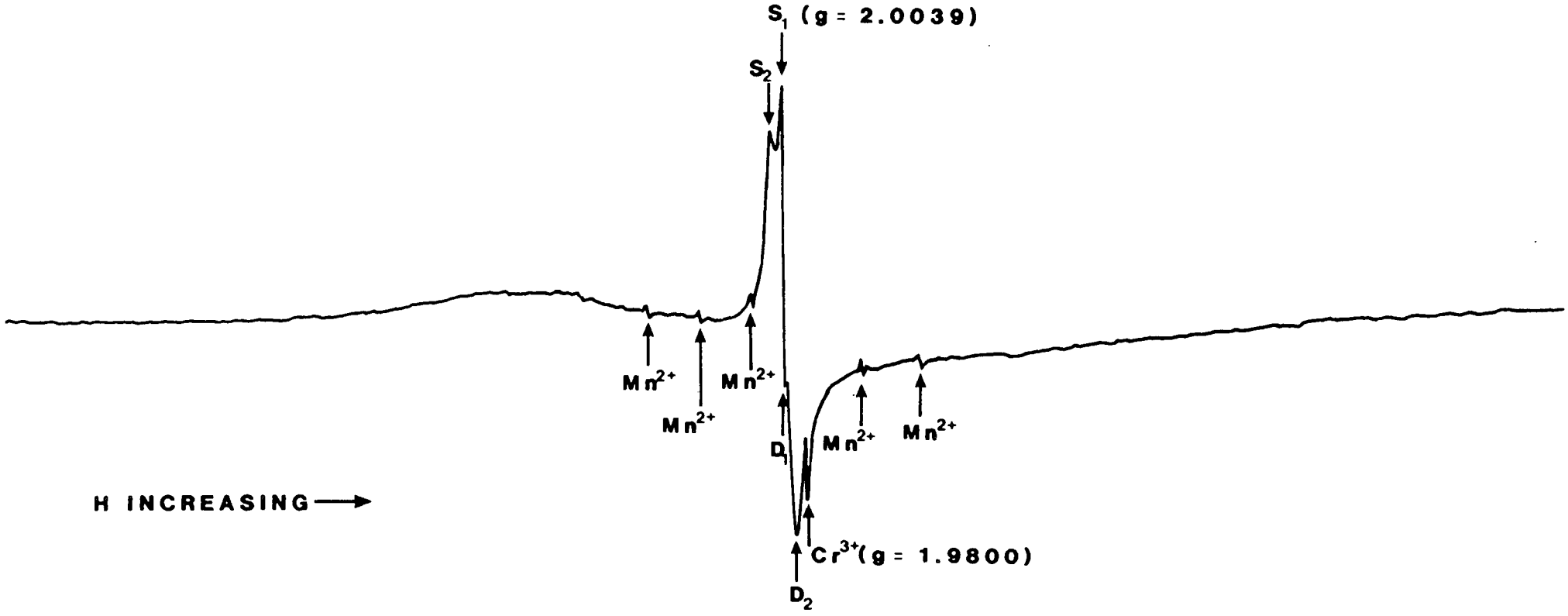

FIGURE 9.4 E.P.R. SPECTRUM OF POWDERED MgO:Fe;
IRON CONCENTRATION = 2,300p.p.m; T = 293K; ν = 9.3795 GHz.

of the recorded spectra.

The experimentally observed behaviour agrees in principle with the predictions of the simulation procedure discussed in section 5.3 and reference 9.24 (namely that the single crystal M = $+\frac{1}{2} \longleftrightarrow -\frac{1}{2}$ transition of $^6S_{5/2}$ ions in a cubic field is split into four components when the sample is powdered). Table 5.2 gives the theoretical positions of the features S_1, S_2, D_1 and D_2 in terms of the g-factor, the fine structure constant, a, and the applied magnetic field.

The g-factors given in Table 9.3 for the three powders examined were determined from the magnetic field position of the shoulder S_1 ($=H_o$) on the experimental spectra since $g = h\nu / \beta H_o$. The fine structure constant, a, was calculated for each sample from the experimentally observed separations of S_1 and S_2 ($=40a^2/27H_o$) and the values obtained are also given in Table 9.3. Finally, the observed separation of D_2 and S_1 ($= 49a^2/30H_o + \tau/\sqrt{3}$) in the powder spectrum of each doped sample was used to determine the linewidth, ΔH_{pp}, ($=2\tau/\sqrt{3}$) between points of maximum slope (this parameter is listed in column four of Table 9.3 for the three samples examined).

The values of a and g given in Table 9.3 agree well both with the single crystal data (see Table 9.1) and also with previously published data.[9.1-9.6,9.24] It is noticeable, however, that the M = $+\frac{1}{2} \longleftrightarrow -\frac{1}{2}$ transition linewidth is somewhat larger for the powders than for the corresponding single crystals.

The broad line of low amplitude observed in the single crystal spectra is also observed in the powder spectra.

IRON CONCENTRATION (p.p.m. by weight)	SPECTROSCOPIC SPLITTING FACTOR g	FINE STRUCTURE CONSTANT, a, ($\times 10^4$ cm^{-1})	ΔHpp $M = +\frac{1}{2} \leftrightarrow -\frac{1}{2}$ TRANSITION mT	MICROWAVE FREQUENCY GHz
310	2.0043	184.4	1.642	9.3785
2300	2.0039	194.3	0.900	9.3790
4300	2.0027	195.4	0.969	9.3785

TABLE 9.3 E.P.R. PARAMETERS FOR POWDERED Fe/MgO SAMPLES:

MEASUREMENTS TAKEN AT 293K.

Its intensity only appears to be greater in Figure 9.4 than in Figure 9.1 because the powder spectra were recorded at higher gains than the single crystal spectra. Higher gains are required to record the powder spectra because the intensity of the single crystal $M = +\frac{1}{2} \longleftrightarrow -\frac{1}{2}$ transition, which consists of a single line, is shared among four lines spread over a much wider field range in the powder. Therefore the height of any one of the four peaks in the powder spectrum is much less than that of the single peak in the single crystal spectrum. As in the single crystal case we attribute the broad line to a clustered iron phase which may be ferrimagnetic or paramagnetic in nature.

The powder spectrum was predicted at each dopant concentration (310 p.p.m., 2,300 p.p.m. and 4,300 p.p.m. of iron) using all the computer simulation methods described in Chapter Five. The variables in the simulation procedure are the g-factor, the fine structure constant, a, the linewidth, ΔH, the microwave frequency, ν , and the lineshape function. In order to deduce the lineshape function the first derivitive lineshapes of the cubic Fe^{3+} $M = +\frac{1}{2} \longleftrightarrow -\frac{1}{2}$ transitions recorded experimentally from the single crystal samples were integrated numerically. The integrated absorption functions were compared with computer generated theoretical Lorentzian and Gaussian lineshapes and found to be Lorentzian in shape. Using the least squares method, the width of the Lorentzian curve which gave the best fit to each experimental absorption function was determined. The integrated experimental lineshape for the sample doped with 2,300 p.p.m. of iron is shown in Figure 9.5 together with the Lorentzian curve whose

linewidth best fits the experimental data at this dopant concentration.

Simulations of the powder spectra of the three most lightly doped samples were produced using both the data in Table 9.1 and also using the data in Table 9.3. A Lorentzian lineshape function was employed for all the simulations generated at each dopant concentration since it was established (see above) that the M = $+\frac{1}{2} \longleftrightarrow -\frac{1}{2}$ transition in the single crystal cubic Fe^{3+} spectrum had this shape. Thus, in all, six simulations were generated at each dopant concentration; each of the three computer simulation methods described in section 5.3 was used to predict the powder spectrum with, firstly, the experimental single crystal data, and, secondly, the experimental powder spectrum data as the variables in the simulation procedure. Typical examples for the sample doped with 2,300 p.p.m. of iron using the experimental single crystal data (Table 9.1) and the experimental powder data (Table 9.3) are shown in Figures 9.6(a) and 9.6(b) respectively.

Comparison of Figures 9.6(a) and 9.6(b) with Figure 9.4 shows that there is reasonable agreement between the experimentally recorded powder spectrum and the simulated powder spectrum for the sample doped with 2,300 p.p.m. of iron whether the observed single crystal spectrum data or the observed powder spectrum data is used in the simulation procedure. Similar agreement between the simulated and experimental powder spectra was also found for the samples doped with 310 p.p.m. and 4,300 p.p.m. of iron. Obviously, the lines due to Cr^{3+} and Mn^{2+} ions in cubic sites and the broad line attributed to clustered Fe^{3+} ions which are

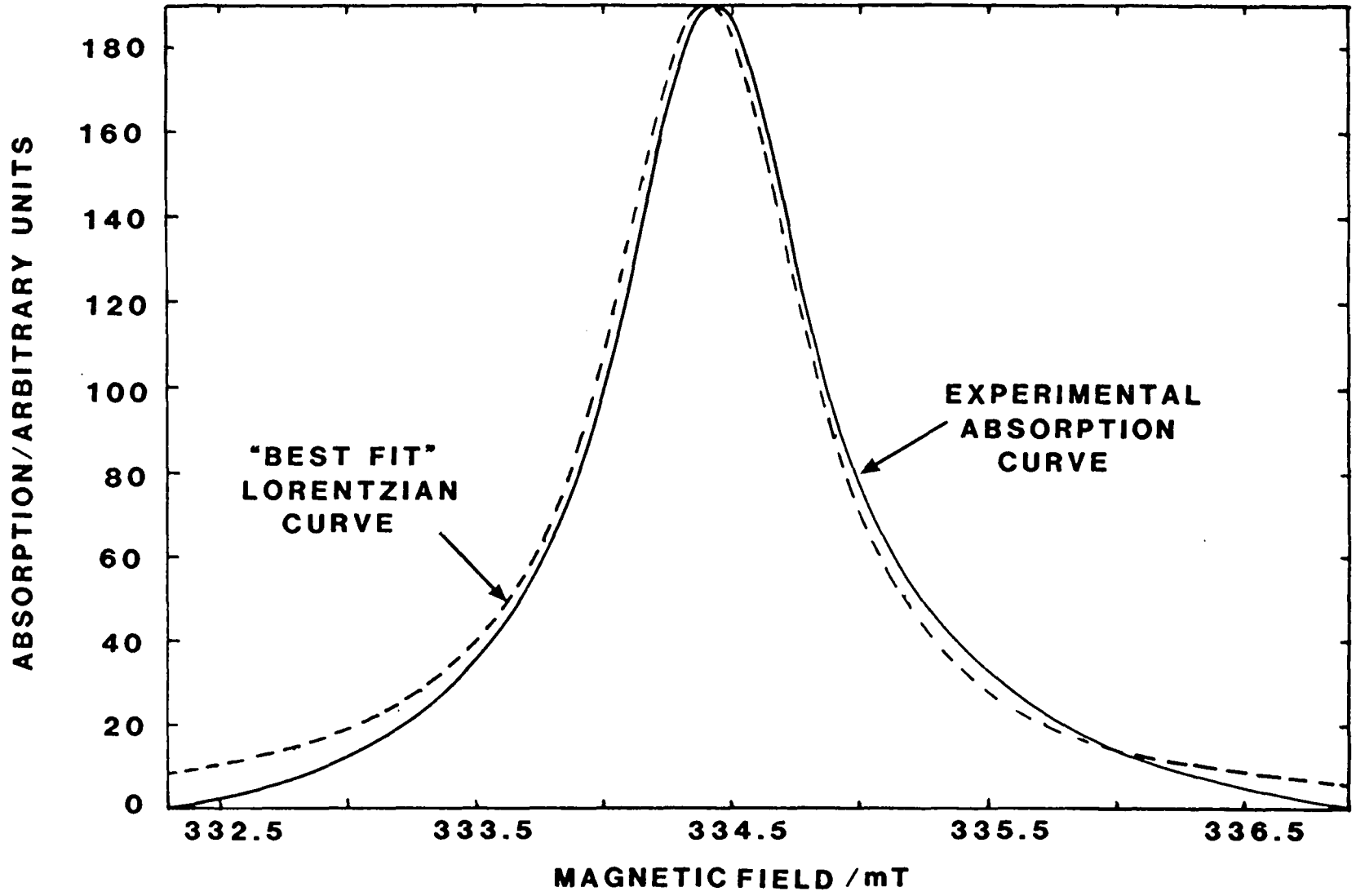

FIGURE 9.5 INTEGRATED EXPERIMENTAL ABSORPTION CURVE (SMOOTH LINE) AND "BEST FIT" LORENTZIAN LINESHAPE FUNCTION (DASHED LINE) FOR SINGLE CRYSTAL MgO:Fe; IRON CONCENTRATION = 2,300p.p.m.

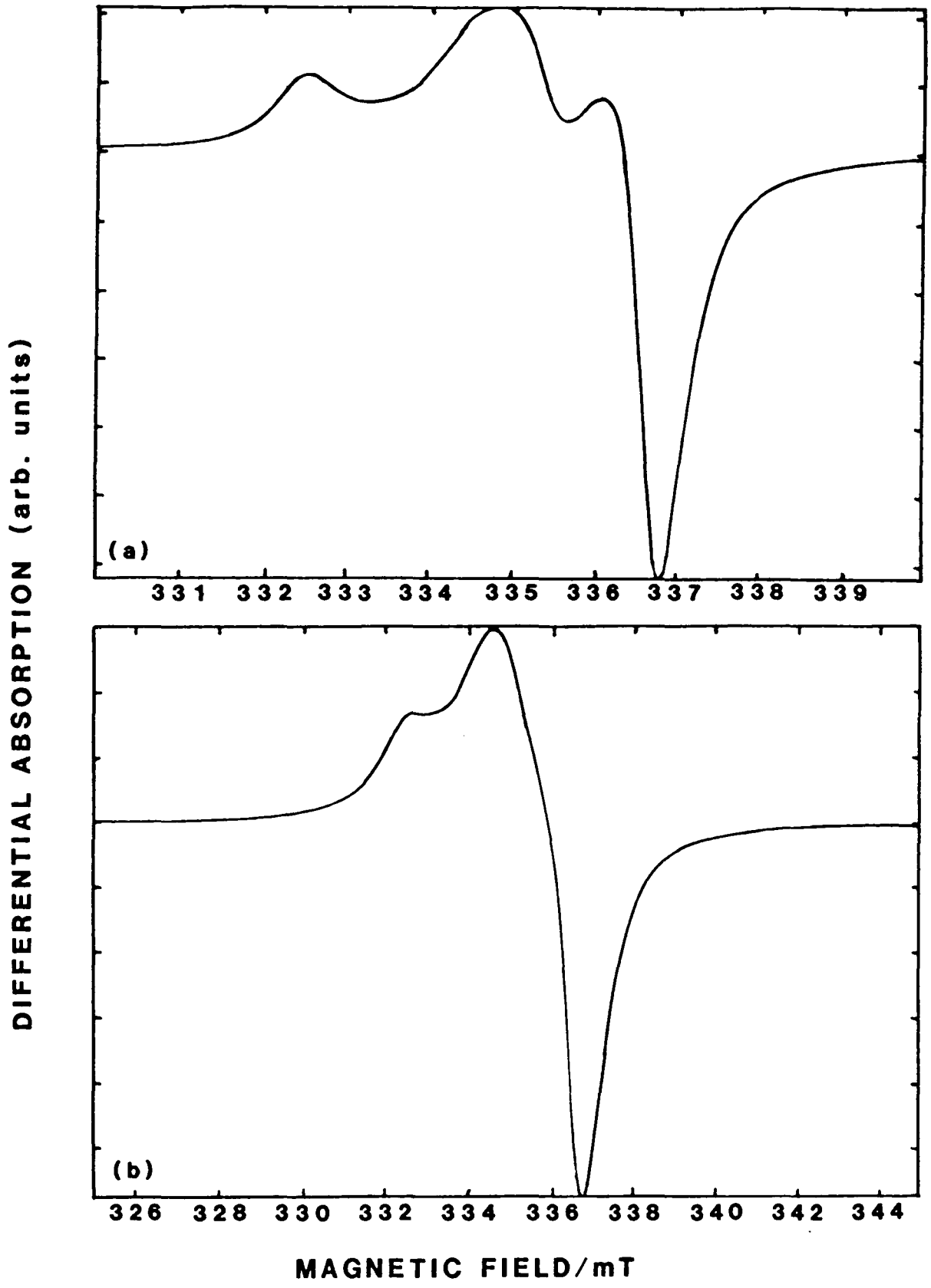

FIGURE 9.6 COMPUTER SIMULATED POWDER SPECTRA FOR MgO:Fe USING (a) SINGLE CRYSTAL DATA (b) POWDER DATA; IRON CONCENTRATION = 2,300p.p.m.

observed in the experimental powder spectra are not present in the simulations which were designed to show the powder absorption curve for Fe^{3+} ions in cubic sites only.

The four features attributable to the $M = +\frac{1}{2} \longleftrightarrow -\frac{1}{2}$ transition of Fe^{3+} ions in cubic sites are clearly visible in the experimentally observed powder spectra and are also particularly prominent in the simulations produced using the measured single crystal parameters. These features are less obvious in the predicted powder spectra when the parameters obtained from the experimental powder spectra are used in the simulation procedure. However, the experimentally observed lineshape more closely resembles the simulated powder absorption curve when powder data is used in the simulation procedure than when single crystal data is used. Furthermore, the field positions of the features visible in the series of simulations produced using powder data are in better agreement with those measured experimentally than are the field positions of the features in the series of simulations produced using single crystal data. This is not surprising since the powder data simulations employ information obtained directly from the experimental spectra they are trying to predict.

At any given dopant concentration, the only parameter which is significantly different for the single crystal and powder data used in the simulations is the linewidth. Thus, the fact that the powder linewidth is found to be greater than the single crystal linewidth for the cubic Fe^{3+} spectra at all the dopant concentrations examined is likely to be the cause of the observed discrepancies between the spectra predicted using the two individual sets of

measurements.

As already mentioned in Chapter Eight, the dipolar linewidth varies with the orientation of the magnetic field to the crystal axes.[9.4, 9.7, 9.25, 9.26] However, the simulations produced using single crystal data assumed the dipolar linewidth at all crystallite orientations to be the same as that when H // <100>. The linewidths used in the powder data simulations were measured directly from the experimental powder spectra and therefore presumably represent the mean dipolar linewidths obtained when the individual values of this parameter at all possible orientations are averaged.

This would seem to indicate that powder data should be used for the simulation procedure in order to obtain the best fit to the experimental powder spectrum. However, as was shown earlier, both series of simulations (one using powder data and the other using single crystal data) have certain (different) attributes which correlate with those of the experimentally observed powder spectra. This implies that the best simulation at any given dopant concentration would be obtained using a Lorentzian line-shape function whose width lies somewhere between those observed experimentally for the M = $+\frac{1}{2} \longleftrightarrow -\frac{1}{2}$ transition in the single crystal (when H // <100>) and in the powder. The reason why this should be the case is not clearly understood.

9.2.2 THE EFFECT OF HEAT TREATMENT UPON THE LIGHTLY DOPED SAMPLES

The powders doped with 310 p.p.m., 2,300 p.p.m. and 4,300 p.p.m. of iron were heat treated at 500^{o}C for 24 hours in an oxygen atmosphere and then gradually cooled down to room temperature over a period of 10 hours. E.P.R. spectra were recorded from each heat treated sample at 293K on the Varian V4205-15 spectrometer system.

Analysis of the traces using the method described in the previous section revealed that the heat treatment had modified the spectra of the samples doped with 2,300 p.p.m. and 4,300 p.p.m. of iron recorded prior to the heat treatment as follows: the relative peak heights of the shoulders S_1 and S_2 were reversed and the linewidth of the isolated Fe^{3+} ion spectrum (deduced from the separations of the features S_1 and D_2) increased (from 0.900 mT prior to heat treatment to 2.043 mT after heat treatment in the case of the sample doped with 2,300 p.p.m. of iron and from 0.969 mT prior to heat treatment to 2.942 mT after heat treatment in the case of the sample doped with 4,300 p.p.m. of iron). In addition, after heat treatment the relative intensity of the broad line attributed to a "clustered" iron phase increased in the spectrum of the sample containing 4,300 p.p.m. of iron. Heat treatment had no effect on the spectrum of the sample doped with 310 p.p.m. of iron.

Let us consider the changes in the spectra of the samples doped with 2,300 p.p.m. and 4,300 p.p.m. of iron brought about by the heat treatment. The reversal of the peak heights of the shoulders S_1 and S_2 caused by the heat

treatment indicates that, to some extent, it removes lattice strain present in the powders prior to heat treatment. This is because lattice strain may result in the crystal field parameters (there is only one parameter, a, in the case of the cubic Fe^{3+} spectrum) having a range of distributed values[9.24] without changing the overall symmetry of the sites occupied by the isolated Fe^{3+} ions (which would drastically alter their E.P.R. spectrum). Hence, as the field position of S_1 is independent of a whereas that of S_2 is not, in a strained sample S_2 will be broadened and consequently its peak height reduced relative to that of S_1. Removal of the strain by the "annealing" heat treatment sharpens up the shoulder S_2 to the extent that its peak height actually exceeds that of the shoulder S_1. As in the single crystal case, the likely source of the lattice strain is cationic vacancies (required to compensate the single excess positive charge of the Fe^{3+} ions relative to the Mg^{2+} ions of the host lattice) which must be far enough removed from the substitutional dopant ions so as to only distort and not to change the symmetry of the sites they occupy.

That heat treatment causes the linewidth of the spectrum of isolated Fe^{3+} ions in cubic sites to increase cannot therefore be attributed to strain since the behaviour of the shoulders S_1 and S_2 shows that heat treatment reduces the lattice distortion in the powders under consideration. Instead, it is presumed to be due to migration of Fe^{3+} ions (which have a high mobility in the MgO lattice[9.27]) to regions adjacent to "clusters". Because the "clusters" contain many Fe^{3+} ions they will

broaden the spectrum of nearby isolated Fe^{3+} ions substantially through the dipolar interaction. Again, the isolated Fe^{3+} ions must be sufficiently removed from the "clusters" so that the symmetry of the sites they occupy is not changed (obviously, the host lattice will be quite seriously disrupted in the region immediately surrounding a cluster of iron atoms).

It is proposed that the broad line attributed to a "clustered" iron phase increases in intensity in the spectrum of the sample doped with 4,300 p.p.m. of iron after heat treatment because the clusters become progressively more ordered during the heating process.[9.9,9.10,9.28,9.29] The ordering of the clustered phase is also aided by the high mobility of Fe^{3+} ions in the MgO lattice.[9.27]

Broadening of the $M = +\frac{1}{2} \longleftrightarrow -\frac{1}{2}$ transition in the single crystal spectrum of isolated Fe^{3+} ions in cubic sites was also observed after heat treatment. In section 9.1.3 this broadening was attributed to partial dissolution of the Fe^{3+} "clusters". However, it is quite possible that this interpretation is wrong. It could be that, as in the powder case, isolated Fe^{3+} ions in the single crystals are migrating towards Fe^{3+} clusters and the ions in the cluster broaden the isolated ion spectrum through the dipolar interaction.[9.30] The broadening of the isolated ion spectrum is much less in a doped single crystal than in a powder doped at the same level. However, this is to be expected (assuming that the source of the broadening is the same in the single crystal and the powder), since the surface area of the powder is much greater than that of the single crystal. . Therefore migration of isolated Fe^{3+}

ions towards clusters (there is a tendency for this to take place in MgO) will be much more rapid in the powder than in the corresponding single crystal at a given temperature. In any case, the isolated Fe^{3+} ions in the single crystal samples must be sufficiently removed from clusters even after heat treatment not to be influenced by the strain fields surrounding them, as the single crystal fine structure linewidths (which are increased in the presence of strain fields) are actually reduced after heat treatment (see section 9.1.3).

No increase in the intensity of the broad line attributed to Fe^{3+} "clusters" was observed after heat treatment in the single crystal spectrum of the sample doped with 4,300 p.p.m. of iron. However, detection of any such increase would be extremely difficult for two reasons. Firstly, as mentioned above, the low surface area of the single crystal severely curtails the mobility of Fe^{3+} ions in the single crystal compared to in the powder. Thus ordering of the clustered iron phase would take place much more slowly in the single crystal than in the powder at a given temperature. Secondly, the amplitude of the broad line compared to the amplitude of the isolated ion spectrum is much less in the single crystal than in the powder. Thus an increase in the intensity of the broad line after heat treatment of the single crystal may occur, but escapes detection because of the initial low intensity of this line before heat treatment.

Not surprisingly, the observed effects of heat treatment appear to be concentration dependent. This is

basically because the number of clusters will increase with iron concentration (the isolated Fe^{3+} ion concentration is virtually constant at all doping levels (see section 9.1.2)). Thus the migration of isolated ions during heat treatment in a sample doped at a low level will not effect the isolated ion spectral linewidths to the same extent as in a sample for which the dopant concentration is higher. In other words, it is statistically less likely that an isolated ion will reside near a cluster at the end of the heat treatment for a lightly doped sample than for a heavily doped sample.

Also, the ordering of the clustered iron phase will proceed more rapidly during heat treatment if the iron concentration is higher because of the higher density of clustered material. This is because, if we assume that "ordering" of the clustered iron phase represents the amalgamation of several small groups of ions, then it is statistically probable that coalescence of small groups of ions into larger clusters will take place to a greater extent the higher the iron concentration. Thus, the ease of precipitation of large, ordered clusters will increase with the iron concentration.

Hence heat treatment has no effect on the spectrum of the sample doped with 310 p.p.m. of iron in which the "clustered" iron concentration is low. Also, when the clustered iron concentration is intermediate (at a nominal dopant concentration of 2,300 p.p.m.), only the broadening of the isolated ion spectrum is observed after heat treatment. Finally, when the clustered iron concentration is high (at a nominal dopant concentration of 4,300 p.p.m.)

both broadening of the isolated ion spectrum and also an increase in the intensity of the broad line attributable to the clustered phase material is observed after heat treatment.

9.2.3 THE POWDER SPECTRA OF THE HEAVILY DOPED SAMPLES

Single crystal chippings of the three most heavily doped samples (those containing 8,500 p.p.m., 11,900 p.p.m. and 12,900 p.p.m. of iron) were crushed with a mortar and pestle and sieved through a 185 μm mesh. This ensured that in the powders thus produced at least 20,000 individual crystallites were absorbing microwave power at resonance.

E.P.R. spectra were recorded at room temperature from the three powder samples prepared in the manner described above on the Varian V4205-15 E.P.R. spectrometer. The trace recorded from the sample doped with 11,900 p.p.m. of iron is shown in Figure 9.7.

In Figure 9.7, as in the powder spectra of all the heavily doped samples, the broad feature attributed to clustered Fe^{3+} ions is much greater in intensity than the group of four lines attributable to isolated Fe^{3+} ions in sites of cubic symmetry. In fact, for these samples, the broad feature is so intense that it heavily distorts the isolated ion spectrum which therefore cannot be analysed using the method described in section 9.2.1.

The lines due to Mn^{2+} and Cr^{3+} ions in sites of cubic symmetry seen in the powder spectra of the lightly doped samples are also seen in the powder spectra of the heavily doped samples and these lines are labelled accordingly in Figure 9.7.

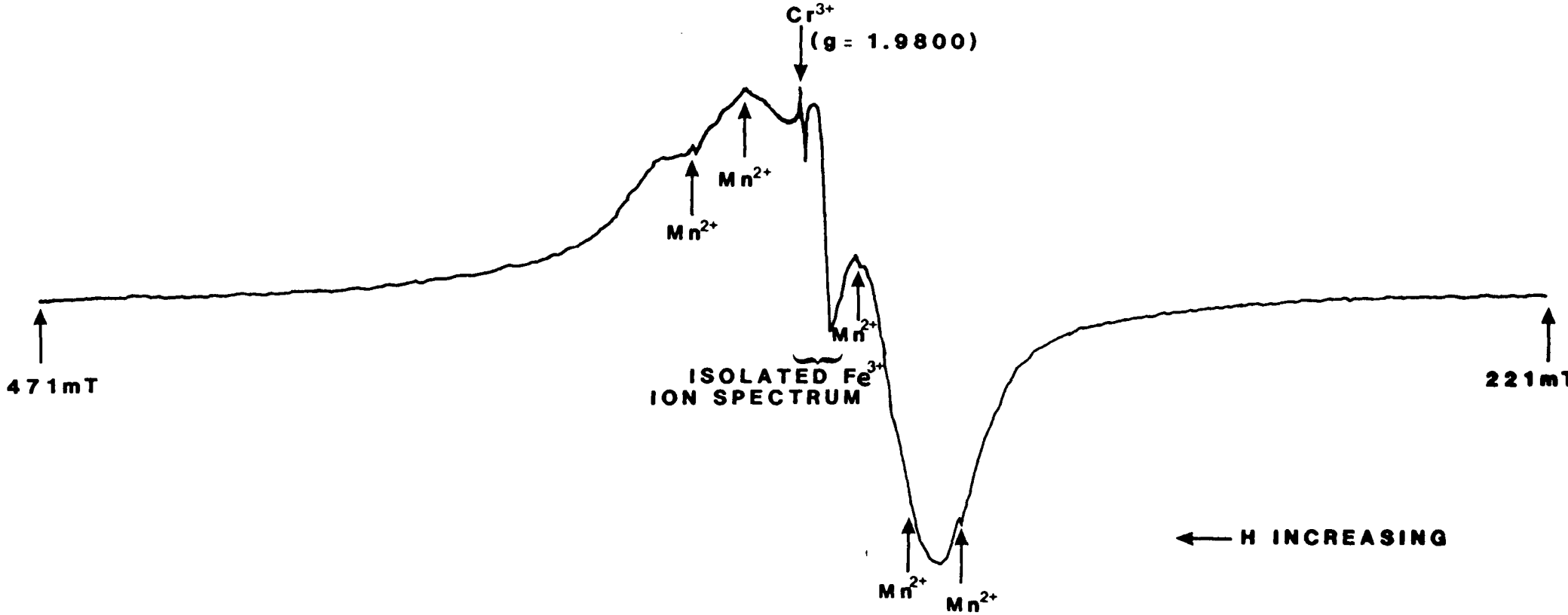

FIGURE 9.7 E.P.R. SPECTRUM OF POWDERED MgO:Fe;
IRON CONCENTRATION = 11,900 p.p.m.; T = 293K; ν = 9.3800GHz.

The nature of the broad feature assigned to clustered Fe^{3+} ions varies with iron concentration for the heavily doped samples. In the spectrum of the sample containing 8,500 p.p.m. of iron it appears as a single line whereas in the spectra of the samples containing 11,900 p.p.m. and 12,900 p.p.m. of iron it consists of two or more overlapping lines and thus the clustered Fe^{3+} ion spectral lineshapes are complex for the two most heavily doped powders.

Attempts were made to calculate the relative intensities of the spectra due to isolated and clustered Fe^{3+} ions for each of the heavily doped samples using the expression:[9.22,9.31]

$$I \quad \alpha \quad (\Delta H)^2 h \qquad (9.1)$$

where I is the relative intensity, ΔH is the peak-to-peak linewidth and h is the peak height of the spectrum in question. The relative intensities of the two spectra in any given doped sample lead us directly to the concentrations of isolated and clustered Fe^{3+} ions in that sample. This is because the ratio of the relative intensities is equal to the ratio of the number of spins involved in the two spectra.

Thus, since the total iron concentration ($=[Fe]_{total}$) is known, if we assume that all the iron either exists as isolated Fe^{3+} ions or clustered Fe^{3+} ions then:

$$[Fe^{3+}]_{isol} = \frac{(I)_{isol}}{[(I)_{isol} + (I)_{clust}]} [Fe]_{total} \quad (9.2)$$

and

$$[Fe^{3+}]_{clust} = \frac{(I)_{clust}}{[(I)_{isol} + (I)_{clust}]} [Fe]_{total} \quad (9.3)$$

where

$[Fe^{3+}]_{clust}$ = concentration of Fe^{3+} ions in the clustered iron phase

$[Fe^{3+}]_{isol}$ = concentration of isolated Fe^{3+} ions

$(I)_{clust}$ = relative intensity of the clustered iron phase spectrum

& $(I)_{isol}$ = relative intensity of the isolated ion spectrum.

Unfortunately, equations 9.2 and 9.3 could not be applied successfully to the spectra of the heavily doped samples. This is probably because of the complex nature of the spectral lineshapes (in the case of the isolated ion spectrum the lineshape is complex for all the heavily doped samples and in the case of the clustered iron spectrum, as mentioned above, it is complex for the samples containing 11,900 p.p.m. and 12,900 p.p.m. of iron). Meaningful results will only be obtained if the lines involved in an analysis using equations 9.2 and 9.3 are isotropic and either purely Lorentzian or purely Gaussian in shape.[9.22,9.31]

9.3 SUMMARY OF RESULTS FOR THE MgO:Fe SYSTEM

Characterization of the E.P.R. spectra indicates that, in both the single crystals and powders examined, a small fraction of the dopant exists as isolated Fe^{3+} ions in cubic sites (the Fe^{3+} ions probably substitute for Mg^{2+} ions) and that the remainder of the dopant exists as Fe^{3+} ions clustered together. The complex defects formed by the clustered Fe^{3+} ions probably vary in size and nature because RHEED investigations suggested that the precipitates have no regular crystal structure.

That the regions of the host lattice immediately surrounding isolated Fe^{3+} ions in both the single crystal and powder samples are strained is indicated by the fact that, prior to heat treatment, the fine structure transitions in the single crystal isolated ion spectrum are broader than the $M = +\frac{1}{2} \longleftrightarrow -\frac{1}{2}$ transition and also by the fact that after heat treatment the peak heights of the shoulders S_1 and S_2 are reversed in the powder spectrum of isolated Fe^{3+} ions. The effect of heat treatment upon the isolated ion powder spectrum indicates that, at least to some extent, it relieves the lattice strain in the regions surrounding the isolated Fe^{3+} ions. Further evidence for the "annealing" effect of the heat treatment is provided by the fact that it reduces the widths of the fine structure transitions in the single crystal isolated ion spectrum.

The annealing process also alters the distribution of the Fe^{3+} ions in the host lattice even though the heat treatment was carried out at a comparatively low temperature ($500^{o}C$). This is probably because Fe^{3+} ions have a high mobility[9.27] and also a tendency to cluster (see below)

in the MgO lattice.

Evidence from single crystal spectra suggested that heat treatment leads to partial dissolution of the clustered iron phase and a consequent increase in the isolated Fe^{3+} ion concentration. However, stronger evidence from powder spectra suggested that during the "annealing" process isolated Fe^{3+} ions migrate towards clusters and, in addition, small clusters coalesce into larger, more ordered structures. On balance, it is believed that the latter explanation most closely resembles the processes taking place in both the single crystal and powder samples during heat treatment.

Precipitates of the spinel $MgFe_2O_4$ have been observed in iron doped MgO by many groups of workers using various techniques[9.7-9.11,9.28,9.29,9.32-9.34] That the "annealing" process leads to growth and ordering of the clustered iron phase suggests that increasing the length of the heat treatment may eventually lead to the formation of $MgFe_2O_4$ in our samples. Indeed, the small clusters of Fe^{3+} ions, vacancies, Mg^{2+} ions and O^{2-} ions of variable composition present in the as received single crystals and powders examined in this work may be similar in nature to those investigated theoretically by Gourdin, Kingery and Driear.[9.35,9.36]

Gourdin, Kingery and Driear[9.35,9.36] concluded that large Fe^{3+} ion/defect aggregates which model a substantial portion of the unit cell of the spinel $MgFe_2O_4$ are the most energetically stable in MgO. These theoretical predictions would seem to be borne out by the behaviour of the Fe^{3+} ions in the samples studied, namely their marked

tendency to cluster. This tendency manifests itself during the sample manufacturing process (as the crystals are cooled from the preparation temperature to room temperature) and also when sufficient energy (i.e. the thermal energy of the heat treatment) is provided to allow the Fe^{3+} ions to diffuse through the MgO lattice.

REFERENCES

9.1 W. Low Proc. Phys. Soc. (London) B69, 1169 (1956)

9.2 F.A. Modine, E. Sonder and R.A. Weeks J. Appl. Phys. 48, 3514 (1977)

9.3 J.E. Wertz, J.W. Orton and P. Auzins J. Appl. Phys. 33, 322 (1962)

9.4 J.S. Thorp, R.A. Vasquez, C. Adcock and W. Hutton J. Mat. Sci. 11, 89 (1976)

9.5 A.D. Inglis and J.S. Thorp J. Mat. Sci. 16, 1887 (1981)

9.6 W. Low Phys. Rev. 105, 792 (1957)

9.7 A.D. Inglis "Clustering in iron-doped Magnesium Oxide" Ph.D. Thesis, University of Durham, 1981 (unpublished).

9.8 A.D. Inglis, G.J. Russell and J.S. Thorp J. Mat. Sci. 17, 2939 (1982)

9.9 D. Cordischi, F. Pepe, M. Schiavello and M. Valigi J. Chem. Soc., Faraday I 73, 62 (1977)

9.10 D. Cordischi, D. Gazzoli and M. Valigi J. Solid State Chem. 24, 371 (1978)

9.11 R.A. Weeks, J. Gastineau and E. Sonder Phys. Stat. Sol.(A) 61, 265 (1980)

9.12 W. Low and M. Weger Phys. Rev. 118, 1130 (1960)

9.13 A.M. Stoneham, K.A. Müller and W. Berlinger Solid State Comm. 10, 1005 (1972)

9.14 J.W. Orton, P. Auzins, J.H.E. Griffiths and J.E. Wertz Proc. Phys. Soc. 78, 554 (1961)

9.15 B. Henderson, J.E. Wertz, T.P.P. Hall and R.D. Dowsing J. Phys. C: Solid State Phys. 4, 107 (1971)

9.16 R.S. de Biasi and A. Caldas J. Phys. C: Solid State Phys. 10, 107 (1977)

9.17 R.S. de Biasi and A.A.R. Fernandes J. Phys C: Solid State Phys. 16, 5481 (1983)

9.18 "Operational considerations with the V4532 Dual Sample Cavity", Varian Publication No. 87-214-002, (Varian, Palo Alto)

9.19 J.H. van Vleck Phys. Rev. 74, 1168 (1948)

9.20 M. Valigi, F. Pepe and M. Schiavello J. Chem. Soc. Faraday I 71, 1631 (1975)

9.21 A. Cimino, M. Lo. Jacono, P. Porta and M. Valigi Z. Phys. Chem(Frankfurt), N.F. 51, 301 (1966)

9.22 D. Cordischi, J.C. Vickerman and A. Cimino Trans. Faraday Soc. 66, 1312 (1970)

9.23 E.R. Feher Phys. Rev. 136, A145 (1964)

9.24 V. Beltran-Lopez and J. Castro-Tello J. Mag. Res. 39, 437 (1980)

9.25 J.S. Thorp, M.D. Hossain, L.J.C. Bluck J. Mat. Sci. 14, 2853 (1979)

9.26 J.S. Thorp, M.D. Hossain, L.J.C. Bluck and T.G. Bushell J. Mat. Sci. 15, 903 (1980)

9.27 S.L. Blank and J.A. Pask J. Amer. Ceram. Soc. 52, 669 (1969)

9.28 G.P. Wirtz and M.E. Fine J. Amer. Ceram. Soc. 51, 402 (1968)

9.29 K.N. Woods and M.E. Fine J. Amer. Ceram. Soc. 52, 186 (1969)

9.30 D.M. Michael (Private communication)

9.31 C.P. Poole "Electron Spin Resonance" Wiley-Interscience, N.Y. (1967)

9.32 G.W. Groves and M.E. Fine J. Appl. Phys. 35, 3587 (1964)

9.33 G.P. Wirtz and M.E. Fine J. Appl. Phys. 38, 3729 (1967)

9.34 K.N. Woods and M.E. Fine J. Appl. Phys. 40, 3425 (1969)

9.35 W.H. Gourdin and W.D. Kingery J. Mat. Sci. 14, 2053 (1979)

9.36 W.H. Gourdin, W.D. Kingery and J. Driear J. Mat. Sci 14, 2074 (1979)